DOCTORAT / BRETAGNE SCIENCES
LOIRE / POUR L'INGENIEUR

UNIVERSITÉ DE NANTES

ANDRA

THESE DE DOCTORAT DE

L'UNIVERSITE DE NANTES

ECOLE DOCTORALE N° 602
Sciences pour l'Ingénieur
Spécialité : *Génie Civil*

Par

Arianna PICCOLO

Tunnel structural health monitoring in radioactive environment based on special distributed optical fibre strain sensing cables

Thèse présentée et soutenue à l'Université de Nantes, le 17 juillet 2020
Unité de recherche : Laboratoire GeM, 2 Chemin de la Houssinière, Nantes, France
Agence nationale pour la gestion des déchets radioactifs (Andra), 1-7 rue Jean-Monnet, Châtenay-Malabry, France

Rapporteurs avant soutenance :

Emmanuel Marin	Professeur	Université Jean Monnet
Jean-Paul Balayssac	Professeur	IUT Paul Sabatier

Composition du Jury :

Président :	Katerina Krebber	Dr., Ingénieur	BAM (DE)
Examinateurs :	Luca Palmieri	Professeur	Università degli Studi di Padova (IT)
Dir. de thèse :	Dominique Leduc	Maître de Conférences, HDR	Université de Nantes
Co-encadrant :	Yann Lecieux	Maître de Conférences	Université de Nantes
Co-encadrant :	Sylvie Delepine-Lesoille	Dr., Ingénieur, HDR	Sodern

Invité(s)

Béatrice Yven	Dr., Ingénieur	Andra
Etienne Friedrich	Dr., Ingénieur	Solifos AG

UNIVERSITÉ DE NANTES

Abstract

Génie Civil et Mécanique (GeM) - Civil and Mechanical Engineering research group

Doctor of Philosophy

Tunnel structural health monitoring in radioactive environment based on special distributed optical fibre strain sensing cables

by Arianna PICCOLO

In the context of Cigéo, the planned underground repository for long-lived radioactive waste, the repository cells must be monitored over the operation period to help guaranteeing the reversibility of the project. Being horizontal and loaded by 500 m of rock, the reduction of the cell, i.e. the convergence, must be followed to guarantee the possibility to retrieve the waste. This is possible with distributed optical fiber strain sensors, which are an adequate feasible sensor for the application. The research focuses on distributed strain sensing based on Brillouin and Rayleigh scatterings. As they will work in harsh environment, first of all we quantify the coupled temperature and γ-ray influence on the Pulse Pre Pump Brillouin Optical Time Domain Analysis (PPP-BOTDA) and Tunable Wavelength Coherent Optical Time Domain Reflectometry (TW-COTDR) response. Ageing tests of these distributed strain measuring systems are performed on-line, up to 1 MGy, at room temperature, 80 °C, 100 °C and 120 °C. Brillouin and Rayleigh measurement errors remain identical regardless of the temperature, while the higher temperature helps increasing the measurement distance range. The performed tests helped also to explain the origin of the Brillouin frequency shift under γ-rays, with an acoustic velocity variation of about 1 m/s in 1 MGy irradiated samples.

In the application optical fibers will be protected into strain sensing cables, so it is important to assess the impact of a harsh environment on the sensor external sheath too. Considering a newly developed strain sensing cable for the specific environment, the analysis focus mainly (but not only) on (i) the impact of the different constituent layers on the behaviour of a strain sensing cable and its strain and temperature sensitivities and (ii) the radiation influence on the optical fiber strain sensing cable response (500 kGy of γ-rays). Radiation impact on strain sensitivity is negligible for practical application, i.e., the coefficient changes by 4% at the max. The influence of the composition of the cable is also assessed: the sensitivity differences remain under 15%. Its elasto-plastic behaviour is also evaluated, highlighting residual strain (about 1600 µε after imposing 10000 µε) of the cable (especially for metallic parts).

Finally, starting from orthoradial strain measurements around the section of a tunnel-like structure, an inverse-analysis finite-element method is developed and used to transform strain into convergence values. Its validation on a mock-up of the high-level waste repository cell is reported, using the same cable type analysed earlier. Brillouin and Rayleigh scattering are exploited, as well as different cable's anchoring methods on the structure's circumference. The proposed innovative solution does not restrict the tunnel practicable section, withstands harsh environment and performs distributed measurement which can provide more information than standard methods. Its performances are assessed by identifying which are the influencing parameters and how their uncertainty plays on the inverse analysis outcome. The validation proved the ability to determine geophysical convergence with 1 mm resolution, consistently with expected performances, not only in a controlled environment but also in Andra's underground laboratory.

Acknowledgements

This Ph.D. thesis would not have been possible without the support of many people, who have given me their help, trust and encouragement along this journey.

First of all, I would like to express my deepest gratitude to my supervisors, Sylvie Delepine-Lesoille, Dominique Leduc and Yann Lecieux. Not only they have helped me with my research, always in a constructive and competent way, but they have also supported me in every aspect of my Ph.D. and personal life, in a very human and heartfelt way. I was very lucky to have them by my side and I will never forget how much they have helped me during these years.

Merci beaucoup !

I would also like to thank my host institutions, Andra and the University of Nantes, and all the people I met and worked with. In particular, the people in the research and development group in Andra and within the GeM group of the University of Nantes. These three years have been very fruitful and I am thankful for all the exchanges we had, their contribution was valuable and made me grow a lot. I would like to thank personally Beatrice Yven from Andra and Cyril Lupi from the University of Nantes, for their very much appreciated support, especially in the last months.

I thank the ITN-FINESSE project, along with the European Union and the Marie-Skłodowska Curie Actions, for the opportunity that has been given to me. I thank all the ESRs, supervisors, scientists, researchers and all the partners involved for the wonderful time spent together and the interesting talks and training we shared. I would also like to thank Etienne Friedrich and Massimo Facchini for their kind support and their contribution to my research and future career.

Regarding this manuscript in particular, I thank all the members of my Ph.D. jury: I thank Emmanuel Marin and Jean-Paul Balayssac for their constructive and useful contributions to the finalisation of my thesis, along with Luca Palmieri and the jury president Katerina Krebber for their inspirational questions and comments during the thesis defence.

I would like to thank Francesca for her precious help during the last moments and last, but not least, I would like to thank all my family and friends who have supported me during these years, be they in Italy or in France. Life would have been much harder without their company, help and love. Thank you all.

Contents

List of Figures

List of Tables

Introduction

Our daily life relies on the proper functioning and physical state of civil structures: the buildings we live in and where we work or study, the roads, railways, bridges, tunnels and all the infrastructures we drive across to move and travel, as well as all the other structures that guarantee the proper delivery of basic services. In all these cases, a major damage of the structure can take to dramatic consequences. If a structure collapses, services cannot be guaranteed anymore, the amount of money and time spent to rebuild it would be huge, without considering the tremendous impact on human lives. This kind of fatalities could be drastically reduced if an effective monitoring would be planned. This would mean to invest in the preventive maintenance, decreasing the need of corrective and extraordinary maintenances whose cost and duration approach those of a total replacement, being not effective. This applies especially to historical buildings, whose value transcends that of the building itself [Mesquita et al., 2016].

The structural health monitoring, especially the non-destructive one, comes in hand for this [Bisby and Briglio, 2004; Farrar and Worden, 2007]. It is possible in fact to use sensors that are tiny and non intrusive, that can be left in place for continuous monitoring and that can be simply attached on the structure's surface in old constructions, or embedded inside new ones. Distributed optical fiber sensors are one of the most promising sensors that fulfil these requirements [Glisic and Inaudi, 2008; López-Higuera et al., 2011]. They are flexible, lightweight, similar in dimensions to a hair but capable to reach several kilometres in length for single-mode fibers, which enable remote sensing (no need for electrical outlets on the structure). Moreover, they are made of glass, which is able to withstand many kinds of harsh environment, such as thunder threats and electromagnetic interference. In this thesis, distributed optical fiber sensors are considered for a particular application: structural health monitoring in a radioactive waste repository.

This thesis is part of an international project, an Innovative Training Network (ITN) called FI-NESSE (FIbre NErvous Sensing SystEms), funded by the European Union's Horizon 2020 research and innovation programme under the Marie Skłodowska-Curie grant agreement n° 722509 [*ITN FINESSE* 2016]. This project is a collaborative research and training network, gathering together 26 European universities, research centers and industrial partners with complementary expertise, with the ultimate vision of a widespread implementation of distributed optical fiber sensor systems for a safer society. In this framework, 15 Ph.D. students, also called Early Stage Researchers (ESRs) from all over the world are doing their research in the distributed optical fiber fields. The project has organised five Training Events gathering also other Ph.D. students and researchers to share one week each of lectures, scientific discussions and also fun. Moreover, the students of the project were offered to perform some months of secondments at beneficiaries and partners laboratories, in order to benefit from other expertises and tools, expand their knowledge and build also a professional network. The ITN-FINESSE research is organised in different work-packages:

- WP1: advanced techniques for distributed sensing;

- WP2: new fibres for distributed sensing;

- WP3: field validation and new applications;

- WP4: technology transfer process of academic research results to the European optical fibre sensor industry (performed by one ESR only).

This thesis is part of WP3, dealing with the field application of distributed optical fiber sensors in a radioactive environment. The thesis subject was supported by Andra, the French National Agency for Radioactive Waste Management, with the civil and mechanical engineering laboratory (GeM) of the University of Nantes, both in France. Andra has been commissioned, under the French law, to build an underground repository for long-lived radioactive waste, those that cannot be disposed in surface centers. The underground center, called Cigéo, will be built 500 m underground in a 100 m Callovo-Oxfordian clay layer [*Cigéo*; Andra, 2016]. The cells where waste will be inserted are horizontal with cylindrical section, and are subjected to the load of the rock. As by law the project must be reversible for the first one hundred years at least, the waste must be in turn retrievable. Hence, the section size of the cells must allow the recovery of waste. In order to check whether the section diameter is reduced, i.e. if convergence occurs, its monitoring is essential. For these reasons, in this thesis a method to measure convergence starting from distributed optical fiber strain sensors will be developed and validated, including the qualification of the cable for strain sensing that will be characterised for an application in a radiation environment as Cigéo.

After this brief introduction, in Chapter 1 the context will be extended regarding Cigéo, the application, and distributed optical fiber sensors, i.e. the main actor in this opera.

As Cigéo environment includes the presence of radiation and temperature higher than the ambient, in the first part of Chapter 2 the coupled impact of these two factors on optical fibers is evaluated. The sole impact of radiation on optical fibers is well known [Girard et al., 2013b] but it is necessary to assess whether the different environmental factors have an impact one on another. As in the application the selected optical fiber will be inserted into a specific cable for strain measurement, in the second part of Chapter 2 its mechanical properties will be also analysed, evaluating how they would change under radiation impact and how the protective layers influence the sensitivities of the sensor.

Once the sensor is calibrated in its whole and validated for the application, in Chapter 3 the convergence measurement method is developed and explained. Starting from orthoradial strain measurements around the section of one cell, an inverse-analysis finite-element method is used to transform strain into convergence values. After its presentation, the parameters involved are detailed and a sensitivity analysis is performed.

In Chapter 4 the validation of the method in a surface test is finally done. The method is validated on a mock-up of the high-level waste repository cell: a steel ring of about 80 cm of external diameter is loaded to reach a representative value of convergence. Convergence results from a distributed optical fiber strain sensing cable, obtained using both Brillouin and Rayleigh scatterings and two anchoring configurations on the structure, are then compared with standard techniques. The error between our method and reference results remains under 10 %, under the required resolution, validating the method. The load is also applied in two different configurations, in order to show how the method can deal with more complex cases.

In Chapter 5 an introduction to the step further of this thesis is described: the application of the method to strain measurements acquired in Andra's underground laboratory in Bure (France), the Centre Meuse/Haute-Marne (CMHM), where real-size mock-ups are instrumented in the same conditions as Cigéo, without however the presence of radioactive waste. The difficulties of this process will be disclosed, as well as the first obtained results.

In Chapter 5.4, finally, the conclusions are summarised and the perspectives listed.

Chapter 1

Radioactive waste repository center: Cigéo context

Contents

1.1 Tunnel convergence monitoring for Andra: Cigéo project

1.1.1 General context

Andra is a governmental institution in charge for the management of the radioactive waste produced in France. Radioactive waste classification in France is primarily based on two parameters, which are important for the determination of the appropriate management method: the activity level and the radioactive half-life of the radionuclides contained in the waste, as reported in the last Synthesis Report [Andra, 2018]. According to this definition, there are different categories, summarised in Fig. 1.1.

Regarding the radioactivity level the waste can be classified in very low- (VLL), low- (LL), intermediate- (IL) and high-level (HL) waste, while regarding the half-life waste it can be very short- (VSL), short- (SL) or long-lived (LL) waste. As in Fig. 1.2A, radioactive waste comes from a variety of economic sectors: apart from nuclear power-plants, waste comes from research, defence, industries (outside nuclear power) and medicine sectors. The majority of waste comes from the nuclear power sector and, contrary to what one could think, only a very very little part of it is of the high-level waste (HLW) type. This is true also in general, as visible in Fig. 1.2B. Most part of waste volume regards the very low or low radioactivity level waste with very short or short half-life, which can be confined in surface centers. For the low-level long-lived waste a near-surface disposal is under development, while for intermediate-level and high-level waste Andra planned to build a deep geological repository, known as Cigéo.

Cigéo, whose schematic is in Fig. 1.3 and whose design and functioning are disclosed more in detail in [Andra, 2016], will host the two types of long-lived waste in two different repository

Category	Very short-lived waste	Short-lived waste		Long-lived waste	
Very low-level waste (VLLW)		**VLLW**	Surface disposal (Industrial facility for grouping, storage and disposal)		
Low-level waste (LLW)	**VSLW**			**LLW-LL**	Near-surface disposal under development
Intermediate-level waste (ILW)	Management through radioactive decay	**LILW-SL**	Surface disposal (Aube and Manche disposal facilities)	**ILW-LL**	Deep geological repository at the project phase
High-level waste (HLW)	Not applicable			**HLW**	

FIGURE 1.1: Classification of radioactive waste and associated management solutions. Picture courtesy of Andra.
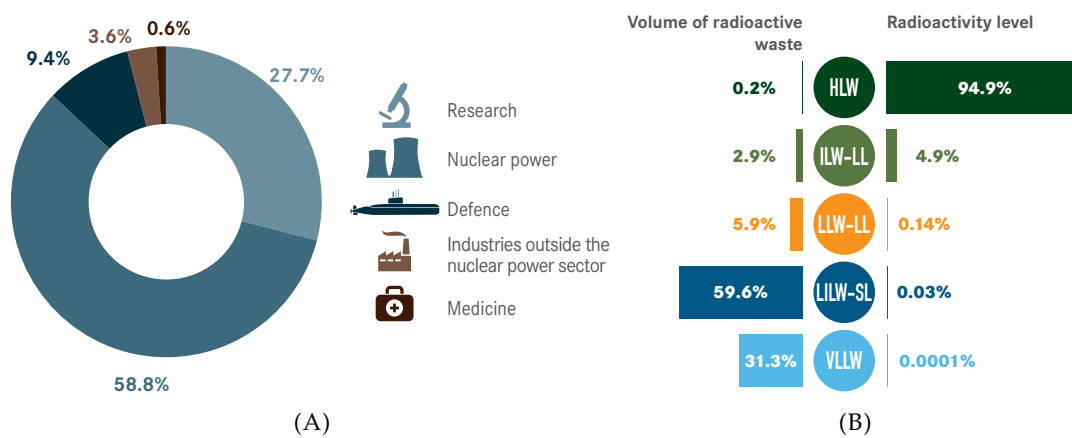
FIGURE 1.2: Breakdown of radioactive waste by economic sector (A) and by volume and radioactivity level of radioactive waste (B) at the end of 2016. Pictures courtesy of Andra.

cells:

- HLW repository cell: horizontal circular tunnels with steel liner, with 25 mm minimum of thickness, with a length that goes from 80 m to 100 m (depending on the exothermicity of the waste) and diameter in the order of 800 mm (about 762 mm external diameter), with one waste package per section

- ILW-LL repository cell: horizontal circular or horseshoe shape, with concrete liner, around 500 m long with 9-12 m of external diameter, with more than one waste package (from 1 to 2-3 columns/levels with excavated sections of the order of 17 to 65-70 m^2).

An example of sections of the two repository cells are represented in Fig. 1.4.

The underground facility is constructed in the Callovo-Oxfordian clay rock layer, at 500 m of depth. The layer is 100 m thick and the rock is the most suitable for the application, thanks to its low permeability. The surrounding clay layer applies an external load on the repository cells' liner, depending on the direction of excavation of the drift [Guayacán-Carrillo et al., 2016]. This is caused by the excavation induced fractures network around the cell. For the HLW repository cells, the load is anisotropic and it takes to around 3000 µε of orthoradial strain around the structure. This results in a radial bending of the liner causing an expected diameter reduction up to 10 mm during the operational phase. This phenomenon is also called "convergence". Apart from strain, convergence and other mechanical induced stress and undesired behaviour, the presence
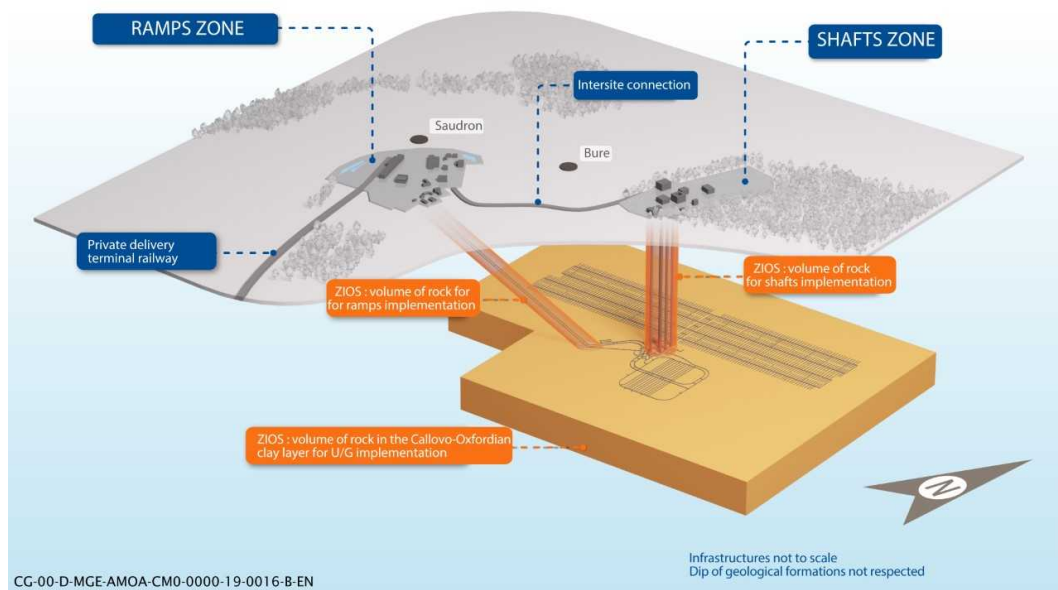
FIGURE 1.3: Schematic of the deep geological repository for intermediate-level and high-level long-lived waste Cigéo.
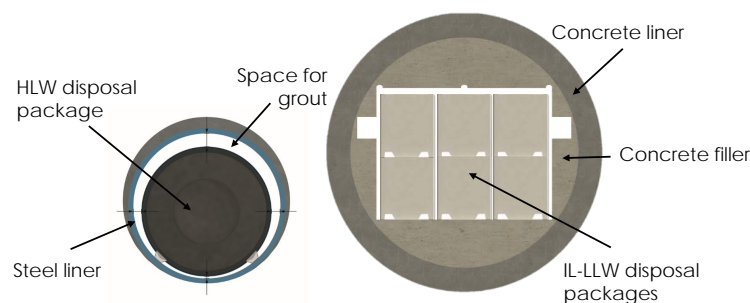
FIGURE 1.4: HLW (0.7 m in diamater) vs ILW-LL (9-12 m in diameter) repository cells sections.

of radioactive waste induces the release of radiation, humidity and other chemicals. The foreseen harsh environment conditions in the connection galleries and in the repository cells, over the first one hundred years of operation, are resumed in Tab. 1.1. The reported values are calculated in the worst case scenario, in order to consider an upper bound for all employed sensors. During the operation phase in fact, the first one hundred years when the first waste packages will be inserted into the repository cells, a monitoring program will be implemented from the construction phase and throughout its operating life, to keep track of repository safety-related parameters. This is also related to another safety condition of the project in accordance with the French law: for the Planning Act 2006-739 on the sustainable management of radioactive waste, the repository must be reversible. One of the conditions to satisfy this requirements is then the monitoring of the repository to follow the operations and contribute also to ensure the safety of the waste and the surroundings.

1.1.2 Monitoring needs

In order to assess which are the main parameters to follow in Cigéo, an underground laboratory has been built in the nearby of the foreseen area for the underground repository construction, the

TABLE 1.1: Environmental harsh conditions inside Cigéo during the first one hundred years.

Parameter	Gallery	ILW-LL cell	HLW cell
Humidity	30-40%	30%	0 to 100%
Atmospheric pressure	1 bar	1 bar	0.8 to 1 bar
Hydraulic pressure	5 to 6.3 MPa	5 to 6.3 MPa	5 to 6.3 MPa
Lithostatic pressure	12 MPa	12 MPa	12 MPa
Pressure due to temperature	3 MPa	3 MPa	3 MPa
Ventilation	$3 \, \text{m}^3/\text{s}$	$10 \, \text{m}^3/\text{s}$ to $3 \, \text{m}^3/\text{s}$	0
Salinity	2-3 g/l	2-3 g/l	2-3 g/l
H_2	ppm	10 mol/package/year	140 mol/package/year
O_2	21%	21%	$21\% \rightarrow 0\%$
Chemistry phenomena	Bacteria activity	Radiolysis, bacteria activity	Anoxic corrosion, radiolysis, bacteria activity
pH	12 to 7	13 to 8	12 to 7
Vibration	Construction machinery	Construction machinery	Introduction of waste packages
Dose rate (γ)		0.1 Gy/h	1 Gy/h
Total integrated dose TID (γ)		0.5-1 MGy	10 MGy
Dose rate (Neutron)		0.03 mGy/h	2 mGy/h
Dust	Abundant	Not yet determined	Not yet determined

so-called Meuse/Haute Marne Center (CMHM) in Bure (France). Mock-ups of the HLW and the ILW-LL repository cells are built and instrumented with many different sensors in order to follow the mechanical and environmental parameters of the area connected to the fact of being underground inside a rock layer, without the presence of radioactive waste. Examples of instrumented mock-ups at the CMHM underground laboratory are showed in Fig. 1.5.

Simulations and testing on these structure have permitted to obtain the foreseen values of the main parameters to be monitored in the future underground repository, which are resumed in Tab. 1.2 (as reported in [Modern2020, 2019]).

In order to follow the parameters in the laboratory, to validate the simulations and obtain a

(A) HLW
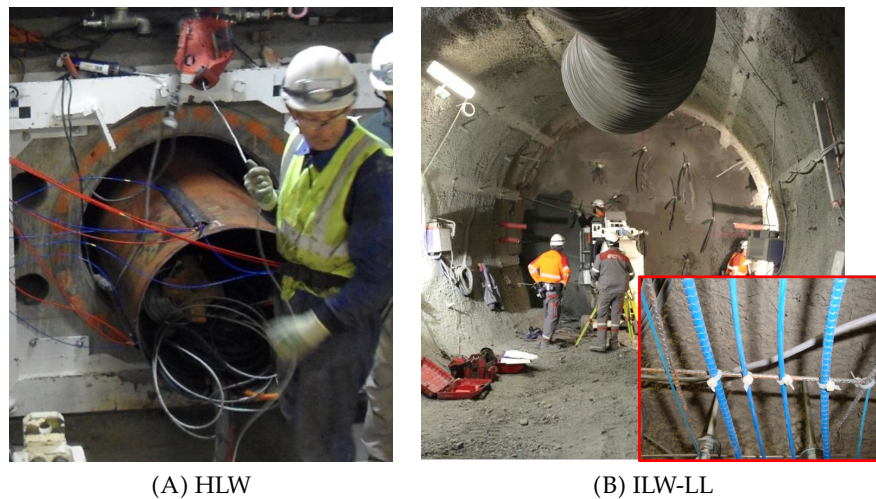
(B) ILW-LL

FIGURE 1.5: Examples of mock-ups in the CMHM underground laboratory: HLW and ILW-LL repository cells mock-ups with detail on some installed optical fiber cables.

TABLE 1.2: Main parameters to be monitored in the underground repository. These are the worst case values considering both HL and IL-LL radioactive waste repository cells.

Parameters	Typical value/range	Uncertainty requirement	Spatial homogeneity of the parameter
Temperature	[20-90°C]	±0.1°C	20 cm
Displacement	+0.5 mm/m to -2.5 mm/m	1 μm/m	10 cm
Strain evolution in concrete element	10 με	3 με	10 cm
Concrete crack	Threshold for openings: 200 μm		10 cm
Convergence evolution	10 mm (in 100 years)		1 m
Hydrogen	[0-4%] sensitivity of 500 ppm; [4-10%] sensitivity of 1%	100 ppm; <1%	3 m (ILW-LL waste package); ~1.5 m (HLW waste package)
Gamma radiation	0.1-1 Gy/h, TID = 1-10 MGy (100 years)	50 mGy	~1.5 m (HL waste package)

database of useful values, Andra employs many different sensors, which are however not necessarily feasible to be used in Cigéo. In the final application the section of the cells must be free to host the waste and to allow the circulation of the robots that will ensure the waste placement and manipulation, therefore the employed sensors and sensing system must be non intrusive. At the same time, the presence of radiation excludes the utilization of electronics nearby the source. These premises suggest the use of distributed optical fiber sensors: these sensors are lightweight,

of very small size, flexible, passive, insensitive to electro-magnetic interference, allow long distance sensing and are able to work also in radiation environment. Allowing remote sensing, only the optical fiber sensing cable will be placed in the harsh environment, while the optoelectronic measuring units would be located at the entrance of the repository cells, where maintenance is possible. This is why ageing tests will only consider the cable and not the device. Optical fiber sensors are able to measure temperature and strain, and therefore they can be used to calculate indirectly the convergence of the structure, which is the goal of this work. Before going to the description of how we do it, we will describe briefly the principles and functioning of distributed optical fiber sensors.

1.2 Optical fiber sensors

Optical fiber sensors are known for many advantageous features that can be really helpful in special applications as the monitoring of Cigéo. First of all, optical fibers are low intrusive. Their dimensions resemble those of a hair: the length is the main dimension, which can reach the kilometers range, while the section is fraction of a millimeter. In Fig. 1.6 a schematic of an optical fiber is represented. Standard silica fibers have a core size of 10 μm in diameter, where light propagates.
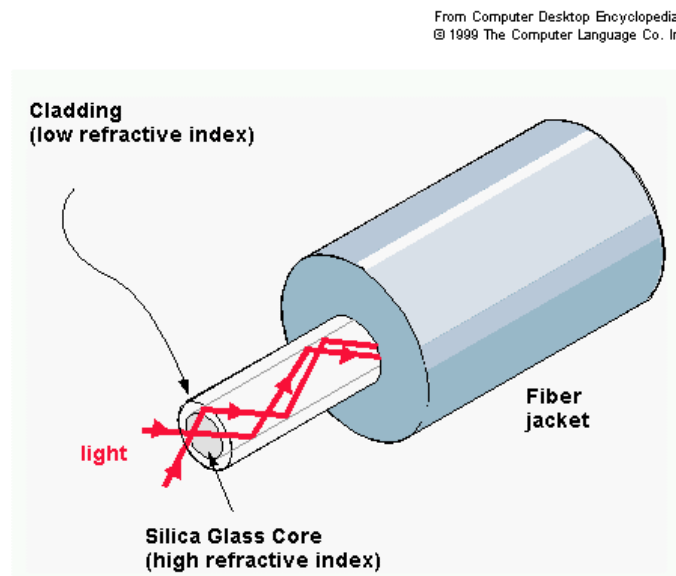
FIGURE 1.6: Schematic of an optical fiber: light propagates in the fiber core, whose diameter is around 10 μm for single-mode fibers and around 50 μm for multi-mode fibers. The glass cladding reaches 125 μm and the protection jacket at 250 μm.

This core is surrounded by a cladding, which is in the order of 125 μm of diameter. In this case the fiber is a single-mode fiber (which is often indicated as SMF), which allows one main light mode to propagate. For some applications, especially when the needed light power is bigger, the core can reach 50 μm in diameter, allowing the propagation of more than one mode. This is the case of multi-mode fibers. The core and the cladding are manufactured from the same glass preform, which is doped during the process in order to obtain two different refractive index of the material. Among the different dopants, the most commonly used for optical fiber sensors are Germanium (Ge), Phosphorus (P) and Nitrogen (N), which increase the glass refractive index, and Fluorine (F) or Boron (B) which decrease it [Girard et al., 2013b]. Standard single-mode fibers (G652 type, whose most famous is "SMF28") have Ge dopants in the optical fiber core, while other dopants (in the core and the cladding) allow the fiber being more or less sensitive to specific environmental factors or chemicals. Fibers N-doped in the core or with F-doped claddings have been developed

for radiation hardening. On the contrary, Phosphorus and Aluminium (Al) dopants are used to obtain radiation sensitive fibers [Faustov, 2014].

Optical fibers are mainly made of silica glass, although many applications are supported by plastic fibers (especially in the medical field). Glass fibers are however the most used in SHM applications, as they are able to reach greater distance ranges, are resistant to most of the chemical degradation in harsh environment and, also, they can survive in radiation environment. They are passive and insensitive to electro-magnetic field, being therefore feasible for many applications where other sensors cannot work.

One of the main drawbacks of optical fiber are the optical distortions like attenuation and dispersion. Attenuation can be due to i) intrinsic reasons, due to the optical properties of pure silica as electronic transitions, molecular vibrations or Rayleigh diffusion, proportional to λ^{-4}, and ii) extrinsic reasons, which are due to impurities of silica as the presence of the ion OH^- and molecular hydrogen H_2. In Fig. 1.7 all these contributions are considered, obtaining the final attenuation spectrum. For this reason, in the telecommunication field it is common to work in
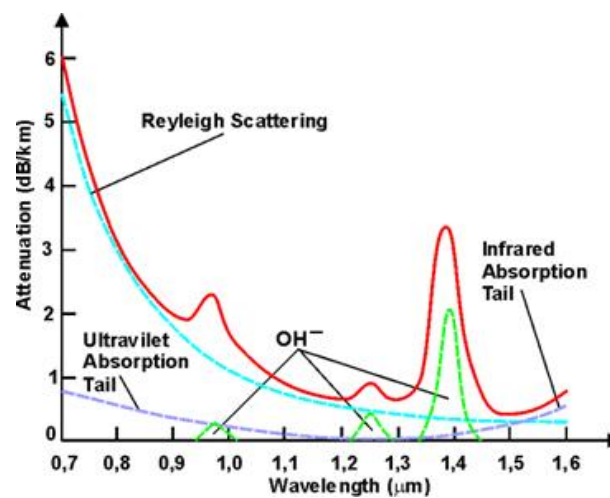
FIGURE 1.7: Optical fiber attenuation spectrum for a single-mode fiber.

the so-called 2nd and 3rd windows of transmission, i.e. around 1310 nm and 1550 nm having attenuation values of 0.35 dB/km and 0.2 dB/km respectively. Losses can also derive from the bending of the fiber or micro-bending inside the fiber.

The dispersion, instead, cause a distortion of the signal: the modal dispersion cause the presence of delayed version of the original light pulse, while the chromatic dispersion cause its broadening (or tapering) in wavelength.

In order to be used in applications, optical fibers are protected by a jacket, a primary coating in single or dual layer, that takes the fiber to a total diameter of 250 μm (Fig. 1.6). The inner primary coating is designed to act as a shock absorber, under the tougher outer layer, to minimize attenuation due to microbending. It has a low Young modulus and crosslink density, to be easily removed from the fiber to facilitate splicing and connecting and adhere properly to the glass. The outer primary coating, sometimes called the secondary coating, is more rigid and has a higher Young modulus. It protects the primary coating against mechanical damage and acts as a barrier to lateral forces and moisture [Biswas, 1993; Schmid and Toussaint, 2007]. In many cases, as for specialty fibers, these two roles are performed by only one layer of coating. Acrylate coatings are the most common for standard fibers and the easiest to strip off from fibers, but they are not able to withstand high temperature over 80°C. High temperature acrylate or polyimide coatings can solve this problem, reaching respectively up to 150°C and 300°C in the long-term (400°C in the short-term for polyimide). Polyimide is however a stronger coating, making it difficult to insert the fiber in a cable, increasing also the difficulties in the stripping off. A carbon layer can be

added on top of these coatings, useful when optical fibers are exposed to humidity and hydrogen [Lemaire et al., 1988] or need to sustain high stress. Its removal for splicing is however at high risk of breaking. Another example are the metallic coatings, like gold or aluminium, that can be used for ultra high temperature and chemical sensing and in very harsh environments.

In SHM applications then the optical fibers are often inserted into cables, to enhance their mechanical and physical resistance and their sensitivities to strain or temperature variations. Sensing cables can be found with a round section or flat, with a smooth or corrugated surface to adhere properly on the host material. They are often made of an external plastic sheath, which can be completed by the insertion of metallic parts to improve strength and stiffness. Depending on the application it is also possible to select specific strain and temperature sensing cables: in the first case (strain sensing) the fiber is integral with the structure of the cable, while in the second (temperature sensing) the fiber must be detached from the internal surface of the cable to be insensitive to physical deformations. All these cases are represented in Fig. 1.8.

(A)   (B)   (C)
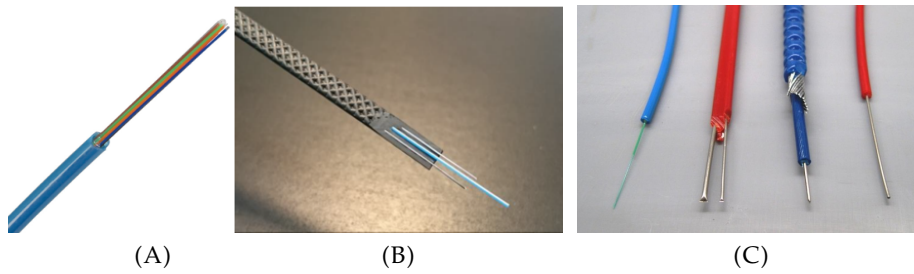
FIGURE 1.8: Cables examples: AFL plastic cable (A), Neubrex flat cable (B), Solifos V1a to V4 strain and temperature sensing cables [Hauswirth, 2015] (C).

Optical fiber can be used as point or distributed sensors, depending on the mechanisms thanks to which it is possible to measure temperature, strain and other quantities. In order to understand the following chapters, we will focus here on one point sensor, the fiber Bragg gratings, and we will then concentrate on distributed sensors, the main actor of this work.

1.2.1   Point optical fiber sensors: fiber Bragg gratings

One of the most mature technology and commercially employed optical fiber sensors is the fiber Bragg grating (FBG). It works as a point sensor: when light propagates through the grating, only the wavelength satisfying the Bragg condition is reflected, while the others are simply transmitted (as showed in Fig. 1.9). The selected reflected wavelength, called Bragg wavelength λ_B, is defined as $\lambda_B = 2n_{\text{eff}}\Lambda$ (Bragg condition), where n_{eff} is the effective refractive index of the fundamental mode and Λ the grating period [Kashyap, 1999]. The grating is in fact a periodic variation of the refractive index, whose most famous inscription technique is by means of ultraviolet (UV) light. Based on the final application it is possible to "inscribe" different periodic (or aperiodic) gratings, with different length L_g, grating period and eventually different shapes of the refractive index distribution. When strain or temperature changes affect a fiber where a grating is inscribed, n_{eff} and Λ change accordingly, resulting into a different reflected λ_B as

$$\frac{\Delta\lambda_B}{\lambda_B} = (1 - p_e)\varepsilon + (\alpha_\Lambda + \alpha_n)\Delta T = C_\varepsilon\Delta\varepsilon + C_T\Delta T; \tag{1.1}$$

where the strain sensitivity coefficient C_ε depends on the strain-optic coefficient p_e and the temperature sensitivity coefficient C_T is related to the thermal expansion coefficient α_Λ and the thermo-optic coefficient α_n. In this way, interrogating an FBG with a wide spectrum light, then retrieving the reflected wavelength, it is possible to have information on the environment where the fibre is placed.
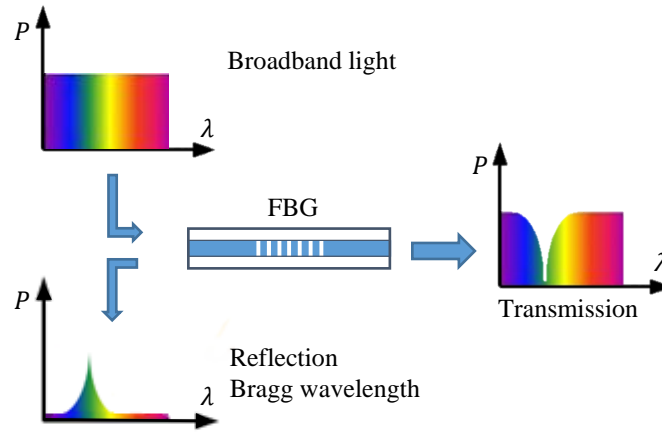
FIGURE 1.9: Functioning schematic of a fiber Bragg grating (FBG).

1.2.2 Distributed optical fiber sensors

Distributed optical fiber sensing is based on the scattering processes that take place within the fiber. In general, a scattering process occurs when light goes through inhomogeneities of size much smaller than the propagating wavelength, that scatter a little portion of light in all directions, reducing the propagating light power. The reduction can be proportional to the incident power, with no energy transferred to the glass. In this case there is therefore no frequency shift compared to the incident wavelength, having then a linear and elastic scattering. On the contrary, scatterings can be said non-linear and inelastic, when light energy interacts with the material.

The inhomogeneities can be of many types, like microscopic or macroscopic variations in density, composition or structure of the material, which cause *Rayleigh* scattering. This is a linear and elastic scattering that causes an attenuation of the forward-propagating signal proportional to λ^{-4} and the creation of a backward-propagating wave. Sound waves or acoustic phonons give rise to
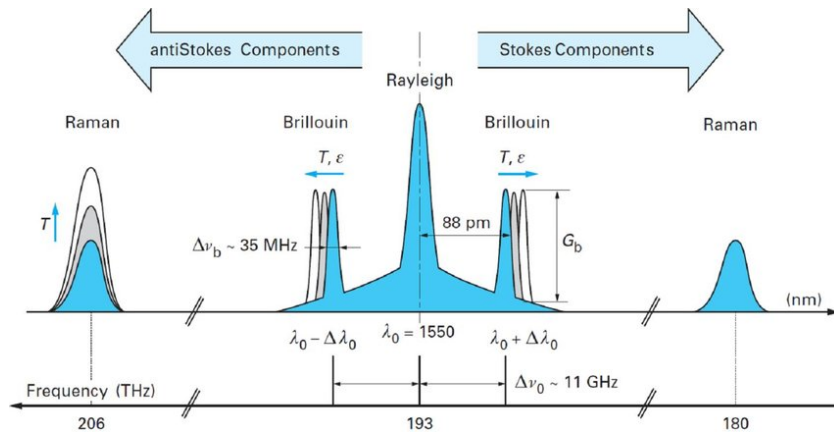
FIGURE 1.10: Scheme of the different spectra resulting from Rayleigh, Raman and Brillouin scattering processes in optical fibers (©Arik Bergman).

the so-called *Brillouin* scattering, a non-linear and inelastic effect where the scatter occurs at some GHz of frequency shift. Molecular vibrations or optical phonons in the medium may also give rise to *Raman* scattering, another non-linear and inelastic process since the scattered wave is frequency shifted of some THz.

Fig. 1.10 shows a schematic representation of the spectra associated with these processes, where the difference between Stokes and anti-Stokes components, i.e. down-shifted or up-shifted with respect to the propagating light, has also been considered. Brillouin and Raman scatterings

can occur in a spontaneous or stimulated manner. Generally, as long as the input light is scattered without strongly altering the properties of the medium, the scattering is considered spontaneous. When the light intensity increases to a level such that the optical properties of the medium are modified, and the scattered light is proportional to the power of the input light, then this regime becomes stimulated [Nikles, Thevenaz, and Robert, 1997].

Regarding the application, Raman scattering is sensitive to temperature variations, while Brillouin and Rayleigh scatterings are sensitive to both strain and temperature variations. The measured frequency shift $\Delta \nu$ of the backscattered light pulse with respect to the source pulse is proportional to strain and temperature variations as the following formula

$$\boxed{\Delta \nu = C_\varepsilon \Delta \varepsilon + C_T \Delta T} \tag{1.2}$$

where C_ε and C_T are respectively the strain and temperature sensitivity coefficients of the selected sensor, which are obtained after its calibration and depend on the exploited scattering and the sensor itself.

Hereafter, as our goal is to find convergence using strain measurement, we will focus only on Rayleigh and Brillouin scatterings. Raman will be however still considered by Andra for temperature measurements.

1.2.2.1   Rayleigh scattering

Rayleigh scattering is the dominant scattering effect and loss mechanism in the low-absorption window between the ultraviolet and infrared absorption tails. The main cause of this effect are inhomogeneities of random nature occurring on a small scale compared with the wavelength of light [Senior and Jamro, 2009]. In general, the result of the presence of these inhomogeneities are refractive index fluctuations and the subsequent scattering, which occurs in almost all directions, giving an attenuation proportional to λ^{-4} following the Rayleigh scattering formula

$$\alpha_R = \frac{8\pi^3}{3\lambda^4} n^8 p^2 \beta_c k T_F.$$

α_R is the Rayleigh scattering coefficient, λ the optical wavelength, n is the refractive index of the medium, p is the average photoelastic coefficient, β_c is the isothermal compressibility, k is the Boltzmann's constant and T_F is a fictive temperature or the glass transition temperature, representing the temperature at which the density fluctuations are "frozen" in the material, i.e. when glass reaches thermal equilibrium.

Rayleigh scattering is a linear scattering, so the scattered power is proportional to the propagating one. However, since this scattering may occur in all directions, only a part of it can be backpropagated in the medium, being then useful for sensing purposes (especially talking about optical fiber sensor systems). In fact, the fraction of captured optical power is

$$S = \frac{(\text{NA})^2}{4 n_{co}^2},$$

where NA is the numerical aperture of the fiber and n_{co} is the refractive index of the core. In this way, the backscattering coefficient is given by the product of the Rayleigh scattering coefficient α_R and the fraction of the captured optical power.

In this case, following

$$\Delta \nu_R = C_\varepsilon^R \Delta \varepsilon + C_T^R \Delta T$$

standard sensitivity coefficients for SMFs are in the order of $C_\varepsilon^R = -0.15$ GHz/µε for strain and $C_T^R = -1.5$ GHz/°C for temperature at 1550 nm.

1.2.2.2 Brillouin scattering

Brillouin scattering is an inelastic and non-linear scattering caused by the propagation of density fluctuations of the medium, resulting in turn from propagating pressure waves. These pressure waves change periodically the refractive index as they propagate, thus they can be seen as moving Bragg gratings and the scattering then is through Bragg diffraction [Yeniay, Delavaux, and Toulouse, 2002].

In the Brillouin case the scattered light is propagated mainly in the backscattering direction, while its intensity is maximum when the frequency shift between the interacting waves (incident and backpropagating) is equal to the so-called Brillouin central frequency [Nikles, Thevenaz, and Robert, 1997]

$$\nu_B = \frac{2n_{\text{eff}}V_A}{\lambda_0},$$ (1.3)

where n_{eff} is the effective refractive index of the fiber, V_A is the effective acoustic velocity of the fundamental acoustic mode and λ_0 is the wavelength of the incident wave in vacuum, called *pump* wave. The backscattered wave is instead called *probe* wave. The acoustic velocity depends in turn on the waveguide material, in particular on its density. The resulting spectrum, the so-called *Brillouin Gain Spectrum* (BGS) shows a Lorentzian spectral profile given by

$$g_B(\nu) = g_0 \frac{(\Delta\nu_B/2)^2}{(\nu - \nu_B)^2 + (\Delta\nu_B/2)^2},$$ (1.4)

where $\Delta\nu_B$ is the full-width half-maximum (FWHM) (usually $\sim$30 MHz) and g_0 is the Brillouin peak at resonance ($\nu = \nu_B$). The central frequency ν_B is dependent from strain and temperature variations occurring to the fiber: some examples of the BGSs acquired during temperature and strain variations are plotted in Fig. 1.11. The scattering can also be seen as resulting from the

(A) Strain
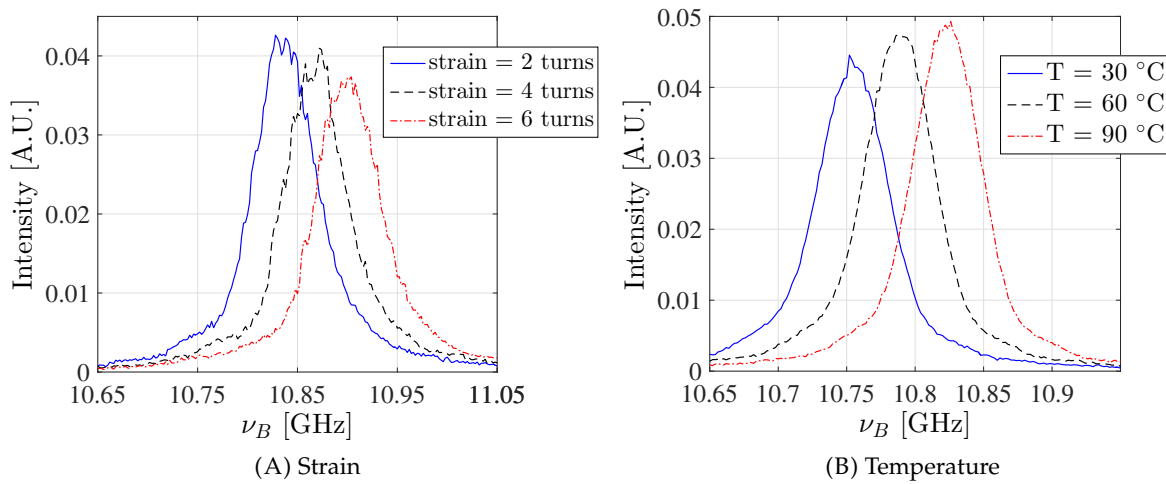
(B) Temperature

FIGURE 1.11: Brillouin gain spectra at 1550 nm of a fiber under strain and temperature variations. Data from [Piccolo, 2016].

Doppler effect, since the acoustic wave is moving inside the medium. Depending on its propagation direction, the frequency of the scattered light is down-shifted (giving the Stokes component) when the acoustic wave is moving away from the incident light, while the frequency is up-shifted for the other case.

For Brillouin scattering to occur, there must be energy and momentum conservation between the waves that propagate in the medium (optical and acoustic); furthermore, the frequencies ν and

the wavenumbers k must be such that[1]:

$$\nu_s = \nu_p - \nu_a \text{ Stokes case,} \qquad \nu_{as} = \nu_p + \nu_a \quad \text{anti-Stokes case} \tag{1.5}$$

$$k_s = k_p - k_a \text{ Stokes case,} \qquad k_{as} = k_p + k_a \quad \text{anti-Stokes case} \tag{1.6}$$

that constitute the typical energy and phase matching conditions of non-linear interactions [Motil, Bergman, and Tur, 2016]. As mentioned before, this can happen in a spontaneous or stimulated manner, when the propagation of a probe wave is natural or forced as in Fig. 1.12.
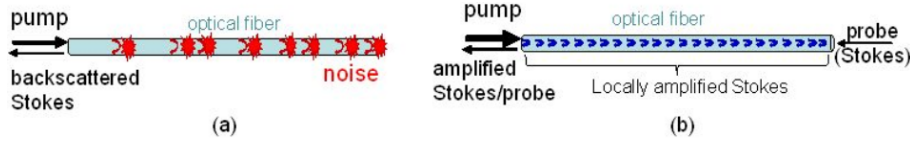
FIGURE 1.12: Spontaneous (a) and stimulated (b) Brillouin scattering in optical fibers [Zou, Long, and Chen, 2015].

For Brillouin scattering,

$$\Delta \nu_B = C_\varepsilon^B \Delta\varepsilon + C_T^B \Delta T$$

standard sensitivity coefficients for SMFs are in the order of $C_\varepsilon^B = 0.05$ MHz/$\mu\varepsilon$ for strain and $C_T^B = 1$ MHz/$^\circ$C for temperature at 1550 nm.

1.2.2.3 Distributed optical fiber sensing techniques and interrogators

These scatterings can be exploited in the time or in the frequency domain, via the Optical Time Domain Reflectometry (OTDR) or the Optical Frequency Domain Reflectometry (OFDR) respectively.

The OTDR is the most common and simple technique. Considering the launch of a pulse of duration τ in a SMF, it is possible to know its spatial position z inside the fiber thanks to the classic space-time relation

$$z = \frac{c_0}{n}t,$$

where c_0 is the speed of light in vacuum, n is the refractive index of the core of the fiber and t the time index. When a reflection occurs, for example when the light reaches the end of the fiber or internal scattering takes place, part of the electromagnetic field can be guided backwards reaching the interrogating extremity. At time t' the photodetector receives the light that was in

$$z' = \frac{1}{2}\frac{c_0}{n}t'$$

as light had to travel back and forth from the source, doing twice the distance in twice the time. Similarly, the spatial resolution (i.e. the location accuracy) can be defined as

$$\Delta z = \frac{\tau c_0}{2n_{\text{eff}}}. \tag{1.7}$$

Exploiting this mechanism it is possible to detect spatial attributes of the fiber (defects, length, etc.) just by measuring the time needed for the light to travel back to the laser source and photodetector [Palmieri and Schenato, 2013]. This space-time relation is exploited to characterize what is happening in the fiber by detecting the backscattered light, and specifically losses, in the time domain [Grattan and Sun, 2000].

---

[1]a is for *acoustic*, p is for *pump* or *incident* wave, s is for *Stokes* and as is for *anti-Stokes*

In the OFDR case a tunable laser is used to scan a frequency range of ΔF and, through Fourier transformation, a spatial resolution of

$$\Delta z = \frac{c_0}{2n\Delta F}$$

is obtained. While the sensing length in the OTDR systems is equal to the fiber length, in the OFDR case it is limited by the coherence length of the laser source and the state of polarization variation along the fiber. OFDR sensors tend to be sensitive to bending loss so, for civil structural monitoring, fibers must be protected from sharp bends by a protective cable, for example. Furthermore, although OFDR often uses single mode fiber, it can also be implemented with multi-mode fibers [Bao and Chen, 2012].

The OTDR takes advantage of Rayleigh backscattering for its functioning and it is the base for many other sensing techniques. Between others, we can have the Photon-Counting OTDR (ν-OTDR), Polarization OTDR (POTDR), Phase OTDR or Coherent OTDR (ϕ-OTDR), and Tunable Wavelength OTDR (λ-OTDR or TW-OTDR). In the frequency domain there is the Polarization OFDR [Palmieri and Schenato, 2013; Yüksel, 2018].

The OTDR technique can also be exploited by Brillouin backscattering, as for the Brillouin Optical Time Domain Reflectometry (BOTDR). It is based on the spontaneous Brillouin scattering, as well as other one-end interrogation techniques like the Brillouin Optical Frequency Domain Reflectometry (BOFDR) or Brillouin Optical Correlation Domain Reflectometry (BOCDR). Stimulating the Brillouin scattering with a double-end configuration, launching light from both ends of the fiber, it is possible to use techniques such as Brillouin Optical Time Domain Analysis (BOTDA), Brillouin Optical Frequency Domain Analysis (BOFDA), Brillouin Optical Correlation Domain Analysis (BOCDA) [Zou, Long, and Chen, 2015; Motil, Bergman, and Tur, 2016].

These techniques can be classified for their spatial resolution and maximum distance range. The spatial resolution, which for elastic scattering is defined as in Eq. 1.7, can be also defined as "the smallest length of fiber for which a sensing system can measure its real condition (hot spot or strain)", or, more technically, "the 10–90% rise time of a transition of measurand" [Bao and Chen, 2012]. The maximum distance range, instead, is the maximum distance reachable by the propagating light being able to maintain an adequate level of SNR to perform sensing measurements.

Excluding the fiber's intrinsic properties that can influence these parameters (as for example internal losses), each of the mentioned techniques has its specific characteristics. Depending on the desired spatial resolution, distance range and measurement sensitivity, it is possible to choose which scattering-based technique to select, and thus which commercial interrogator. Rayleigh scattering-based techniques like OFDR (via Luna Inc. OBR [Inc., 2018]) are known for the high spatial resolution and high sensitivity, which is however compensated by the very short distance range. On the contrary, Brillouin-based techniques as the BOTDA are preferred for long distance range, although the spatial resolution remains broader (as for the DiTeSt of Omnisens [*DiTeSt Dual Reading Unit*]). In Cigéo, optoelectronic devices would be placed in cabinets, nearby the access galleries and the instrumented repository cells. The total distance range would remain smaller than few kilometers. However, circumferences of HLW repository cells would be smaller that 3 m. This is why a high spatial resolution, at least 10 cm, was the target. In order to overcome these differences, we chose to use another instrument, that is able to exploit both Brillouin and Rayleigh scattering with a spatial resolution of 2 cm. The Neubrescope NBX-7020 from the company Neubrex Co., Ltd. was selected to respect the features of the application: a km distance range with high spatial resolution. The Brillouin-based techniques is an original technique called Pulse-Pre-Pump Brillouin Optical Time Domain Analyser (PPP-BOTDA). The Rayleigh-based is the TW-COTDR instead, which takes advantage of the coherent configuration to obtain results by the cross-correlation of the Rayleigh scattering "fingerprints" traces of the sensors [Kishida, Yamauchi, and Guzik, 2014]. In order to compare all the mentioned instrument and get an idea of the considered order of magnitudes, the measurement performances and parameters are reported

in Tab. 1.3. Despite the majority of our tests will be performed with the Neubrescope, we will also consider the OBR 4600 in a particular case.

TABLE 1.3: Comparison between distributed strain sensing instruments possessed by Andra.

	OFDR (OBR)	TW-COTDR (Neubrescope)	BOTDA (DiTeSt)	PPP-BOTDA (Neubrescope)
Spatial Resolution	1 cm	2 cm (1 m)	1-20 m	2 cm (1 m)
Sampling Resolution	10-20 μm	1 cm (20 cm)	25 cm - 1 m	1 cm (20 cm)
Max. Distance Range	30-70 m	2.5 km (25 km)	60 km	2.5 km (25 km)
Measurement time	3-4 s	few/some minutes (depends on other parameters)	1-5 min standard, 5-15 min high resolution	few/some minutes (depends on other parameters)
Strain accuracy	±1 με	0.5 με	2 με	10 με

1.2.3   OFSs in structural health monitoring

Optical fiber sensors, in primary coating or, more often, protected into cables, can be used in structural health monitoring thanks to their ability to measure strain, over long distances and without dead zones. In about twenty years the amount of diverse applications is wide, for both distributed sensors and FBGs: from pipelines in the oil and gas industry, to the transportation like railways and airplanes, or civil engineering structures. Some of these are reported in the following reviews [Li, Li, and Song, 2004; López-Higuera et al., 2011; Leung et al., 2015; Barrias, Casas, and Villalba, 2016; Joe et al., 2018]. Within the latter set of applications, along with bridges, dams and mines, optical fiber sensors are employed also in tunnels, especially to follow the deformation due to the excavation of tunnels or when in operation [Mohamad et al., 2011; Di Murro et al., 2016; Barrias, Casas, and Villalba, 2017; Li, Soga, and Kechavarzi, 2018].

In our case, the repository cells can be seen as tunnels, with similar shape, dimensions and materials of those already studied. The biggest challenges here are i) to monitor the convergence of the cells keeping their section clear for the allocation of radioactive waste while ii) using a sensing system that can handle the present harsh environment.

The majority of convergence measurement systems needs to be used inside the structure's section (e.g. invar wires [Dunnicliff, 1993], laser theodolites [Alba et al., 2010], displacement sensors [Li, Liu, et al., 2015], etc.), while for what we have explained in this chapter optical fiber sensors appear very suitable for this kind of job. In this regard, new methods that rely on data processing over optical fiber sensors as fiber Bragg gratings (FBGs) have been developed, like in [Barbosa et al., 2009], however FBGs are limited for the considered application. Indeed, distributed measurements should be preferred for large structures to reduce the installation time, blind zones, influence of localization accuracy and cost. For this reason, we will here propose an alternative based on distributed optical fiber strain sensing cables, whose strain measurements are coupled

with an inverse-analysis finite-element method to compute convergence values. For the considered application, a convergence resolution of 1 mm is foreseen for the worst case scenario. A spatial resolution of 10 cm is then needed around the repository cells, with a longitudinal homogeneity of 1 m. A total distance range of a couple of km is also needed. After this, we will validate it in a laboratory test and underground laboratory tests will be anticipated.

In Cigéo the harsh environment is preponderant and must be taken into account for the selection of the suitable sensor. A maximum temperature of 70 °C for ILW-LL repository cells and 90 °C for the HLW is foreseen for the first one hundred years of monitoring, while a maximum of 1 MGy of γ-rays dose is given by the first HLW packages. It is known that radiation impacts on optical fibers by inducing defects and changes in the density of silica, which in turn cause losses and radiation induced frequency shifts from the backscatterings point of view [Girard et al., 2013b]. However, radiation is not the only harsh physical agent that could influence the optical fiber sensors. It is therefore necessary to analyse whether the coupling of more than one factor, for example the joint impact of radiation and temperature, takes to different results than considering the single factors, radiation *or* temperature, and then summing the outcomes. Moreover, the majority of these studies are done on optical fibers in their primary coatings, while in SHM applications they are often put into cables. It would be then required to study how radiation impacts also on the protection layers, especially on their mechanical properties. Regarding cables it would be also interesting to analyse whether these layers have an impact on the sensitivities, as only few papers in the literature deal with the topic, while the calibration of sensors is very important for applications in SHM.

This will be assessed from the next chapter on: we will consider the whole convergence measurement chain, from the choice and characterisation of the sensor, to the development of the convergence measurement method and its application to experimental measurements. In Fig. 1.13 the organisation of the work is represented, to visually follow its progression along the chapters.
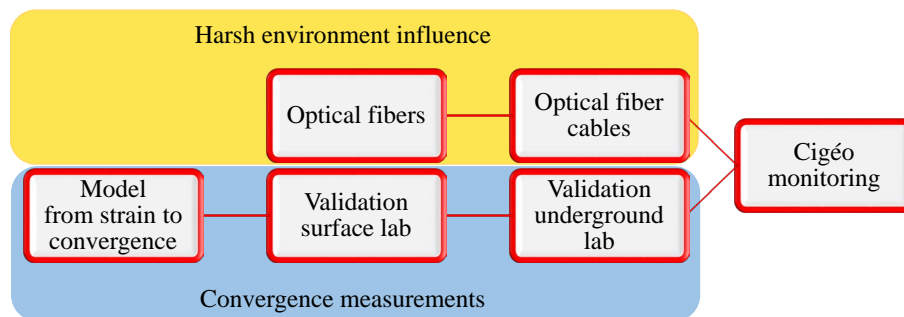
FIGURE 1.13: Schematic of the Ph.D. methodology: two main topics are considered in this work: the first is the validation of distributed optical fiber sensors in harsh environment, the second is their use as convergence measurement sensors.

Chapter 2

Harsh environment influence

Contents

2.1 Introduction

This chapter deals with the validation of optical fiber sensors as suitable for applications where radiation harsh environment is present, as Cigéo. After reporting the bibliography, the coupled impact of radiation and temperature (the two at the same time) on the optical and physical properties of optical fibers in primary coating is determined. Afterwards, as in-situ optical fiber sensing cables are preferred to enhance the mechanical and chemical resistance, post-mortem radiation and temperature combined influence (one after the other) is evaluated on optical fiber strain sensing cables. At the same time other aspects are evaluated: for optical fibers in primary coating the radiation impact on the physical properties of backscattering, while the impact of the different protection layers on the behaviour of the strain sensor is analysed for cables. Thanks to the unique ability to perform remote sensing, only the sensing cables are exposed to harsh environments, without considering the interrogating device. These two topics are addressed performing experimental tests, which confirmed the feasibility to use optical fiber sensing in environment where radiation is present.
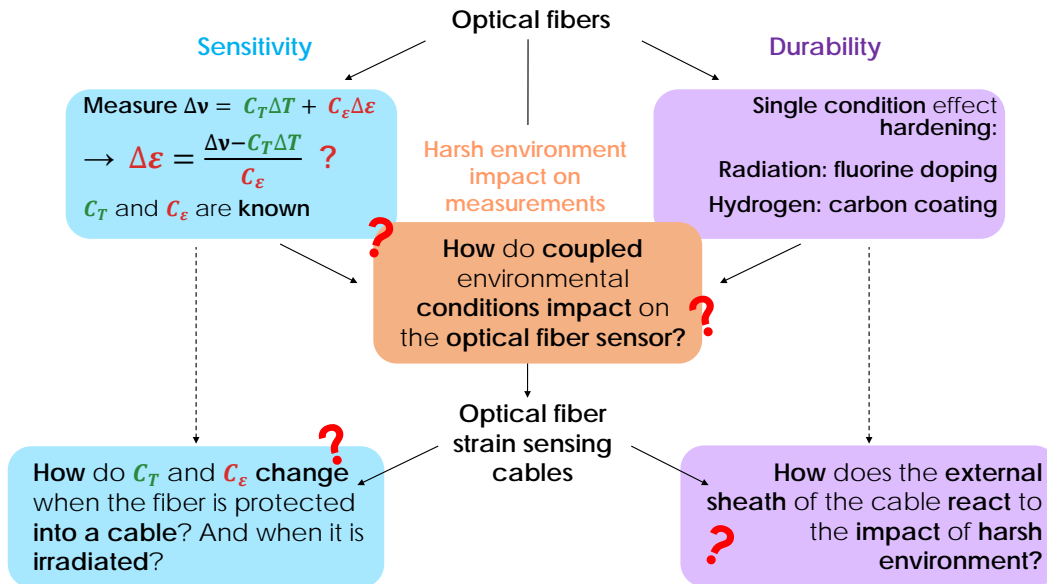
FIGURE 2.1: Focus of this chapter: coupled radiation and temperature effect on OFSs, sensitivity and mechanical influence of cables' protective sheath and its behaviour after irradiation.

2.2 Coupled radiation and temperature influence on bare optical fiber sensors

2.2.1 State of the art

In many cases, structural health monitoring must be performed in harsh conditions, for example in presence of radiation. This is true for nuclear structures as nuclear power-plants, or physics reactors (like CERN), or even for aerospace applications, as well as for radioactive waste repositories. In order to assess whether optical fiber sensors are suitable for this kind of application, during the years many researchers focused their studies on how radiation influences the physical and optical properties of optical fibers. It was found [Girard et al., 2013b] that radiation degrades the optical fiber properties through three different mechanisms: radiation-induced attenuation (RIA), radiation induced emission (RIE) and compaction. The RIA and compaction are directly
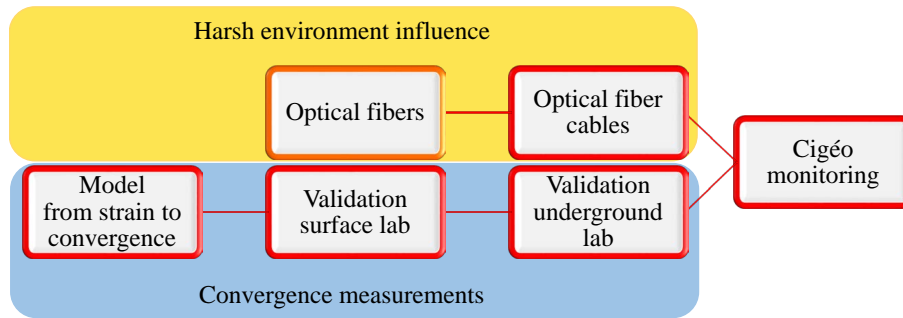
FIGURE 2.2: Schematic of the Ph.D. methodology: the first part of the chapter will be dedicated to the analysis of harsh environment influence on optical fiber sensors.

related to optical fiber sensors. The RIA increases the glass linear attenuation (taking to a reduced distance range), and depends in turn on (i) the absorbed total dose, (ii) the dose-rate, (iii) the working wavelength, (iv) the optical injected power for the measurement which may bleach radiation-induced-defects and (v) the temperature during irradiation. Compaction instead leads to changes in the density of silica. This corresponds to a change in the refractive index and, consequently, a change in the frequency shift obtained from backscattering measurements.

The impact on Rayleigh and Brillouin backscattering responses can be observed concerning losses and frequency shift. In [Alasia et al., 2006] a Brillouin frequency shift of 5 MHz was obtained after putting commercial optical fiber sensors under a total dose of 10 MGy of γ-rays. [Phéron et al., 2012] and [Planes et al., 2017] analysed γ-rays influence under different conditions, reporting a general low change in sensitivity coefficients, while observing the dependence of the impact of radiation on the composition of the fiber. The nature of the dopants used to constitute the fiber refractive index profile has a major impact on the fiber radiation induced attenuation (RIA): F-doped fibers are particularly advantageous with respect to more standard Ge-doped ones. In [Morana et al., 2018] all these aspects are resumed, with tests via BOTDA (γ-rays) and BOTDR (X-rays): the RIA is lower for F-doped fiber than for Ge-doped ones, as well as the radiation induced frequency shift.

Rayleigh backscattering is the source of RIA measurements reported previously, as it is calculated starting from the OTDR trace of optical fibers. Some results on Rayleigh backscattering (for example [Rizzolo et al., 2015b]) pointed out also the influence of irradiation temperature on temperature measurements using an OBR under X-rays absorption. In fact, it was reported in [Girard et al., 2013a] and [Alessi et al., 2017] that the absorption of X-rays is influenced by the irradiation temperature, which helps to reduce some defects that induce losses in the fibers.

This leads us to the realisation that practically all the studies about the impact of harsh environment on optical fiber backscattering mechanisms are done taking into account all the conditions (temperature, radiation, hydrogen, etc.) separately one from another. However in-situ all these elements are present altogether: there is the necessity of coupled studies of environmental conditions on the sensors. Moreover, the combined use of Rayleigh and Brillouin scatterings should provide hints to determine the origin of the Brillouin frequency shift under radiations, regularly observed (as in [Alasia et al., 2006]), but never deeply quantified.

In order to move a step further, two of the harsh conditions that will be encountered in the radioactive waste repository cells (among others) are then applied on the sensors at the same time. The coupled radiation and temperature influence on bare optical fiber sensors is hereafter analysed: we use the term "coupled" and not "combined" as we want to assess whether the two elements influence each other, i.e. if their combined influence is equal to the sum of their individual influences. As briefly mentioned before, temperature might influence how radiation affects optical fiber sensors.

Therefore, during the thesis, we have organised an irradiation campaign dedicated to this goal.

2.2.2 Laboratory experience: irradiation campaign

In November 2017 we went to the IRMA ^{60}Co facility of IRSN (Saclay, France) to irradiate at different stable temperatures some samples of optical fiber sensors. Online measurements are acquired during irradiation in order to follow the radiation induced change over time (with growing absorbed dose). This campaign followed a previous attempt done by other colleagues to analyse the same aspects, which however did not take to the desired results. The details of the experimental test done here are hereafter reported.

2.2.2.1 Tested samples

The fiber samples under test are two single mode fibers (SMFs), representative for the topic. The first is a standard Ge-doped fiber, from ex Fibertronix (now Fibercore) company, with 5.2 wt% Ge-SiO$_2$ core and pure silica cladding, numerical aperture 0.12 ± 0.015 and core diameter 8.4 µm, selected for its representativeness of the most standard SMFs, usually encountered into strain sensing cables. The second is a F-doped fiber from ex iXFiber (now iXblue) company, with 0.3 wt% F core and 2.3 wt% F cladding, numerical aperture 0.14 and core diameter 7.2 µm, selected for its tolerance to harsh environment [Girard et al., 2013b]. As the fibers had to withstand temperatures in the order of (and over) the maximum representative temperature of the application, i.e. 90 °C, all samples have a polyimide primary coating. This coating is able to withstand temperatures over 80 °C, contrary to standard acrylate coatings. The interest in analysing hydrogen hermetic fibers took also to select a fiber with a combined carbon coating [Lemaire et al., 1988]. This specific coating is however not easily accessible for every fiber type: this is why only the Ge-doped fiber samples are equipped with it.

2.2.2.2 Test setup

Samples of these optical fibers have been placed in the irradiation chamber (as in Fig. 2.3A), placed in a vertical position and in circle around the irradiation rods support. This ensures the absorption of the same total dose and dose rate along the entire fiber length and between each of the samples. Once the cobalt rods were out, optical fibers started to absorb a dose rate of about 3.3 kGy/h ± 0.1 kGy/h (precise value depends on position, dose in air), up to a total dose of about 1 MGy in two weeks. Temperature was imposed simultaneously on different fiber samples: room temperature (RT), 80 °C, 100 °C and 120 °C. Similar conditions would be encountered if the strain sensing system was placed at the external surface of the metallic liner of high-level waste (HLW) repository cell envisioned in Cigéo, from the start of the insertion of the first disposal packages until the end of the first phase of operation.

Every sample, long 30 m, was connected to the measuring device, located in a radiation-free zone outside the chamber, thanks to 20 m long connection cables. The three heated samples, which were constituted by one F-doped fiber and a Ge-doped fiber put in series, were packaged inside thermally-controlled silicones able to withstand radiation environments up to 1 MGy and to regulate temperatures up to 180 °C (see Fig. 2.3B). In the previous irradiation campaign there were too many samples inside the silicones, which took to induce strain on the fibers due to the packaging. This helped us choosing a better way to insert the samples inside, without compressing too much the silicones sandwich. Fibers at room temperature were instead interrogated separately. Precise temperature values during irradiation for the three temperatures, measured by thermocouples inside the silicones, were in average about 86 °C, 106 °C and 129 °C (± 1 °C). Another thermocouple was positioned near the room temperature samples, to guarantee afterwards the independence of the result from the chamber temperature variations. Fibers were coiled with a 10 cm (F-doped) and 9 cm (Ge-doped) diameter to limit curvature influence.

(A) Irradiation chamber setup

(B) Heating Silicones
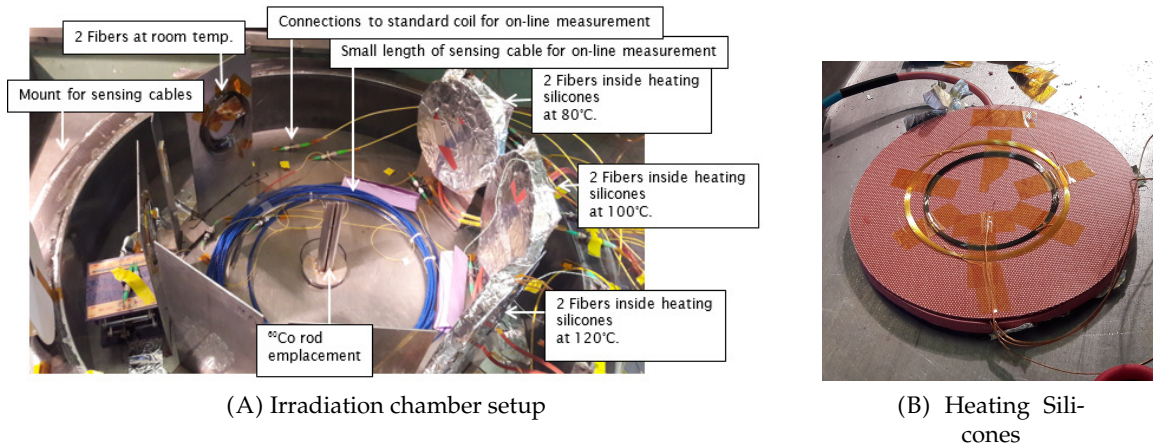
FIGURE 2.3: (A) Irradiation chamber setup prior to the radioactive rod emplacement with optical fibers heated at three controlled temperatures; (B) heating silicone with optical fiber samples and thermocouple.

2.2.2.3 Measurements: Brillouin and Rayleigh scattering

Each optical line was interrogated separately thanks to an optical switch connected to the instrument, the Neubrescope NBX-7020. It is able to perform TW-COTDR and PPP-BOTDA measurements, the main interrogation techniques used for this experimental test. A trade-off between having a short measurement duration, a proper frequency scan range and a good signal level was needed, in order to be able to perform a fair number of good measurements and do not overcharge the computer's memory. Moreover, the short duration is necessary to take into account the gradual and small variations induced by radiation and temperature, this latter only on the room temperature samples. Starting from the parameters used for the previous campaign, we have chosen a spatial resolution of 100 cm with a sampling interval of 20 cm, taking to about 150 measurement points. Some days before the campaign however we have carefully tested the samples in order to determine the best parameters, to reduce the noise and improve the results obtained previously. In order to obtain a single value for each fiber conditions, the measurement points values of the most central 20 m of fiber are averaged into a single one. Each measurement is referenced to the one taken right before the start of the irradiation, while the temperatures of the silicones were already stable. In this way, the obtained values are only due to radiation influence (which can be in turn affected by temperature). In order to obtain good measurements with the TW-COTDR technique, it is necessary to cross-correlate subsequent measurements, summing partial results up to the desired reference. This would reduce the eventuality of cross-correlation fails, which occur especially when the variations in the sensors are big enough to move the Rayleigh spectrum out from the original cross-correlation window. With the chosen parameters, specified in Tab. B.1, each measurement lasted 6 minutes for PPP-BOTDA, 17 minutes for TW-COTDR. As the instrument must interrogate the whole sequence of optical lines one at a time, each of them is interrogated around every 2 hours.

2.2.3 Temperature and radiation coupled influence on Brillouin and Rayleigh scatterings: induced Frequency Shift

Radiation impacts on both Brillouin and Rayleigh frequency shifts. The radiation induced Brillouin frequency shift is obtained by looking at the Brillouin gain spectrum (BGS) and subtracting the Brillouin central frequency ν_B of the fiber at each irradiation step to the one of the reference (i.e. no radiation, stable temperature). The same is applied to Rayleigh scattering, where the frequency shift is acquired cross-correlating subsequent Rayleigh raw traces and then summing up

the partial results to the reference. The results during irradiation from 0 to 1 MGy for the tested fibers at different temperatures are plotted in the following. For Brillouin scattering, results are in Fig. 2.4, 2.4A for Ge-doped fibers and 2.4B for F-doped fibers.
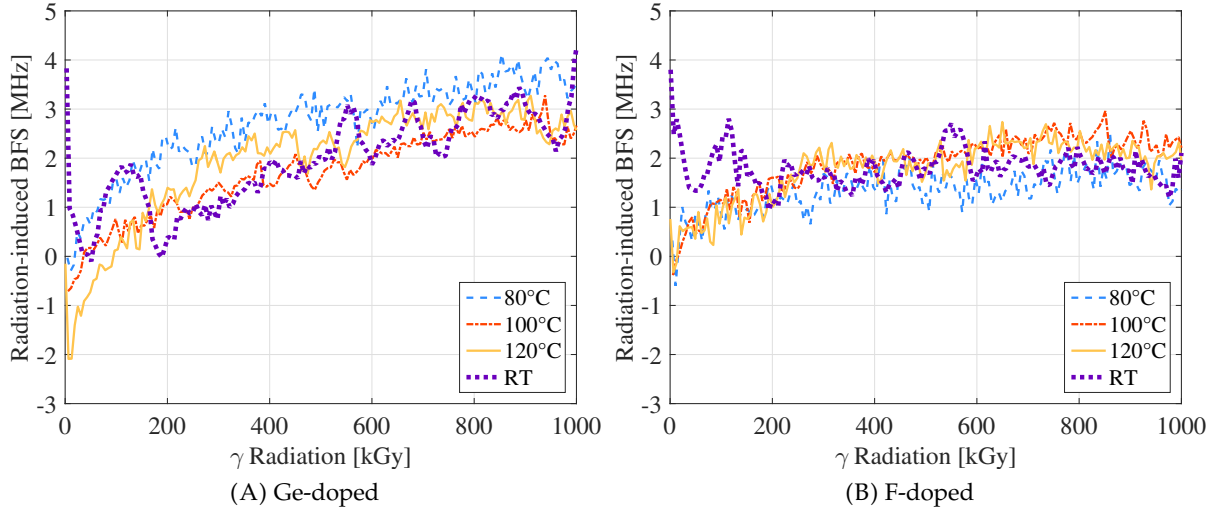
FIGURE 2.4: Radiation influence on heated fibers at different temperatures: radiation induced Brillouin frequency shift (BFS) total dose trend for (A) Ge-doped and (B) F-doped optical fibers.

For Rayleigh scattering, results are instead represented in Figs. 2.5A and 2.5B, respectively for Ge-doped and F-doped fiber samples. In the Rayleigh case we show also measurements acquired
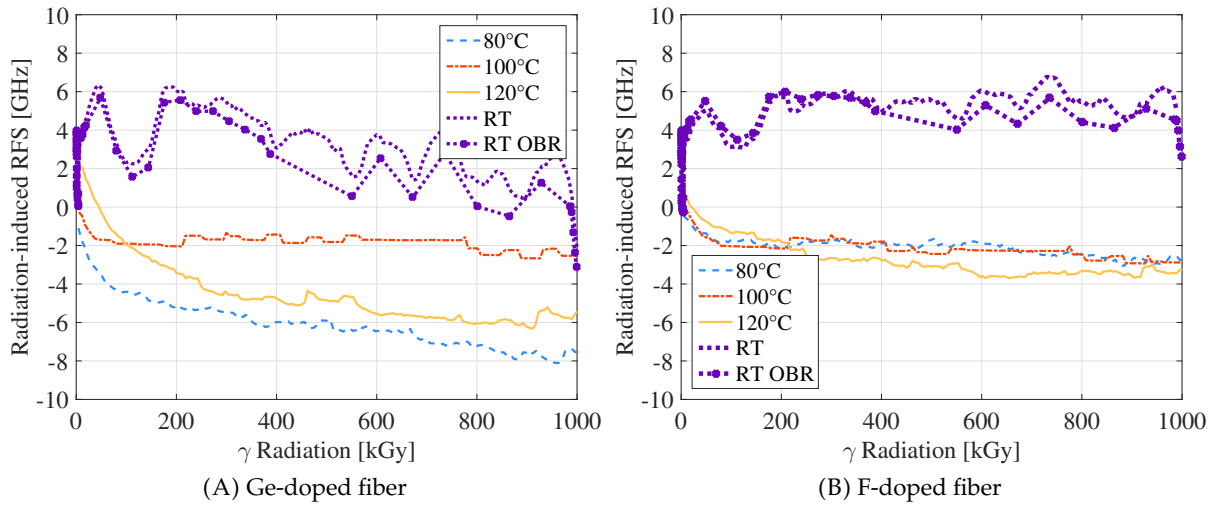
FIGURE 2.5: Radiation influence on fibers at different temperatures: radiation induced Rayleigh frequency shift (RFS) total dose trend for (A) Ge-doped and (B) F-doped optical fibers.

with the OBR (from Luna Inc.), which performs measurements based on Rayleigh scattering with a technique similar to the OFDR. We have used this instrument, taking care that parameters are the same of the NBX-7020, in order to confirm and generalise the results and the corresponding literature. The measurements are acquired from two samples of the same optical fiber spool (Ge and F-doped fibers), which were coiled on two nearby supports to be irradiated. The acquired traces

are cross-correlated and the temperature induced frequency shift is then compensated, having the attention to refer traces to the same initial state (i.e. letting traces superpose at 0 MGy).

Analysing the results of each backscattering after 1 MGy of total absorbed dose, it is possible to notice how the temperature does not impact on the radiation induce frequency shifts.

Regarding Brillouin scattering and looking at the heated fibers, for Ge-doped fibers the radiation induced frequency shift $\Delta\nu_B \simeq 3$ MHz which would take to an error in strain of about 60 $\mu\varepsilon$, while for F-doped fibers $\Delta\nu_B \simeq 2$ MHz which corresponds to about 40 $\mu\varepsilon$ at the end of the first monitoring phase. These results well agree with previous studies on radiation influence on Brillouin frequency shift with BOTDA interrogation. In [Alasia et al., 2006] a Brillouin frequency shift on Ge-doped fibers of 1.3 MHz is observed post-mortem after a received dose of about 1 MGy (5 MHz after 10 MGy). In [Phéron et al., 2012] a reduced effect of about 0.8 MHz of frequency shift is found for F-doped fibers after 1.1 MGy of total dose while 1 MHz is found for a standard SMF-28 fiber (respectively 2.3 MHz and 4 MHz after a total dose of 10 MGy). On-line tests have been also performed, revealing no transient degradation of the Brillouin response during a low dose-rate exposure (1 kGy/h for ∼6 days) up to a total doses of 160 kGy in [Cangialosi et al., 2015].

Regarding Rayleigh scattering instead, after 1 MGy heated F-doped fibers reach -3 GHz of frequency shift, which would correspond to a 20 $\mu\varepsilon$ error for strain sensing, while it reaches up to -8 GHz (∼53 $\mu\varepsilon$) for Ge-doped fibers, with a difference between all temperatures of about 6 GHz, i.e. 40 $\mu\varepsilon$.

Regarding the traces at RT, they seem to have a different behaviour with respect to samples at highest temperature, especially at the beginning of irradiation. Room temperature oscillations are due to (i) natural day and night cycles during the 2 weeks of the irradiation test, (ii) periodic lightning in the irradiation chamber for visual inspections, (iii) the rods temperature is about 60 °C and they heated the samples from the beginning of the test. To compensate these unwanted temperature fluctuations, a temperature sensor was located inside the chamber near the samples at RT. However, its location was changed once during the test, at the beginning of irradiation, in order to optimise its measurement. Consequently, temperature could not be perfectly compensated during the whole measurement. Residual RT fluctuations still affect measurements acquired on the non-regulated samples. Even with residual fluctuations however, results are promising as the shift for Ge-doped and F-doped samples at RT are in the order of 6 GHz, which means only 40 $\mu\varepsilon$ of maximum error for strain sensing in radiation environment. These results for Rayleigh scattering at RT demonstrate also that the outcomes do not depend on the interrogating device, as long as they have similar functioning parameters (operating wavelength, output power, . . .), as one would desire exploiting the same scattering technique. As a consequence, it is possible to take the literature devoted to OBR paired with fibers in radiation environment as reference for predicting durability of other similar strain sensing systems based on Rayleigh scattering, especially the TW-COTDR one (given their operating wavelength and power remain similar).

From these results, two preliminary conclusions can be drawn: i) F-doped fibers are able to better endure radiation (as already known in the literature); ii) coupled temperature and radiation effect on fibers interrogated by Brillouin and Rayleigh scatterings is not significant on the retrieved frequency shift, thus strain sensing performances are not deteriorated nor improved by the higher temperatures. More in general, it has to be said that the expected sensitivity for the application is about 10 $\mu\varepsilon$, in order to enable seeing the mechanical evolution of the structure during the first monitoring phase (first years). In this case the estimated error would be therefore higher than the desired sensitivity. However in the long term (several decades), where such error occurs, the strain range reaches about 1500 $\mu\varepsilon$ [Bumbieler et al., 2015]. With this perspective, the error due to irradiation (2 MHz for F-doped fibers) is not an issue for long term monitoring.

This confirms the feasibility of using the two scatterings-based strain sensing techniques even in harsh radiation environment for long term measurement. The fibers at 100 °C are in general the ones which withstand better radiation, independently from the dopant.

2.2.4 Temperature and radiation coupled influence on Brillouin and Rayleigh scatterings: Radiation Induced Attenuation

The radiation induced attenuation is a crucial indicator of fiber performances and is known to be influenced by irradiation temperature [Girard et al., 2013a]. For Brillouin scattering, it is possible to analyse the impact of radiation on the evolution of the Brillouin gain spectrum (BGS). First of all, let's call $g_B(\ell, \gamma)$ the BGS central peak amplitude at a certain length ℓ of the fiber and after a received dose of γ MGy. We define

$$\Delta g_B(\ell, \gamma) = g_B(\ell, \gamma) - g_B(\ell, 0) \tag{2.1}$$

the central peak amplitude difference caused by a total irradiation of γ MGy at a certain point ℓ of the fiber. In Fig. 2.6 the $\Delta g_B(\ell, 1 \text{ MGy})$ over the length of the samples is represented.

(A) Ge and F-doped fibers

(B) Detail on F-doped fibers
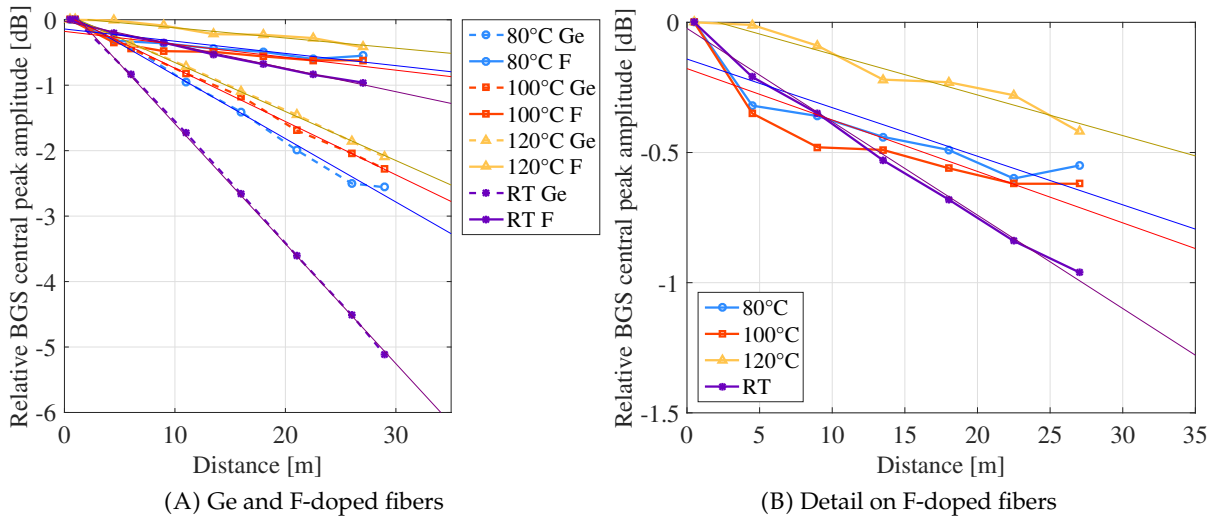
FIGURE 2.6: Radiation influence on the Brillouin spectrum around 1550 nm on the four samples at 1 MGy along their length. A linear fit is plotted along the traces.

The same can be done for Rayleigh scattering, starting from the Rayleigh spectrum loss trace at 1550 nm. In Fig. 2.7 an example of loss trace is depicted. Let's call $\alpha_{dB}(\ell, \gamma)$ the Rayleigh spectrum loss at 1550 nm at length ℓ and after a received dose of γ MGy. We define

$$\Delta \alpha_{dB}(\ell, \gamma) = \alpha_{dB}(\ell, \gamma) - \alpha_{dB}(\ell, 0) \tag{2.2}$$

as the loss at a certain length of fiber ℓ due to a received dose of γ MGy. In Fig. 2.8 $\Delta \alpha_{dB}(\ell, 1 \text{ MGy})$ is plotted for each tested sample, similarly to $\Delta g_B(\ell, 1 \text{ MGy})$.

In both cases, the traces at 1 MGy report that: i) losses grow with the distance, as standard for optical fibers; ii) the slope of the trace (which represent the attenuation) is bigger for Ge-doped fibers than F-doped fibers, i.e. radiation impacts less on F-doped fibers; and iii) the slope of the traces at higher temperature is smaller than that of samples at RT, indicating a smaller radiation impact on higher temperatures.

The radiation induced Brillouin gain attenuation RIGBA and the radiation induced attenuation RIA for Rayleigh scattering are then calculated as

$$\text{RIBGART}(\gamma) = \frac{\Delta g_B(L, \gamma) - \Delta g_B(0, \gamma)}{L} \tag{2.3}$$
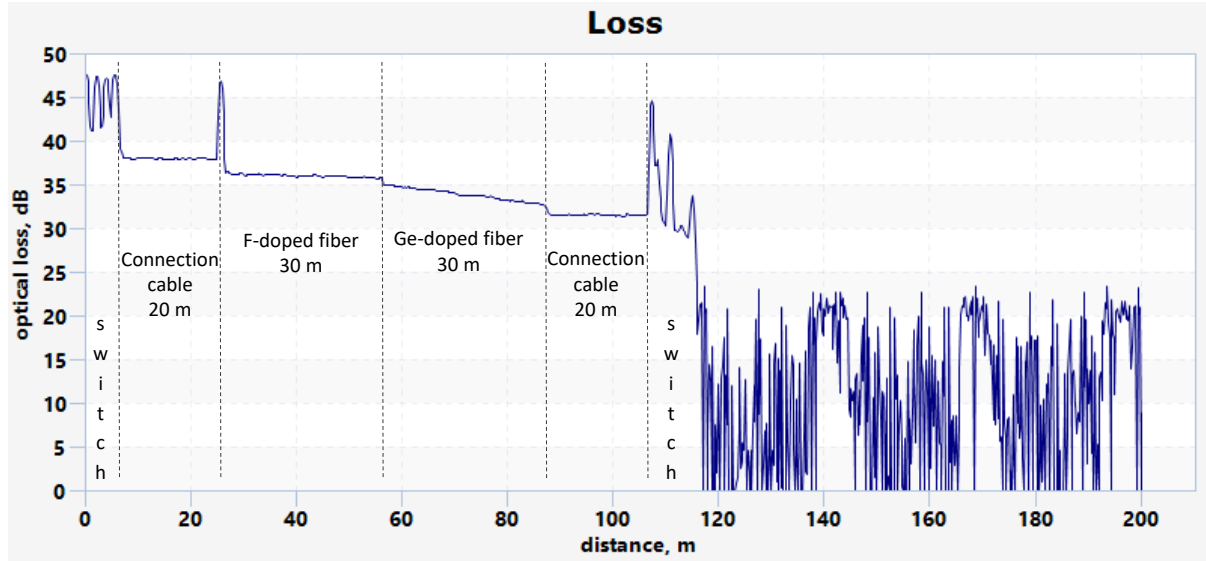
FIGURE 2.7: Example of loss trace at 1550 nm for one of the fiber samples at 100°C. It is possible to see the losses caused by connections and the different cables segments.

(A) Ge and F-doped fibers

(B) Detail on F-doped fibers
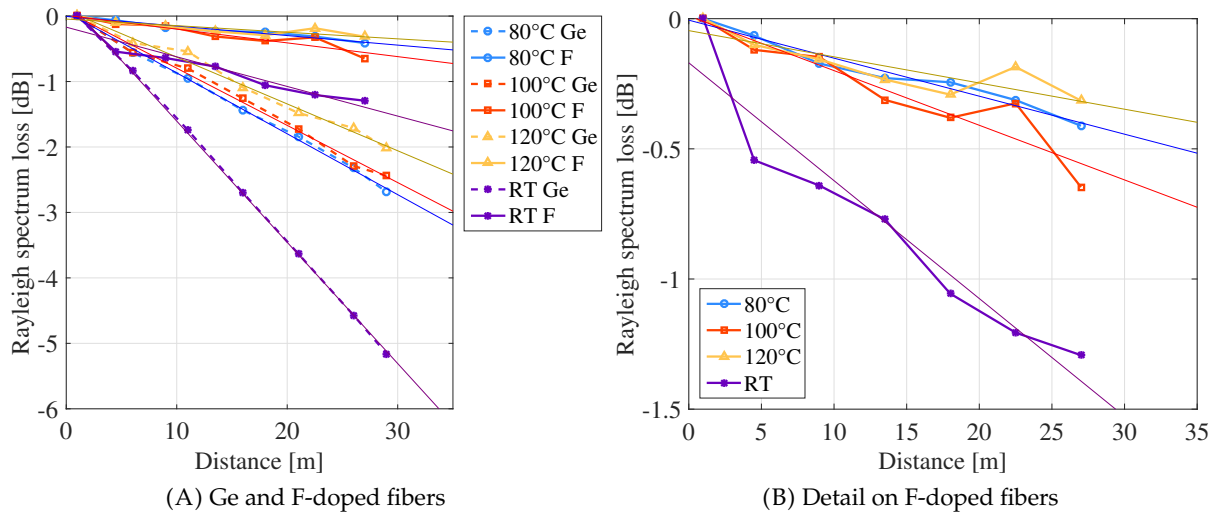
FIGURE 2.8: Radiation influence on the Rayleigh spectrum around 1550 nm on the four samples at 1 MGy along their length. A linear fit is plotted along the traces.

$$\text{RIA}(\gamma) = \frac{\Delta\alpha_{dB}(L,\gamma) - \Delta\alpha_{dB}(0,\gamma)}{L}, \qquad (2.4)$$

which are the attenuation differences between the two ends of the fiber, divided by its length L. The RIGBA(γ) is represented in Fig. 2.9A for each considered fiber type while in Fig. 2.9B a focus on F-doped fibers is shown.

The same is reported for Rayleigh's RIA overall results, plotted in Fig. 2.10A while in Fig. 2.10B a focus on F-doped fibers is shown.

Regarding Brillouin scattering, for Ge-doped fibers, at RT the attenuation after 1 MGy is about 0.18 dB/m while for the other temperatures it goes from around 0.08 to 0.09 dB/m. For the F-doped fiber at RT the attenuation is around 0.036 dB/m while for samples at higher temperature is around 0.02 dB/m. For Rayleigh scattering, for Ge-doped fibers at RT the attenuation after 1 MGy is about 0.18 dB/m while for the other temperatures it goes from around 0.07 dB/m to
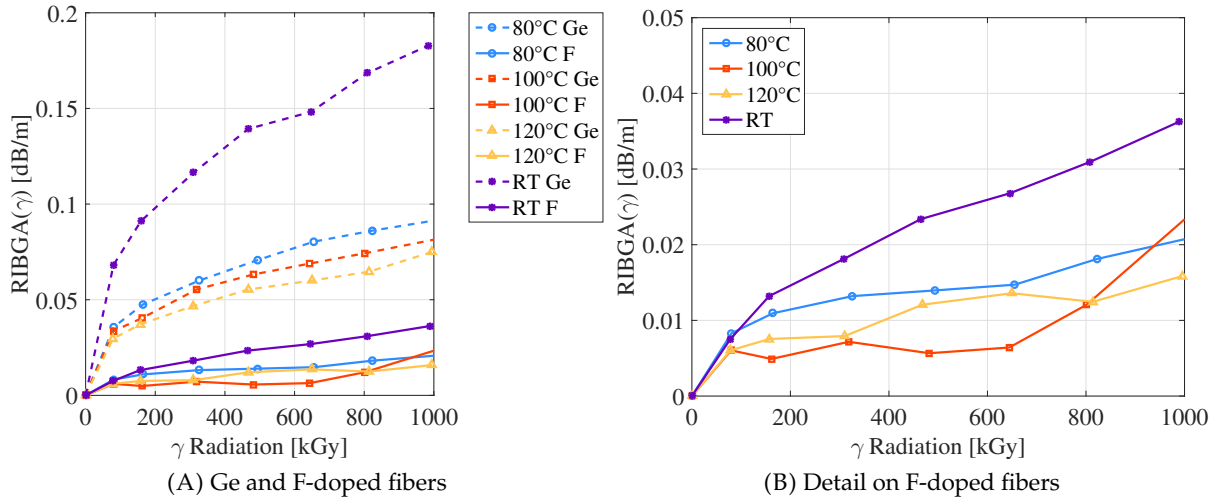
FIGURE 2.9: Radiation induced BGS attenuation (RIBGA) at 1550 nm for Ge-doped and F-doped fibers.
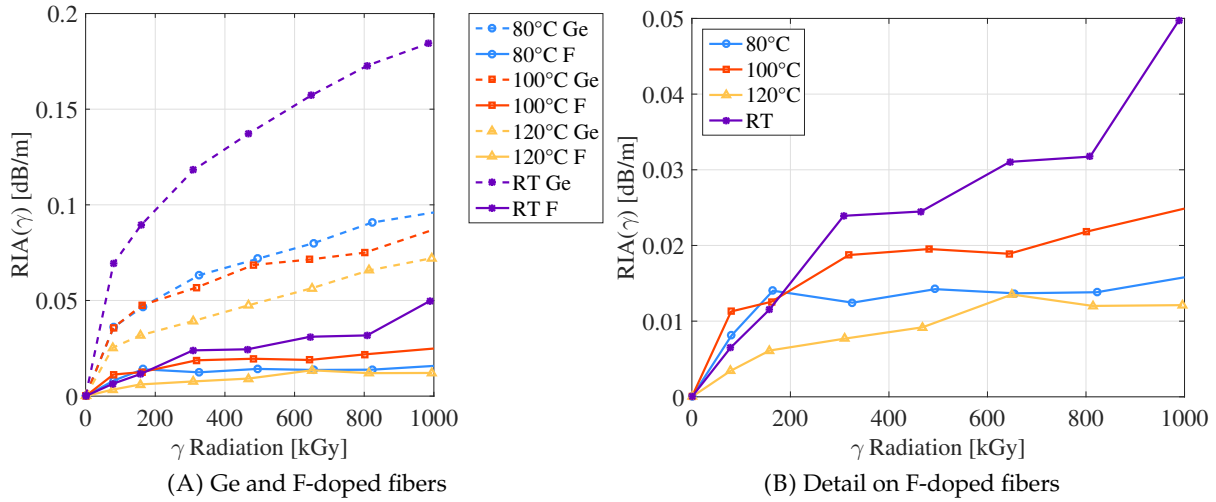
FIGURE 2.10: Radiation induced attenuation (RIA) for the Rayleigh spectrum at 1550 nm.

$\sim$0.1 dB/m. For F-doped fiber at RT the attenuation is $\sim$0.05 dB/m while for samples at higher temperature it goes from $\sim$0.01 dB/m to $\sim$0.025 dB/m at 100 °C.

This is the first time that this parameter is analysed for Brillouin scattering, while the radiation influence on the attenuations was evaluated for Rayleigh scattering in [Planes et al., 2017], online up to 56 kGy and post-mortem up to 10 MGy. RIA was evaluated online via an OTDR, giving $\sim$30 dB/km and $\sim$5.8 dB/km for Ge-doped and F-doped samples respectively at 45 kGy. Even if the fibers' dopants composition is not the same, resulting RIA values are in the same order of magnitude of what is found here. Rayleigh scattering via OBR was exploited to evaluate the changes induced by a total dose of 10 keV X-rays up to 1 MGy, varying the temperature from 40 °C up to 75 °C [Rizzolo et al., 2015a]. In this case the results led to the conclusion that temperature influence, coupled with radiation, leads to an error in distributed measurements. In [Phéron et al., 2012] a RIA of 230 dB/km after 10 MGy of total dose was found on Ge-doped fibers after irradiation, while on F-doped fibers the attenuation was of 50 dB/km. Values at 1 MGy (around 80 dB/km for Ge-doped and 25 dB/km for the F-doped fiber) are similar to the results obtained

during this test, yet they are slightly lower. This slight discrepancy is attributed to the recovery of the fiber in the post-mortem measurement configuration and the different compositions of the fibers under test.

The radiation induced attenuation, for both Brillouin and Rayleigh scatterings, presents a parabolic behaviour: it grows faster at the beginning of the irradiation and then tends to saturate a bit towards 1 MGy, while is still growing. Temperature and radiation coupled effect is here evident: the attenuation is greater for samples at RT for both dopants, while the impact of 80 °C, 100 °C and 120 °C on samples is very similar at 1550 nm. As previously concluded regarding the radiation induced frequency shift, F-doped fibers better withstand radiation suffering less losses with respect to Ge-doped fibers. This is another confirmation of the fact that i) F-doped fibers better withstand radiation overall, and that ii) high temperature helps fibers being less attenuated by radiation influence.

2.2.4.1   Brillouin vs Rayleigh: measurement distance range

Once the optical fiber is shown to withstand harsh environment, it is possible to derive the performances of the proposed strain monitoring system. Knowing the attenuation caused by the coupled influence of temperature and radiation along the length of the fibers, the expected total distance range for a distributed strain sensing system used in such complex and harsh environment can be determined.

Assuming an optical budget of 10 dB, in Tab. 2.1 values of expected maximum distance range are reported. "High Temperature" includes all three temperatures (80 °C, 100 °C and 120 °C): an average of the results for the three values is reported.

TABLE 2.1: Maximum distance range reachable under different conditions (scattering, dopant and operating temperature) if an optical power budget of 10 dB is assumed.

	Brillouin		Rayleigh	
	Ge	F	Ge	F
Room Temperature	55 m	270 m	54 m	200 m
High Temperature	122 m	500 m	120 m	600 m

In general, results show that operating at a temperature that is higher than the ambient doubles at least the maximum distance reachable with the chosen sensing system. This is extremely positive for all environments, as Cigéo, where radiation presence is coupled with high temperature, as radiation negative influence on the attenuation is drastically reduced. This is the first time where the influence of temperature on radiation impact is confirmed under Brillouin and Rayleigh scattering interrogation. Regarding the three high temperatures, the radiation induced frequency shift and the RIA for F-doped fibers show a non-monotonic response for the three heated samples with respect to the imposed temperatures. This could be due to the fact that (i) temperature affects both the generation and bleaching efficiencies of point defects and that (ii) the temperature impact also depends on the irradiation time [Girard et al., 2013a]. It is possible to finally observe that Brillouin and Rayleigh scattering sensing response show the same behaviour under irradiation, and that the F-doped fiber reaches four times the maximum distance range of the Ge-doped one. For the HLW repository cells, which are 100 m long, the reached range is more than enough. Moreover, the radiation induced Brillouin gain attenuation has the same meaning as the RIA defined for Rayleigh scattering, as calculated in Section 2.2.4. In both cases, Brillouin and Rayleigh scatterings, the optical power is high enough to induce a photobleaching effect on the two tested fiber types. The effect however has not been quantified precisely, leaving to the hypothesis that the measured RIA is the sole part of RIA that is not photosensitive. The similarity between the RIA measured with the two different interrogation techniques could be in this way explained.

2.2.5   Radiation effects on light propagation in silica

Once the coupled influence of temperature and radiation is analysed for Brillouin and Rayleigh scattering-based interrogation techniques, the step further is to combine all the information and try to understand which are the mechanisms causing radiation induced frequency shifts in fibers. More precisely, the Brillouin central frequency ν_B is related to the acoustic velocity in the fiber V_A, the (effective) refractive index n_{eff} and the interrogation wavelength λ_0 recalling Eq. 1.3

$$\nu_B = \frac{2n_{\text{eff}}V_A}{\lambda_0}.$$

For Rayleigh scattering, instead, the general definition is valid, that is

$$\nu_R = \nu = \frac{c_0}{n_{\text{eff}}\lambda_0}, \tag{2.5}$$

where c_0 is the speed of light in vacuum. Considering the interrogation of a fiber at a given λ_0, radiation could influence both n_{eff} and V_A regarding Brillouin scattering [Alasia et al., 2006; Bao and Chen, 2011], while only n_{eff} in Rayleigh scattering. As a consequence, assuming the two quantities are independent one from the other (for a given fiber composition), the frequency shift can be described as following for Brillouin scattering

$$\Delta\nu_B(n_{\text{eff}}, V_A) = \frac{2\Delta n_{\text{eff}}V_{A,0}}{\lambda_0} + \frac{2n_{\text{eff},0}\Delta V_A}{\lambda_0}; \tag{2.6}$$

and for Rayleigh scattering

$$\Delta\nu_R(n_{\text{eff}}) = -\frac{c_0}{\lambda_0}\frac{\Delta n_{\text{eff}}}{n_{\text{eff},0}^2}, \tag{2.7}$$

where $V_{A,0}$ and $n_{\text{eff},0}$ are respectively the acoustic velocity and the effective refractive index of the fiber in pristine conditions. As Δn_{eff} plays a role in the frequency shift for both scatterings, it is possible to use it to understand how coupled temperature and radiation induce a variation in the acoustic velocity V_A. From Eq. 2.7 we can get the radiation induced Δn_{eff}, to be then substituted into Eq. 2.6, obtaining

$$\Delta n_{\text{eff}} = -\frac{\Delta\nu_R n_{\text{eff},0}^2\lambda_0}{c_0} \Rightarrow \Delta V_A = \left(\Delta\nu_B - \frac{2\Delta n_{\text{eff}}V_{A,0}}{\lambda_0}\right)\frac{\lambda_0}{2n_{\text{eff},0}}, \tag{2.8}$$

where $c_0 \simeq 3 \cdot 10^8$ m/s and $\lambda_0 = 1550$ nm. At this point, as experimental values for $\Delta\nu_B$ and $\Delta\nu_R$ are known from Section 2.2.3, only $V_{A,0}$ and $n_{\text{eff},0}$ are missing in order to calculate the radiation induced Δn_{eff} and ΔV_A. Knowing the fiber composition, its refractive index profile $n(x,y)$ and its acoustic velocity profile $V_L(x,y)$ can be modelled. Through a collaboration with Camille Sabatier, Ph.D. student of the University of St. Etienne (FR), it is possible to calculate the refractive index profile by using the coefficients given in [Jen et al., 1993] and considering a refractive index value of 1.444 for the pure silica at 1550 nm. The fiber acoustic velocity profile can be calculated through Eq. 2.9 [Kobyakov et al., 2005]:

$$V_L(x,y) = V_{LSiO_2} \times \left(1 + \Delta V_{L,D} \times \%\omega t_D\%(x,y)\right) \tag{2.9}$$

where $V_L(x,y)$ is the longitudinal acoustic velocity profile, V_{LSiO_2} is the longitudinal acoustic velocity of pure silica, $\%\omega t_D\%(x,y)$ is the percentage of the weight percent of the dopant, and the $\Delta V_{L,D}$ is the dependence of the longitudinal acoustic velocity on the doping with element D. The used dependencies for Ge and F-doped fibers are given in Tab. 2.2 and compiled from [Mamdem, 2012; Dragic, 2009].

TABLE 2.2: Dependencies of the acoustic velocity on fiber doping for different dopants.

Dopants	V_L^0 [m/s]	V_T^0 [m/s]	ΔV_L [m/s] $\%\omega t_D\%$	ΔV_T [m/s] $\%\omega t_D\%$
SiO$_2$	5944	3767	-	-
GeO$_2$	3310	2233	-0.47	-0.49
F	-	-	-3.60	-3.10

Having the refractive index and acoustic velocity profiles, it is possible to solve with COMSOL Multiphysics™ the optical propagation and the mechanical Eqs. [Tartara et al., 2009; Koyamada et al., 2004]:

$$\Delta^2 E(x,y) + \left(\frac{2\pi}{\lambda_0}\right)^2 \left(n(x,y)^2 - n_{\text{eff}}^2\right) E(x,y) = 0 \tag{2.10}$$

$$\Delta^2 U(x,y) + \left(\frac{\Omega^2}{V_l(x,y)^2} - \beta_{\text{acoustic}}^2\right) U(x,y) = 0 \tag{2.11}$$

where $E(x,y)$ is the transversal distribution of the electric field, $U(x,y)$ and Ω are the transversal distribution and the pulsation of the acoustic mode, and β_{ac} is the acoustic propagation constant, as defined by:

$$\beta_{\text{ac}} = 2\beta_{\text{opt}} = \frac{4\pi}{\lambda_0} n_{\text{eff}}. \tag{2.12}$$

From this simulation it has been found, for tested Ge-doped fibers, that $V_{A,0} \simeq 5739$ m/s and $n_{\text{eff},0} \simeq 1.447$, while for F-doped fibers $V_{A,0} \simeq 5896$ m/s and $n_{\text{eff},0} \simeq 1.439$ to be used in Eq. 2.8.

Combining all experimental ($\Delta \nu_B$ and $\Delta \nu_R$) and simulated ($V_{A,0}$ and $n_{\text{eff},0}$) values into Eq. 2.8, results for the refractive index evolution due to radiation Δn_{eff} are plotted in Figs. 2.11A and 2.11B, while the acoustic velocity change under irradiation ΔV_A is represented in Figs. 2.12A and 2.12B for Ge and F-doped fibers respectively. Samples at RT are not considered due to the aforementioned measurement fluctuations.
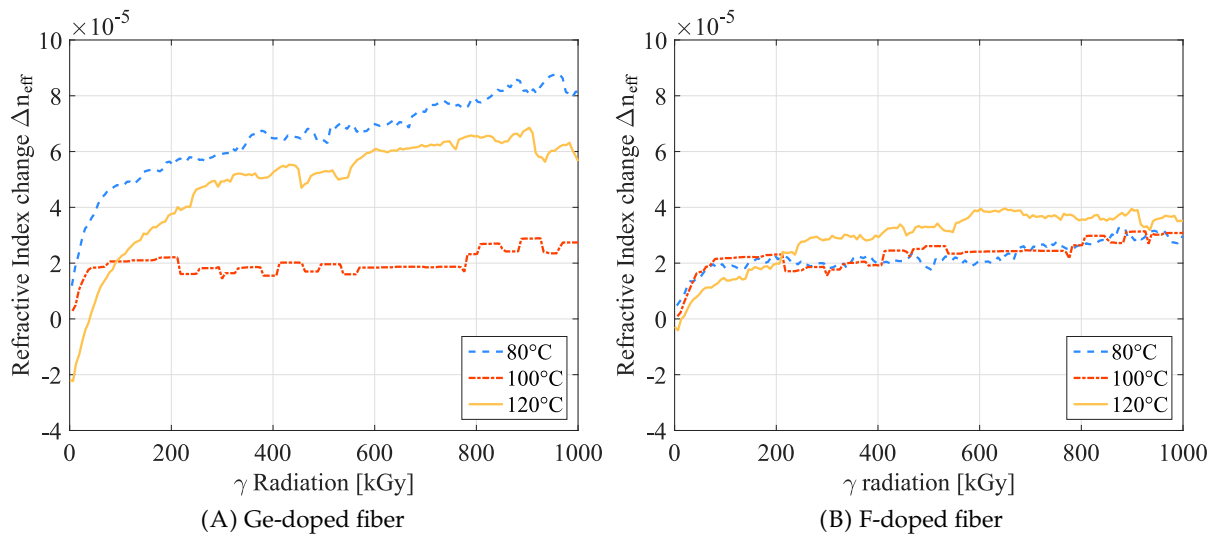
FIGURE 2.11: Radiation influence on fibers at different temperatures, effective refractive index variation: (A) for Ge-doped and (B) for F-doped fibers.

Results reflect what was found in Sections 2.2.3 and 2.2.4: F-doped fibers react in a better way than Ge-doped fibers in view of their exploitation in radiation environment. The change in
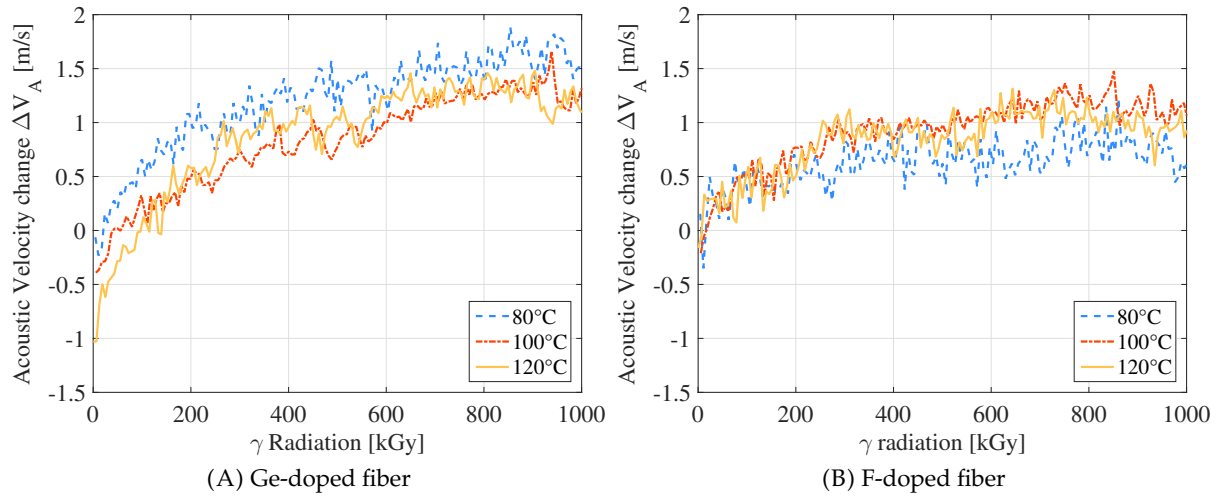
FIGURE 2.12: Radiation influence on fibers at different temperatures, acoustic veloc-
ity variation: (A) for Ge-doped and (B) for F-doped fibers.

refractive index measured via TW-COTDR is observable especially in germanosilicate fibers. The samples at 100 °C are the ones which are less impacted, regardless of the dopants. The variation in the acoustic velocity in Figs. 2.12A and 2.12B is less apparent (1 m/s over 5800 m/s in 1 MGy absorbed dose) but it is present: it depends on the dopant type and grows with the absorbed radiation dose. Results confirm also the hypothesis of [Alasia et al., 2006] where the Brillouin frequency shift is related to a change in density of the silica, even if it is very low [Laurent et al., 2016]. In our case the variation of the density of silica is with high probability represented by the variation of the acoustic velocity. In any case, although the impact of radiation on the fiber density change is minimal, the variation occurs and it causes frequency shift in Brillouin scattering whose amplitude is not negligible for strain sensing purposes. This calculation allows to determine the origin of Brillouin frequency shift under radiations, which was never deeply explained and quantified before.

2.2.6 Section conclusion

At this point, before going to the step further, it is important to resume what we have obtained assessing the coupled temperature and γ-radiation influence on bare optical fibers, using Rayleigh and Brillouin scattering-based interrogations. Here, online measurements have been performed on Ge-doped and F-doped fibers up to 1 MGy of irradiated total dose. Temperature coupled impact on radiation influence is negligible regarding the frequency shift, while it is significant for the radiation induced attenuation. This is true for both Rayleigh and Brillouin scatterings and for both Ge-doped and F-doped fibers. Temperature around 100 °C reduces the RIA, thus its presence in radiation environment actually helps the proper operation of distributed optical fiber strain sensing. Operating at high temperature doubles at least the maximum distance reachable with the sensing systems taken into account, compared to working at ambient temperature. The study confirmed also the convenience of adopting F-doped fibers in harsh environment, being more robust to radiation than Ge-doped fibers. The combined analysis of harsh environment (coupled temperature and radiation) on both Brillouin and Rayleigh scattering allowed also to deeply assess the physical properties related to light propagation which are impacted. Radiation impacts on the refractive index (regarding both scatterings), Brillouin scattering suffers also the acoustic velocity change. The change in the acoustic velocity is very little (around 1 m/s) but the effect is well observable for strain sensing purposes. The effect of coupled temperature and radiation influence is also for the first time demonstrated to be the same for two different Rayleigh-based

interrogation techniques (TW-COTDR and OBR). This allows to have a generalized literature in the field. It is also proven that the ageing qualification of optical fiber sensing systems must be performed taking into account the influencing parameters (temperature and radiation here) altogether. The superposition of the results of the influence of each parameter took alone would not be representative, thus not correct. Finally, it is once more proven the feasibility of using optical fiber in radiation environment, as the radiation impact is almost negligible overall for strain sensing purposes. All these results were object of a journal publication, [Piccolo et al., 2019a], introduced by an oral presentation at the 26th International Conference on Optical Fiber Sensors in Lausanne (CH), [Piccolo et al., 2018a].

The step further is to perform similar analyses on an optical fiber strain sensing cable. The comparison between measurements performed on an irradiated cable and on another one in pristine conditions would lead to understand the impact of radiation on the fiber coating and external jacket, as well as the role of the coating in protecting the fiber from external conditions.

2.3   Post-mortem radiation and temperature influence on strain sensing cables
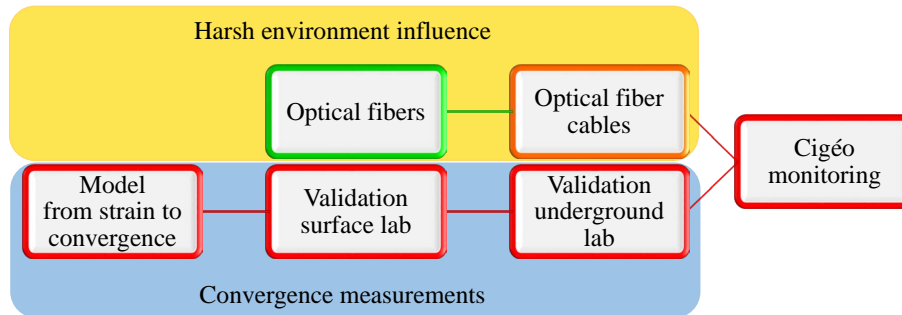
FIGURE 2.13: Schematic of the Ph.D. methodology: once the harsh environment influence is assessed on the optical fibers, we analyse the radiation impact on strain sensing cables' outer sheaths, as well as on cables' mechanical behaviour.

2.3.1   State of the art

In SHM applications, optical fibers are often inserted in cables to improve the sensitivity performances, enhance their mechanical robustness and protect the fiber from the harsh environment in which they are employed. The structure of the cable may however have an influence in both the short and the long-term sensing characteristics of the fiber. An harsh environment, in fact, can affect not only measurement results but also the mechanical behaviour of the sensor itself and its durability. In the majority of the applications, however, the maintenance over the monitoring period is possible only on the interrogation instrument, while the sensor is definitively embedded in its environment and cannot be accessed to be repaired nor replaced. It is therefore important to select not only the best interrogation method, to reduce at maximum measurement errors, but the sensing cable as well, able to resist the application's load level and harsh environment over the needed monitoring period. In nuclear structures monitoring, such as nuclear power-plants operation and dismantlement phases, physics reactor (CERN...) or space industry, sensing systems face radiation while monitoring period must exceed 50 years. Investigations on the impact of these harsh conditions on optical fibers in their primary coating have been and are still being carried out, in order to select the best optical fiber composition and interrogation method [Planes et al., 2017; Piccolo et al., 2019a]. Nevertheless, as distributed optical fiber sensors (DOFS) are often put into cables when employed on-field, their composition and the structure of the cable must be therefore carefully selected to be sufficiently resistant and, at the same time, keep as much as possible the elasticity of the sensor. The external sheath should also be chosen in order to maintain or even improve its sensitivity to the measured variable. For this reason, tests should be carried out in order to analyse the physical and sensitivity characteristics of pre-existent or brand new optical fibers and optical fiber cables. A lot of work has already been devoted to optical fibers (in primary coating): for example, in [Li, Ren, and Li, 2012] the mechanical properties and strain transferring mechanism of optical fiber sensors are analysed, on the different layers of an FBG, while in [Her and Huang, 2011] the role of the coating is studied for strain transfer. In [Stolov, Simoff, and Li, 2008] the concept of thermal stability in optical fibers is clarified and in [Li et al., 2018] the coating thermal stability and mechanical strength at elevated temperatures of optical fibers is evaluated on different samples. The physical properties of the coating are also evaluated in [Li, Li, and Wang, 2003] where the elasto-plastic bond mechanics of the fiber coating are evaluated, while in [Barrias, Casas, and Villalba, 2019] a fatigue test was carried out assessing the performance stability of DOFS over 2 million load cycles.

Regarding cables, however, the bibliography is not so wide. As strain sensing cables are deployed to measure the strain of the structure, many papers are focused on the analysis of the strain transfer function, i.e. to know how much of the structure's strain is transferred to the fiber:

$$\varepsilon_{\text{FO}}(s) = \varepsilon_{\text{struct}}(s) \otimes \text{MTF}(s).$$

The mechanical transfer function $\text{MTF}(s)$, which translates the strain of the structure $\varepsilon_{\text{struct}}(s)$ in the sensor strain $\varepsilon_{\text{FO}}(s)$, represents the behaviour of the sensor without the need to specify its physical and mechanical characteristics. The strain transfer function of different kinds of cables is already assessed (for example, [Henault, 2013; Billon et al., 2014; Bassil, 2019]), however the physical and sensitivity characteristics of strain sensing cables, as the elasto-plastic behaviour and the impact of the protection layers on the optical fiber measurements, are not well considered in the literature. Two exceptions are found: in [Monsberger et al., 2017] the strain sensitivity of different strain sensing cables is analysed, with attention to the initial residual hysteresis, while in [Hauswirth, 2015] the mechanical properties of various distributed optical fiber temperature and strain sensing cables are assessed prior the application to soil displacement monitoring.

In the market many different optical fiber strain sensing cables are present, designed to fulfil different requirements. From standard cables, made of a kevlar fiber layer between the fiber and the plastic outer sheath, the cables are nowadays composed by layers of different materials, dimension and shape. In this thesis, many cables have been considered for different reasons. Some cables have only one fiber inside, while some others have more than one in order to discriminate more easily strain and temperature influence. This can be obtained having singlemode and multimode fibers in the same cable (as AFL) or singlemode fibers inserted differently in the cable: free from constraint to measure temperature, more jointed to the cable to follow strain.

The AFL cable (Fig. 2.14) is made of plastic only, while some other cables are reinforced with other materials, as for example metal.

(A)   (B)
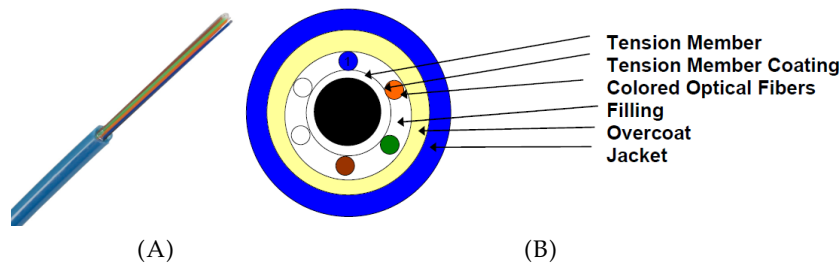
FIGURE 2.14: Plastic cable: AFL cable. (A) prospectus, (B) section.

This is the case of many cables from Solifos AG (ex Brugg cables) which have a metal tube (V9, Fig. 2.15A) or a spiral of metal wires (V3, Fig. 2.15B) around the optical fiber, which help the fiber be more joint to the cable. Other cables have metallic parts, as for example cables from Neubrex (Fig. 2.15C) or Fujikura (Fig. 2.15D), which have metallic wires put in parallel to the fiber to reinforce the cable's mechanical behaviour. Metallic parts in general are good for the reinforcement of the cable and for the fact that metal is less impacted by harsh environment with respect to plastic, however it's important to notice that metal tends to expand more than glass at high temperatures, which impacts on the sensitivity coefficients of the cable in a non negligible way.

The cables are also of different shapes: the majority has circular section, as the V3, V9 or the AFL, while others have a flat outline. The Fujikura and Neubrex cables, for example, have a flat section that is more adapted than circular ones to be fixed more homogeneously to the surface of a structure. The surface of the cable can be also more or less suited in this regard. Some cables, as the AFL, have a smooth surface, while others (as the V3, V9 or some flat ones) have a corrugated
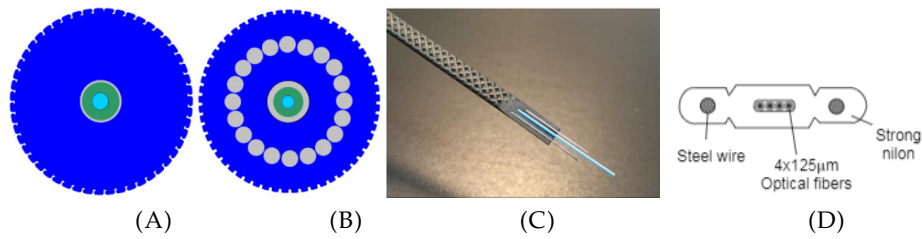
FIGURE 2.15: Strain sensing cables with metallic parts: V9 (A) and V3 (B) from So-
lifos AG, Embossed from Neubrex (C) and the flat ribbon JBT-03813 from Fujikura
(D).

surface, which helps the bonding between the cable and the material into which is embedded (for
example inside concrete).

While some of these cables have been tested during the Ph.D., one of them has been selected
to perform the ensemble of the experimental tests. A strain sensing cable for an application as
Cigéo must be the more resistant as possible to harsh environment, which requires the presence
of metallic parts to protect the fiber. Moreover, a rough surface might improve the strain transfer
of the cable in concrete of ILW-LL repository cells' liners thanks to a higher level of bonding be-
tween the materials. Considering these requirements and a good trade off between tensile strength
and minimum curvature radius, the V9 type optical fiber strain sensing cable has been selected
to investigate on the durability and mechanical behaviour of such a sensing cable under harsh
environment influence.

Different aspects are here considered:

- i) how does radiation influence the durability, mechanical behaviour and sensitivity of the
  sensing cable?

- ii) how do the protection layers of the cable impact on the durability, mechanical behaviour
  and sensitivity of the fiber?

- iii) how do optical fiber strain sensing cables behave under high strain?

For this reason a series of experimental tests have been organised. During the Ph.D., in the frame-
work of the Innovative Training Network FINESSE, the requirement of performing some months
of secondments took to visit Solifos, AG, in Switzerland. In their facility there are many machines
and tools dedicated to perform different kind of mechanical tests (traction, crush, impact, bend-
ing, etc.) as well as thermal tests. This was a perfect occasion to acquire expertise in the field of
optical fiber strain sensing cables, as I have personally done on my own all the tests (under the
eye of the laboratory head for safety reasons) and the consequent data analysis.

2.3.2   Laboratory experience: secondment in Solifos

During the secondment some of the testing machines in Solifos' laboratory have been used, eval-
uating the characteristics of different samples of cables and fibers. The considered cable, the V9
type, is a 3.2 mm mini armored fiber optic strain sensing cable with ∼0.9 mm central metal tube
(FIMT, Fiber In Metal Tube), structured polyamide (PA) outer sheath and one optical single mode
fiber (SMF) inside. For the specific application, in the framework of the European project Mod-
ern2020, a suited optical fiber (F-doped for radiation hardening, carbon coated for hermeticity
to hydrogen) has been inserted in a V9 type strain sensing cable. This custom SMF has 0.3 wt%
F-doped core and 2.3 wt% F-doped cladding, numerical aperture 0.14 and core diameter 7.4 μm,
with an attenuation at 1550 nm of 0.40 dB/km and an effective refractive index of about 1.439.
The preform of this fiber is a copy of the one used for the fiber reported in Section 2.2.2.1, i.e. they
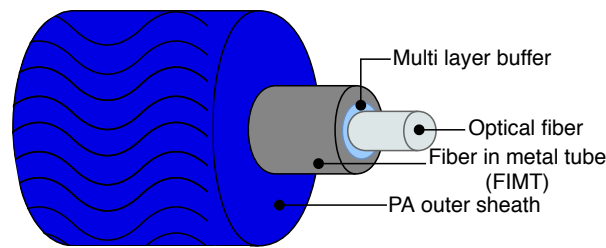
FIGURE 2.16: Schematic of the V9 type strain sensing cable, composed by a polyamide sheath of 3.2 mm of diameter, a steel tube (FIMT) of ∼0.9 mm of diameter, a multi-layer buffer which helps the strain transfer and a SMF (250 µm).

share the same refractive index profile, however it has improved characteristics for the insertion in a strain sensing cable. The fiber is made to be more resistant to micro-curvatures, it is tested up to 200 kpsi (1.38 GPa) and the main coating is not polyamide but high-temperature acrylate.

Before its use on site, however, it is necessary to know its characteristics in sensitivity and durability. Once the fiber is protected into a cable, its sensing characteristics may change as the composition of the sensor (materials, dimensions, etc.) changes. For these reasons, the tests here presented are meant to assess i) the sensitivity of the newly developed sensor, ii) the influence of the different protective layers on the behaviour of the sensor and iii) the impact of harsh environment (radiation, in this case) on its performances.

The considered experimental tests are the following:

- Traction: to analyse the strain sensitivity and elasto-plastic behaviour, under high strain;

- Crush and impact: to analyse the resistance of the cable to localised shock and stress, before and after the radiation influence. Only V9 type samples have been considered for these tests;

- Bending: to assess whether the bending of the cable at a certain radius affects measurement results;

- Thermal: to determine the temperature sensitivity and the impact on the durability of the cable → cables put under thermal cycle go through a traction test to check whether there are differences in the behaviour due to temperature.

2.3.2.1   Tested samples

In order to characterise the sensor, some of the tests are conducted not only on the custom V9 type cable samples (Figure 2.17A), but also on its constitutive parts: the FIMT (with the custom radiation hard fiber inside, Figure 2.17B) and the naked fiber itself (only primary coating). Besides, the same analysis has been carried out on standard commercial samples of the same types (V9, FIMT and bare fiber), which are constituted of a standard SMF G657 with acrylate coating. It is in fact interesting to assess whether the different fibers inside the cable influence in different ways the performances of the sensors. Furthermore, as the goal is also to assess the impact of radiation, part of the V9 and FIMT samples have been previously irradiated up to 500 kGy, which is half of the absorbed total dose during the first 100 years of monitoring of Cigéo first HLW repository cells. The cables have been irradiated during the same campaign at IRMA in November 2017: the different distance of the cables from the irradiation source and their support in metal let them absorb less dose, i.e. up to 500 kGy. The position of the cable with respect to the other irradiated samples (depicted in Fig. 2.3A) is shown in Fig. 2.18. The received dose rate in this way was about 1.5 kGy/h.

(A) V9

(B)
FIMT
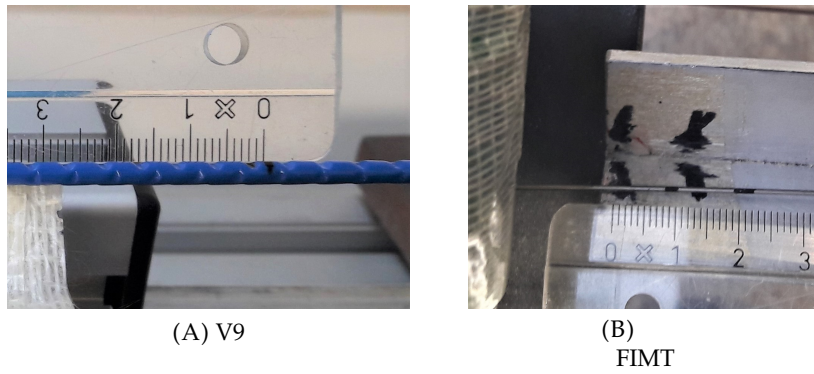
FIGURE 2.17: Tested cables: V9 (A) and FIMT (B) types.
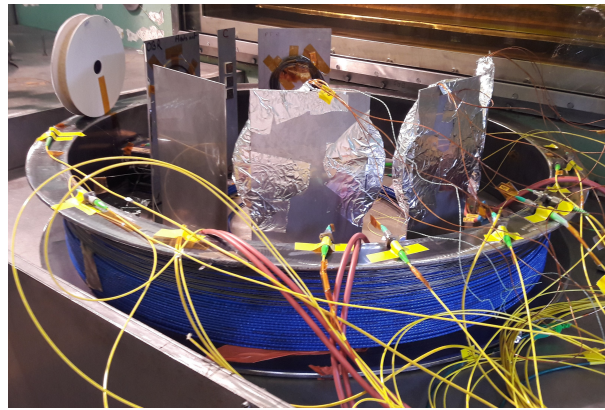
FIGURE 2.18: Disposition of the cabled samples (V9 and FIMT type) in the irradiation chamber.

For the sake of comprehension, the different samples under tests are synthesised in Tab. 2.3 and will be so addressed from now on.

TABLE 2.3: Tested samples.

	V9	FIMT	Fiber
Standard SMF G657 acrylate coating	V9	FIMT	OF
Custom (not irradiated) SMF F-doped carbon acrylate coating	$V9_F$	$FIMT_F$	OF_F
Custom (irradiated) SMF F-doped carbon acrylate coating	$V9_F^{☢}$	$FIMT_F^{☢}$	-

2.3.3   Traction: strain sensitivity

The strain sensitivity of a sensor is calculated imposing strain on it, with the help of a traction bench, and measuring the frequency shift with respect to the unstrained sensor. The value of the slope of the trace obtained by plotting the frequency shift over the imposed strain is the corresponding strain sensitivity coefficient of the considered sample.

2.3.3.1 Test setup

Traction tests are performed by fixing the samples at a 10 m manual traction bench. The samples are elongated using a winch, checking the new length with a ruler and a laser distance meter (millimetric precision). Measurements, whose parameters are reported in Tab. B.2, are acquired every 500 µε in strain (nominal value, 5 mm of elongation). Every 1000 µε the sample was taken back to the initial position (no elongation) in order to check whether there is residual strain, i.e. to analyse the plastic strain of the sample. Another measurement was then acquired. This is performed up to 10,000 µε, while for the FIMT type samples the measurements back to zero are performed up to 7000 µε. Once the maximum strain range is reached (1% of strain by datasheet, i.e. 10,000 µε), measurements are acquired every 1000 µε (10 mm in elongation), without taking the sample back to its original position (no elongation), up to the 30,000 µε or up to the breaking point. The generalised traction cycle is depicted in Figure 2.19.
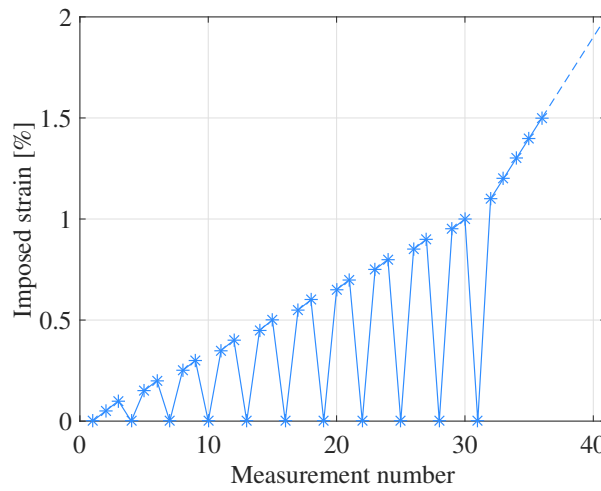
FIGURE 2.19: Traction cycles.

2.3.3.2 Strain sensitivity values

During elongation, the cabled samples, especially of the V9 type, slipped from the anchoring due to difficulties in the fixation of samples with diameter bigger than the millimeter. This led to an error, between the desired strain value and the one obtained in reality after the slippage, that remains however under the 5% and it grows in a distributed and homogeneous way from 0 µε to the maximum elongation reached by the sample. Despite the error, the homogeneity guarantees the correct analysis process.

Measurements have been taken with a resolution of 20 cm and a sampling of 10 cm, obtaining about 100 measurement points over the 10 m bench (excluding connection cables). It has also to be specified that, as all tests have been performed in the same period of time and in the same place, the temperature is supposed to be stable (differences in the order of $\pm 2°C$, i.e. about ± 2 MHz for Brillouin and ± 1.3 GHz for Rayleigh). Therefore, the measured frequency shift is attributed solely to the imposed traction. The results presented in the following are the outcome of the analysis of one sample of each specimen summarised in Tab. 2.3. In this case, only measurements up to 10,000 µε in traction are considered.

The strain sensitivities of the tested samples are obtained by averaging the frequency shift $\Delta\nu$, obtained by interrogating the samples with Brillouin and Rayleigh scatterings, over the central 9 m of the samples to avoid measurement values on the anchoring points. An example of frequency shift obtained under different levels of traction, for example for the standard V9 sample, along the fiber length is represented in Fig. 2.20. The curves $\Delta\nu$ over strain so obtained for Brillouin and
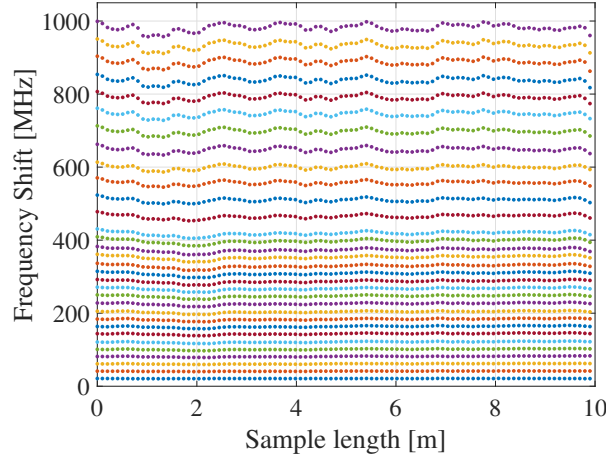
FIGURE 2.20: Frequency shift traces during traction (higher frequency shift for higher traction) for the standard V9 type sample, showing no relaxation of the sample.

Rayleigh scatterings are plotted in Fig. 2.21, while the strain sensitivity coefficients are calculated as the slopes of these curves (linear fit from 0 to 10,000 μɛ). The values so calculated are reported in Tab. 2.4. The values for the irradiated custom fiber are not available as the fibers irradiated in the mentioned campaign have absorbed a higher total dose with respect to the cable, at a different temperature and they were also difficult to unravel after irradiation to be tested under traction. The strain sensitivity coefficients of both types of bare fiber are perfectly in agreement with stan-

| (A) Brillouin | (B) Rayleigh |
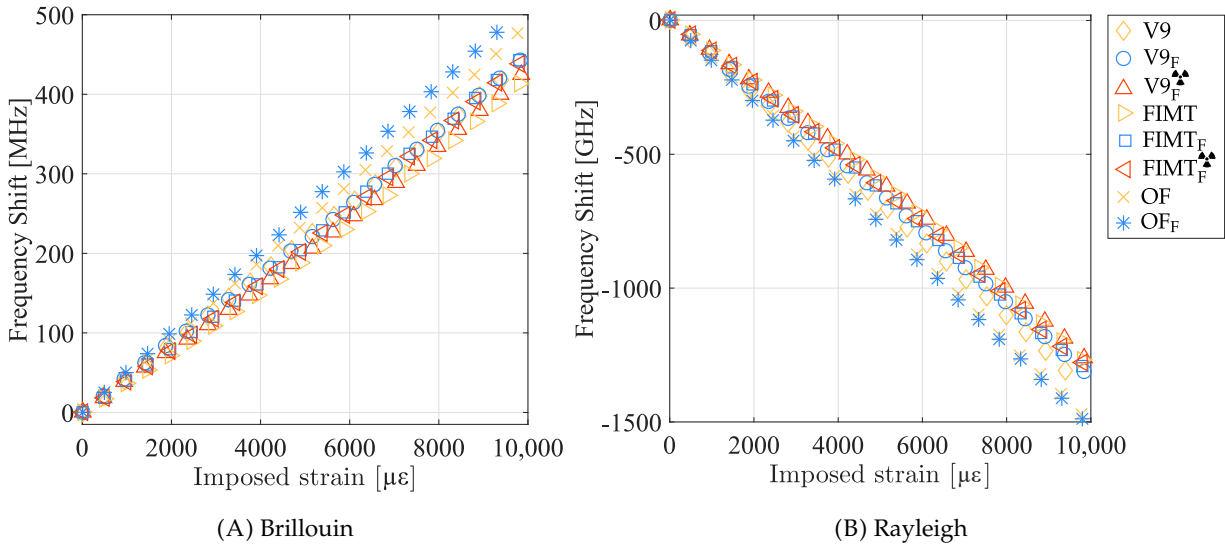
FIGURE 2.21: Frequency shift over strain curves for all the tested samples, for Brillouin and Rayleigh scatterings.

dard values, $C_\varepsilon^B = 0.050$ MHz/μɛ for Brillouin and $C_\varepsilon^R = -0.15$ GHz/μɛ for Rayleigh, while the cables' coefficients stay respectively around $C_\varepsilon^B = 0.045$ MHz/μɛ and $C_\varepsilon^R = -0.13$ GHz/μɛ. V9 and FIMT type samples Rayleigh strain sensitivity coefficients found in [Monsberger et al., 2017] are in the order of -0.15 GHz/μɛ, probably based on the different calibration approach which takes into account the hysteresis of the cable.

Observing the results, especially the cabled samples (V9 and FIMT types), it is noticeable how the strain sensitivities do not differ very much from one sample to another. The strain sensitivity

TABLE 2.4: Strain sensitivity coefficients of the different tested samples.

B: [MHz/µε]	Custom		Standard
R: [GHz/µε]	Not irradiated	Irradiated	
V9	B: 0.0450	B: 0.0430	B: 0.0443
	R: -0.134	R: -0.128	R: -0.138
FIMT	B: 0.0456	B: 0.0452	B: 0.0425
	R: -0.133	R: -0.132	R: -0.131
Fiber	B: 0.0516	B: -	B: 0.0488
	R: -0.152	R: -	R: -0.151

difference between the final sensor (V9 type) and the original bare fiber goes from 9% (standard type) to 12% (custom radiation hard), revealing the possibility to insert the desired fiber into the cable, keeping as much the information on its strain sensitivity. The sensitivity differences remain thus under 15%, a standard variation range when different cable compositions and structures are considered. When it comes to analyse the impact of radiation on the sensor, the sensitivity difference between irradiated and not irradiated samples is as low as 1% (FIMT type) and 4% (V9 type), which means that the sensitivity remains stable. This is a very promising result: if we consider radiation influence as linear, 4% in error over 500 kGy would mean an error in strain of 8% in 100 years (1 MGy), i.e. only about 220 µε over 2700 µε. In every case, sensitivity coefficient values for irradiated samples are lower than for those not irradiated. Most of the radiation impact is exerted on the physical properties of the cable: the PA outer sheath becomes more fragile and less ductile due to radiation [Porubská, 2016], leading to more cracks during elongation and, therefore, to break sooner than non-irradiated samples (Figure 2.22).

FIGURE 2.22: Impact of the radiation on the V9 type cable: radiation reduces the ductility of the plastic, causing cracks when curved.

With exception of the fibers, the standard samples and the not irradiated V9 type, some cables broke during the test. The custom irradiated V9 type broke reaching the nominal value of 12,000 µε, while custom FIMT type cables broke at 21,000 µε and 29,000 µε, respectively for the pristine and the irradiated one. In practice, the only cable that suffered from radiation influence is the V9 type. This is mainly attributed to the impact of radiation on the polyamide, while FIMT type cables broke mainly due to its structure: the traction leads the cable to bend and fold, which causes the fiber and the metallic tube to break at high tension. In all cases, if breaks occurred during traction, it is always after 10,000 µε, therefore the datasheet guaranteed strain range remains valid. These results are very promising for the use of such a cable in an application where radiation is present.

2.3.4 Traction: elasto-plastic behaviour

The same setup is used to assess the elasto-plastic behaviour of the tested samples. As the cable is partially composed by steel, which is the most rigid component of the cable and tends to show a plastic behaviour after a certain strain (typically 0.2% [Smith and Hashemi, 2010], i.e. 2000 µε), it is interesting to look for the possible plastic behaviour of the tested cabled samples (FIMT and V9 types). Let's take as example the standard FIMT type sample, in order to directly observe the behaviour of the steel protecting the fiber. In Figs. 2.23A and 2.23B the frequency shift over strain curve is plotted, respectively for Brillouin and Rayleigh scatterings.

(A) Brillouin

(B) Rayleigh
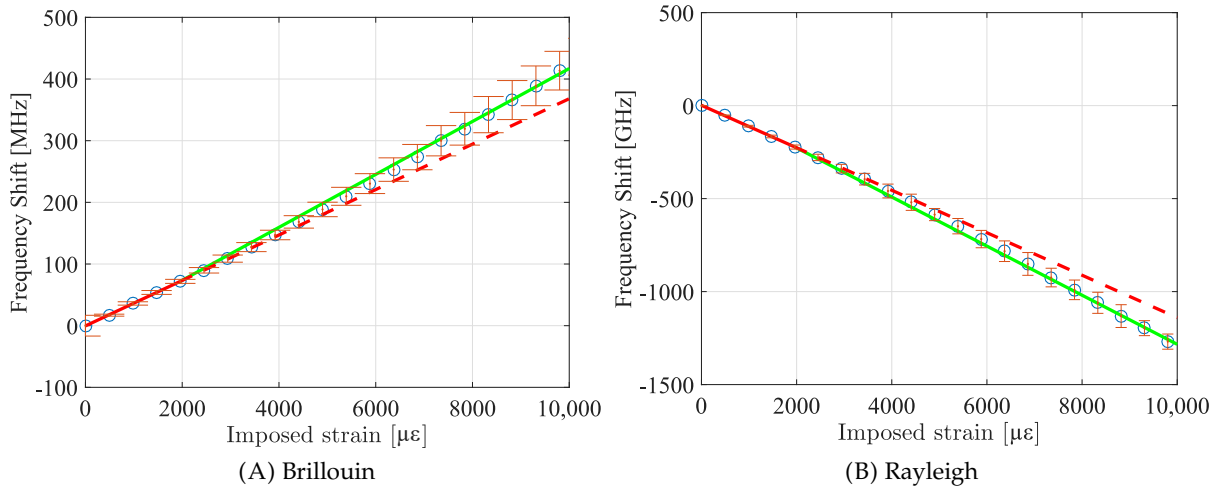
FIGURE 2.23: Detail of the mechanical behaviour of the FIMT standard type sample. The curve presents two zones with different slopes (highlighted in red and green): this represents the plasticity of the steel of which the FIMT is made.

The uncertainty of the measurements is reported as error bars, while the slope of the curve is calculated separating the strain behaviour into two zones: before and after 2000 µε. It is visible how the linear regressions of these two zones are different: before 2000 µε (red line) the strain coefficient (i.e. the slope) is smaller than afterwards (green line), showing a possible plastic behaviour of the sample due to traction. This is valid also for the other samples, which strain coefficient values are reported in Tab. 2.5. To make it more immediate to evaluate, the strain sensitivities are

TABLE 2.5: Strain sensitivity coefficients of the different tested samples.

B: [MHz/µε] R: [GHz/µε]	Custom				Standard	
	Not irradiated		Irradiated			
	<0.2%	>0.2%	<0.2%	>0.2%	<0.2%	>0.2%
V9	B: 0.0447 R: -0.131	B: 0.0459 R: -0.136	B: 0.0402 R: -0.116	B: 0.0445 R: -0.132	B: 0.0432 R: -0.137	B: 0.0453 R: -0.139
FIMT	B: 0.0410 R: -0.122	B: 0.0473 R: -0.136	B: 0.0398 R: -0.118	B: 0.0470 R: -0.135	B: 0.0368 R: -0.114	B: 0.0446 R: -0.136
Fiber	B: 0.0502 R: -0.152	B: 0.0519 R: -0.152	B: - R: -	B: - R: -	B: 0.0463 R: -0.147	B: 0.0491 R: -0.152

plotted in Fig. 2.24. The biggest difference between the sensitivities of the two identified zones (and therefore, the biggest plastic effect) appears to be exerted on the FIMT, as the V9 type is composed also of the external PA layer which limits the permanent strain of the steel.

This behaviour should be then confirmed looking at the measurements performed when the samples are in their original position, i.e. when they are not elongated. The frequency shifts of

(A) Brillouin

(B) Rayleigh
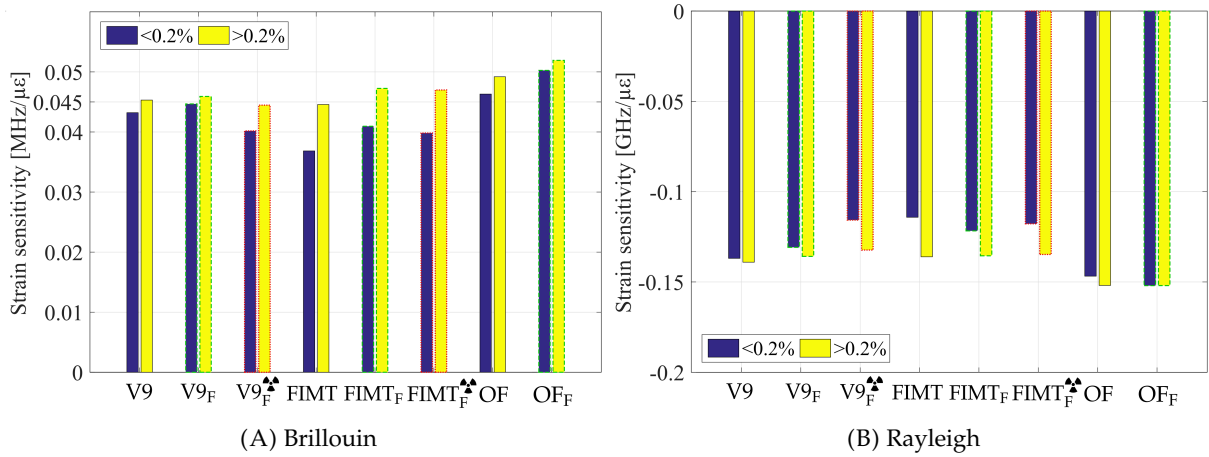
FIGURE 2.24: Strain sensitivity coefficients for different linear fittings: "<0.2%" and ">0.2%" represents the fit done considering only the values before or after 2000 µε. The different contours of the bars define the type of sample: black and straight line are the standard samples, green and dashed for the custom not irradiated, red and dotted for the custom irradiated.

the samples, obtained by interrogating the samples via Brillouin and Rayleigh scatterings at their original position, are plotted in Figs. 2.25A and 2.25B respectively.

(A) Brillouin

(B) Rayleigh
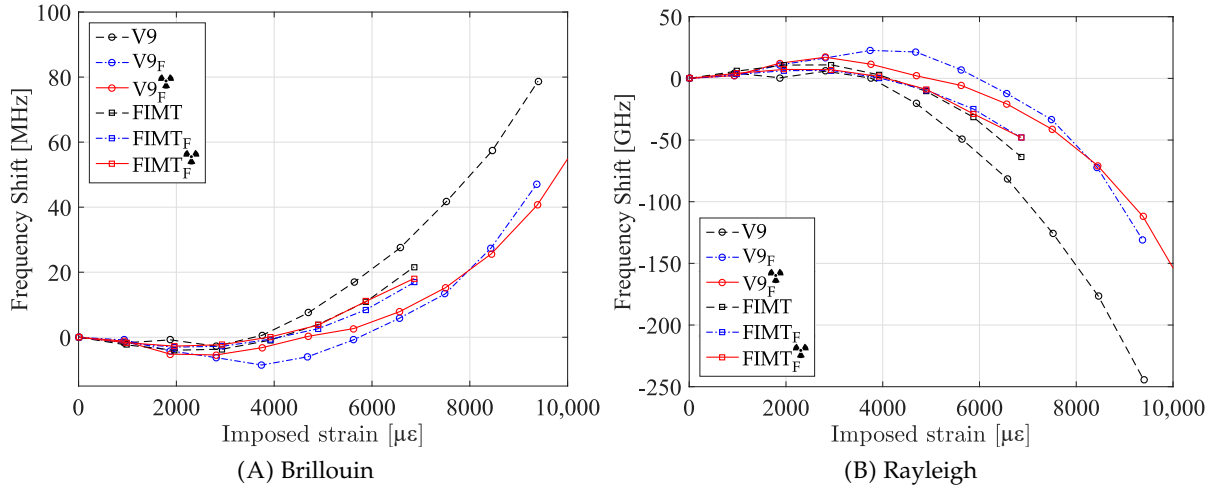
FIGURE 2.25: Residual frequency shift of the cabled samples (V9 and FIMT) after elongation (represented in the *x* axis) for the three tested types of condition (standard fiber, custom radiation hard fiber, custom radiation hard fiber irradiated).

It is remarkable how the cabled samples (V9 and FIMT types) show a permanent frequency shift, i.e. residual strain, after being elongated. This does not happen for the fiber, which undergoes only a slight relaxation (Fig. 2.26). This is related to the multilayered nature of the cable: parts of it undergo permanent strain and there may also be slippage at the interface between the layers. This underlines the importance of characterising the whole sensing cable and not only the fiber in primary coating for the sensitivity.

This is similar whatever the fiber (custom radiation hard or standard), as the main actors in this behaviour are the protective layers of the fiber (polyamide, steel tube), and whether the samples are irradiated or not. From about 2000 µε, the samples are increasingly and permanently
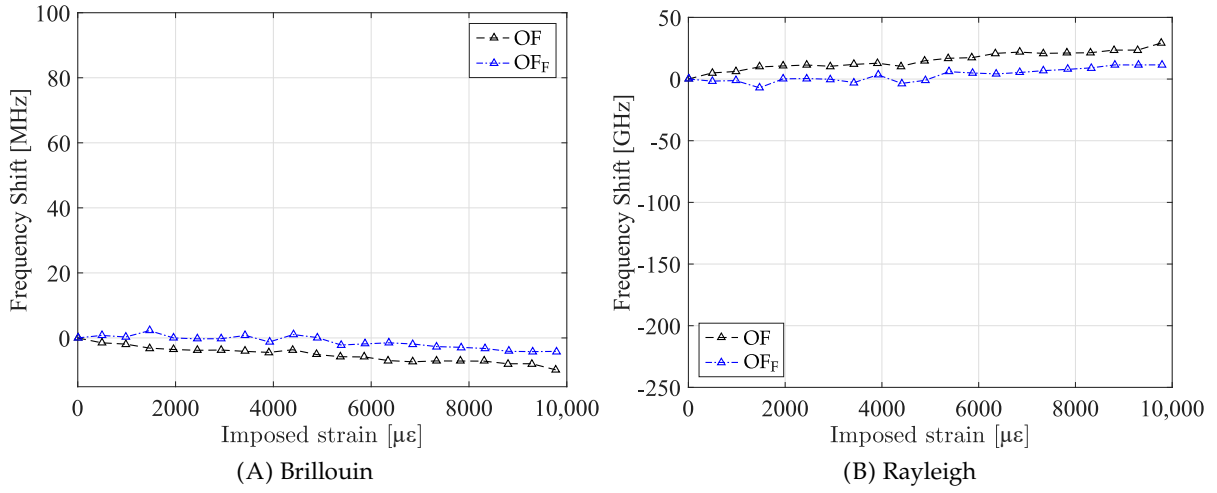
FIGURE 2.26: Residual strain of the fiber samples after elongation (represented in the x axis) for the two tested types of condition (standard fiber, custom radiation hard fiber).

deformed, reaching about 60 MHz for Brillouin and -170 GHz for Rayleigh scatterings, which correspond to about 1400 με, a non negligible value. When the strain range reaches 10,000 με, plasticity is an important phenomenon to consider in the design phase. For Cigéo reference scenario, as the foreseen maximum strain would be around the ±3000 με, the error due to this permanent strain is practically none, being around 100 με in compression.

Using the strain sensitivity coefficients previously calculated, it is possible to check whether the sensors, interrogated with two different scatterings, measure the same strain values. Using the values in Tab. 2.5, it is possible to transform the frequency shift into strain following Eq. (1.2). The results are plotted in Fig. 2.27.
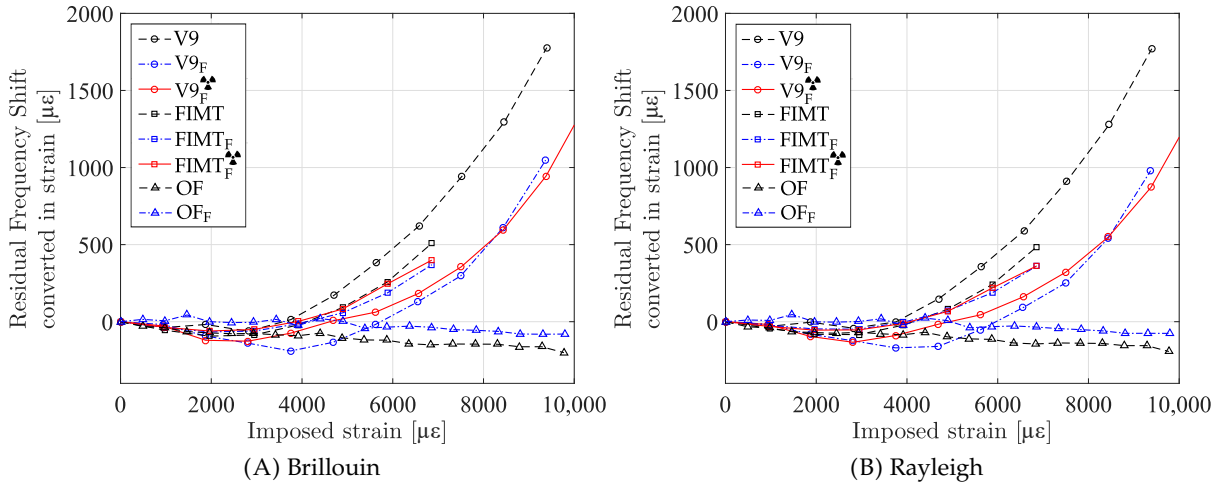
FIGURE 2.27: Residual strain of all the samples after elongation (represented in the x axis).

The two strain profiles, deriving from Brillouin and Rayleigh scatterings, are very close to each other. The results are in general in agreement with the conclusions drawn from Figs. 2.24: FIMT type samples (FIMT, $FIMT_F$ and $FIMT_F^{\text{☢}}$) are the most plasticised, with a higher residual strain with respect to sample $V9_F$ and $V9_F^{\text{☢}}$ (the custom V9, not irradiated and irradiated). However,

the standard V9 sample is the one which shows the highest permanent strain between all, even if it is of the V9 type. This behaviour, that has yet to be explained, could be due to the different adhesion between the fiber and the internal surface of the FIMT. In any case, as for the sensitivity, there is practically no difference between not irradiated and irradiated samples (V9$_F$ and V9$_F^{☢}$, FIMT$_F$ and FIMT$_F^{☢}$), taking to consider as negligible the impact of the absorbed dose. This is very important for environment where radiation is present, as this means that the behaviour of the sensor is practically not impacted by it, then being suitable to work in such applications.

Even if Cigéo repository cells are not concerned by the plasticity of the cable during the monitoring phase, it is very important to keep in mind that its conditions may change with an unexpected rise in the strain. Nevertheless, this is a general useful reminder for all kind of applications where the strain is over 4000 με.

The difference between the residual strain obtained with Rayleigh and Brillouin scattering is lower than the uncertainty on the Brillouin measurements (of the order of 20 με) up to 6000 με of imposed strain, and remains smaller than 10% in relative value for higher imposed strains. This is very positive, as it shows that the results are the same despite the use of two interrogation methods, based on two different scatterings, underlining the interoperability of the two (as reported for example in Section 2.2.4.1). Moreover, since the measurement principles are different, it proves that the residual strain is related only to the variation of the cable's structure (i.e. not on backscattering properties).

2.3.5 Crush

In the crush test, 10 cm of cable have been put under a press, as depicted in Fig. 2.28, under different loads, to check whether the cable withstands or not a heavy load along time and if irradiation changes the behaviour of the external sheath.
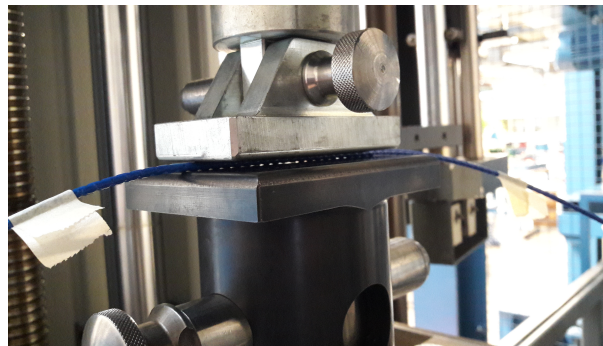
FIGURE 2.28: Crush test.

In order to perform proper measurements, the cable must be fixed in the same position from the start to the end of the measurements: in this way, differences are only due to the higher crush amplitude. For this reason, it is necessary to refer the measurements to the condition where the cable is already under crush. For example, a sample of the standard V9 type has been loaded from 100 to 300 daN (the load able to deform the FIMT of 15%) with a step of 100 daN, having the reference measured at 1 daN. Each load was kept for 23 minutes. Frequency shifts obtained via Brillouin and Rayleigh backscattering, using the acquisition parameters reported in Tab. B.3, is plotted in Fig. 2.29, where the 10 cm under crush are shown. Results show how the cable undergoes tension that is higher when crush amplitude is higher, in agreement with the common knowledge. What is more evident is how Rayleigh-based results are clearer and more accurate than Brillouin based ones, thanks to the cross-correlation method between subsequent measurements. The crushed zone is more visible and more homogeneous, reporting a more stable value. The cable, at a first visual inspection after the release at 0 daN, reported no physical alteration.
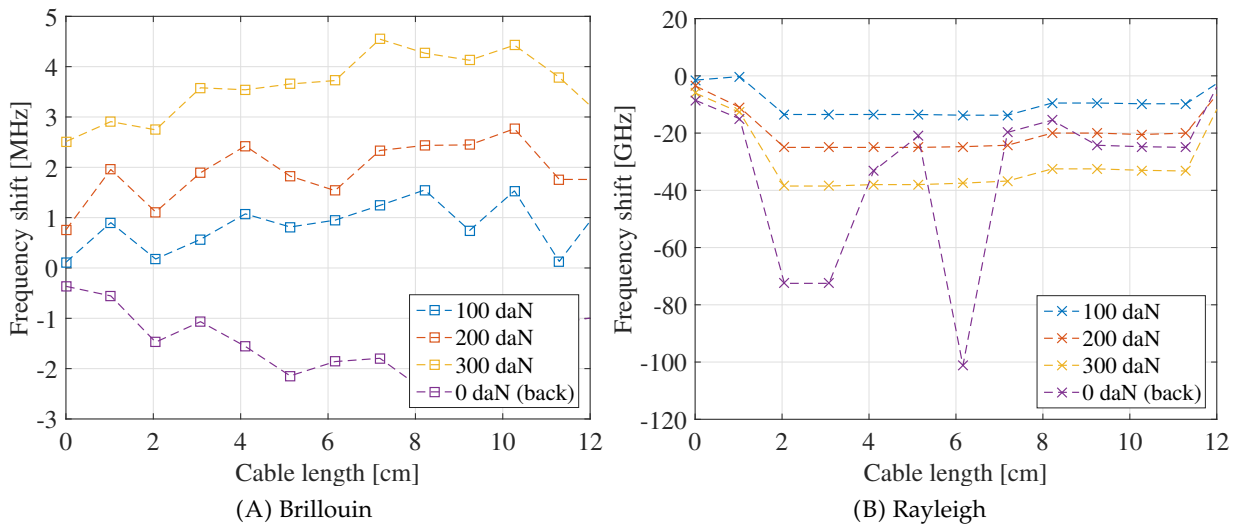
FIGURE 2.29: Crush results for the standard V9 type. Reference 1 daN.

Measured traces in Fig. 2.29 reveal however a permanent strain due to the load. The same kind of results is observable for the other V9 type samples (V9$_F$ and V9$_F^{\text{☢}}$), which were similarly loaded with steps of 50 daN to thicken results. These are represented in Fig. 2.30 only for Rayleigh scattering. Results reveal also that there is no evident difference between irradiated and not irradiated samples.
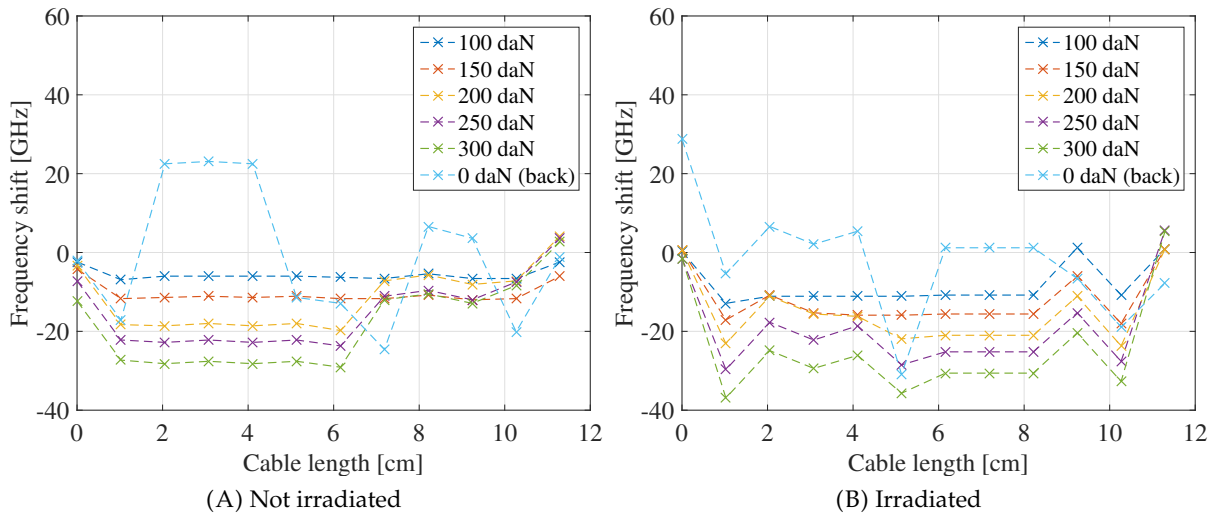
FIGURE 2.30: Crush results for the custom not irradiated V9 type (sample V9$_F^{\text{☢}}$). Reference 50 daN.

In general, the following conclusions can be drawn: i) crush induces tension in the cable, ii) loads up to 23 minutes and up to 300 daN do not visibly affect the physical integrity of the cable, nor they prevent the optical transmission, iii) with Rayleigh scattering it is possible to obtain clearer results and iv) radiation does not appear to impact in any way the behaviour of the cable.

2.3.6 Impact

V9 type samples have been tested under impact, where a load (a hammer) hits locally and punctually a part of the cable (setup in Fig. 2.31). For this test, different weights have been chosen: a measurement was acquired every 2 or 3 hit of a 1 kg hammer, while a 3 kg hammer was used after 6 total hits of 1 kg. This approach was suggested by the experience of the supplier. This test is meant to assess the resistance of the cable to accidental hits and installation handling, that occur locally and not continuously, like crush test. Measurement parameters are reported in Tab. B.4.

(A)　　　　　　　　　　(B)
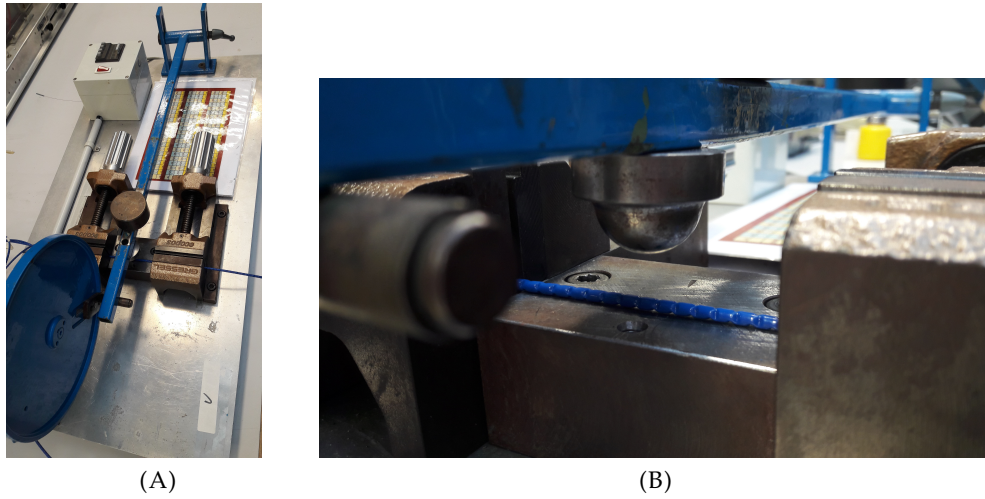
FIGURE 2.31: Impact test setup (A), the hammer falls on the cable thanks to an automatic mechanism (B).

Results are plotted in Fig. 2.32 for the standard V9 type, in Fig. 2.33 for the custom not irradiated V9 type and in Fig. 2.34 the custom irradiated V9 type. As for crush, results are clearer and

(A) Brillouin　　　　　　　　　　(B) Rayleigh
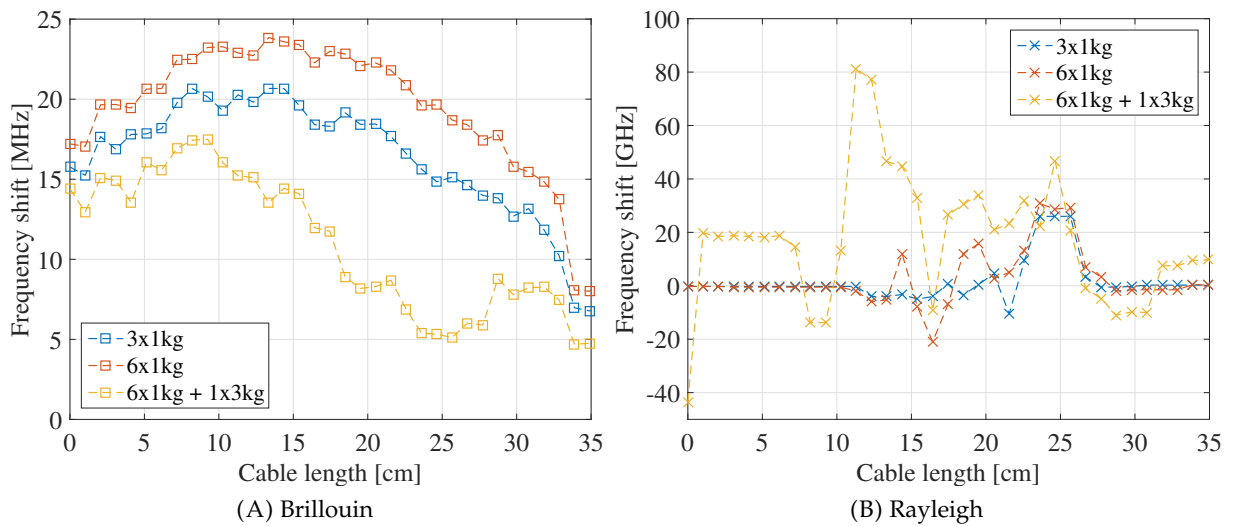
FIGURE 2.32: Frequency shift induced by impact, on the standard V9 type sample.

more accurate with Rayleigh-based interrogation with respect to the Brillouin ones, as we remain in the range of small deformations (less than 100 µε between each measurement). The difference between not impacted and impacted area is more visible, as the different levels of loads are more evident. With higher loads the impact induced Rayleigh frequency shift is correspondingly higher, while it is not so clear looking at Brillouin-based results. In any case, the cable samples resisted
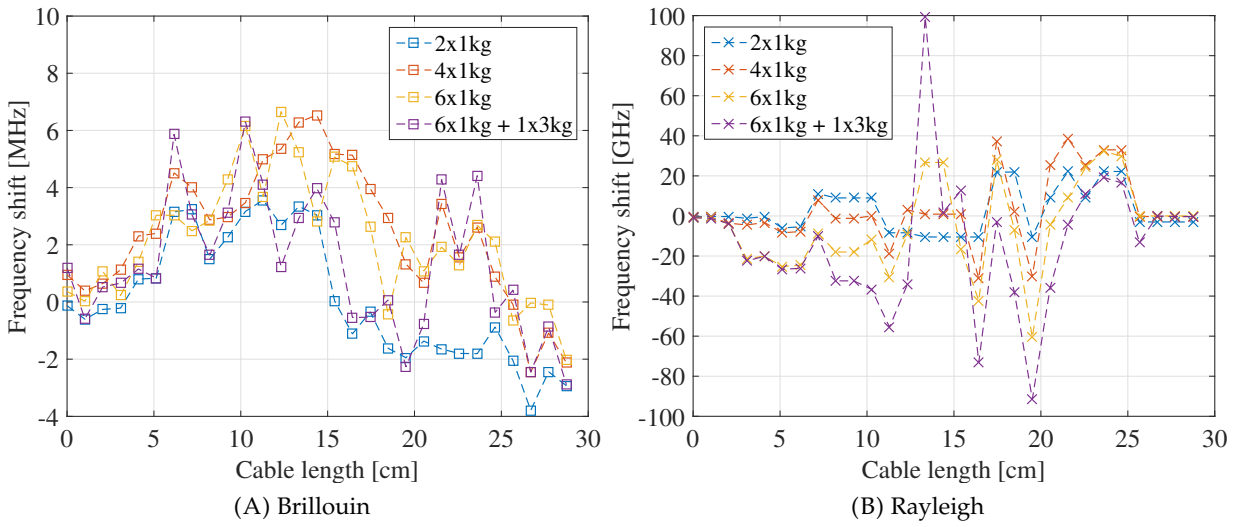
FIGURE 2.33: Frequency shift induced by impact, on the custom not irradiated V9 type sample.
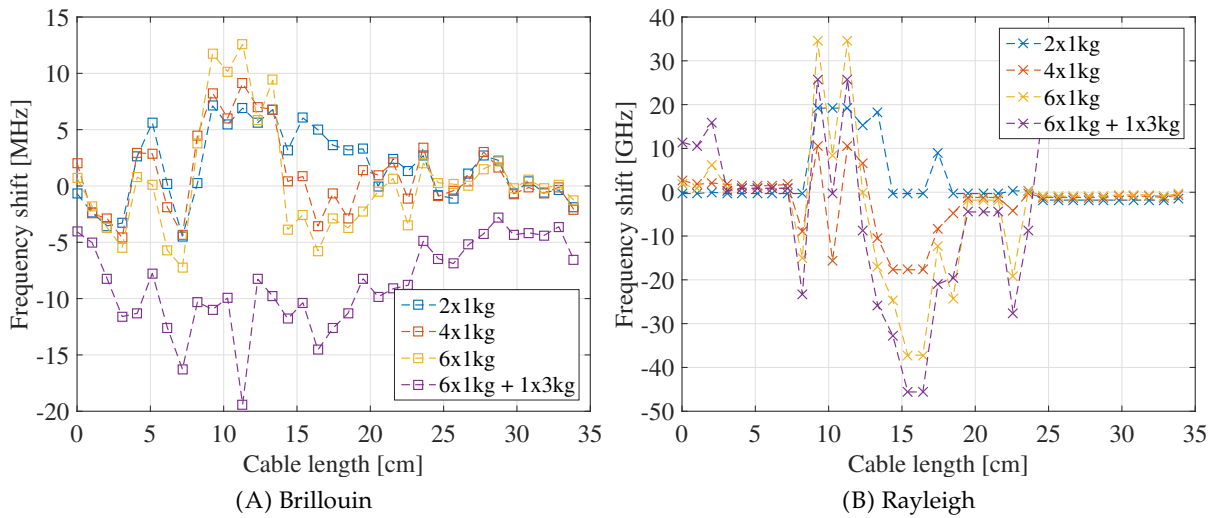
FIGURE 2.34: Frequency shift induced by impact, on the custom irradiated V9 type sample.

the impact as the optical line continued working. It is however not possible to indicate whether there is a difference between irradiated and not irradiated samples, or not. Results are in fact more qualitative than quantitative. Looking at the physical impact, the cable under impact suffers deformation and cracks (as visible in Fig. 2.35). The deformation is generalised and of the same order of magnitude for each sample, while cracks are more evident on the irradiated sample. This is due to the radiation effect on the ductility of the polyamide external sheath, which is reduced.

2.3.7 Bending

In many applications the sensing cables are fixed on a surface or embedded in a material, forcing the sensor to be in a curved position. Optical fiber sensors are particularly sensitive to curvature effects, as light travels inside the core of the fiber. Depending on the guidance of the fiber (i.e. from

(A) Cracks on the irradiated
sample

(B)
Top
view
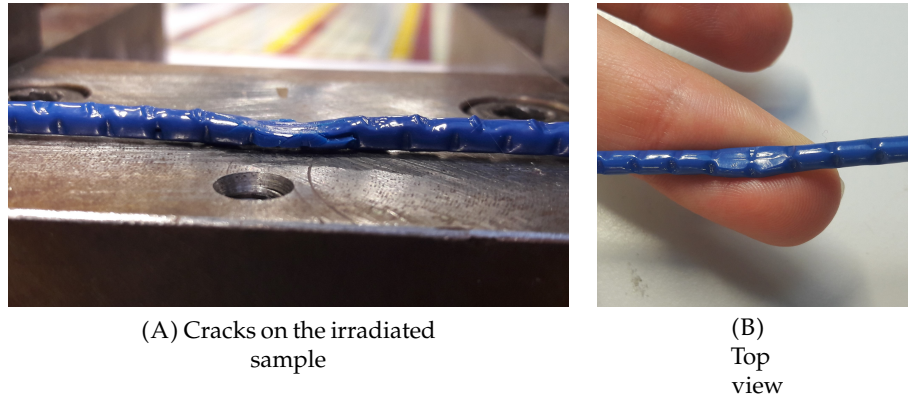
FIGURE 2.35: Cable samples deformation induced by impact. Irradiated samples
show a stronger impact (A) while all types show a permanent deformation (B).

the refractive index profile), when the curvature exceeds the limit the light is no longer guided inside the core, taking to losses and errors. In order to evaluate if this would impact measurements, we coiled 2 m of cable (V9 and FIMT types) around cylinders of different diameters. In this case results are obtained only via Brillouin backscattering-based interrogation. Samples are coiled and taken off of the cylinders one at a time manually, hence it is not possible to be sure that the only thing that changes between measurements is the coiling diameter. For example, the manual coiling could also change the twist given to the cable, while it is sure that also the position of the cable changes. In such a case the cross-correlation does not work properly, therefore we will not consider results acquired via Rayleigh-based interrogation. Measurements parameters are reported in Tab. B.5.

Averaging the frequency shift values over the 2 m, a single frequency shift value is obtained for each condition and for each cabled samples (V9, $V9_F$, $V9_F^{\spadesuit\spadesuit}$, FIMT, $FIMT_F$ and $FIMT_F^{\spadesuit\spadesuit}$) and represented in Fig. 2.36A for the V9 type and in Fig. 2.36B for the FIMT type. Results for each type of sample (standard, custom not irradiated and custom irradiated) are shown in Fig. 2.37.
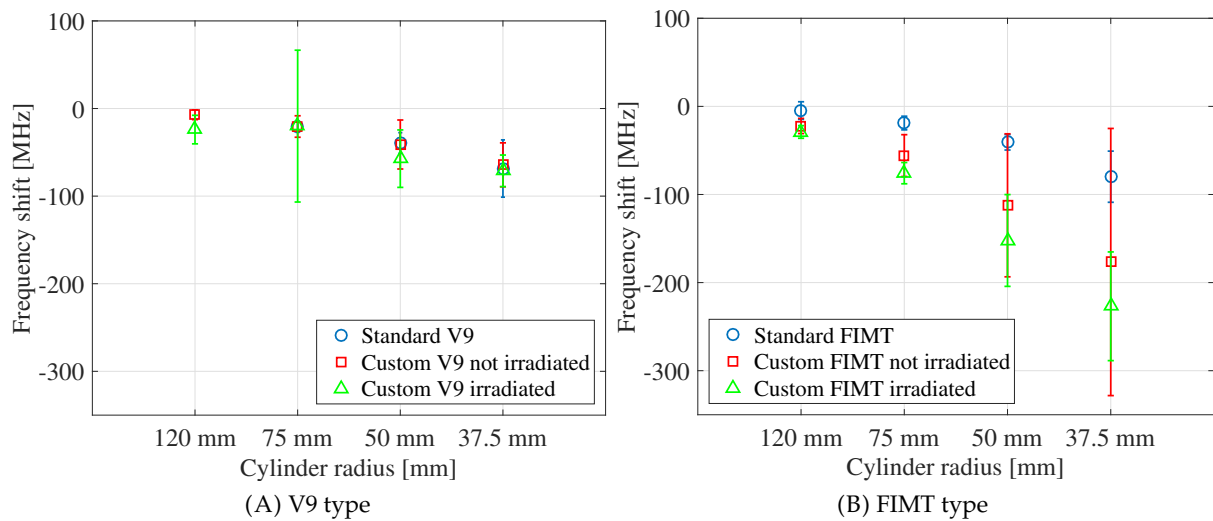
(A) V9 type

(B) FIMT type

FIGURE 2.36: Cabled samples frequency shift induced by bending, for V9 type samples (A) and FIMT type (B).

Both V9 and FIMT type samples show a compressive behaviour that grows with smaller curvature radius. The effect is stronger on FIMT type samples, and it appears to be generalised, thus
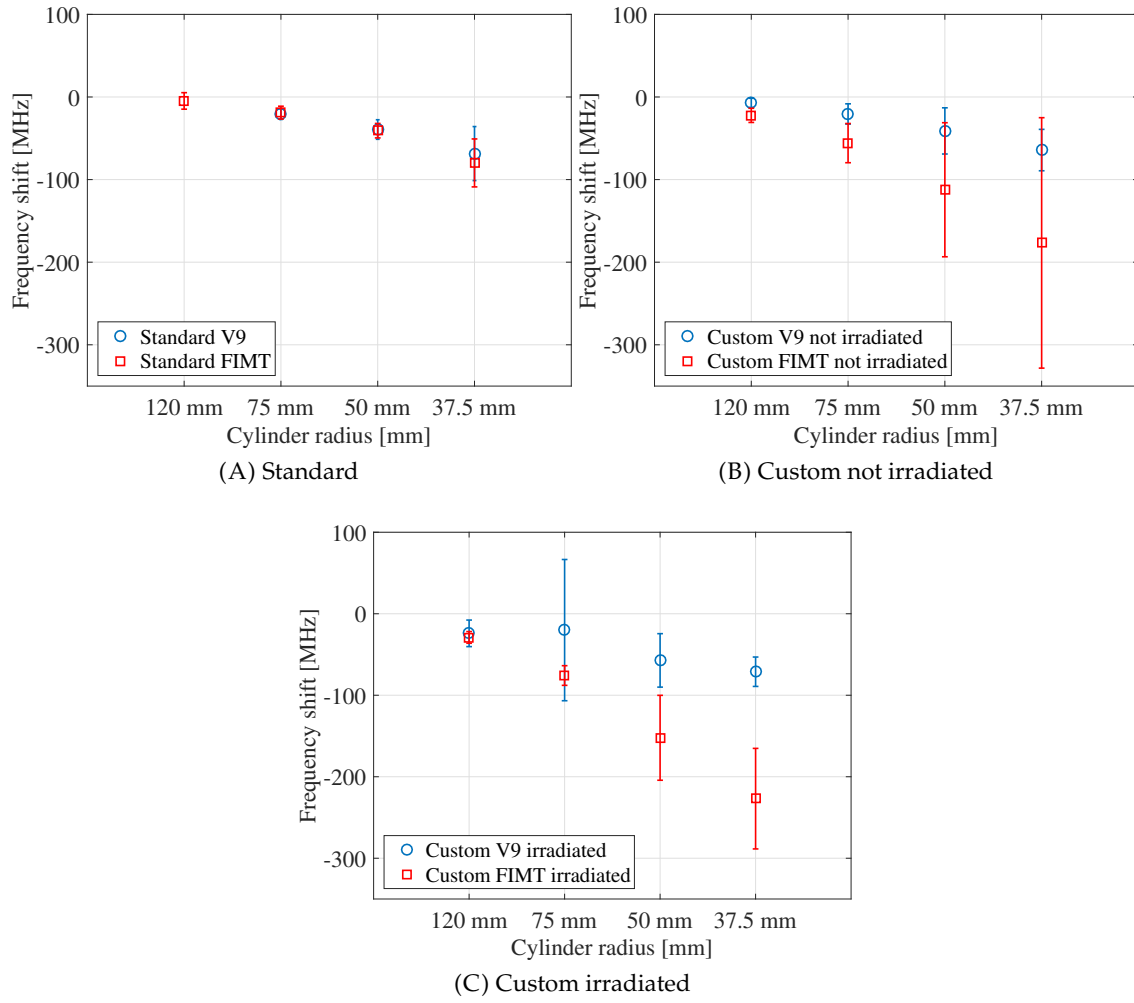
FIGURE 2.37: Cabled samples frequency shift induced by bending, for standard type samples (A) custom not irradiated (B) and custom irradiated (C).

independent from how the sample has been fixed. The difference between V9 and FIMT types is not so visible for standard type samples, while is significant for custom samples. Moreover, the impact of radiation is higher on FIMT types, leading to bigger compression. It is also worth to notice how standard type cables are less impacted by curvature with respect to custom ones. This is due to the guidance of the fiber: standard type samples have a G.657 fiber inside, which is a bending-loss insensitive single-mode fiber. Even if the custom fiber was developed to be more resistant to micro-curvatures, its characteristics do not comply the G.657 standard, i.e. its curvature losses are bigger. Results are therefore coherent with the theoretical knowledge. Furthermore, V9 type samples' frequency shift reaches about 100 MHz, underlining the necessity to take the reference measurement when the sensor is already installed.

The interest of these results is also given by the fact that the reasoning under the behaviour of the cables is not clear. When a fiber is coiled on cylinders of different diameters, a positive frequency shift is expected (i.e. tension) [Minardo, Bernini, and Zeni, 2013]. This is also reported in [Guyard, 2015], where the simulation of the curvature of optical fibers was performed. An increase in the effective refractive index of the fibers was obtained by reducing the curvature radius, which, following Eq. (1.3), determines an increase in the frequency shift. Our result goes instead in the opposite direction.

Some hypothesis have been formulated. It could be due to the acrylate between the fiber and

the FIMT that, being coiled, pushes the fiber towards the inner part (the one in contact to the cylinders surface), thus removing the fiber from the neutral axis and taking it to the compressive part. A numerical simulation of the cable under flexion (Fig. 2.38), performed by the Ph.D. candidate Fabien Menard of the École Centrale of Nantes, showed no theoretical impact on the frequency shift of the eventual slippage between the layers of the cable, especially between the fiber and the FIMT. These results suggest the need for further investigations to justify the phenomenon.
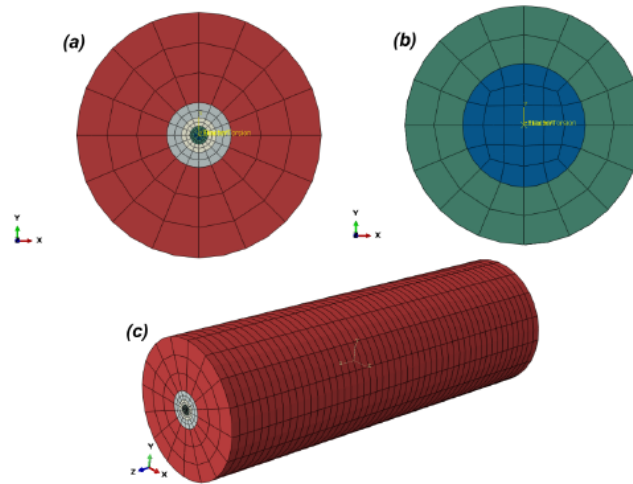
FIGURE 2.38: Finite element model of the V9 type cable for bending simulation: a) mesh of the section of the cable, b) mesh of the section of the coated fiber, c) mesh of the whole cable (courtesy of Fabien Menard).

2.3.8   Thermal sensitivity

In order to attain the thermal sensitivity, 10 m of all considered samples (from V9 types to bare optical fibers) are put in series and inserted in a climatic chamber to undergo temperature cycles. The temperature profile is reported in Fig. 2.39: the samples, from room temperature (20 °C), are taken to the maximum value of 120 °C, in order to exceed the maximum temperature to be reached during the monitoring phase in Cigéo. The samples are then taken down to -20 °C, to understand how the cable behave under zero, and again up to room temperature. The temperature step is 10 °C, while each temperature (except the initial 20 °C) was kept for 60 minutes, in order to be sure that the temperature reaches the inner part of the cable (i.e. the core of the fiber). The mea-
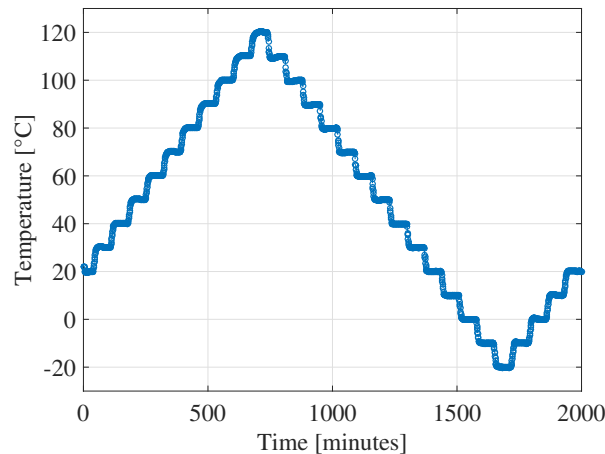
FIGURE 2.39: Temperature cycle.

surement points, acquired with the interrogation parameters reported in Tab. B.6, are averaged to obtain one single frequency shift value for each temperature and sample type. The temperature induced frequency shift going from 20 °C to 120 °C is represented in Fig. 2.40, for Brillouin and Rayleigh scattering. Results are very interesting: the presence of the protective layers doubles the
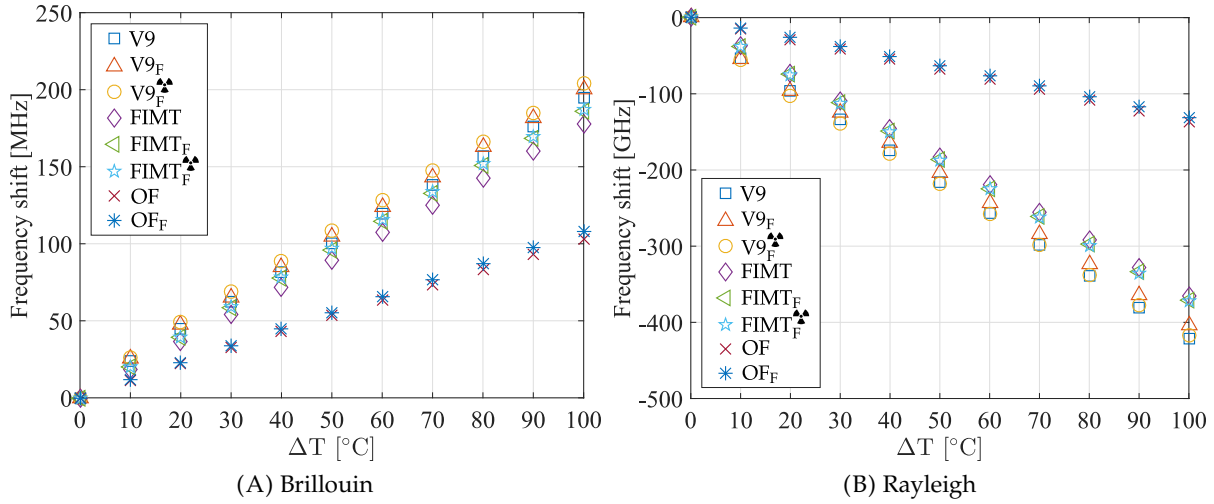
FIGURE 2.40: Temperature induced frequency shift for temperatures from 20 °C to 120 °C for Brillouin (A) and Rayleigh (B) basckscatterings.

sensitivity to temperature for Brillouin and it triples it for Rayleigh backscattering, with respect to the bare fiber. This is attributed to the fact that the protective layers, especially the FIMT in metal, have a different dilatation factor, which possibly induce further stress on the fiber. It is also interesting to observe how the different types of cables behave during heating. In Fig. 2.41 the central frequencies of a V9 and FIMT type samples are depicted. FIMT type traces show more and more irregularities as temperature increases, more than the V9 type sample. These deformations are almost neutralised in case of the V9 type as the FIMT is protected by the polyamide layer, physically imposing in turn a bigger deformation due to the higher dilatation coefficient ($\sim$10 times bigger thanks to dimensions).
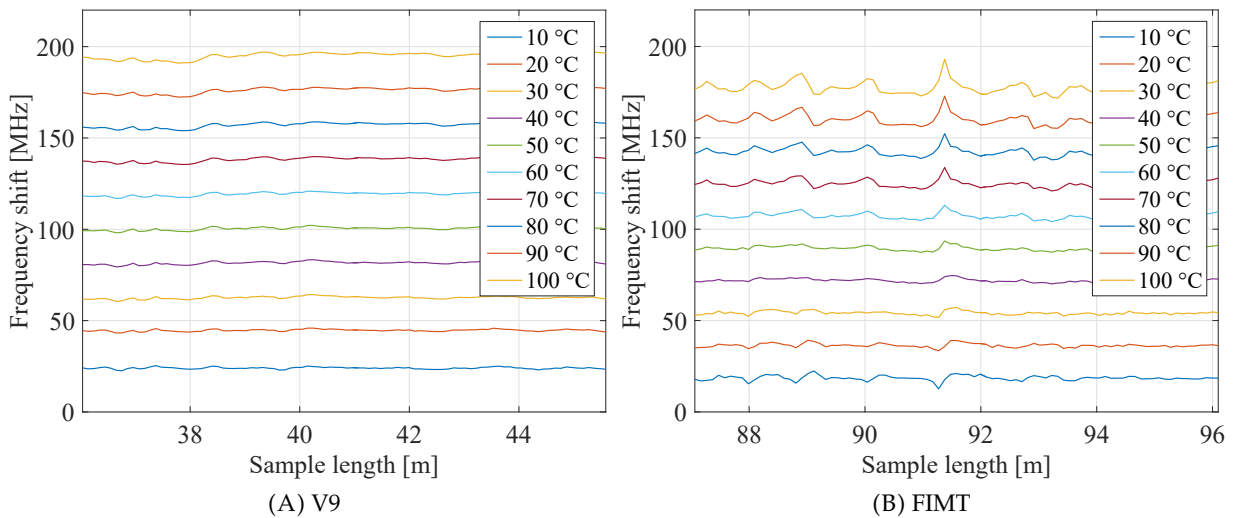
FIGURE 2.41: Brillouin frequency shift for temperatures from 20 °C to 120 °C.

By comparing measurements from 20 °C to 120 °C with those from 120 °C to 20 °C it is possible to notice how the dilatation of the materials impacts on the sensing behaviour, causing hysteresis. In fact, looking at the V9 type cable (for example, the standard V9 type sample) in Fig. 2.42, it is possible to see the presence of hysteresis after the cycle.

(A) Brillouin   (B) Rayleigh
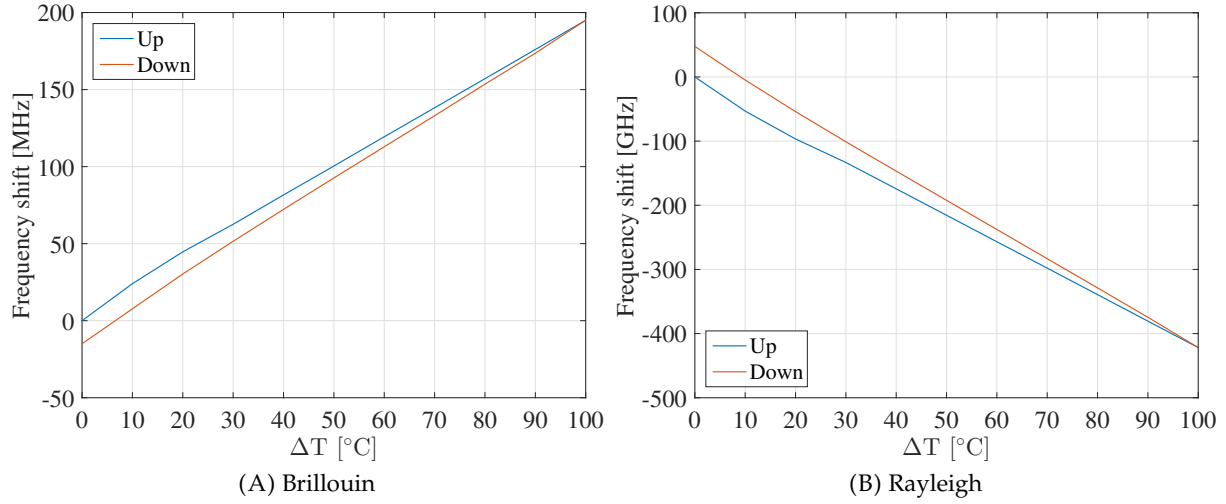
FIGURE 2.42: Temperature induced frequency shift for temperatures from 20 °C to 120 °C (up) and from 120 °C to 20 °C (down) for the standard V9 type sample, for hysteresis analysis.

It is then possible to classify the amount of hysteresis for each sample, defined as

$$\text{Hysteresis} = \frac{|v_{up}^{0°C} - v_{down}^{0°C}|}{max(|v|)}, \tag{2.13}$$

i.e. the ratio between the residual frequency shift at $\Delta T = 0$ °C after a cycle $up - down$ and the maximum absolute frequency shift reached. This quantity, reported as a percentage, is represented in Fig. 2.43 for each tested sample type. The V9 shows a higher hysteresis (around 10% for Brillouin scattering, 15% for Rayleigh) with respect to FIMT type and fiber samples (less than 5%). In fact, the thermal expansion coefficients of the component materials of the V9 type cable are different, which means that during the heating the interface between the two is subjected to residual stresses due to the different dilatation. The difference between Brillouin and Rayleigh results could be due to measurement errors and the different data treatment between the two scatterings.

When the samples are cooled to negative temperatures right after, from 20 °C to -20 °C, the frequency shifts are obtained and represented in Fig. 2.44.

Results shows again a clear difference between the different types of sensors, in this case also between V9 and FIMT types. Moreover, the differences between the samples with standard and custom fibers are more evident for Brillouin scattering (Fig. 2.44A).

Once the temperature is back to 20 °C, it is possible to compare the temperature sensitivity coefficients calculated from 20 °C to 120 °C, from 120 °C to 20 °C, from 20 °C to -20 °C and from -20 °C to 20 °C, which are plotted in Fig. 2.45, for Brillouin and Rayleigh scatterings. Results shows how V9 type temperature sensitivity coefficient grows during the cycle, confirming that it is the sample type which shows the most of hysteresis impact due to temperature change. FIMT type samples coefficients remain stable along the measurements, while bare fibers reveal a change when temperature decrease under the ambient. These results are in full accordance with temperature sensitivities of the constitutive materials. The analysis of these aspects is important in order to be able to predict the sensitivity coefficients variation during the implementation on site. This
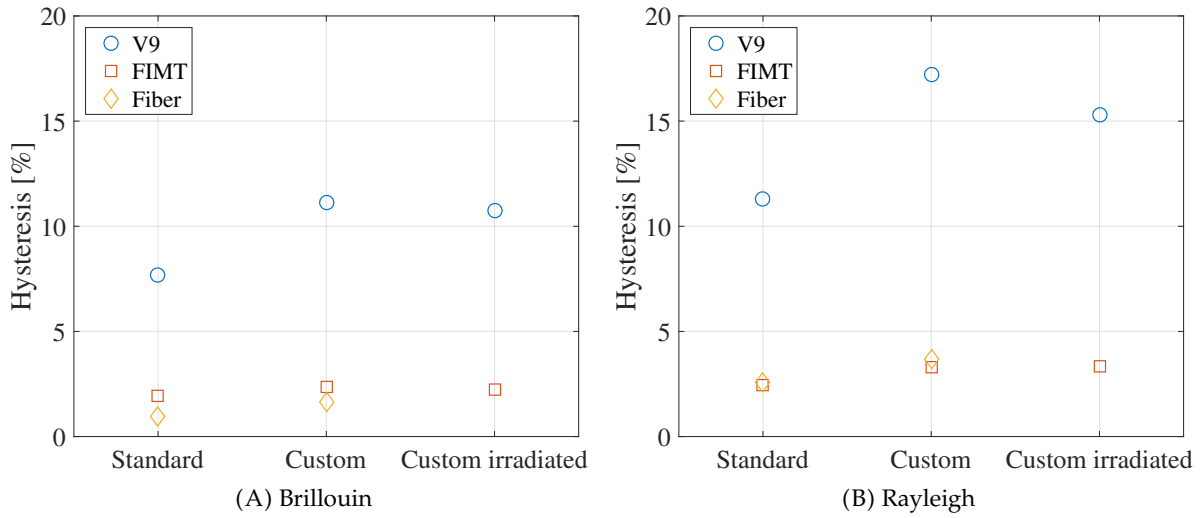
FIGURE 2.43: Ratio between the residual frequency shift at $\Delta T = 0\,°C$ and the maximum (absolute) reached frequency shift.
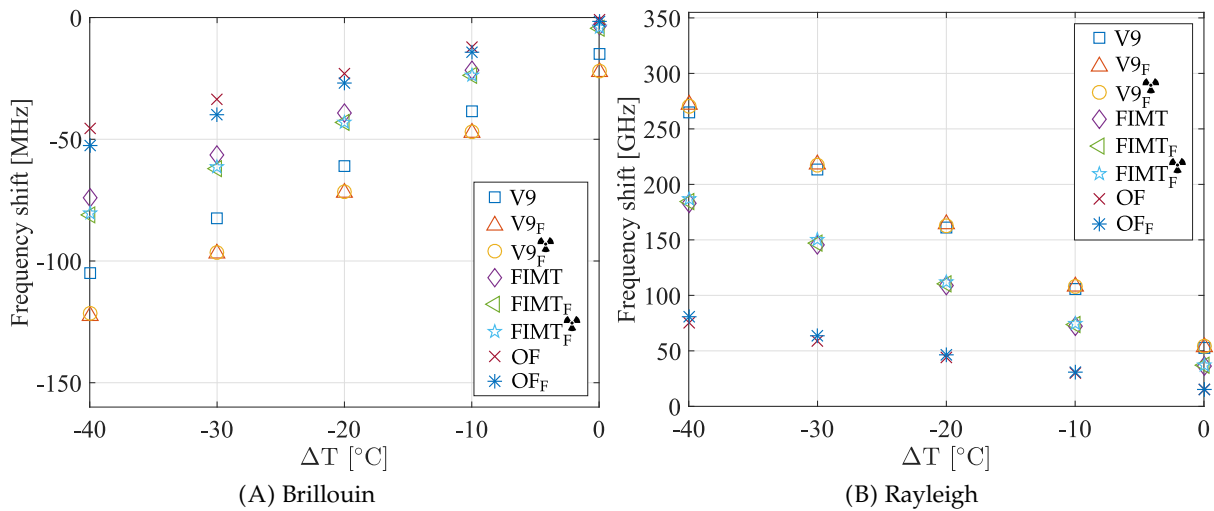
FIGURE 2.44: Temperature induced frequency shift for temperatures from 20 °C to -20 °C for Brillouin (A) and Rayleigh (B) backscatterings.

is important especially when cables are used to monitor heterogeneous materials, like in concrete structures (for example, embedded in concrete tunnel liners) where temperature distribution and dissipation are difficult to follow. In any case, as temperature in Cigéo cells tends to grow (ignoring the seasonal temperature variations), we can assume that the cable will not be impacted by materials hysteresis and temperature sensitivity coefficient will be considered stable.

2.3.9 Strain sensitivity and elasto-plastic behaviour after thermal cycle

After the temperature cycle, it is interesting to check whether the strain sensitivity of the samples is also changed. For this reason, the same analysis performed as in Section 2.3.3 on the strain sensitivity and Section 2.3.4 on the elasto-plastic behaviour can be performed on these new samples. First of all, it is possible to notice the effect of the radiation revealed by the exposure to the temperature cycle. The sample $V9_F^{\text{☢}}$+T (sample $V9_F^{\text{☢}}$ after temperature cycle) is darker with respect to sample $V9_F^{\text{☢}}$ or $V9_F$+T. Apart from the physical and visible differences, we focus on the me-

(A) Brillouin

(B) Rayleigh
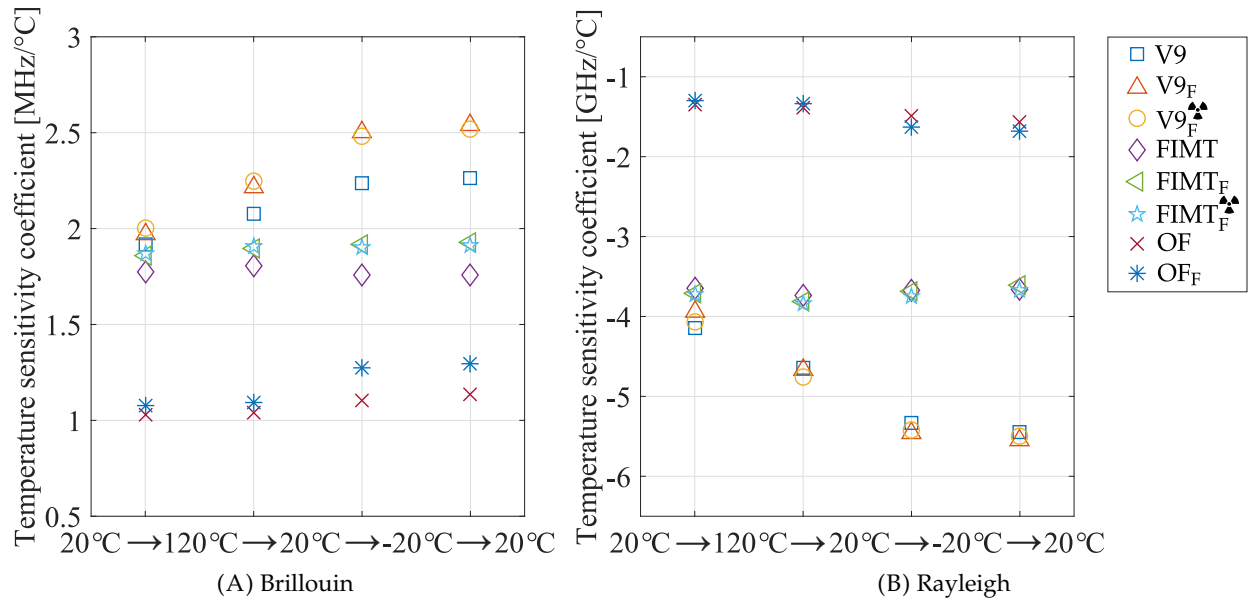
FIGURE 2.45: Temperature sensitivity coefficients variation during the temperature cycle.

FIGURE 2.46: V9$_F^{☢}$ type samples before (bottom) and after (top) exposure to the temperature cycle. The temperature impact reveals that the absorbed radiation darkened the cable.

chanical characteristics of the samples, such as the strain sensitivity coefficients, the elasto-plastic behaviour, comparing V9 type to FIMT type samples and, most of all, searching whether the temperature cycle impacted significantly on them. In this case, only the two cable types samples have been tested, as optical fibers were difficult to remove from the oven without breaking.

2.3.9.1 Strain sensitivity coefficients

As performed before, we obtain the sensitivity coefficients by calculating the slope of the traces of frequency shifts over the imposed strain, and as before we distinguish from an imposed strain smaller than 2000 µε or greater than 2000 µε. Results are plotted in Fig. 2.47, where, for more clarity, the strain sensitivity coefficients obtained with no temperature cycle exposure are also represented. Results show that there is no general evolution of the coefficients from before to after the temperature cycle. There is no specific tendency due to the temperature exposure and results are stable.
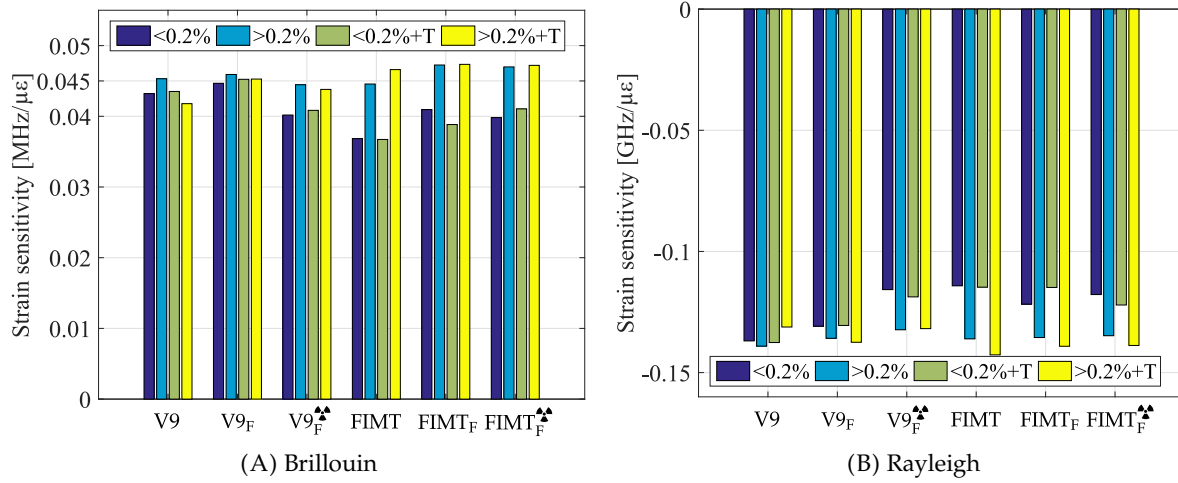
FIGURE 2.47: Comparison of the strain sensitivity coefficients between V9 type samples (V9, V9$_F$ and V9$_F^{\text{☢}}$) and FIMT type samples (FIMT, FIMT$_F$ and FIMT$_F^{\text{☢}}$) before and after temperature cycle exposure.

2.3.9.2   Elasto-plastic behaviour

With the same procedure as in Section 2.3.4, measurements acquired when the cable is unloaded are useful to determine the elasto-plastic behaviour of the samples. Converting the obtained frequency shifts to strain, using the previously calculated coefficients, we obtain the results represented in Figs. 2.48A and 2.48B, for Brillouin and Rayleigh scatterings respectively.
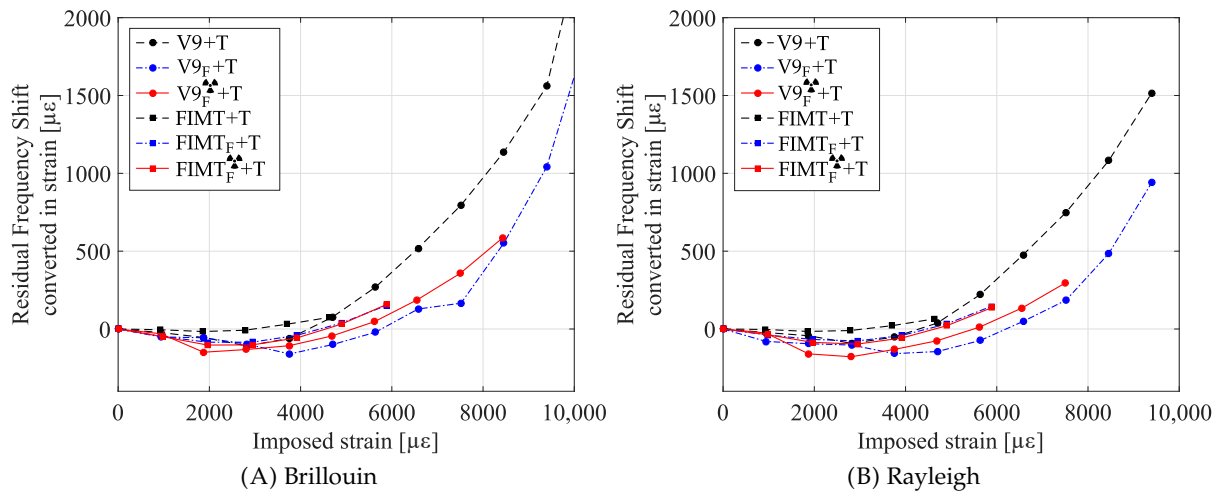
FIGURE 2.48: Residual strain comparison between V9 type samples (V9, V9$_F$ and V9$_F^{\text{☢}}$) and FIMT type samples (FIMT, FIMT$_F$ and FIMT$_F^{\text{☢}}$) after temperature cycle exposure.

Comparing V9 type and FIMT type samples we notice, differently from before, a lower residual deformation on FIMT type samples, for both Brillouin and Rayleigh scatterings. In order to understand the reason, it might be useful to compare each cable type sample, after the temperature cycle, to the results obtained on the same cable type without temperature influence. We always assume that the intrinsic characteristics of each cable type remain the same despite the different samples. The comparison of V9 type samples is depicted in Fig. 2.49. In each case, the
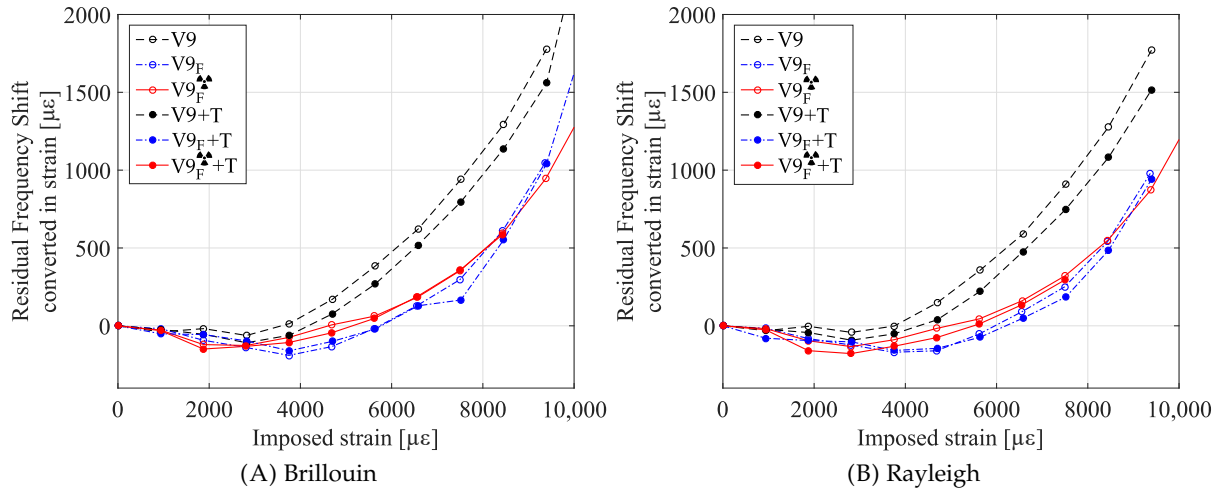
FIGURE 2.49: Residual strain comparison between V9 type samples (V9, V9$_F$ and V9$_F^{\text{☢}}$) before or after (+T) temperature cycle exposure.

residual strain obtained from samples passed through the temperature cycle is lower than if they where not, with a greater impact on standard V9 type sample than on V9$_F$ and V9$_F^{\text{☢}}$.

The same is visible for FIMT type samples in Fig. 2.50, with exception of the standard FIMT type sample. Despite such differences on a reduced study, it is possible to conclude that the impact
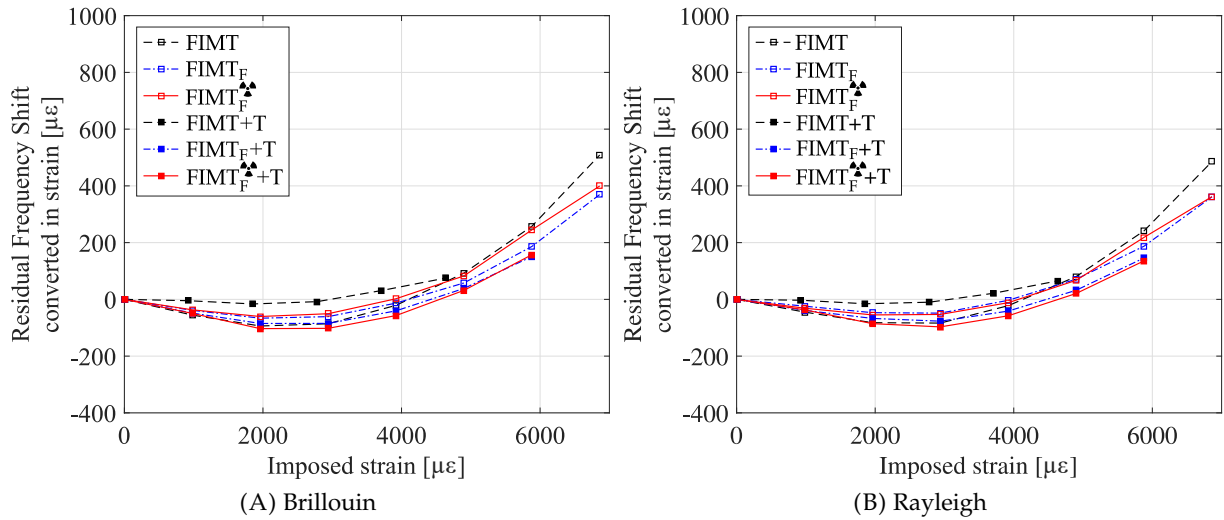
FIGURE 2.50: Residual strain comparison between FIMT type samples (FIMT, FIMT$_F$ and FIMT$_F^{\text{☢}}$) before or after (+T) temperature cycle exposure.

of the temperature cycle is not so preponderant on the mechanical characteristics of the samples.

2.3.10 Section conclusion

This section assesses the mechanical characteristics of an optical fiber strain sensing cable, composed of a layer of steel and polyamide external sheath. The considered samples, i.e. the cable in its whole, the steel tube alone and the optical fiber in primary coating, are tested under mechanical and thermal tests, in order to analyse their strain and temperature sensitivity, the elasto-plastic behaviour and their resistance to mechanical stress. The first two topics are examined under two

aspects: i) the influence of the different layers of the cable and ii) the impact of radiation on the mechanical behaviour on the samples. In fact, the protective layers that compose the cable influence both the strain sensitivity and the elasto-plastic behaviour. The strain sensitivity changes at most of 12% going from the one of the bare fiber (external primary coating only) to the complete cable (fiber, steel tube and PA external sheath), while the external sheath materials tend to plasticise, differently from the purely elastic behaviour of the fiber. Radiation impact is not significant, at least for the tested total dose of 500 kGy: at most, the change in strain sensitivity coefficient is of 4% (between irradiated and not irradiated samples), which is a very promising result for monitoring nuclear structures. The same is observed for the elasto-plastic behaviour, which is practically unchanged in accelerated ageing conditions whether the sample absorbed a radiation dose or not. The presence of other materials than the glass let the sensor show a plastic behaviour after 2000 µε, which is the elasto-plastic limit for steel. After reaching 10,000 µε of imposed strain, the cabled samples undergo from 1300 to 2000 µε of residual strain even if the sample is relaxed and not elongated, which is not negligible for some applications. Part of these results where published in a journal paper, [Piccolo et al., 2020], introduced by an oral presentation at the 12th International Workshop on Structural Health Monitoring in Stanford, CA (USA), [Piccolo et al., 2019c].

Similar results are found analysing the same (strain sensitivity and elasto-plastic behaviour) on samples which went through a thermal cycle, dedicated to analyse the behaviour of the samples from ambient temperature to 120 °C to -20 °C. The presence of the protective layers increases the temperature sensitivity coefficient of the sensor (doubles for Brillouin, triples for Rayleigh scatterings). This deeply confirms the need for a sensor calibration, especially in applications where temperature varies taking to the dilatation of materials.

The other mechanical tests (crush, impact) reveal mainly a higher impact of radiation on the plastic, which tends to crack before the non irradiated samples. Lastly, we have observed that bending the V9 type samples leads to a redshift when samples are coiled in smaller diameters.

2.4   General conclusions

FIGURE 2.51: Schematic of the Ph.D. methodology: at this point we have assessed the harsh environment influence, of radiation and temperature, in a coupled way for optical fibers and separately for strain sensing cables. Results confirmed the suitability of these sensors for a use in harsh environment.

This chapter assesses two new research topics in the evaluation of harsh-environment influence on distributed optical fiber sensors. First of all, we have evaluated the coupled influence of temperature up to 120 °C and radiation up to 1 MGy on optical fibers in their primary coating. Apart from confirming the choice of the fluorine doped fiber for radiation hard sensors, we have observed that temperature around 100 °C reduces the impact of radiation on fiber attenuation, allowing a longer maximum distance range. Radiation induced frequency shift is however not impacted by temperature.

Regarding optical fiber strain sensing cables analysis up to 500 kGy, radiation appears to impact especially the polyamide external sheath of the cable, reducing its ductility and taking to early cracks and breaks. The difference between irradiated and not irradiated samples' strain sensitivity is lower than 5%, hence negligible. A greater influence is attributed to the protection layers, which change the sensitivity of the optical fiber sensor of about 10%. The same is found for the temperature sensitivity of the considered optical fiber strain sensing cable: coefficients values are very close to each other between irradiated and not irradiated samples, while the major difference is due to the external sheath and the influence of their different dilatation coefficients.

Generally, radiation appears to have a low impact on optical fiber sensors, proving their suitability for long-term monitoring in harsh-environment.

Chapter 3

Convergence monitoring: theoretical model

Contents

3.1 Introduction

Once the sensor has been validated for its use under the coupled temperature and radiation of Cigéo's harsh environment, it can be used for the monitoring of convergence. As distributed optical fiber sensors are sensitive to strain, in this chapter we will explain how to transform it into convergence measurements with the help of an inverse-analysis finite-element method.
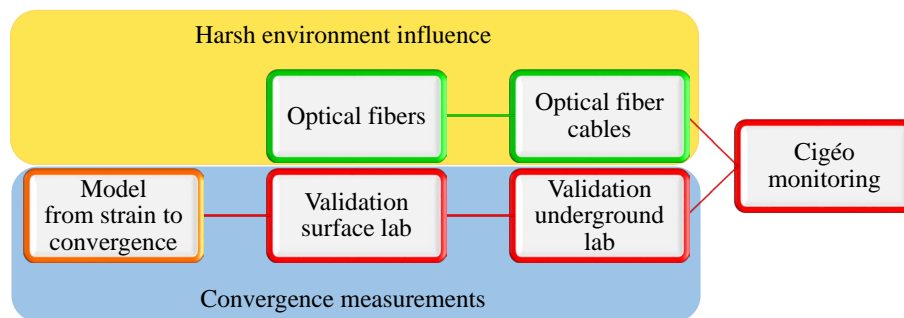
FIGURE 3.1: Schematic of the Ph.D. methodology: once the sensor is selected, we can start focusing on convergence measurements, firstly on how to obtain convergence values starting from optical fiber strain sensing measurements.

After having summarised the available sensing methods for convergence measurements, we will consider the case we are working on, a mock-up of a HLW repository cell, setting the parameters for the finite element (FE) modelling. Going through the general FE method we will reach the explanation of the specific method developed here for convergence measurement. At this point, a brief analysis on the sensitivity of the method is done.

3.2   State of the art

Convergence, the relative displacement of two diametrically-opposed points, is a crucial parameter in structural health monitoring for tunnels. Considering that the tunnel section tends to reduce over time, especially if the structure is placed underground, it is an important parameter to monitor in order to ensure the tunnels' expected functionalities and behaviour. For each structure, standard tunnel's convergence monitoring methods use sensors which are in many cases inside the tunnel section (e.g. invar wires [Dunnicliff, 1993], laser theodolites [Alba et al., 2010], angular encoders [Ariznavarreta-Fernández et al., 2016], LiDAR [Lynch et al., 2017], displacement sensors [Li, Liu, et al., 2015], tilt sensors and inspection vehicles [Huang and Zhang, 2018]). Some of them are depicted in Fig. 3.2.

(A)   (B)   (C)
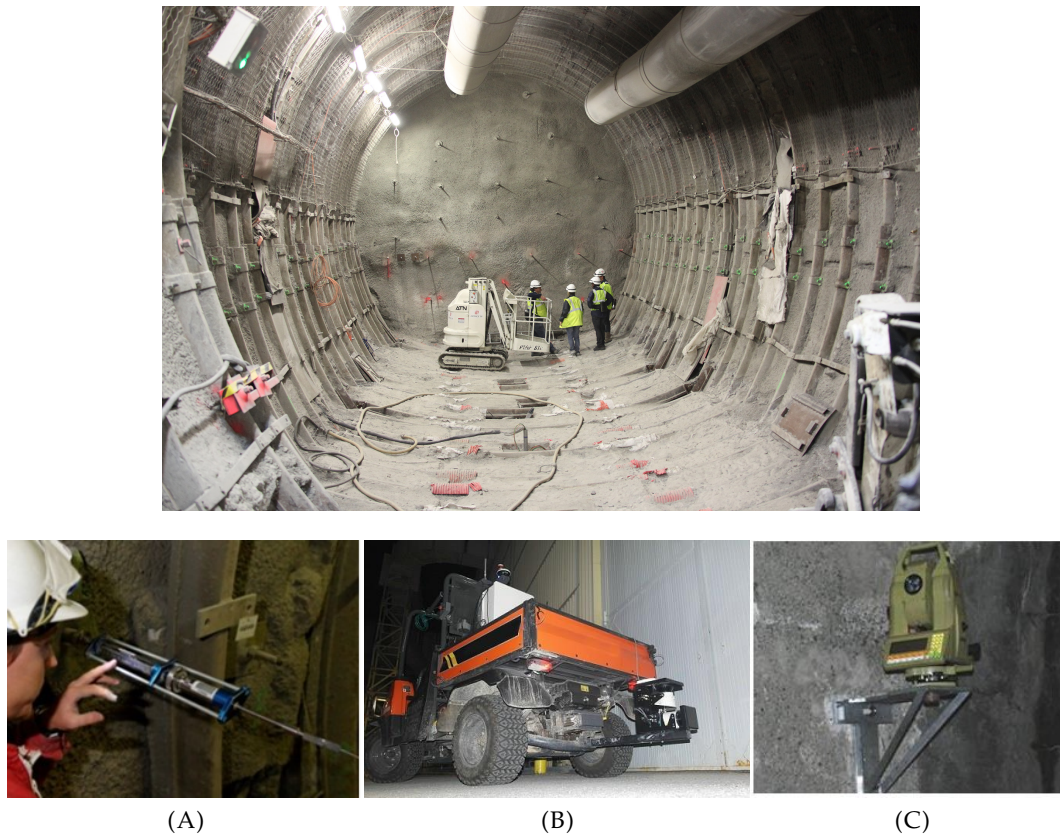
FIGURE 3.2: Some sensing systems for convergence measurements employed the inside tunnel section: (A) invar wire fixed at one extremity of the tunnel, (B) mobile LiDAR scanning system [Lynch et al., 2017], (C) photogrammetry theodolite [Alba et al., 2010].

The majority of these sensors or sensing systems are fixed at the inner circumference of the section and, most of the time, they are used and eventually installed only during the measurement campaign. This means that they do not measure convergence continuously and, besides, it is necessary to limit the passage during that period, losing time and money for normal operations. Moreover, in case of radioactive waste repository cells, this is even not considerable. The section

must be free to host the waste packages and allow the circulation of the monitoring robots. For these reasons, another convergence measurement method should be defined, for example using a sensor to be put inside the tunnel liner or at its interface with the host-rock surrounding the structure. These requirements are valid for railway and highway tunnels monitoring, and in particular for Cigéo. For the specific radioactive waste disposal environment, the sensing system has to ensure convergence measurement all around the section of the structure and to use an interrogation device placed remotely to enable maintenance (distance range up to 1 km). For HLW structures in the Cigéo concept, the surrounding clay layer applies an anisotropic external load on the steel liner. This behaviour is directly related to the anisotropic extent of the excavation induced fractures network around the cell [Bumbieler et al., 2015]. This results in a radial bending of the liner causing an expected diameter reduction up to 10 mm during the operational phase (i.e. 100 years), where retrievability must be guaranteed.

Lastly, the design should consider the required strain sensitivity to reach the millimetre sensitivity for the convergence measurement. The flexibility and compression resistance of optical sensing cables, along with their small dimensions and silica intrinsic characteristics, are particularly suitable for new techniques [Bao and Chen, 2012] as they are widely used in standard civil engineering structural health monitoring, as recalled in these review papers: [Li, Li, and Song, 2004; López-Higuera et al., 2011; Leung et al., 2015; Barrias, Casas, and Villalba, 2016; Joe et al., 2018]. Along with bridges, dams and mines, optical fiber sensors are employed also in tunnels, especially to follow the deformation due to the excavation of tunnels or when in operation [Mohamad et al., 2011; Di Murro et al., 2016; Barrias, Casas, and Villalba, 2017; Li, Soga, and Kechavarzi, 2018]. For convergence monitoring, however, it is necessary to develop a method allowing the computation of a tunnel-like structure actual geometry starting from the initial geometry and the suffered strain. In this regard, new methods that rely on data processing over optical fiber sensors as fiber Bragg gratings (FBGs) have been developed, like in [Barbosa et al., 2009], however FBGs are limited for the considered application. Indeed, distributed measurements should be preferred for large structures to reduce the installation time, blind zones, influence of localization accuracy and cost. For instance, for the structure considered in [Barbosa et al., 2009], 872 FBGs have been necessary in order to monitor a tunnel of 2.6 km, while it could have been done with only one distributed optical fiber sensor. The considered method for convergence calculation is the MEMCOT [HBM, 2016], which calculates the radial displacement of a structure starting from axial strain, based on the theory of bending of initially curved bars. This method has been validated in various applications, however it is very useful when measurements are few (five/seven at each section).

In this chapter we propose an alternative general method for convergence measurement based on the analysis of the strain measured on tunnel-like structures. The final objective is the calculation of the geometry of a loaded structure, knowing its initial geometry and the strain to which it is subjected. Afterwards, a sensitivity analysis will be done, to predict the performances of the method applied to distributed or punctual optical fiber sensors. An analysis on how the parameters and possible noise affect the results is also done, taking into consideration a structure similar to the HL waste repository cell.

Distributed optical fiber sensors allow to measure strain all along their length, in their longitudinal direction. If a structure is instrumented with optical fibers, they are able to measure the deformation it undergoes, once the strain transfer function and sensitivity coefficients are known. For structures like tunnels, it is more useful to put the distributed optical fiber sensors all around the circumference of the cell rather than in the longitudinal direction along its length, since the value of interest is the radius change. An example of instrumentation is reported in Fig. 3.3, which can be done by putting the sensor in helix or around a single section of the structure. In this way, the strain around the structure is obtained, which is a quantity in the orthoradial direction.
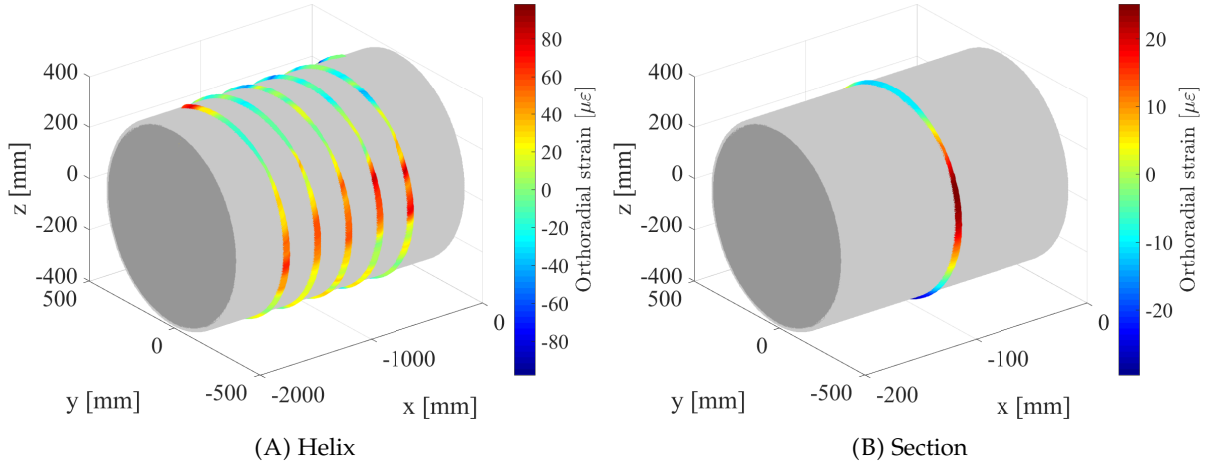
FIGURE 3.3: Schema of a helix or section instrumentation of a repository cell with distributed optical fiber sensors. Strain values are an example from measurements acquired in the CMHM underground laboratory.

3.3   Inverse-analysis finite-element method for convergence measurement via optical fiber sensors

Convergence is a value that quantify a displacement in the radial direction, i.e. towards the geometrical center of the section, and there is no direct formula that allows calculating radial displacement from orthoradial strain. Therefore, an inverse-analysis finite-element method can be used. In the following, before going to the main topic of this manuscript, we briefly present the model of the considered structure.

3.3.1   Modelling of the behaviour of a tunnel-like structure with a finite-element method

In order to propose a general analysis method for different kinds of repository cells, we have chosen to model their behaviour using the finite-element method. The finite element (FE) method is the most extensively used tool for numerical modelling in mathematics, civil and mechanical engineering [Zienkiewicz, Taylor, and Zhu, 2005]. Through the discretization of objects and structures in nodes and elements of a mesh, it is possible to resolve the equation that links the forces exerted on the structure (which include the imposed forces F_{imp} and the reaction forces R) and the corresponding displacements u, knowing its stiffness matrix $[K]$:

$$\begin{bmatrix} & K & \end{bmatrix} \cdot \begin{Bmatrix} u_{\mathrm{unk}} \\ u_{\mathrm{imp}} \end{Bmatrix} = \begin{Bmatrix} F_{\mathrm{imp}} \\ R \end{Bmatrix}, \tag{3.1}$$

where "imp" stands for "imposed" and "unk" for "unknown". The classic mechanical problem is to calculate the displacement u_{unk} and the reaction forces R knowing the boundary conditions u_{imp} and the loading F_{imp}. Here, in order to validate the finite-element model and describe the convergence measurement method, we will consider a structure with dimensions and behaviour similar to the HLW repository cell. For this reason, it is necessary to choose the parameters of the mesh, number of nodes of the circumference end elements in the thickness, that will represent the structure in the finite-element method. Before that, we have to decide how to define the 2D finite element used in this study.

3.3.1.1 Definition of the quadrangle finite element of 4 nodes

The displacement field is interpolated with the help of the shape functions matrix $[\mathbf{N^e}(\mathbf{x}, \mathbf{y})]$:

$$\{\mathbf{u}\} = \left\{ \begin{array}{c} u_x \\ u_y \end{array} \right\} = \left[\begin{array}{cccccccc} N_1 & 0 & N_2 & 0 & N_3 & 0 & N_4 & 0 \\ 0 & N_1 & 0 & N_2 & 0 & N_3 & 0 & N_4 \end{array} \right] \left\{ \begin{array}{c} u_x^1 \\ u_y^1 \\ u_x^2 \\ u_y^2 \\ u_x^3 \\ u_y^3 \\ u_x^4 \\ u_y^4 \end{array} \right\} \tag{3.2}$$

These shape functions N^e in the (ξ, η) space expressed for the reference element represented in Fig 3.4 are written as:

$$N_1(\xi, \eta) = \frac{1}{4}(1 - \xi)(1 - \eta) \tag{3.3}$$

$$N_2(\xi, \eta) = \frac{1}{4}(1 + \xi)(1 - \eta)$$

$$N_3(\xi, \eta) = \frac{1}{4}(1 + \xi)(1 + \eta)$$

$$N_4(\xi, \eta) = \frac{1}{4}(1 - \xi)(1 + \eta)$$
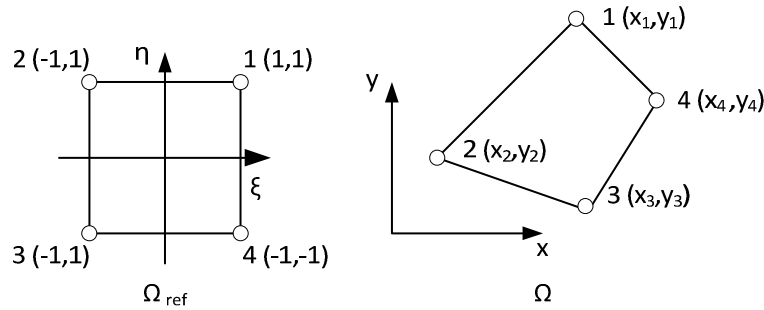
FIGURE 3.4: Reference quadrangle of 4 nodes: geometry and parameters.

Deriving the displacement field, we obtain the strain field $\{\varepsilon\} = [\mathbf{B^e}] \{\mathbf{u^e}\}$ where $[\mathbf{B^e}]$ is the shape function's derivative matrix and:

$$\{\varepsilon\} = \left\{ \begin{array}{c} u_{x,x} \\ u_{y,y} \\ u_{x,y} + u_{y,x} \end{array} \right\} = \left[\begin{array}{cccccccc} N_1,x & 0 & N_2,x & 0 & N_3,x & 0 & N_4,x & 0 \\ 0 & N_1,y & 0 & N_2,y & 0 & N_3,y & 0 & N_4,y \\ N_1,y & N_1,x & N_2,y & N_2,x & N_3,y & N_3,x & N_4,y & N_4,x \end{array} \right] \left\{ \begin{array}{c} u_x^1 \\ u_y^1 \\ u_x^2 \\ u_y^2 \\ u_x^3 \\ u_y^3 \\ u_x^4 \\ u_y^4 \end{array} \right\} \tag{3.4}$$

In order to represent these derivatives, $N_{i,x}$ or $N_{i,y}$, we use the shape functions of the reference element:

$$\langle\ N_{i,x}\quad N_{i,y}\ \rangle\ =\ \langle\ N_{i,\xi}\quad N_{i,\eta}\ \rangle\,[\mathbf{J}]^{-1} \tag{3.5}$$

where $[\mathbf{J}]$ is the jacobian of the transformation between the reference element and the element in its initial configuration:

$$[\mathbf{J}]\ =\ \begin{bmatrix} x_1 & x_2 & x_3 & x_4 \\ y_1 & y_2 & y_3 & y_4 \end{bmatrix} \begin{bmatrix} N_{1,\xi} & N_{1,\eta} \\ N_{2,\xi} & N_{2,\eta} \\ N_{3,\xi} & N_{3,\eta} \\ N_{4,\xi} & N_{4,\eta} \end{bmatrix}. \tag{3.6}$$

In this expression the coordinates x_i and y_i correspond to the coordinates of the nodes of the quadrangular element in its initial configuration.

Now that we have defined the reference element, we can define the elementary stiffness matrix $[\mathbf{K^e}]$ by integration on the reference element. The elementary stiffness matrix of the quadrangle element is:

$$[\mathbf{K^e}]\ =\ \int_{\Omega_{ref}} [\mathbf{B^e}]^T\,[\mathbf{C}]\,[\mathbf{B^e}]\,|det([\mathbf{J}])|\ d\Omega_{ref} \tag{3.7}$$

where $[\mathbf{C}]$ is the elasticity matrix, that can be defined for two different cases:

$$\begin{aligned} \text{Plane stress: } C &= \frac{E}{1-\nu^2} \begin{pmatrix} 1 & \nu & 0 \\ \nu & 1 & 0 \\ 0 & 0 & \frac{1-\nu}{2} \end{pmatrix} \\ \text{Plane strain: } C &= \frac{E}{(1-2\nu)(1+\nu)} \begin{pmatrix} 1-\nu & \nu & 0 \\ \nu & 1-\nu & 0 \\ 0 & 0 & \frac{1-2\nu}{2} \end{pmatrix} \end{aligned} \tag{3.8}$$

where E is the Young's modulus and ν the Poisson's ratio.

The integration on the reference element is done by sum of n Gauss points as:

$$[\mathbf{K^e}]\ =\ \sum_{k=1}^{n} ep\,w_k\,[\mathbf{B^e}(\xi_k,\eta_k)]^T\,[\mathbf{C}]\,[\mathbf{B^e}(\xi_k,\eta_k)]\,|det([\mathbf{J}(\xi_k,\eta_k)])| \tag{3.9}$$

where the parameters w_k are the integration weights associated to the Gauss points of coordinates ξ_k, η_k and ep is the thickness of the element. For a quadrangle of 4 integration points, the coordinates of the Gauss points and the value of the weighting parameter are given in Tab. 3.1.

3.3.2 Validation of the direct model computation algorithm and discretization choice

The mesh of a structure must be built not only representing the real shape of the considered structure, but also (and mainly) its mechanical behaviour under stress. This means that the number of nodes and elements, in thickness and around the circumference, must be chosen in order to obtain

Point	ζ_k	η_k	w_k
1	$\frac{1}{\sqrt{3}}$	$\frac{1}{\sqrt{3}}$	1
2	$\frac{-1}{\sqrt{3}}$	$\frac{1}{\sqrt{3}}$	1
3	$\frac{-1}{\sqrt{3}}$	$\frac{-1}{\sqrt{3}}$	1
4	$\frac{1}{\sqrt{3}}$	$\frac{-1}{\sqrt{3}}$	1

TABLE 3.1: Quadrangle of the reference of 4 nodes: coordinates of the Gauss points and associated weighting.

the most satisfactory approximation of the real behaviour of the structure. In other words, it is necessary to minimize the error between the analytical and simulated results in function of the mesh parameters, keeping reasonable the computation duration.

We consider then a cylindrical repository cell of infinite length as represented in Fig. 3.5, of internal and external radius respectively *a* = 371 mm and *b* = 381 mm. The component material is homogeneous and isotropic. In order to validate the finite-element algorithm we have written
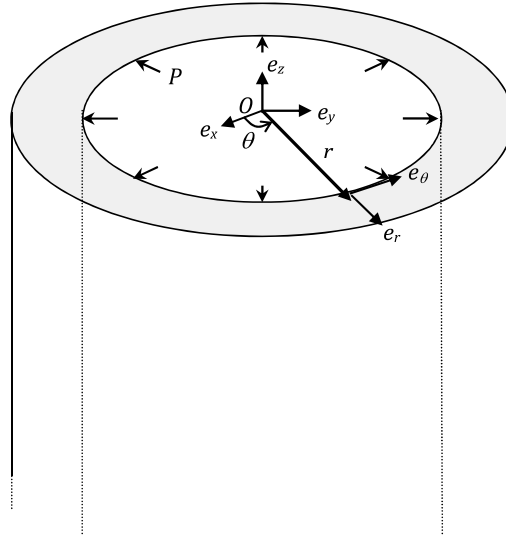
FIGURE 3.5: Schematic of the infinite cylinder for the validation of the finite-element model.

in a MATLAB environment, we will consider first of all the case of the cell subjected to internal pressure, using the plane strain 2D model. In this case, as an analytical formula to evaluate the displacement and strain exists, we will compare its results to the finite-element simulation. The analytical results follow these equations:

$$u_r = \frac{P}{E} \left[\frac{(1+\nu)(1-2\nu)r + (1+\nu)\frac{b^2}{r}}{\frac{b^2}{a^2} - 1} \right] \tag{3.10}$$

$$\varepsilon_\theta = \frac{u_r}{r} \tag{3.11}$$

For the mesh, we consider a fixed number of nodes in the circumference, for example *N* = 720, which means a node every 0.5°. Regarding the number of elements in the thickness of the structure, we test elements from 1 to 10.
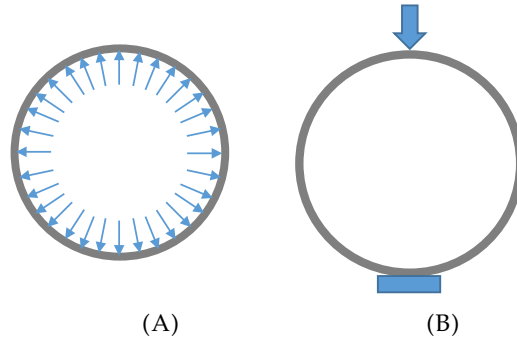
FIGURE 3.6: Different types of load for the choice of the mesh: (A) Internal pressure, (B) Vertical load.

Once we have validated the MATLAB algorithm, we will consider also a typical case for the repository cells. In reality they will be loaded by the rock around them, which can be simplified simulating a punctual vertical load on the structure. In that case, as an analytical formula does not exist, we will compare the different meshes defined on a portion of cell (using thus a 2D plane stress model) with the result obtained by considering a simulation with a fine mesh, like for example with elements of 1 mm^2. In Fig. 3.6 we have represented the two kinds of loading, the internal pressure (Fig. 3.6A), to be compared with the analytical solution, and the vertical load (Fig. 3.6B), to be compared with the simulation using a fine mesh.

The relative error between the strain results obtained with the different testing meshes ε_{FE} and the reference of the two cases ε_{ref} (analytical formula or fine mesh) are calculated as

$$e_\varepsilon = \frac{\varepsilon_{FE} - \varepsilon_{ref}}{\varepsilon_{ref}} \tag{3.12}$$

and represented in Fig. 3.7, for each different number of elements.
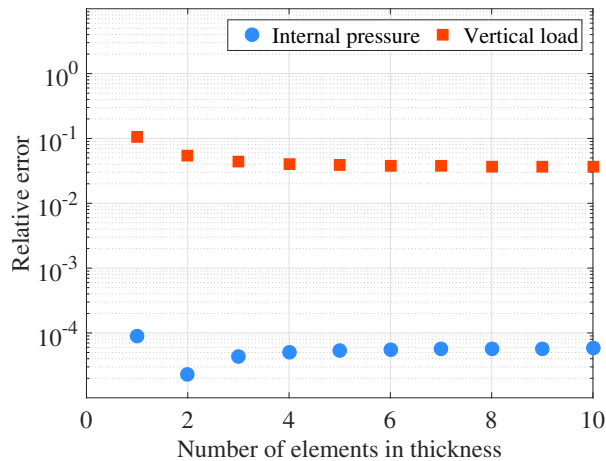
FIGURE 3.7: Error between simulated (FE model) and reference strain: analytical for the internal pressure case (A), numerical for the vertical load case (B) of Fig. 3.6.

The error stabilizes as the number of elements in the thickness increases, thus we will choose as number of elements at the beginning of the stabilization of the curve. For this reason we choose to use a mesh of 720 nodes in the circumference and 3 elements in the thickness. The mesh is then represented in Fig. 3.8.
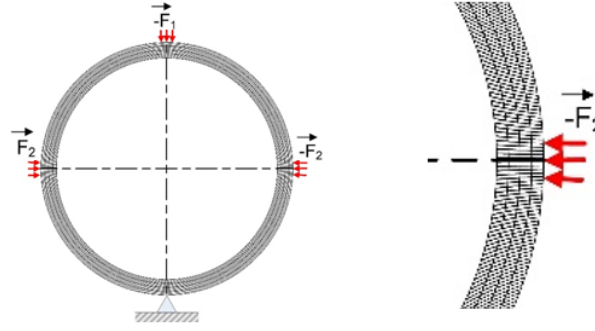
FIGURE 3.8: Example of mesh of the structure, with a zoom to highlight the elements in the thickness. The proportion are thus not maintained.

3.3.3 Inverse-analysis

Many real problems in experimental science consist in determining a not directly observable quantity x from a set of finite measurements of an observed quantity y depending on parameters p according to a model $\mathcal{M}(p, x) = y$. When $\mathcal{M}$ is a linear operator, the previous equation can be written either as $\mathcal{M}(p)x = y$. The type of problems to be solved can be classified as follows:

- knowing $\mathcal{M}$, p and x, the computation of y is a direct problem;

- knowing $\mathcal{M}$, p and y, the computation of x is an inverse problem;

- knowing $\mathcal{M}$, x and y, the computation of p is an inverse problem of parameters identification;

- knowing $\mathcal{M}$ and y, the computation of p and x is a blind problem.

Since these problems are sensitive to the presence of uncertainties in the model and in the measurements, it is more realistic to write $\mathcal{M}(y, x, p, e) = 0$ where e represents the errors commonly known as noise. Noise may be such that the measurements are not the image of any model, so that it is not possible to find a model that produces the measured data but rather find the optimal model, i.e the model that best matches the data. This involves the minimization of an objective function, namely a functional that quantifies how far the predicted data are from the observed data. This leads to the definition of the residuals:

$$r = \tilde{y} - y(p, x) \tag{3.13}$$

where $\tilde{y}$ is a set of measured data and $y(p, x) = \mathcal{M}(p, x)$ the data predicted by using the model $\mathcal{M}$. A standard objective function Φ, to minimize, is of the form:

$$\Phi(p, x) = \|r\|^2 = \|\tilde{y} - y(p, x)\|^2 \tag{3.14}$$

where $\|\|$ is the Euclidean norm (or norm $\|\|_2$) but can also be a norm $\|\|_1$ in some applications. If perfect data are used (i.e. no noise) then the recovered model should fit the observed data perfectly. In the following section, we will apply this to the design of an inverse-analysis finite-element method for convergence measurement.

In this study the model $\mathcal{M}$ is known, as well as the stiffness coefficients which are represented by p. The measured value is the strain ε, which in turn is the derivative of the displacement field u. We want to calculate the geometry of the repository cells while the loading level to which the structure is subjected is unknown. Various strategies can be approached to solve this problem. For example, we could obtain the displacement (and therefore convergence) by integrating the measured strain. However, we have chosen to use an inverse-analysis approach to use the finite-element method as a filter for outliers which are more common in case of on-site measurements.
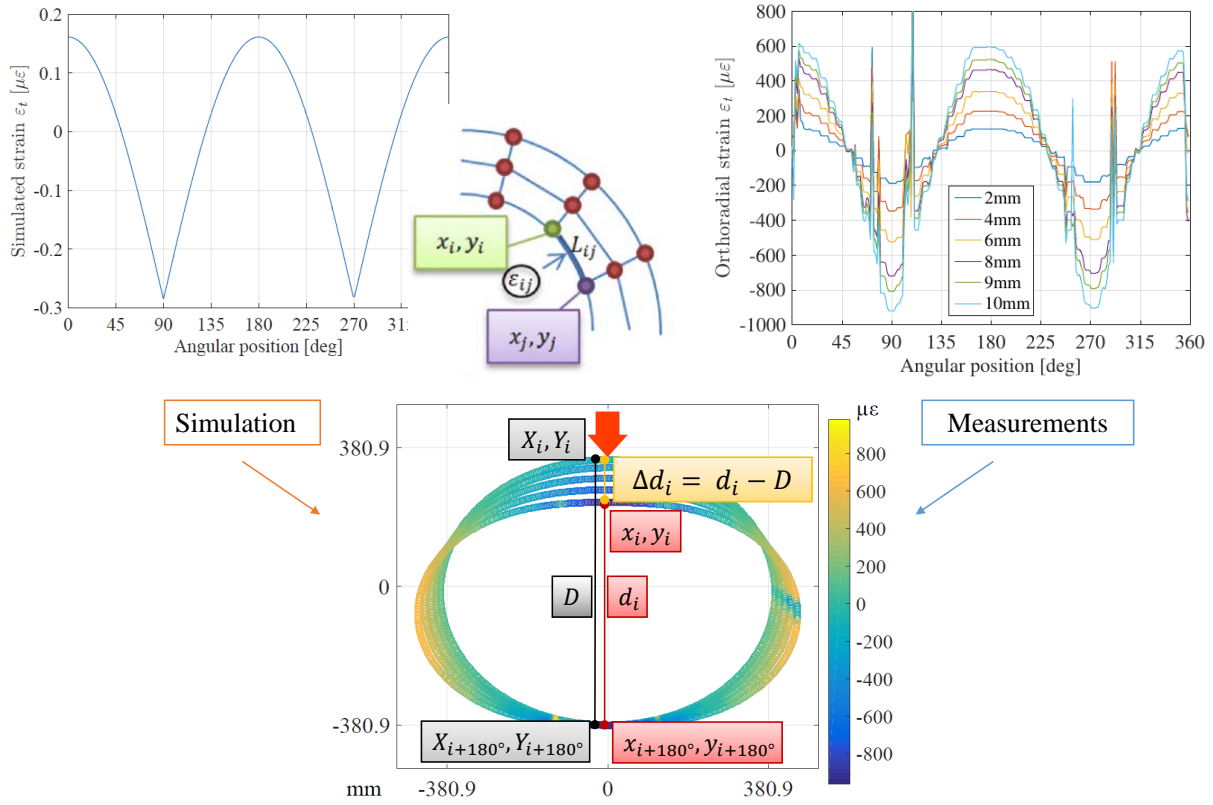
FIGURE 3.9: Schematic of the inverse-analysis finite-element convergence method: the simulation of strain with the FE method is compared to experimental measurements, minimising the error between the two and giving the deformed geometry, i.e. convergence.

3.3.4 General working principle

The inverse-analysis method involves a search for a set of parameters which minimizes an objective function. In this case, the loading of the structure is the main role player, as depending on the loading areas and amplitudes the imposed stress (and therefore strain) is different. Let's call F^i the loading parameters, which represent the force(s) F applied at a specific node i of the structure's mesh. The objective function to minimize Φ can then be defined as

$$\Phi(F^i) = \frac{1}{2} \left\| \varepsilon(F^i) - \tilde{\varepsilon} \right\| \tag{3.15}$$

where $\tilde{\varepsilon}$ is the measured orthoradial strain and $\varepsilon(F^i)$ represents the computed orthoradial strain by means of a finite element model. To solve it and transform strain measurements into convergence, the following method is being developed (which is summarised in Fig. 3.9):

1. For a set of forces, the displacement field is computed with the FE method, for each node i of the finite element mesh. The displacements in the x and y directions are respectively $u_i = X_i - x_i$ and $v_i = Y_i - y_i, \forall$ node i, where (X_i, Y_i) are the original coordinates of the structure and (x_i, y_i) are the coordinates after the displacement. Isotropic elasticity is considered for the steel structure behaviour law.

2. From displacement, it is possible to calculate strain ε_{ij} as Cauchy or engineering strain with the following formula:

$$\varepsilon_{ij} = \frac{((X_i - X_j) \cdot (u_i - u_j))}{L_{ij}^2} + \frac{((Y_i - Y_j) \cdot (v_i - v_j))}{L_{ij}^2}. \qquad (3.16)$$

The same notation as before is valid for node $j = i + 1$. L_{ij} is the distance between nodes i and j of the structure mesh. These quantities are illustrated in Fig. 3.9.

3. This numerical strain has to be compared with the experimental one, to retrieve the loading force(s) and the corresponding deformed geometry. The numerical strain must be therefore calculated in the same position, with respect to the structure, in which the sensor is located. To perform the comparison, it is necessary to calculate the difference (error) between the two orthoradial strains and choose the loading F^i which minimizes its Root Mean Square (RMS). The detailed formulas will be given later on, once symmetry properties of the proposed loading cases are taken into account to simplify the calculation.

4. Once the appropriate load is found, the corresponding displacement can be selected from previous calculation. Then the deformed geometry and finally convergence can be calculated, for each node, as

$$x_i = X_i + u_i; \; y_i = Y_i + v_i \; (\forall i, i \text{ mesh node}) \qquad (3.17)$$

$$d_i = \sqrt{(x_{i+180°} - x_i)^2 + (y_{i+180°} - y_i)^2} \qquad (3.18)$$

$$\Delta d_i = d_i - D \qquad (3.19)$$

where D is the original diameter of the structure, which is constant for circular sections. The new diameters are simply calculated as distances between opposite points. The difference between the diameters of the deformed and original geometry gives the diametrical convergence Δd (as in Fig. 3.9).

This short and very simple method is the heart of the monitoring system based on the use of distributed optical fiber sensor measurement, allowing to calculate convergence from strain values. The method will be validated on a real scale mock-up of the HL waste repository cell, but before it is useful to examine how the method parameters must be chosen to exploit it in the best way. Both numerical structure and measurement characteristics are evaluated, as well as the impact of noise.

3.3.5 Parameters influencing measures

In order to apply the model to a structure, it is necessary to know which are the known variables, which are the parameters onto which the model works and how it is influenced by them. In many cases, for example, the behaviour of the rock that is loading the structure is known, i.e. the zones of major and minor stress, while the magnitudes are not. We can then select as loading parameters $\|F^i\|$, which are the amplitudes of the forces imposed at the node i of the structure's mesh. Another aspect to consider is whether we know the sensing points location: in case of affirmative answer, the position of each sensing point along the sensor is paired with the coordinates of a point of the mesh. On the contrary, the position becomes another parameter if, during the sensor installation, one does not have the shrewdness to link the sensor position to the measured trace. A technique is, for example, to impose local changes to the sensor at a known position, preferably easily accessible, which are then visible on the optical trace.

Regarding the structure's shape, the direct model used in the inverse analysis procedure relies on a simplification of a 3D finite element model: we use a 2D plane stress finite element model as

we consider only a portion of structure, while in a real case the structures would be long enough to be considered of infinite length, leading to consider a plane strain case. As we consider a numerical model of a simple structure, it is possible to establish an analytical model based on simplified hypothesis of beam theory in the case of the mock-up study. Even if this analytical model is not the most suitable as it tends to underestimate strain, it can be useful to assess which are the parameters that play an important role in the convergence measurement model. A circular ring of average radius r is considered to be subject to two sets of diametrically opposed concentrated forces (see Fig. 3.10A). Due to the symmetries, the study is limited to the analysis of the internal forces on the upper half ring (see Fig. 3.10B). For this kind of structure, considering the parametrization of
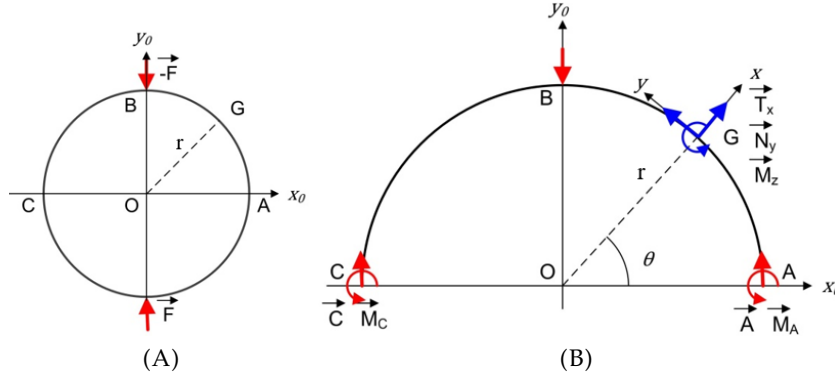
FIGURE 3.10: Model for the analytical resolution based on beam theory: (A) analytical model and (B) parametrization of the half ring.

Fig. 3.10, the internal forces are:

$$\text{the shear force } T_x = -\frac{1}{2}F\sin\theta, \tag{3.20}$$

$$\text{the normal force } N_y = -\frac{1}{2}F\cos\theta \tag{3.21}$$

$$\text{and the bending moment } M_z = -\frac{Fr}{2\pi}(\pi\cos\theta - 2), \tag{3.22}$$

where F is the applied force. The axial stran ε_{yy} yielded by the optical fiber sensor is given by equation 3.23:

$$\varepsilon_{yy} = \frac{Ny}{ES} - \frac{Mz}{EI}x \cong -\frac{Mz}{EI}x \cong \frac{3Fr}{\pi Ebe^3}(2 - \pi\cos\theta)x \tag{3.23}$$

where S is the ring section, E the Young's modulus, I the second moment, e the thickness of the structure and b its width. x is the distance between the strain sensor axis and the neutral axis of the ring, i.e. $x = \frac{e}{2} + \frac{d}{2}$. In fact, if we do not take into account the eventual space left between the sensor's and the structure's surfaces, we define d as the diameter of the sensor and $\frac{d}{2}$ as the distance of the center of the fiber from the surface of the ring. The relation 3.23 shows which parameters influence the final result: both the material and the shape of the structure have an impact on the yielded strain. Uncertainties on the structure's thickness (elevated by a cubic factor in the formula) and diameter can take to measurement evaluation errors, as well as the real position of the fiber. All these variables must be well determined when the model is applied to a real structure, building the corresponding mesh. However, in a real application, it is not easy to have a perfect structure. For example, the thickness of the cell could be not homogeneous all around the circumference, with errors in the order of a tenth or hundredth of a millimeter. The same can be applied to the diameter of the structure, having irregularities in the shape of the

structure. Although low, this uncertainty must be taken into account to correctly evaluate the obtained results.

3.3.6 Sensitivity analysis

Once the numerical model's parameters and variables are determined, a sensitivity analysis is performed in order to understand the robustness of the adopted model to calculate convergence. This study is meant to assess i) the interest of using distributed optical fibers instead of FBGs (i.e. the importance of the number of measurement points) and ii) how much the measurement noise impacts on results.

A theoretical perfect frequency shift trace was obtained by simulating the load onto a point of the structure using the finite element method, where the mesh is made of 720 nodes all around the circumference and 3 elements in thickness. The applied load is of 4500 N, which represents a little more than 10 mm of convergence (the reference value for convergence at the end of 100 years for the HL waste repository cell). Convergence calculation is performed applying the inverse analysis method to measurements obtained by adding to the frequency shift trace different levels of noise B (from 0.1% to 10% of the maximum frequency shift value obtained by simulation). Noise values are chosen to be representative of experimental data. More precisely, noise is added to each measurement point value. Its amplitude is a random number, chosen from the uniformly distributed interval $[-B; B]$. The error between the convergence obtained with and without noise is then calculated. The simulation is performed 1000 times for each noise level, in order to compute the mean value m and standard deviation σ distributions of the error. This procedure is repeated assuming a different number of measurement points N: the perfect trace is interpolated to obtain a measurement with a different number of points (50, 100, 200, 360, 500, 600 and 720) and then adding noise accordingly to the chosen level. Some results are shown in the following. The distribution of errors in case of 10% noise level is shown in Fig. 3.11, for different N. In each case their distribution follows a normal distribution, as foreseen in case of a good simulation.
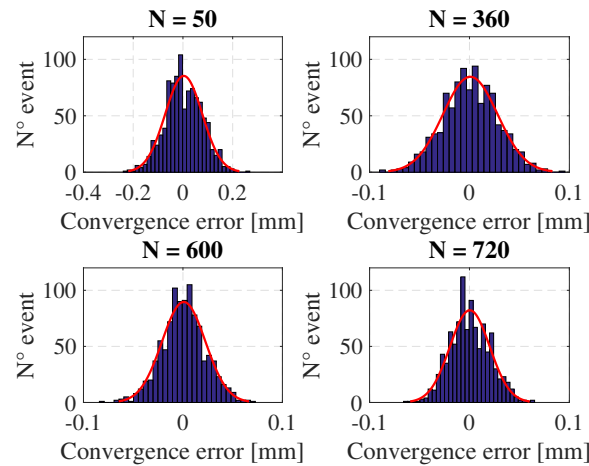
FIGURE 3.11: Distribution of convergence calculation error at 10% noise level for different N.

The standard deviations decrease with increasing number of measurement points and increase with increasing noise, as shown in Fig. 3.12A. Their trend over different noise levels is similar between different N. The same evolution is followed by the maximum error in Fig. 3.12B. A focus on the 10% noise level is reported in Fig. 3.13, where the evolution of the standard deviation for

(A) Standard Deviation
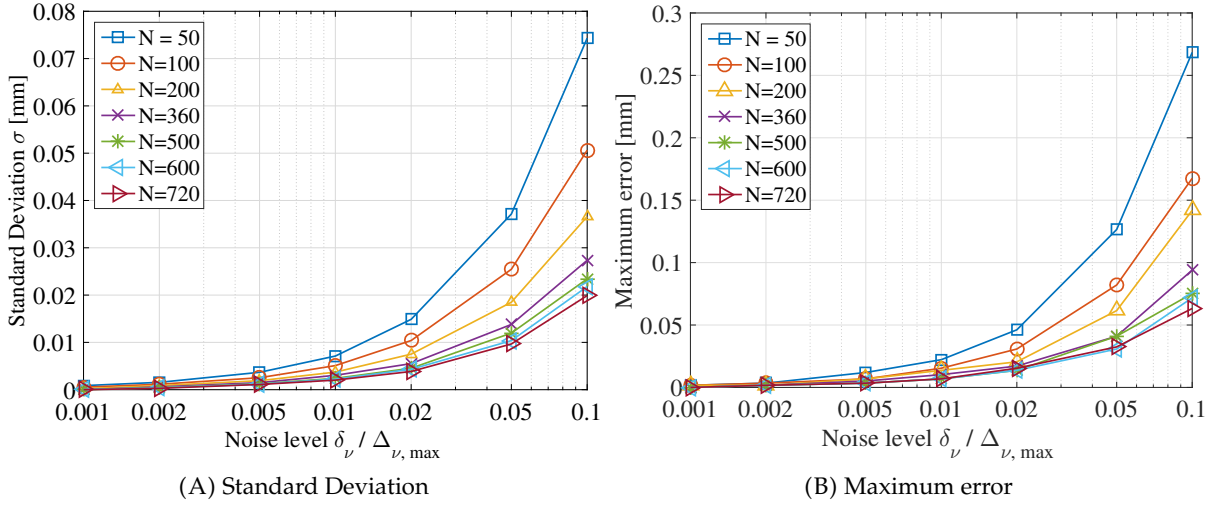
(B) Maximum error

FIGURE 3.12: Standard deviation of convergence error (A) and maximum convergence error (B) for different noise levels and N.

different N is represented. It is then compared with a theoretical distribution where

$$\sigma_x = \sigma_0 \sqrt{\left(\frac{N_0}{N_x}\right)}$$

which represents the relationship between each couple $(N; \sigma)$. The two curves are almost superimposed.
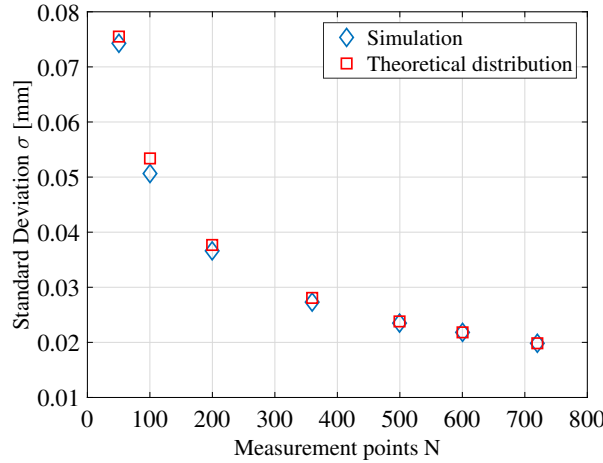
FIGURE 3.13: Standard deviation of convergence error for different N at 10% noise level.

From these figures it could be noticed that the retrieved convergence error is in the order of 1%-3% for the worst cases ($N = 50$ or 100 for example and highest noise), as the imposed convergence is a little more than 10 mm, hence it is very small for the application. The method is thus very accurate and tends to smooth the noise effect, which is a useful feature when in-situ measurement is to be done. The study shows that a high number of measurement points makes the geometry identification procedure more robust. This result thus emphasizes the interest of distributed strain measurement technology, rather than a local one (as FBGs) capable of performing a more precise measurement but only locally.

3.4 Conclusion

This chapter aims to describe and evaluate the performances of the inverse-analysis finite-element method to calculate structures' convergence from orthoradial strain measurements. Although short, this chapter is essential to understand the convergence measurement functioning. Thanks to distributed optical fiber cables it is possible to measure many structural parameters, however convergence cannot be measured directly with them. We have therefore developed a method in order to exploit the distributed strain measurements in every point, which can be used not only for tunnels but also for other structure's shape, differently from other methods (as MEMCOT). Comparing the strain obtained by a numerical simulation of the structure and the experimental one it is possible to get the force that has been applied, minimising the error between the two. These forces are then applied to the finite-element model of the structure to finally calculate the geometry of the loaded structure.

Once the method has been explained, we have performed some performances evaluations: it is important to have good knowledge of the structure's dimension to improve the accuracy of measurements and build a mesh that represents at its best the behaviour of the structure without overcharging the calculations. We have thus evaluated the impact of uniform noise and the number of measurement points, highlighting that, while the error remains under 3%, a higher number of measurement points decrease the error and its standard deviations. This means that it is preferable to use distributed sensors rather than local ones in order to obtain better results.
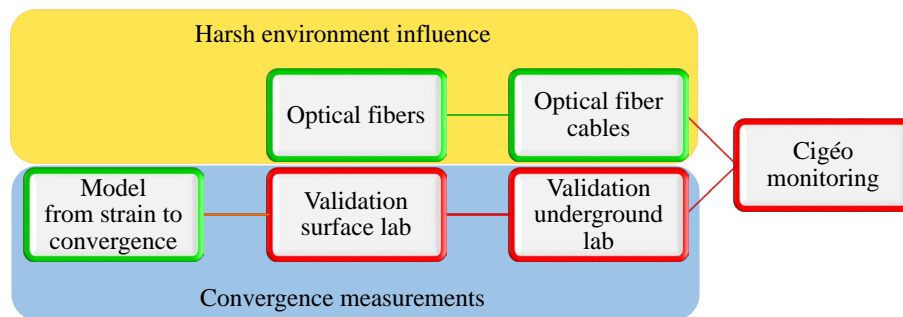
FIGURE 3.14: Schematic of the Ph.D. methodology: thanks to an inverse-analysis finite-element method, it is possible to compute convergence values from strain measurements. The distributed nature of measurements increases the noise filtering ability of the model.

The step further now is to validate the developed method in a laboratory test, where a mock-up of a HL radioactive waste repository cell is considered.

Chapter 4

Convergence monitoring: experimental validation

Contents

4.1   Introduction

In order to validate the inverse-analysis finite-element method for convergence measurement described in the previous chapter, we have designed an experimental test in collaboration with Egis Géotechnique (Grenoble, FR). The design was made to be as much as possible representative of a real-case scenario within Cigéo environment. After the description of the practical test, along with the employed tools and the structure under test, we analyse results from different points of view. The characterisation can be done by distinguishing between the employed scatterings, the different anchoring methods, and comparing our method with other convergence measurement techniques.

4.2   Laboratory mock-up

The considered real-case scenario for this test is the HLW repository cell, as it is the one which undergoes the bigger convergence during the initial (at least) 100 years of monitoring (operational
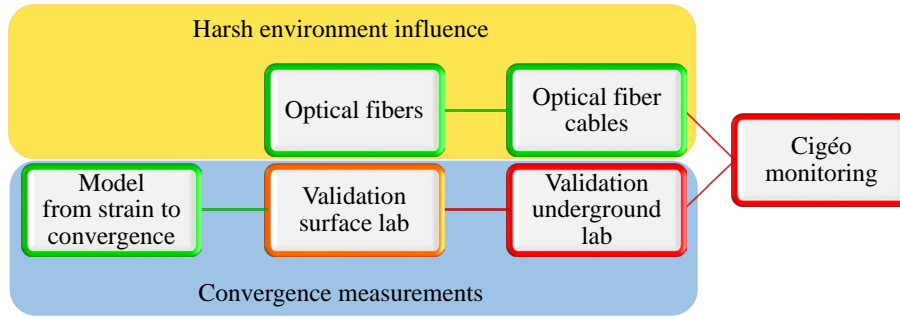
FIGURE 4.1: Schematic of the Ph.D. methodology: once the convergence measurement method is developed, it is now the turn for its validation in a laboratory test, to evaluate its ability to follow representative convergence values properly.

phase). The dimensions, materials, loading and sensors installation were chosen to be as close as possible to the true ones, remaining however feasible for an implementation in a laboratory. In the real case, a total of 10 mm of convergence is expected during the operational phase, which are due to 500 m of rock pressure above the cell. The rock is the Callovo-Oxfordian claystone, which exhibits a time-dependant behaviour due to the creep of the rock matrix. This phenomenon is responsible for long term deformation of the drifts or the disposal cells. The deformation rate however decreases with time and becomes lower than 10^{-10} s^{-1} after one year [Armand et al., 2013].

The laboratory mock-up is a steel ring which simulates the liner of the HLW repository cell. Its design took into consideration the fact that, in the laboratory, it is not possible to reach the same levels of stress as in an underground scenario. In order to obtain the representative displacement using the laboratory equipments, the thickness of the structure was therefore reduced with respect to the real disposal cell liner (25 mm). Also, it was not possible to consider the whole repository cell, being long a hundred of meters, but it was necessary to consider a proper section size. The result of these considerations is the design of a steel ring of nominal dimensions: 762 mm of external diameter, 10 mm thickness and 200 mm depth. The 2D model of this structure was also used in the previous chapter to analyse the performances of the developed method. As a consequence for the reduction of the thickness, for identical convergence value the strain levels are expected to be smaller in the laboratory test compared to real conditions. This makes the feasibility demonstration and validation of the method in the laboratory more difficult than what it would be in reality, as the measured strain is only 30% of what would be encountered on-site. Here, therefore, the sensing accuracy needs to be higher than in the real application. In the previous chapter we have also determined the importance of using the right dimension of the structure for the mesh creation. After the construction of the structure, a mean thickness value of 9.88 mm is measured (with a variance of about 0.1 mm), leading to take 9.9 mm instead of 10 mm as the reference value to be used in the numerical model. As determined in Section 3.3.2, we set the mesh for the structure with 720 nodes along the circumference and 3 elements in the thickness.

At this point, the experimental strain is used as input to the model, in order to find the displacement field of each point of the structure. The characteristics of the steel are reported in Tab. 4.1. The simulation considers the convergence evolution up to the representative maximum value of 10 mm. In practice, the ring is anchored to a reaction frame (green wheel in Fig. 4.2), consisting of some movable runners with screws that can be fixed at specific positions on the frame. It is then possible to set the runners around the circumference to load or block the structure at desired positions. The imposed displacements are applied rotating the screws, which apply a perpendicular load on the metallic surface, and monitored with the help of a ruler. In the following, two loading schemes will be considered: the so-called "two-points loading case" and the "four-points loading case", based on how many points of the structure are subjected to imposed forces and

displacements. Details will be disclosed case by case.

TABLE 4.1: Mock-up material: characteristics.

Name	Steel S235J
Type	Linear isotropic elastic
Elasticity limit	$2.35 \cdot 10^8$ N/m^2
Traction limit	$3.6 \cdot 10^8$ N/m^2
Young's modulus	$2.1 \cdot 10^{11}$ N/m^2
Poisson's ratio	0.28
Density	7800 kg/m^3
Shear modulus	$8.2 \cdot 10^{10}$ N/m^2
Thermal expansion coefficient	$1.1 \cdot 10^{-5}$ K^{-1}
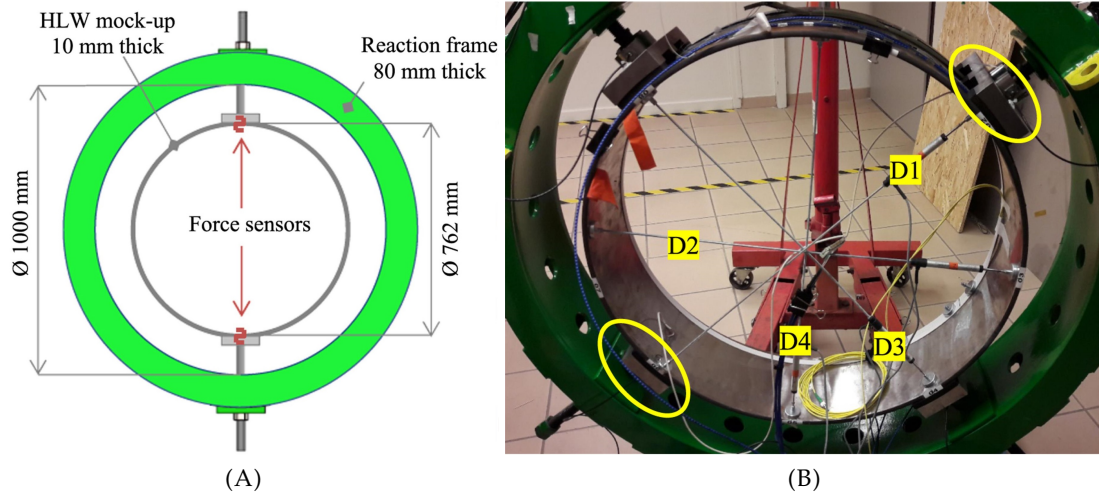
FIGURE 4.2: Test mock-up: (A) scheme of the mock-up, (B) full experimental setup: reaction frame (in green) with instrumented metallic ring. In detail the four displacement sensors "D#" and the load application runners (yellow encircled).

4.3 Sensors

In order to validate the convergence measurement, many sensors have been considered. Not only optical fiber sensors, but also some reference sensors in order to compare results with standard methods. Sensors are installed on the structure following the real instrumentation approaches that will be carried out in Cigéo. In the real case scenario, distributed optical fiber sensors will be fixed on the external circumference of the cell, i.e. between the liner and the host rock, in order to let the section be free from obstacles. In this laboratory test for convergence measurement validation the majority of sensors has been therefore fixed at the extrados of the structure, with some exceptions due to the lack of space or implementation needs.

4.3.1 Reference sensors: displacement sensors

The main reference sensor for convergence measurement is the displacement sensor, which is the alternative to invar wires for small structures. The mock-up is instrumented with four displacement sensors which are positioned as in Fig. 4.2, from diameter $D1$ to $D4$. They are fixed to the inner side of the structure, at the four quadrants, having a functioning similar to micro-tunnel's standard convergence monitoring sensors. The radial displacement is imposed at one extremity of $D1$, in order to measure exactly the desired convergence. These sensors are position transducers, pivot head mounting potentiometric up to 300 mm, of the Ingress Protection classification IP67 (IEC standard 60529) suitable for harsh environmental conditions, with a resolution better than 0.01 mm.

4.3.2 Reference sensors: force sensors

As an additional reference sensor, a force sensor is mounted on each movable runner, which applies the load to the structure. They are fixed between the metal plate of each runner and the screw which controls the load. Four of these sensors are employed, being of the FTCN series (sensors of traction/compression) from the company Mesurex with a maximum measurable load of 10 kN and a resolution of 0.1%. In this way it is also possible to perform a comparison between the force that is applied on the structure and the one that is found by the inverse-analysis model, being the main parameter of the simulation.

4.3.3 Optical fiber strain sensing cable

Concerning the employed distributed optical fiber sensor, the BRUsens V9 from Solifos AG was chosen for its high resistance to tensile loading and its high curvature radius tolerance, besides previous results under radiation influence. After deployment, the cable runs around the external circumference twice, being fixed in two different ways on the structure. One portion, that represents one turn, is glued all along its length (with Araldite 2021-1 glue). The other is fixed with a spot welding technique, where soldered supports are distanced from each other of about 4 cm. The two anchoring methods are depicted in Fig. 4.3. The two portions of cable are then connected together using connectors.

(A) Implementation   (B) Scheme
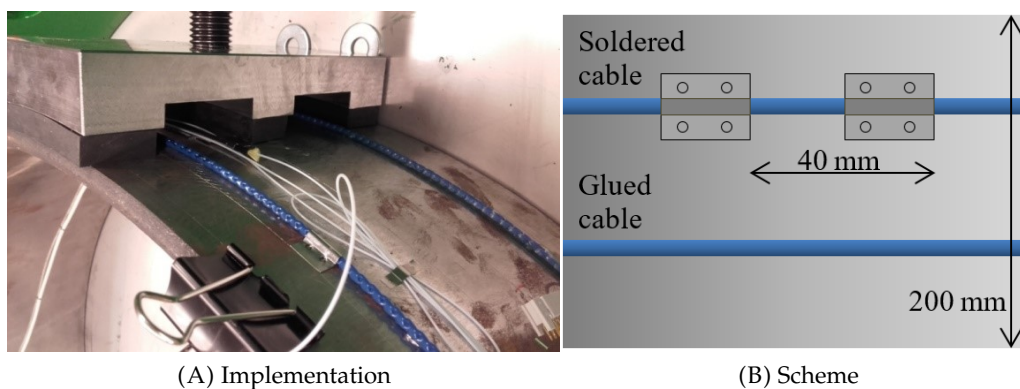
FIGURE 4.3: Optical fiber strain sensing cable anchoring methods: glued and soldered portions of cable.

The anchoring methodology is very important, as strain measurement values strictly depend on the implementation and the strain transfer function. Glueing the cable allows it to be sensitive all along its length and to possibly be influenced in the same way by compression and tension. For this particular application it is however necessary to analyse if the glue could resist over the operational period (a hundred of years at least) and to note that its implementation time is long (it

takes hours for the glue to dry properly). Soldering instead resists in time and is faster to deploy, however the cable is only fixed punctually. As a result, longitudinal compression may induce different strain than tension, since the cable may slip between anchors. A more careful installation to take into account compression is therefore needed, for example pre-tensioning the cable before the anchoring.

In this case we have installed a standard V9 type sample, which supports a single mode fiber with high curvature radius tolerance, of the type G657 standard. The frequency shift is then transformed into strain, thanks to the strain sensitivities coefficients $C_\varepsilon^B = 0.0432$ MHz/µε and $C_\varepsilon^R = -0.137$ GHz/µε respectively for Brillouin and Rayleigh scatterings, and given as input to the convergence measurement model.

4.3.4 Fiber Bragg gratings

Along with distributed optical fiber sensors, fiber Bragg gratings (FBGs) have also been installed, in order to assess the difference with distributed sensing. Eight FBGs have been fixed welding the extremities on the external circumference of the mock-up, at specific angular positions. At the same time, a 250 µm fiber with inscribed four FBGs was glued on the extrados with the EPO-TEK 302 glue (suggested by the FBGs seller), while kept in light tension to be able to properly measure compression (the imposed strain was in the order of 1500 µε). The obtained frequency shift is then given as input to the convergence measurement method developed earlier. The structure's surface instrumented with the optical fiber sensors (distributed and punctual) is shown in Fig. 4.4.
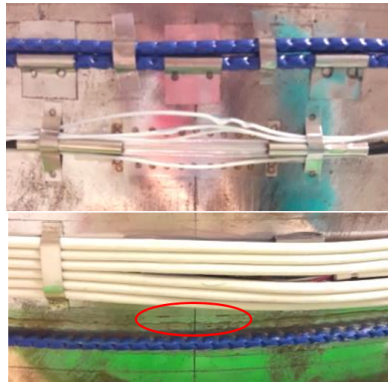
FIGURE 4.4: Sensors installation. From top to bottom: soldered cable, soldered FBG, electrical cables for resistive sensors alimentation (not mentioned in this thesis), glued FBG (circled in red) and glued cable.

4.3.5 Commercial sensing systems

Finally, we have also installed two commercial sensing systems in order to compare our technique to what is already present on the market. One is the Real Time Fiber Optic Sensing by the company Sensuron, which is based on a quasi-continuous FBGs inscribed on a cable and a software that correlate strain measurements with curvature. The other is from Morphosense, using MEMS accelerometers which, thanks to the software, estimate the 3D shape of a structure using the knowledge on their tilts. Details on their functioning will be better explained in the corresponding section 4.4.5.

4.4 Two-points loading case

The first loading case is the simplified version of the load evolution on a real HLW repository cell. The main loading comes in fact from the rock above the cell, therefore the load on the laboratory

mock-up is applied to a defined position while the diametrically opposite point is fixed and cannot move. In this case the load is applied in the direction of *D*1. In this way a vertical load, as well as the corresponding reaction of the ground, are induced. This is the case illustrated in Fig. 4.5. From now on it will be addressed as "two-points" or "2P". It was conceived to demonstrate the feasibility of the inverse FE method. The load is controlled in displacement with the help of a ruler placed along *D*1, whereas the imposed force is registered with the force sensor. We have imposed convergence with a step of 2 mm, up to the representative value of 10 mm, adding a step at 9 mm. In this way it is possible to check whether the 1 mm resolution is attained.
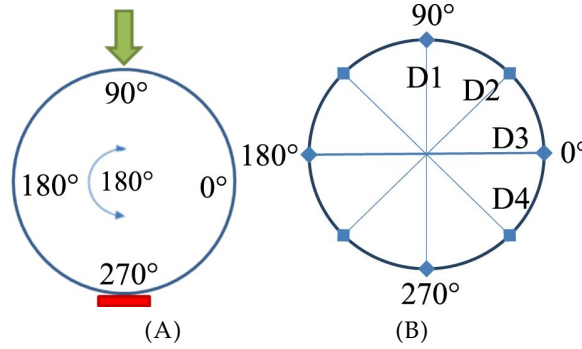
FIGURE 4.5: 2P loading case (A) and displacement sensors position scheme (B).

In order to properly represents the results, the measured strain will be illustrated as a function of the angular position around the structure. That's why we have highlighted the angular repartition as reference for plots and the displacement sensors position is shown.

The cable is interrogated with the Neubrescope NBX-7020 by Neubrex, using both Brillouin (PPP-BOTDA) and Rayleigh (TW-COTDR) scatterings. After the measurement of the reference when no loading is applied, a measurement is acquired after every imposed displacement, being careful to wait that the structure has settled. The chosen parameters for the measurement are reported in Tab. B.7. The measurements have been taken in laboratory in a controlled environment, thus we assume as negligible the impact of temperature variation (assumption also validated by temperature sensors on the mock-up). The frequency shifts are obtained by subtracting the central frequencies for Brillouin scattering, while for Rayleigh scattering we need to perform the cross-correlation between subsequent measurements to avoid error peaks, then sum up the results up to the reference. A more detailed comparison between the different cross-correlation approaches is reported in Section 4.4.2. Once the frequency shifts are collected, they are transformed in strain using the strain sensitivity coefficients $C_\varepsilon^B = 0.0432\,\text{MHz}/\mu\varepsilon$ for Brillouin and $C_\varepsilon^R = -0.137\,\text{GHz}/\mu\varepsilon$ for Rayleigh scatterings. These are in fact the strain sensitivity coefficients obtained and reported in Tab. 2.5, as strain is below 2000 $\mu\varepsilon$. The results are plotted in the following: strain obtained via Brillouin scattering, in the 2P configuration, for the glued and the soldered anchoring style, is plotted in Fig. 4.6; in the same configuration but via Rayleigh scattering in Fig. 4.7.

Brillouin traces are generally more noisy, while Rayleigh scattering depicts more accurate and distinguishable strain behaviours thanks to cross-correlation. Despite this, Rayleigh traces suffer from error spikes due to cross-correlation fails, which diminishes the clarity of the representation. Between glued and soldered samples, the preliminary analysis reveals differences that are higher for Brillouin traces (due to their lower resolution) and, for both scatterings, around the negative peak at 270°. The latter is due to a damage on the cable in that area, after a heedless maneuver during installation. A more precise evaluation of the differences between scatterings and anchoring methods will be performed after reporting the convergence results.
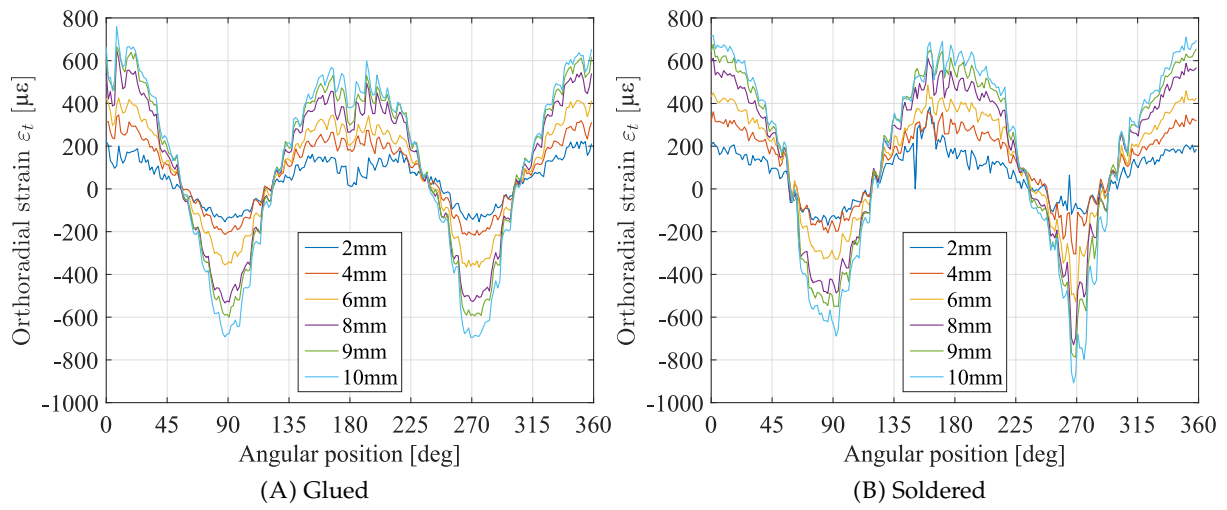
FIGURE 4.6: Strain evolution for the Brillouin scattering and the 2P loading case, in the glued and soldered anchoring configurations.
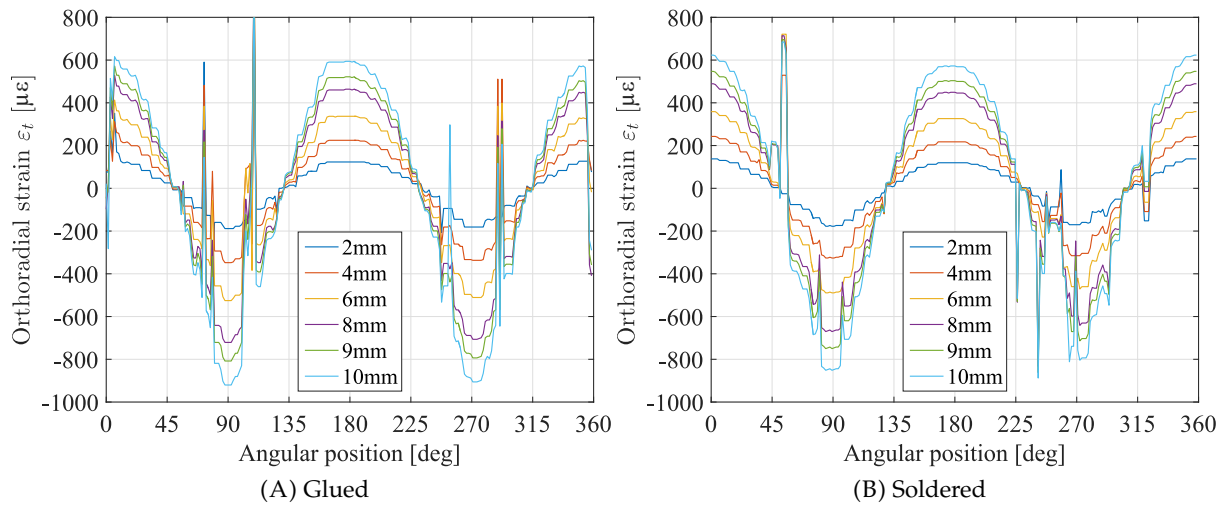
FIGURE 4.7: Strain evolution for the Rayleigh scattering and the 2P loading case, in the glued and soldered anchoring configurations.

4.4.1 Convergence measurement and results

Once strain values are obtained, we use them as input to the inverse FE model for convergence measurement. At this point, we need to perform the minimisation of the error between the experimental strain and the calculation.

In the two-points case, a force and the corresponding opposite reaction are vertically imposed to the ring, which remains elastic. As it is possible to apply the hypothesis of small strain and small displacement, the structure is modelled according to the principle of superposition of the effects for which

$$\text{if } F^u \to (u^u, \varepsilon^u), \text{ then } \alpha F^u \to (\alpha u^u, \alpha \varepsilon^u)$$

where the exponent u means here "unitary", $\|F^u\| = 1$ N. It is then possible to numerically load the ring with a unitary force and find the experimental applied force magnitude as

$$\Phi(\alpha) = \sqrt{\frac{1}{N} \sum_{i=1}^{N} (\alpha \varepsilon_i^u - \tilde{\varepsilon}_i)^2} \tag{4.1}$$

$$\alpha_{\text{opt}} = argmin(\Phi) \rightarrow F_{\text{opt}} = \alpha_{\text{opt}} F^u \quad \text{and} \quad u_{\text{opt}} = \alpha_{\text{opt}} u^u$$

where N is the number of elements of the mesh, α represents the magnitude of the load, ε^u is the theoretical orthoradial strain resulting from the unitary force and $\tilde{\varepsilon}$ is the experimental strain. In this case α is swept with unitary precision, obtaining displacement and strain values every 1 N. The point opposite to the loading spot is kept fixed by imposing no displacement for it while building the finite element model.

In order to perform a proper comparison, it is necessary to account for the real position of the sensor with respect to the neutral axis of the structure (x in 3.23). In fact, the cable has a diameter $d = 3.2$ mm, therefore the fiber lies at least at $d/2$ over the surface of the mock-up, as visible in Fig. 4.8.
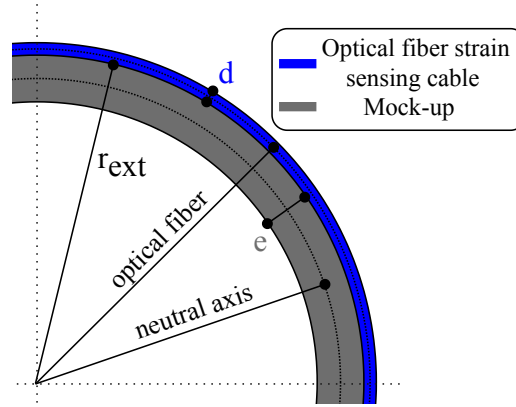
FIGURE 4.8: Position of the cable with respect to the mock-up structure.

In order to compare the simulated strain ε, calculated at r_{ext}, and the experimental strain $\tilde{\varepsilon}$, measured at the optical fiber position $r_{\text{ext}} + d/2$, we have to "move" the simulated strain of $d/2$ to be at the same distance with respect to the neutral axis. Being $e/2$ the distance between the structure's external surface and the neutral axis, and $e/2 + d/2$ the distance of the optical fiber with respect to the neutral axis, we multiply the simulated strain by the ratio $\dfrac{e/2 + d/2}{e/2} = \dfrac{6.55}{4.95} = 1.32$.

Now that the experimental and the numerical crucial factors of the model are assessed, it is possible to calculate convergence. The first step is to compare and minimize the error between the experimental and the simulated strain, to obtain α_{opt}. For example, if we consider the case of 10 mm of imposed displacement, we obtain the results represented in Figs. 4.9 for Brillouin and 4.10 for Rayleigh scatterings. Both of them regard both the glued and the soldered samples.

Thanks to the cross-correlation approach we apply, considering subsequent measurements, Rayleigh scattering results appear more accurate and regular, as they are better followed by simulation than Brillouin-based results. While both F_{opt} obtained via Rayleigh are very close to each other (4335 N and 4333 N for glued and soldered cables respectively), showing how the result is not depending from the anchoring method, Brillouin results are different, even if still around 4000 N for the 10 mm case (3957 N and 4154 N for glued and soldered cables respectively).

If we look at each F_{opt} obtained for each imposed displacement level, however, the results are unexpected. Comparing each acquisition (Brillouin or Rayleigh) and anchoring (glued or soldered) type, along with the force sensor installed at the loading runner, we obtain the graphics in Fig. 4.11. If we consider the force sensor as the reference sensor in this case, we can observe how

(A) Glued cable

(B) Soldered cable
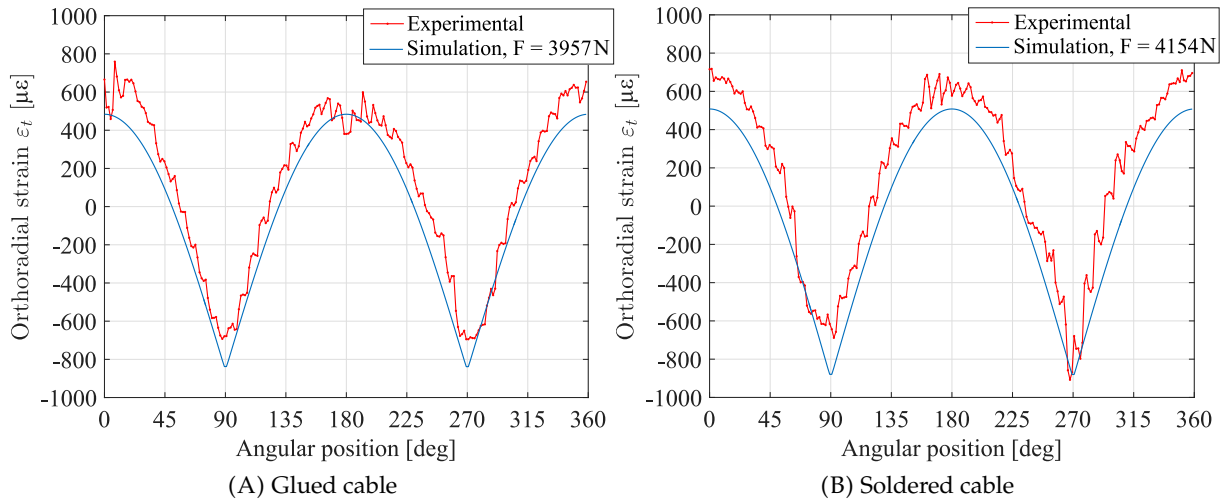
FIGURE 4.9: Brillouin experimental and optimised simulated strain comparison for the two-points load case, at 10 mm of imposed displacement.

(A) Glued cable

(B) Soldered cable
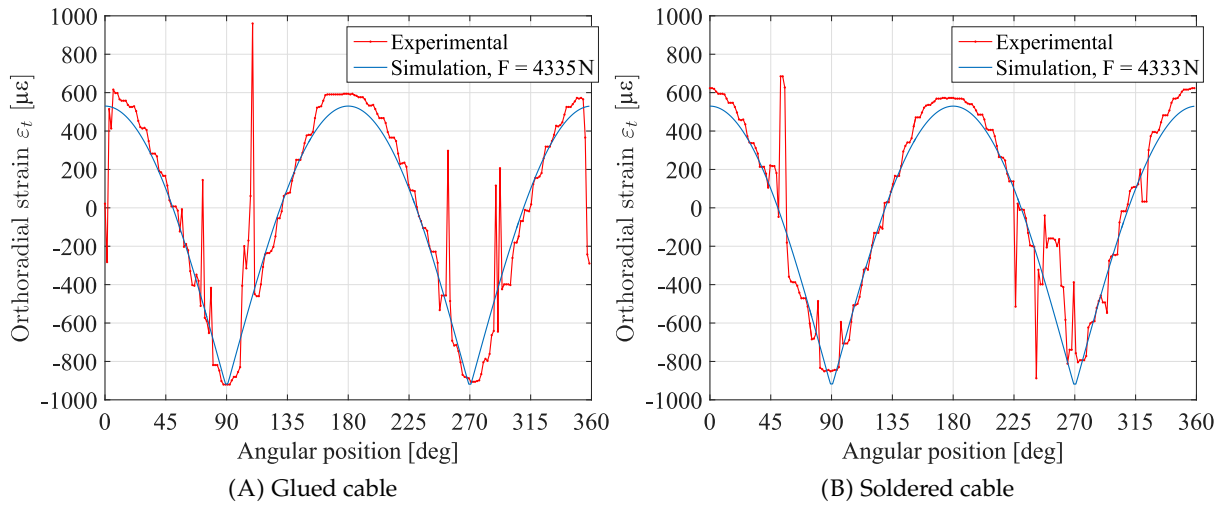
FIGURE 4.10: Rayleigh experimental and optimised simulated strain comparison for the two-points load case, at 10 mm of imposed displacement.

the Brillouin soldered sensor is the one that is mostly superimposed to the reference. The only exception is for the 2 mm of imposed displacement, where Brillouin has not the proper accuracy to follow the strain profile of the structure being far from the reference of about 30%.

The other measurement configurations are anyhow accurate enough to report results in the surroundings of the force sensor, with a margin of less than 5% for high imposed displacements. Each different imposed displacement level takes to distinct values, out of the range of values obtained at other displacement levels. This means that each sensing technique is able to discriminate properly the different imposed convergence values.

Having α_{opt}, we can calculate u_{opt} and, consequently, convergence with formulas from Eq. (3.17) on. Here the reference sensors are the displacement sensors, that give direct values of convergence. Moreover, we obtain convergence also using the force values obtained with the force sensors. It is possible to give them as input to the direct finite element model and calculate displacement consequently. In practice, force sensors magnitudes are multiplied by u^u.

As strain is measured all around the structure by strain sensing cables, it is possible to obtain a
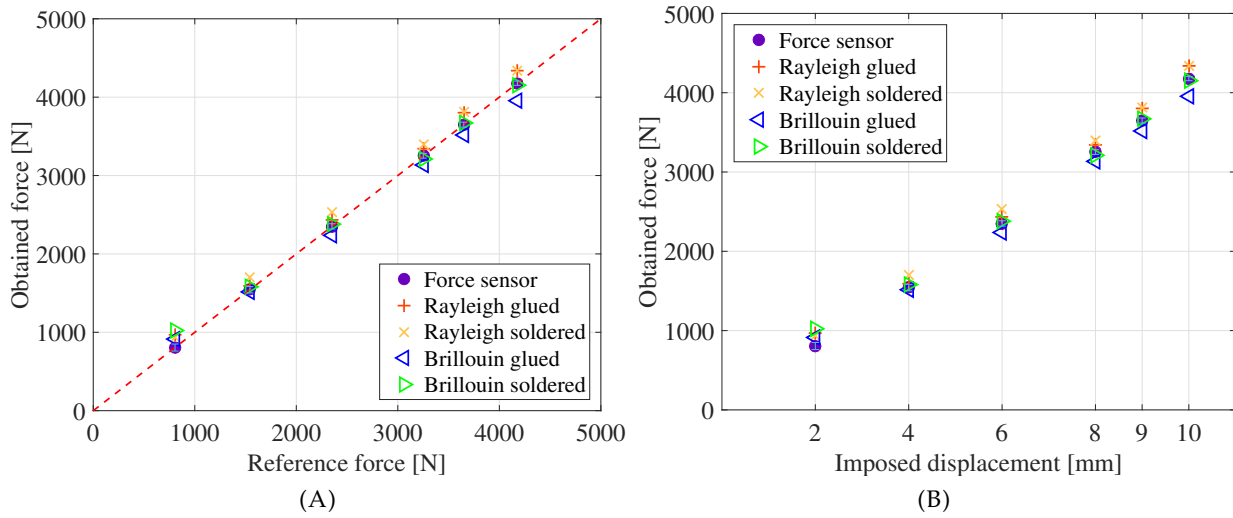
FIGURE 4.11: Force values obtained with the different considered sensors for each imposed displacement level, as a function of the reference force (A) or imposed displacement (B) for the two-points configuration, in the direction of the load.

convergence measurement all around the structure, with the use of only one sensor. For example, for 10 mm of imposed displacement, the convergence results all around the ring are plotted in Fig. 4.12.
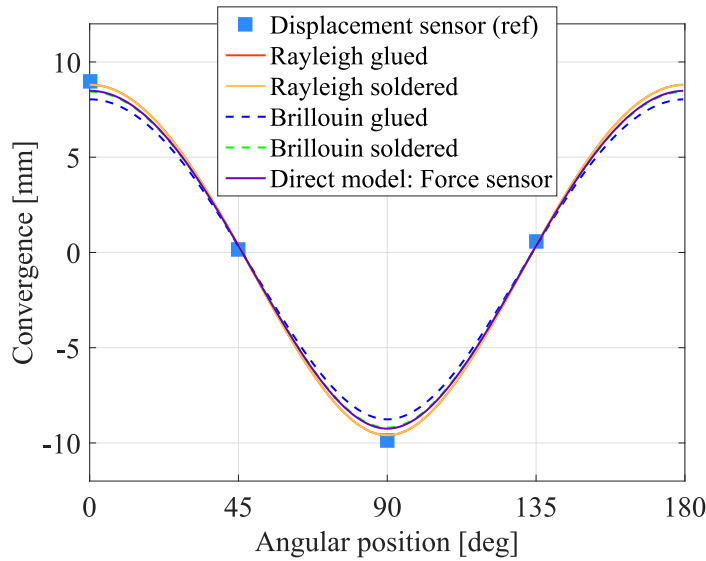
FIGURE 4.12: Convergence values obtained with the different considered sensors for 10 mm of imposed displacement for the two-points configuration, all around the structure.

This plot confirms the ability of the method to achieve convergence measurement using distributed optical fiber sensors. The calculation is in line with reference values: even with a shallow observation, the traces are all close to each other and to the reference. If we focus on the values in the direction of the load ($D1$ at $90°$ as in Fig. 4.5B), we obtain the plot in Fig. 4.13.

The closest results are the ones attained via Rayleigh scattering: the glued and the soldered samples give the same result, which is less than half a millimeter from the reference. Brillouin values are more distant, with a little more than 0.5 mm for the soldered cable and a little more
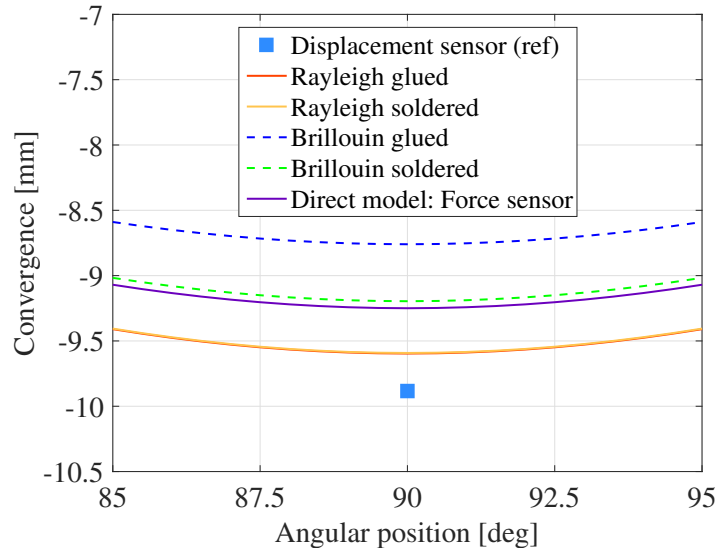
FIGURE 4.13: Detail on the convergence values reached in the direction of the load for 10 mm of imposed displacement for the two-points configuration.

than 1 mm for the glued one. Finally, convergence calculated from force sensors is at the same level of the Brillouin soldered case. More in general, results in the direction of the load for all the imposed displacements are represented in Fig. 4.14.

FIGURE 4.14: Absolute value of the convergence obtained with the different considered sensors for each imposed displacement level for the two-points configuration, in the direction of the load.

It is immediately possible to notice how none of the sensors, not even the reference, perfectly attained the imposed displacement values. This is due either to the sensors or to the actual imposed displacement, which was only checked with a ruler (with millimetric precision). Furthermore, the two reference sensors do not take to the same results. This can be due to discrepancies between the experimental and numerical loading on the structure or due to a bad calibration of the sensors, which however seems less probable.

These results, even if in their early stages, were published in [Piccolo et al., 2019d], anticipated by [Piccolo et al., 2018b], with an oral presentation at the 9th European Workshop on Structural Health Monitoring (EWSHM 2018) in Manchester, UK.

4.4.2 Brillouin vs Rayleigh

Results guarantee the possibility to retrieve convergence starting from whichever sensing techniques, as it is based on the knowledge of the structures and strain measurements. Therefore, the discrimination between Brillouin or Rayleigh scattering-based sensing techniques is mainly based on their intrinsic characteristics. As already mentioned in this manuscript, Rayleigh scattering has an higher measurement resolution and therefore accuracy with respect to Brillouin scattering sensing. Considering the measurement frequency scan step of the instrument and taking the smallest one for each technique, with 1 MHz with Brillouin scattering we scan every about 20 με, while with Rayleigh with 100 MHz it is possible to scan as low as 0.6 με. Along with the cross-correlation method, which tends to smooth up the measurement noise, Rayleigh is therefore able to better follow the strain behaviour, which could explain why it is the technique which takes to convergence values closer to the convergence reference measurement. Examples of this are reported in Fig. 4.15.
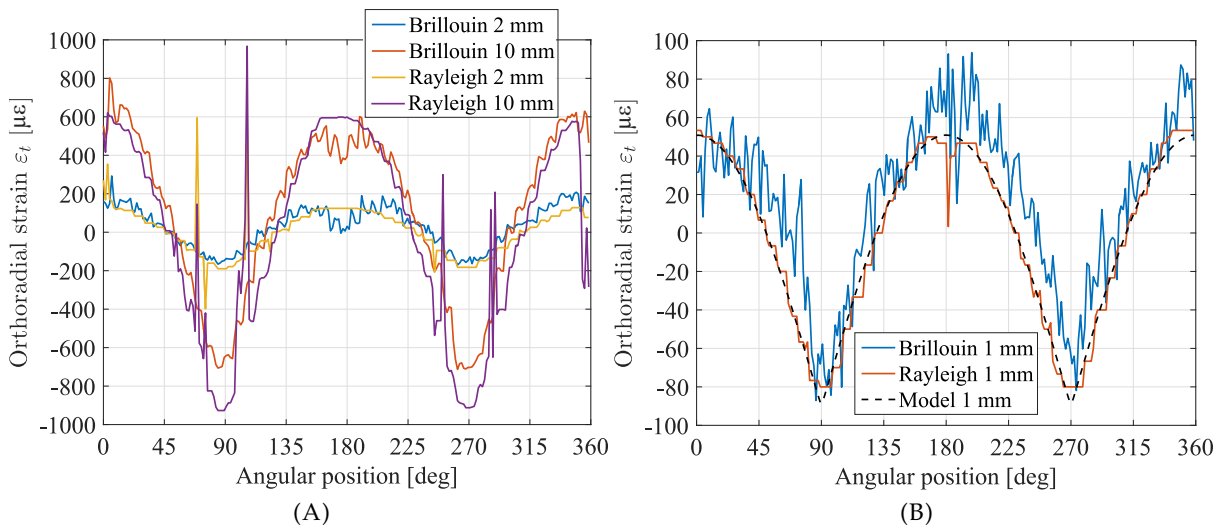
FIGURE 4.15: Comparison between Brillouin and Rayleigh scatterings: (A) comparison regarding strain measurement at 2 mm and 10 mm of imposed displacement; (B) comparison for low strain (1 mm) with the FE model simultion.

In Fig. 4.15A Brillouin and Rayleigh scatterings strain measurements are reported for an imposed displacement of 2 mm and 10 mm, revealing a more regular and less noisy trace for Rayleigh than for Brillouin. More in detail, considering now the case where the convergence evolution is 1 mm, it is possible to quantify the measurement quality in the two cases by looking at the standard deviation of the traces. The comparison between Brillouin and Rayleigh experimental strains and the FE model at 1 mm is reported in Fig. 4.15B. It is visually evident how the standard deviation of Brillouin measurement is higher (17.3 με) compared to Rayleigh (5.5 με), always in relation to the calculated model. For our strain sensitivity coefficients (C_ε^B = 0.0432 MHz/με and C_ε^R = -0.137 GHz/με), resolution is 0.75 GHz and 0.75 MHz for respectively Rayleigh and Brillouin scatterings. These values are in accordance with the acquisition parameters. It highlights that Rayleigh scattering is able to measure smaller deformations.

It is worthy to recall, however, that as Brillouin relies on central frequencies differences, it is easier to exploit than coherent Rayleigh scattering, which needs cross-correlation. Brillouin is more reliable and stable whichever the level of strain, while cross-correlation might fail if the frequency scan range is not sufficiently large. In Fig 4.16 the comparison between the results of two cross-correlation approaches is shown, for an imposed convergence of 10 mm. Strain obtained by cross-correlating subsequent measurements (two-by-two, with step of 2 mm of convergence) is much more accurate than the one obtained via direct correlation with the reference (0 mm of
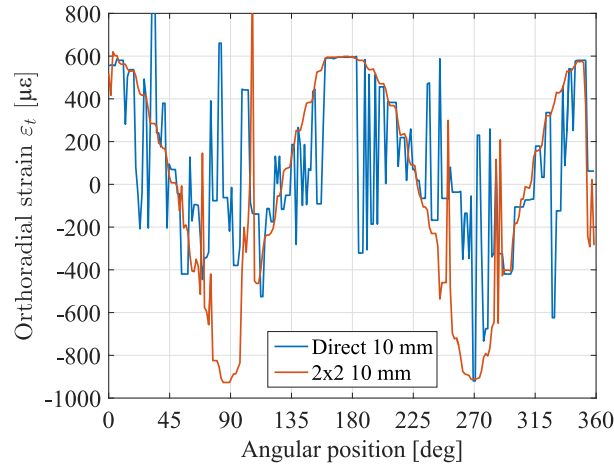
FIGURE 4.16: Comparison between two approaches of cross-correlation: "direct" is the direct cross-correlation between raw measurements and the reference, "2x2" is the cross-correlation between subsequent measurements.

convergence). Some error peaks are though still visible and this is due to the random nature of Rayleigh spectral response: they can occur in every cross-correlation based technique when strain levels reach several tens of microstrains [Zhang et al., 2018]. It was experimentally observed that the cross-correlation tends to fail when strain difference becomes higher than 500 με. As a first conclusion, it is preferable to cross-correlate subsequent measurements, two by two, in order to be sure that the difference between the two is minimal, summing then each trace up to the desired reference. This method is more time-consuming but more accurate than correlating each measurement directly to the selected reference. It also suggests that, for some applications when strain range is large, Brillouin scattering-based techniques are more robust. These results were part of a conference paper presented in a poster session at the 7th European Workshop on Optical Fibre Sensors (EWOFS19) [Piccolo et al., 2019b].

4.4.3 Strain sensitivity impact

At this point, we have observed a very good accordance between the developed method for convergence monitoring and the reference sensors. Still, in Fig. 4.14 we remarked a gap between the reference sensor results and the ones obtained via distributed optical fiber sensors. We can thus evaluate the impact of the chosen parameters and hypothesis made in the calculation, for example dealing with the strain sensitivity coefficient. If we calculate the percentage error between the convergence measured via displacement sensors and the optical fiber based sensing, for each imposed displacement level, we have the result in Fig. 4.17.

It is generally observable how the error for Rayleigh scattering remains almost always <5%, while for Brillouin it's between 10-15%. Although these values do not represent an issue, it would be possible to improve even more our results by changing the strain sensitivity coefficients used to transform the frequency shifts in strain curves. In fact, we used the coefficients found in our tests at Solifos, which were however obtained considering only one sample in a laboratory test. The sensitivity coefficient to be used on-site could indeed depend a lot from implementation as the strain transfer function could be different once the sensor is installed on the monitored structure. For this reason, we can try to adjust the strain sensitivity coefficients for the optical fiber cable to reach the least error when compared to the reference sensor. We can also consider a different coefficient not only for each scattering but also for each anchoring method, as it can affect the strain transfer function and therefore the effective sensitivity. We therefore change the sensitivity increasing it of the mean relative error between the optical fiber sensors convergence results and the
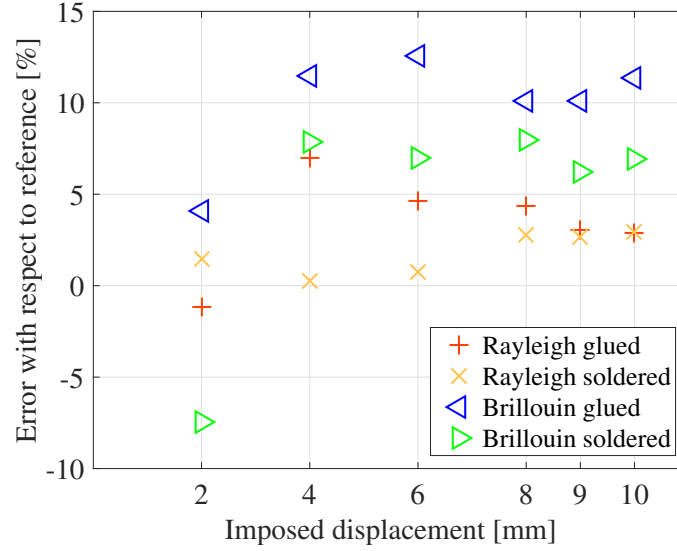
FIGURE 4.17: Percentage convergence error between the displacement sensor and the optical fiber based sensing, for the two-points case with the different considered sensors for each imposed displacement level, in the direction of the load.

reference, along the imposed displacement, i.e.: 4.4% for Rayleigh glued (R,G), 1.8% for Rayleigh soldered (R,S), 11% for Brillouin glued (B,G) and 7.2% for Brillouin soldered (B,S). These values have been obtained excluding the first value (for 2 mm of imposed displacement) as it is out of the trend especially for Brillouin scattering. The coefficient so obtained are: $C_\varepsilon^{B,G} = 0.0389$ MHz/µε, $C_\varepsilon^{B,S} = 0.0403$ MHz/µε, $C_\varepsilon^{R,G} = -0.131$ GHz/µε and $C_\varepsilon^{R,S} = -0.135$ GHz/µε. These values take to the convergence results plotted in Fig. 4.18, with the corresponding error shown in Fig. 4.19. Disregarding the value at 2 mm, the mean relative error between the convergence calculated via
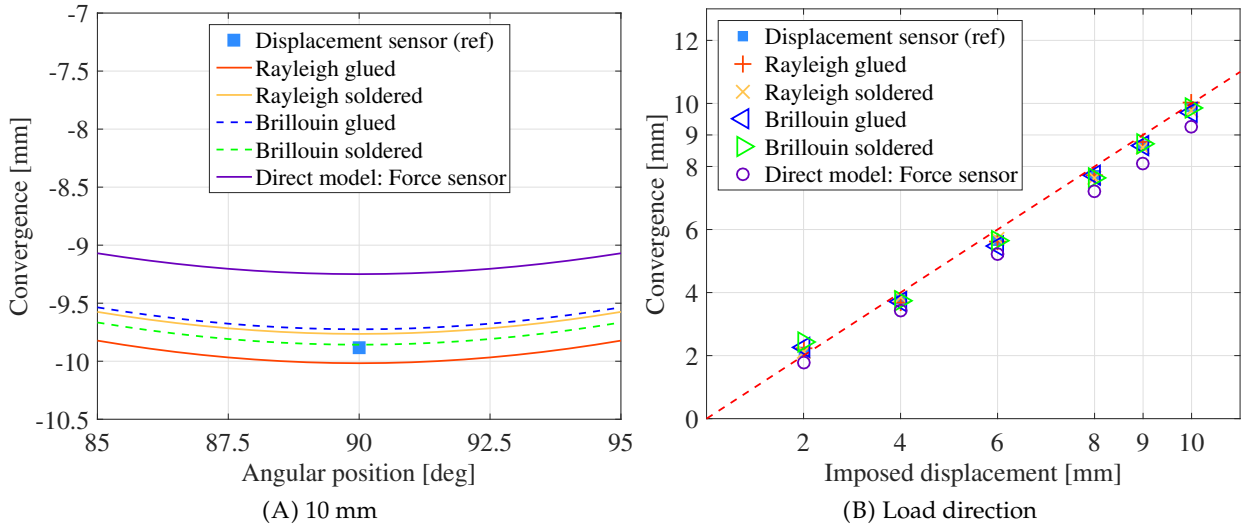
FIGURE 4.18: Detail on the convergence values reached for the two-points configuration in the direction of the load for 10 mm of imposed displacement (A)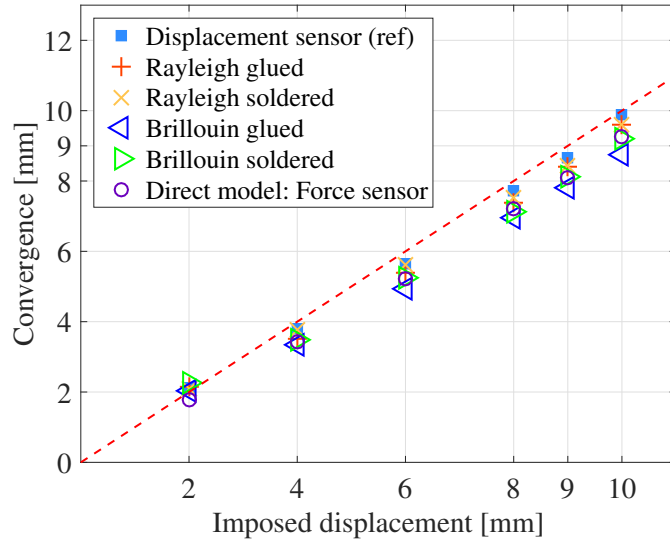. Absolute value of the convergence obtained with the different considered sensors for each imposed displacement level, in the direction of the load (B) using the optimised strain sensitivity coefficients.

optical fiber sensors and the reference is now the following: (R,G) 0.2%, (R,S) 0.11%, (B,G) 1.3% and (B,S) 0.5%. This means that a little adjustment of the strain sensitivity coefficients can take to a
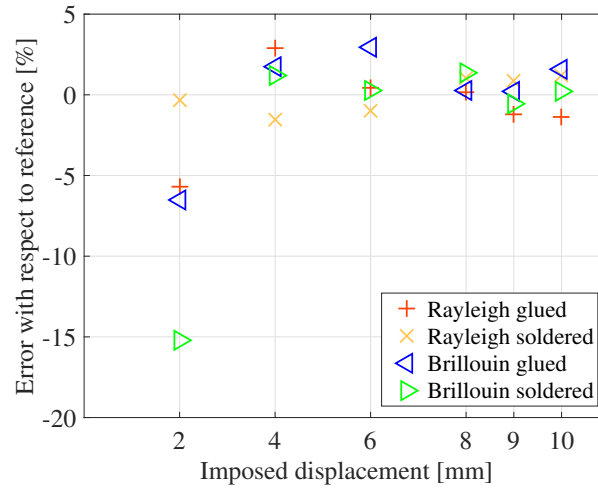
FIGURE 4.19: Percentage convergence error between the displacement sensor and the optical fiber based sensing, for the two-points case with the different considered sensors for each imposed displacement level, in the direction of the load, using the optimised strain sensitivity coefficients.

drastic reduction of error. This underlines how it is important to characterise properly the sensor and, also, to analyse results with a critical eye, for example evaluating the order of magnitude of results rather than the exact value.

4.4.4 Anchoring method

In section 4.3 we reported the two methods for the anchoring adopted for the optical fiber strain sensing cable: glueing and soldering. Apart from determining which technique is the most feasible for the application (concerning duration over time, installation speed, etc.) it is useful to assess the dependency of the results from the choice of anchoring method. Results displayed previously, as for example in Fig. 4.17, show generally lower error for the soldered cable, even if this can be changed by adjusting the sensitivity coefficients (as in Fig. 4.19). Looking at strain measurements (like Figs. 4.6 or 4.7) there is no apparent difference apart from what is due to the manipulation of the cable during installation. In conclusion, it may be better to use soldering for durability and results closer to the reference, but the difference with glueing is not so tremendous. Further analysis is required to assess properly this point. At the moment, in Andra's underground laboratory in Bure (FR), where different mock-ups are instrumented to monitor various parameters, as the behaviour of the rock, without waste packages, the optical fiber cables are glued on the surface of the metallic repository cells (HLW).

4.4.5 Comparison with other sensing techniques

Once we have assessed the performances of distributed optical fiber sensing, it is useful to check whether local sensors as FBGs, which are more commonly used in SHM, have the same performances. The acquired strain is used, like for optical fiber sensing cables, as input to calculate convergence with the inverse-analysis finite-element method here developed and compared with results above reported.

Moreover, in the application it is preferred to employ sensing systems whose output data is freely available and manageable without the need of a third party. This took to the need of building a convergence monitoring method based on commercial instrumentations with some degrees of freedom, as the possibility to directly access to raw measurements. However, it is convenient to try other sensing paradigms in order to find what is already present in the market

and compare them to our approach. For this reason we also evaluate the working principle of two commercial sensing systems from Morphosense and Sensuron companies.

The following results have been the main object of a conference presentation, along with the corresponding paper, at the International Conference on Technological Innovations in Nuclear Civil Engineering in the 2018 in Paris-Saclay (FR), [Piccolo et al., 2018c].

OFSs: distributed vs local

We have already discussed the advantage of having a distributed sensor, a multipoint sensor which can acquire many sensing points around the structure, in section 3.3.6. However, it is worth to analyse what the fiber Bragg gratings installed on the structure are able to achieve. The glued FBGs are installed at 90, 180, 270 and 360 deg, while the soldered are at 45, 90, 120, 180, 240, 270, 315 and 360 deg. Strain acquired via FBGs is depicted is Fig. 4.20. The strain is then used as input in the convergence measurement method, giving the results in Fig. 4.21 compared to distributed optical fiber sensors.

(A) Glued   (B) Soldered
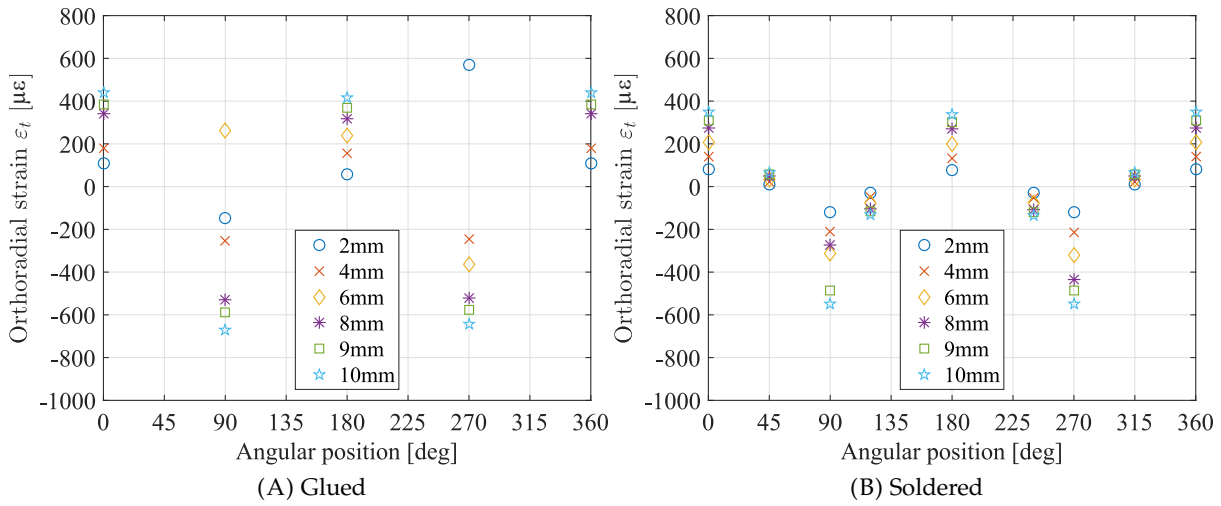
FIGURE 4.20: Strain evolution for the fiber Bragg gratings and the 2P loading case, in the glued and soldered anchoring configurations.
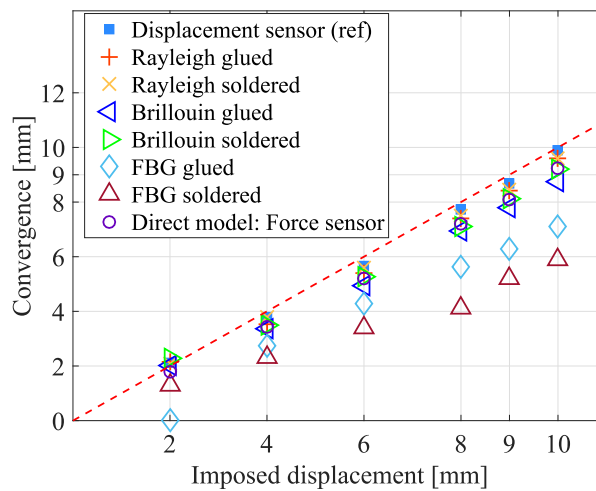
FIGURE 4.21: Convergence comparison between distributed and punctual (FBG) optical fiber sensors in the direction of the load, for each imposed displacement level.

FBGs results are quite far from the reference, both the glued and the soldered sensors do not reach the same performances of optical fiber sensing cables: compared with the reference sensor, the error is 27% for the glued FBGs and 41% for the soldered ones. The soldered FBGs exhibits therefore the worst behaviour, although the number of sensors is higher than for the glued FBGs. Although the maximum attention and professionalism have been given to the installation of soldered and glued FBGs, this result is probably more due to the installation, calibration or data treatment of the sensors rather than the number of sensing points. Distributed measurements reduce the impact of implementation as they give strain values all around the structure. In such case, an erroneous correspondence between measurement points and coordinates of the structure is less problematic than for punctual sensors, which acquire measurements only locally.

OFSs vs commercial sensing techniques

In parallel, we have tested two commercial sensing techniques, to compare our method with what is already present in the market. Both instruments, one from Sensuron and the other from Morphosense companies, are able to compute the shape of a structure, from which convergence can be easily obtained. In order to compare the different techniques, we first consider the results obtained with the two commercial instruments, after a brief description. Afterwards, the comparison with the distributed optical fiber strain sensors and reference sensors will be done.

The first considered commercial sensing system is the Real Time Fiber Optic Sensing (RTS125+) by the company Sensuron. It claims to guarantee a spatial resolution down to 6.3 mm and a maximum total distance range of a hundred meters. The software correlates strain measurement with curvature, retrieving the 3D shape of the instrumented structure. The sensor itself, already provided as part of the sensing system, is an optical fiber with inscribed quasi continuous FBGs, interrogated via an OFDR technique. The interrogator accuracy is given to be 1.25 $\mu\varepsilon$ for strain and 0.15 °C for temperature. The optical fiber is then protected by a flat plastic sheath, which allows to better adhere to the structures' surface. The sensing cable, with a length of almost 2.6 m, is in this case glued at the structure's inner surface (as there was not much space left on the extrados) and it is shown in Fig. 4.22.
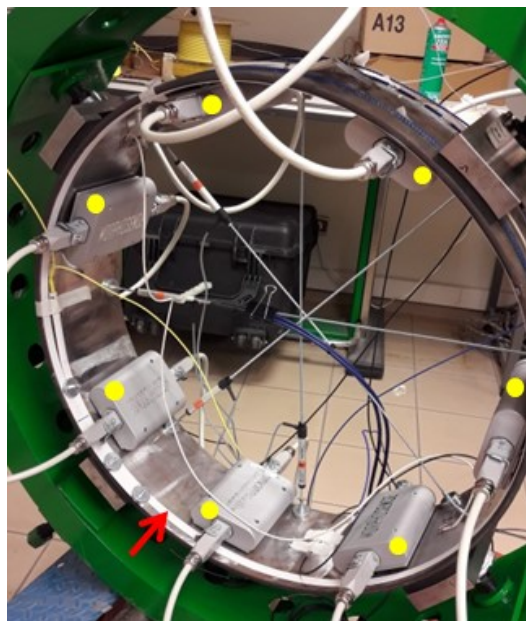
FIGURE 4.22: Instrumented mock-up with commercial sensing systems: Sensuron sensing cable (red arrow) and Morphosense sensors (yellow points).

The calibration is done in two steps: one needs the cable to be straight, in the other it must be fixed on the structure. While the sensor is put in place it is possible to define and locate the measurement starting and ending points over the fiber length, in order to be able to obtain a curved and closed shape, taking as reference the straight cable calibration measurement.

After the long calibration, measurements are very fast to acquire strain or 3D shape coordinates, as in 0.5 s more than 10 traces are already obtained. The shape of the structure is given as coordinates, as represented in Fig. 4.23A for different imposed convergences. At an immediate

(A) 3D shape sensing: structure coordinates

(B) Convergence all around the ring
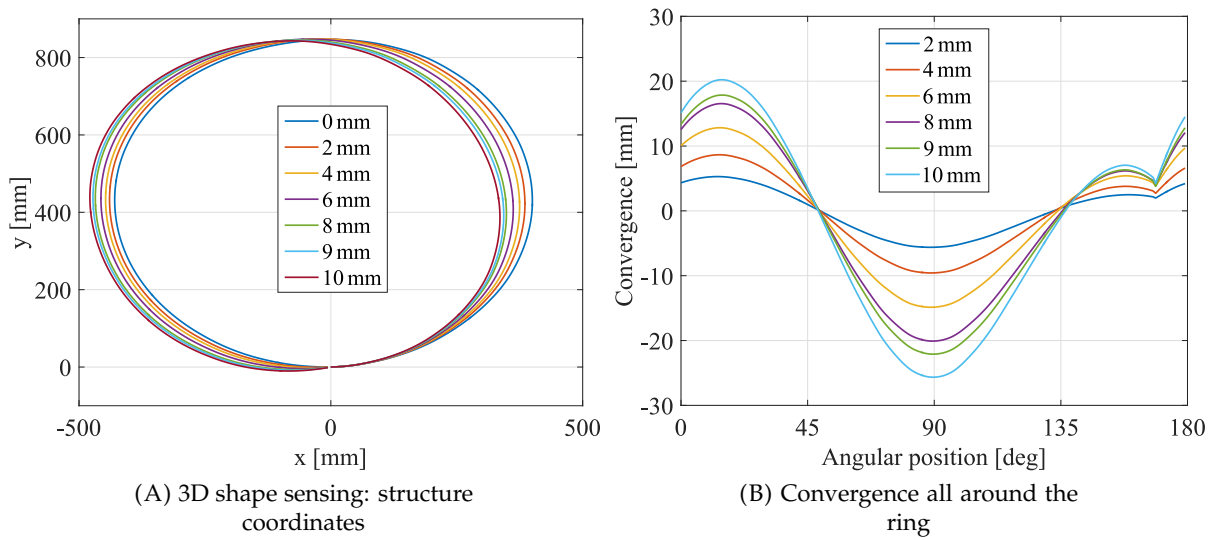
FIGURE 4.23: Sensuron results for each imposed displacement.

glance, the shape of the structure is nicely observable: the round shape is represented and the different imposed convergence levels are recognizable, even for the smaller displacement of 1 mm between 8-9-10 mm. Looking more carefully, it is possible however to notice two issues. First, the zero of the coordinates is not located at the center of the structure but is right where it was defined when implemented. This means that if the corresponding point on the structure moves due to the loading, it will not be detected with a measurement. To avoid the issue, the cable starting point has then to be chosen carefully and put, for example, where a displacement is imposed and therefore known. At the same time, the cable starting point is the reference for all the coordinates, thus its choice is very important when it comes to compare the result with different techniques. Second, looking more specifically to the reported values, the diameter appears to be in general bigger than what it is in reality: the inner diameter should be in the order of 742 mm while the measured value is around 840 mm. The same consideration can be done looking at the calculated convergence around the structure, as in Fig. 4.23B. This bias is attributed to the calibration of the strain measurement; indeed, several strain traces values are greater than the ones obtained with the optical sensing cables taken as comparison. This last point will be crystal clear when convergence is compared. In short, it has to be noted the huge influence of the implementation procedure, especially the parameters insertion in the data analysis software, which needs to be carefully studied prior to perform proper measurements.

The other commercial sensing system here considered is from Morphosense company. The technology is based on a network of MEMS accelerometers which estimate the 3D deformation and vibrations of instrumented structures. These sensors measure their tilts and, knowing their position on the structure, the software estimates the shape of the instrumented body. For this reason the system is not sensitive to purely rotational movements. From the reconstructed geometry of the structure the system can calculate the radiuses giving in turn convergence values. In

this case seven MEMS sensors are employed and fixed thanks to magnets at the structure's inner surface, as shown in Fig. 4.22.

Differently from Sensuron and other sensing techniques, the Morphosense system is managed only by Morphosense's technicians, which gives only access to results. The coordinates of the structure (which move due to the loading) are plotted in Fig. 4.24.
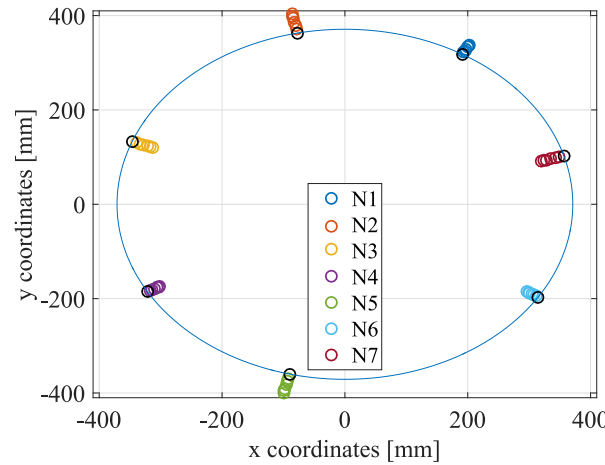
FIGURE 4.24: Morphosense convergence for each different MEMS sensor, with the original ring shape in a continuous blue line.

Once these partial results are obtained, it is necessary to find a way to compare the different sensing systems. The developed FE model that processes raw strain measurements of optical fiber sensing cables and FBGs (Section 3.3.4) can provide both the coordinates and the convergence all around the ring. Sensuron provides the coordinates (i.e. the shape) of the structure, while it is possible to obtain convergence locating the loading position by rotating and shifting the coordinates. Finally, Morphosense directly provided the convergence data for the desired position.

The comparison of the computed convergences is shown in Fig. 4.25A. For Sensuron, the obtained convergence is much bigger than the imposed displacement. However, the convergence steps between each imposed displacement level are regular: almost 5 mm between each imposed 2 mm, while it is 2.5 mm when the imposed step was 1 mm. It is thus possible to say that the different loadings outcomes are properly discriminated, despite the different precise values. With this in mind, Sensuron measurements were divided by 2.5. In this way, as illustrated in Fig. 4.25A, both Morphosense and Sensuron convergence results are comparable to the imposed displacement measured by the reference sensor.

Regarding Sensuron coordinates, their apparent erroneous position can be explained with a possible erroneous calibration of strain measurements, for example not using the proper strain sensitivity coefficient to transform the FBG frequency shift into strain. If this hypothesis should be confirmed, it would mean that a careful Sensuron system setup is even more necessary, but it would also prove to be an effective sensing system to monitor convergence, as measurements are performed at high-frequency. The comparison between glued and soldered optical fiber cable, Sensuron, Morphosense and displacement sensors is reported in Fig. 4.25B, representing convergence along the loading direction. Here only the "adjusted" Sensuron results are being shown. These results confirm that the two commercial sensing systems are therefore able to retrieve convergence properly. However, the drawbacks of these techniques are important. Morphosense requires the presence of its own technicians and the MEMS accelerometers occupy space inside the structure, which is not allowed. Moreover, a study on the durability of the sensors in harsh environment would be necessary. Regarding Sensuron, even if the FBG-based sensor allows its presence on the structure (being low intrusive and resistant to harsh environment), the need of a
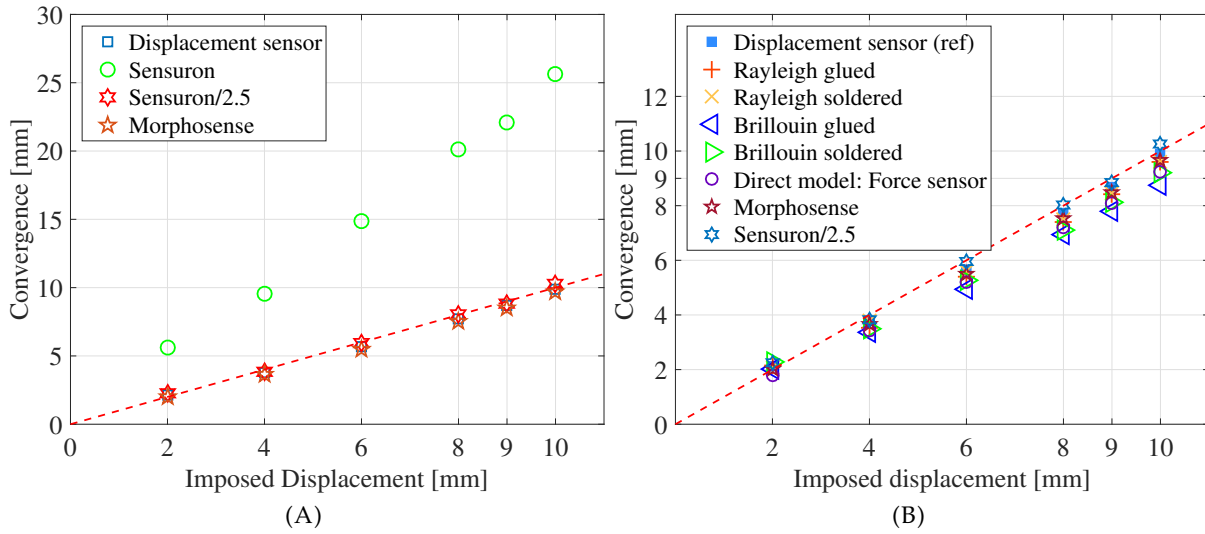
FIGURE 4.25: Sensuron vs Morphosense convergence results (A). Convergence comparison between distributed optical fiber sensors and commercial sensing systems (Morphosense, Sensuron) in the direction of the load, for each imposed displacement level (B).

long and careful calibration and data treatment makes the sensor uneasy to employ in an environment which is already "difficult" on its own.

4.5   Four-points loading case

This second case is more representative of the application with respect to the two-points loading case analysed previously. As before, a vertical loading is applied to the mock-up in the direction of $D1$, loading a point and blocking the movement of the opposite one, at 180 deg. In the real application, the cell will be surrounded by the rock, so here two other runners are positioned in the orthogonal direction (along the direction of $D3$) in order to simulate the rock constraints. They are fixed 2 mm away from the structure, in order to simulate the gap between the cell and the host rock as on-site. This is the case illustrated in Fig. 4.26. From now on it will be addressed as "four-points" or "4P" case. In this case the convergence is imposed with a step of 2 mm, up to the representative value of 10 mm.
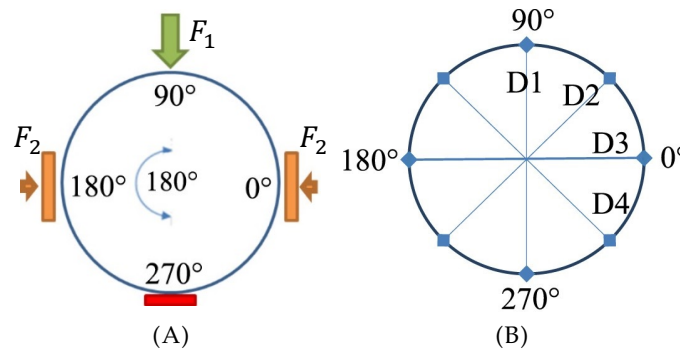
FIGURE 4.26: 4P loading case (A) and displacement sensors position scheme (B).

Measurements are acquired with the same approach as before, taking first the reference on an unloaded structure and waiting for the structure to settle, after each new loading, before taking

a new acquisition. Measurements are acquired via Brillouin (PPP-BOTDA) and Rayleigh (TW-COTDR) scatterings, with parameters reported in Tab. B.7. Once the frequency shifts are collected, by central frequencies subtractions for Brillouin and cross-correlation for Rayleigh, they are transformed in strain using the same strain sensitivity coefficients as before, $C_\varepsilon^B = 0.0432$ MHz/με for Brillouin and $C_\varepsilon^R = -0.137$ GHz/με for Rayleigh scatterings.

Experimental strain for the 4P configuration, for both glued and soldered cables and for each imposed displacement, is plotted in Fig. 4.27 for Brillouin scattering and in Fig. 4.28 for Rayleigh scattering.

(A) Glued   (B) Soldered
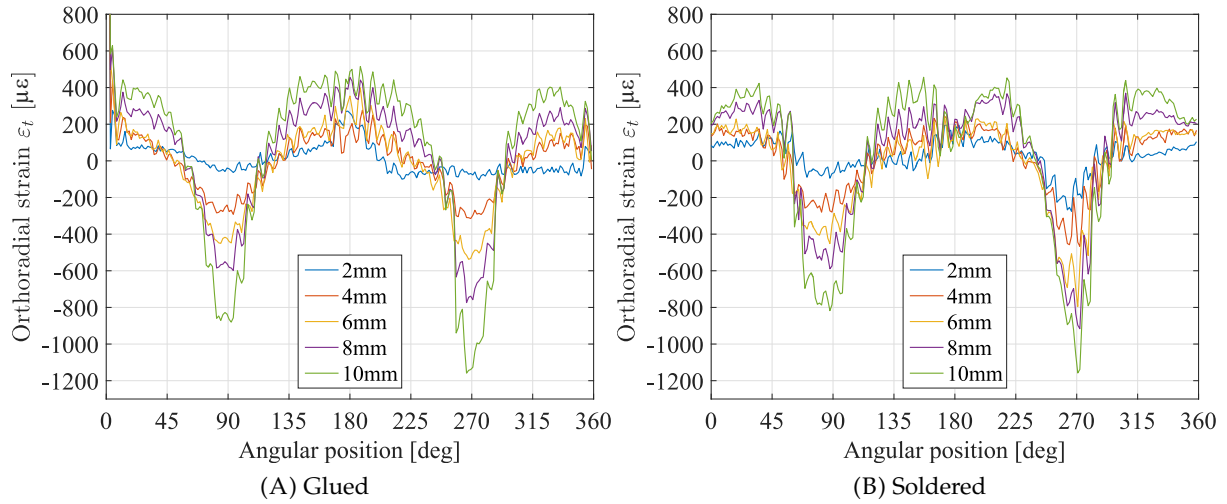
FIGURE 4.27: Strain evolution for the Brillouin scattering and the 4P loading case, in the glued and soldered anchoring configuration.

(A) Glued   (B) Soldered
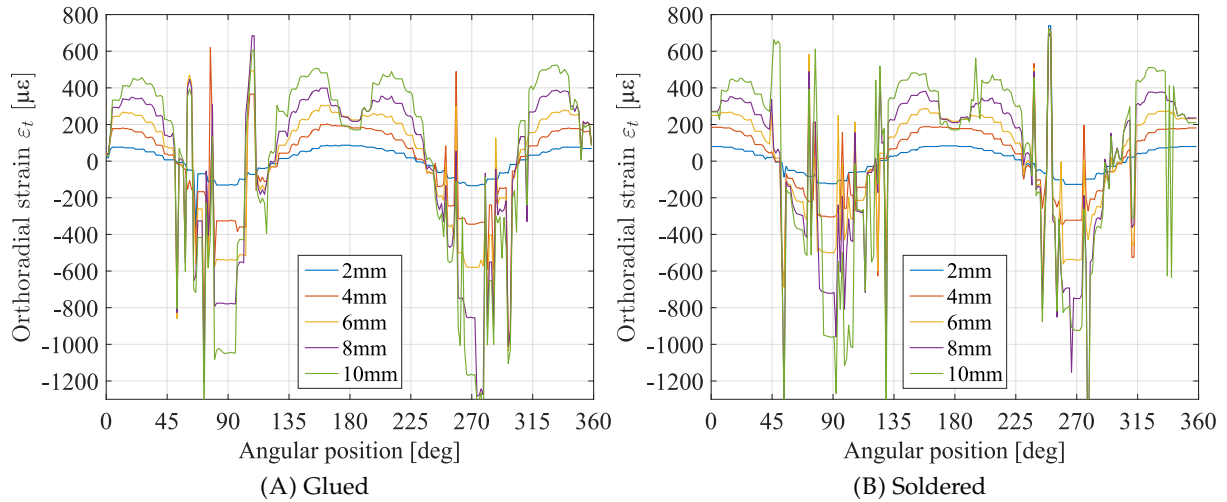
FIGURE 4.28: Strain evolution for the Rayleigh scattering and the 4P loading case, in the glued and soldered anchoring configuration.

These plots lead to the same comments as for the two-points loading case. The Rayleigh cross-correlation, performed between subsequent measurements, helps reducing the measurement noise, which is higher for Brillouin measurement values. At the same time, the cross-correlation can fail when strain variations are high, taking to error peaks. The comparison between measurement techniques will be further discussed after convergence values will be reported.

4.5.1   Convergence measurement and results

This case can be seen as an extension of the two-points loading case with the addition of two more forces, which represent the reactions at the two lateral runners. As the two reactions should be equal, being positioned symmetrically with respect to the load, only one amplitude (i.e. one coefficient) for these two forces is searched for optimisation. They are represented as the two orange forces in Fig. 4.26(A). If, as before, the loading of unitary forces is considered for the simulation, the model should be optimised to find two amplitudes α and β. In fact,

$$\text{if for } F_1, \left\|F_{(1,X)}\right\| = 0, \left\|F_{(1,Y)}\right\| = 1 \rightarrow u_1, \varepsilon_1$$

$$\text{and if for } F_2, \left\|F_{(2,X)}\right\| = \pm 1, \left\|F_{(2,Y)}\right\| = 0 \rightarrow u_2, \varepsilon_2,$$

$$\text{then } \alpha F_1 + \beta F_2 \rightarrow \alpha u_1 + \beta u_2 \rightarrow \varepsilon_{TOT} \text{ (via 3.16)}.$$

In order then to find α_{opt} and β_{opt}, arbitrary values of α and β are coupled to calculate the displacement. The overall orthoradial strain ε_{TOT} is then computed and F is retrieved proceeding as before, so

$$\Phi(\alpha, \beta) = \sqrt{\frac{1}{N} \sum_{i=1}^{N} (\varepsilon_{TOT,i}^u - \tilde{\varepsilon}_i)^2} \tag{4.2}$$

$$(\alpha_{\text{opt}}, \beta_{\text{opt}}) = argmin(\Phi) \rightarrow F_{\text{opt}} = \alpha_{\text{opt}} F_1 + \beta_{\text{opt}} F_2 \quad \text{and} \quad u_{\text{opt}} = \alpha_{\text{opt}} u_1 + \beta_{\text{opt}} u_2$$

The convergence measurement method, already validated for a simple case, is now applied to a more complex case in order to verify its robustness. After comparing the simulated and the experimental strain, having multiplied the numerical strain for 1.32 to account for the position of the sensor, we obtain α_{opt} and β_{opt} for each considered case. We represent in Figs. 4.29 and 4.30 the comparison between the optimised simulated strain and the experimental one for, respectively, Brillouin and Rayleigh scattering.
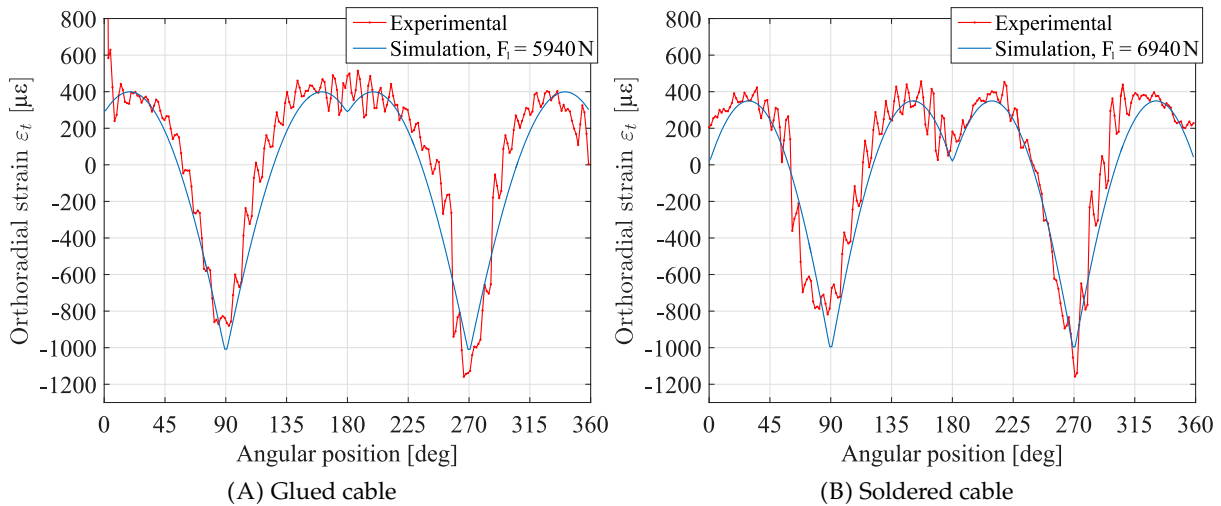
FIGURE 4.29: Brillouin experimental and optimised simulated strain comparison for the four-points load case, at 10 mm of imposed displacement.
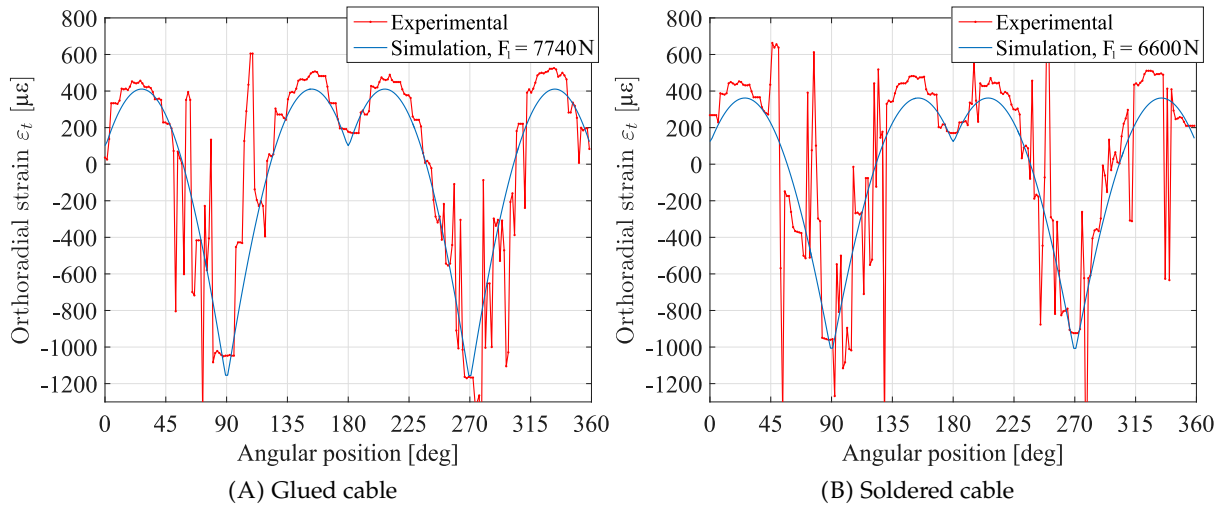
FIGURE 4.30: Rayleigh experimental and optimised simulated strain comparison for the four-points load case, at 10 mm of imposed displacement.

The retrieved amplitudes α_{opt} and β_{opt} for each imposed displacement level and for each distributed optical fiber sensing technique are represented respectively in Figs. 4.31 and 4.32.
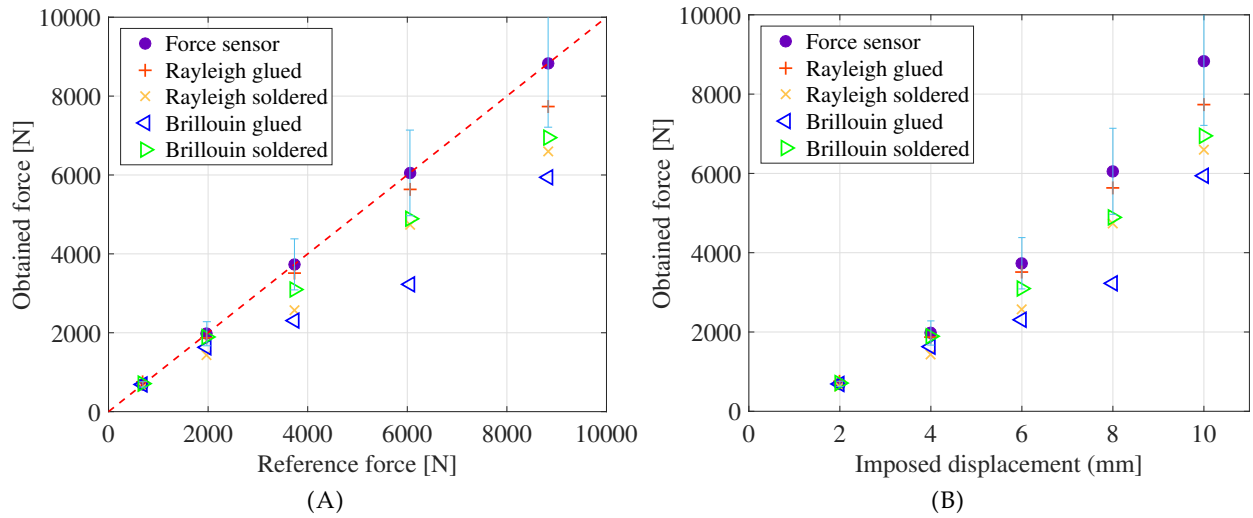
FIGURE 4.31: Force values for F_1 obtained with the different considered sensors for each imposed displacement level, as a function of the reference force (A) or imposed displacement (B) for the four-points configuration, in the direction of the load.

Differently from before, using the strain sensitivity coefficients obtained in Tab. 2.5, there is no clear tendency linked to the anchoring method comparing the forces amplitudes with the reference sensor. The closest results are given by the Rayleigh glued and the Brillouin soldered configurations. Once the forces amplitudes are obtained, it is possible to calculate then the displacement field of the structure using (4.2) and, consequently, convergence with formula (3.17). We obtain convergence all around the structure, as for example showed in Fig. 4.33A for 10 mm of imposed displacement reading the ruler installed on the structure. A focus in the direction of the load (at 90 deg) in Fig. 4.33B reveals how close the glued cable results are to the reference, whose value however does not reach 10 mm of convergence but just 9 mm. The reason behind this has not been
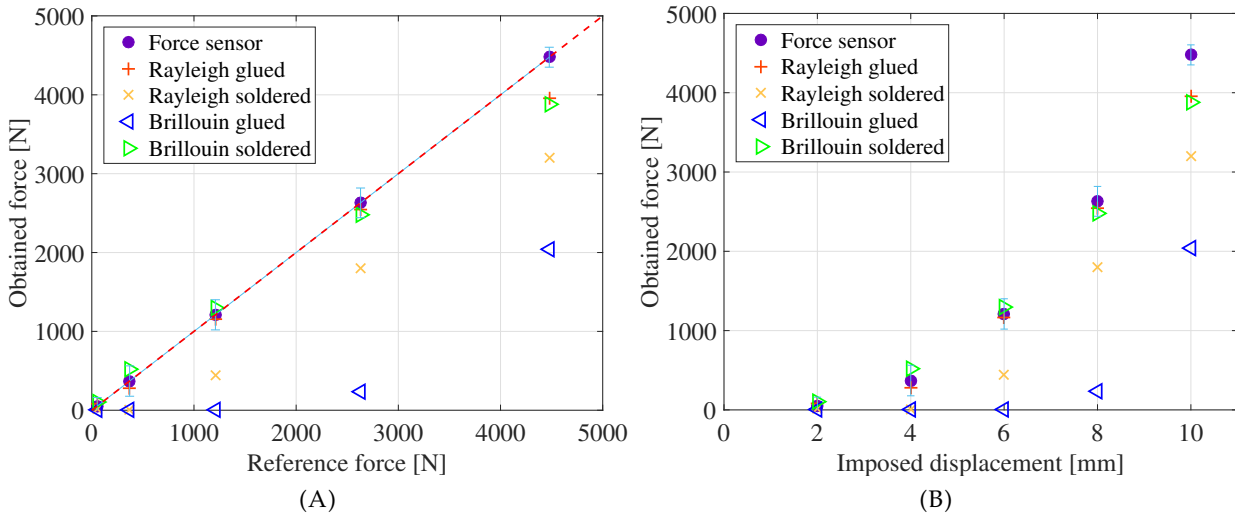
FIGURE 4.32: Force values for F_2 obtained with the different considered sensors for each imposed displacement level, as a function of the reference force (A) or imposed displacement (B) for the four-points configuration, orthogonally to the direction of the load.
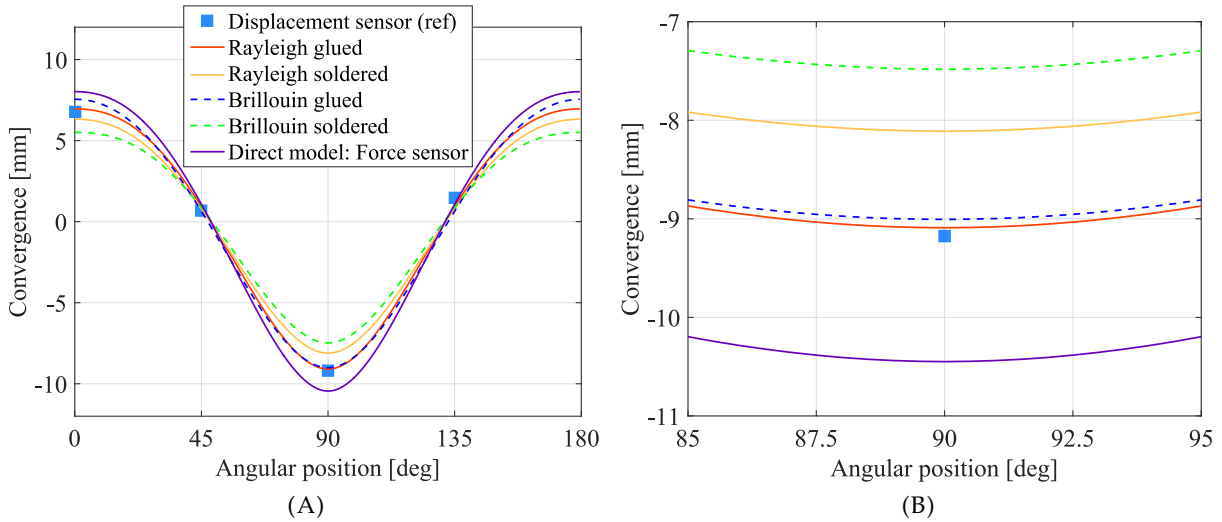
FIGURE 4.33: Convergence values obtained with the different considered sensors for 10 mm of imposed displacement for the four-points configuration, all around the structure (A), with a detail on the convergence values reached in the direction of the load (B).

discovered yet: it could be the calibration of sensors or a not perfect implementation of the test. In any case, we still consider as correct the values obtained with the reference sensor.

The same gap between reference measurements and the desired imposed displacement is visible also for the other cases as in Fig. 4.34, while the difference between the results of each technique and the reference is represented in Fig. 4.35. The best sensing approach varies with the imposed displacements. For low displacement the soldered configuration gets a lower error, while going towards higher values the glued cable gets closer to the reference. This can be linked to the great amount of compressive strain, which grows with the imposed load. A big part of cable is in compression (as visible, for example, in Figs. 4.29 and 4.30) which can take it to get distanced from the surface of the structure, more than for the glued portion. In this way, the soldered cable could

measure strain with less accuracy, giving less accurate results. In each case, only the Brillouin soldered case reports an error with respect to displacement sensors that is bigger than 10%. For Rayleigh scattering, if the maximum imposed displacement had been of 10 mm, the error would have been less than 1 mm which is the desired accuracy. Convergence is anyhow obtained with good accuracy from at least one of the sensing techniques, which validate the inverse-analysis finite-element method also in this more complex case.
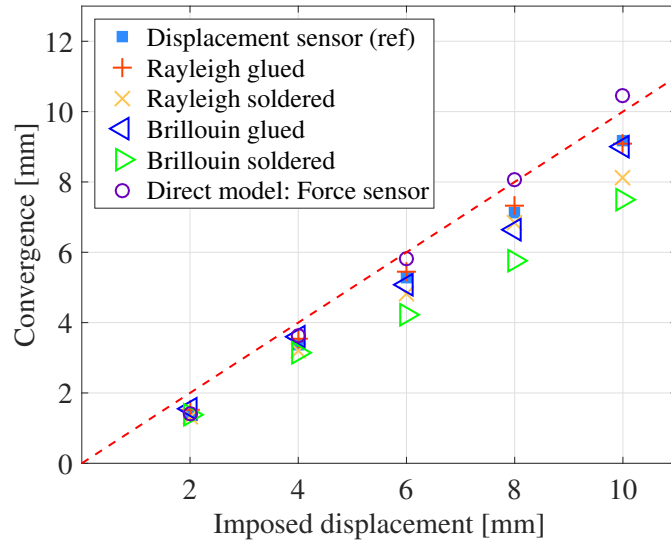
FIGURE 4.34: Absolute value of the convergence obtained with the different considered sensors for each imposed displacement level for the four-points configuration, in the direction of the load.
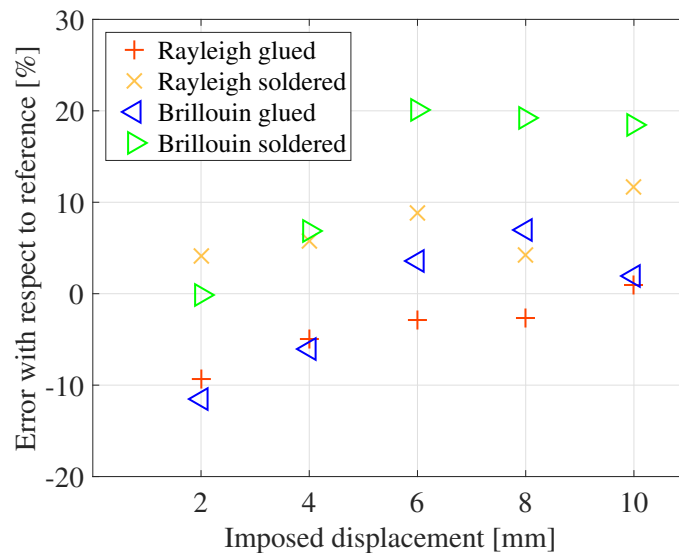
FIGURE 4.35: Percentage convergence error between the displacement sensor and the optical fiber based sensing, for the four-points case with the different considered sensors for each imposed displacement level, in the direction of the load.

4.6 Conclusion

This chapter validates the inverse-analysis finite-element method for convergence measurements, which transforms strain measurements obtained via distributed optical fiber sensors into convergence values. This validation has been performed on an experimental tests, where a mock-up of the HL waste repository cell, readapted for a laboratory test, has been instrumented and loaded to reach a maximum of 10 mm of convergence, the representative value for the compulsory 100 years of monitoring. In this test we have considered two configurations of loading and many other sensors to perform the comparison. A glued and a soldered configurations of the sensing cable have been considered, as well as both Brillouin and Rayleigh backscatterings. For the simplest loading case, where the structure is loaded along one direction, the optical fiber cable is able to obtain results with a resolution of 1 mm as required by the application, whatever the anchoring method or the backscattering choice. In fact, the most of the impact is given by the calibration of the sensor and the consideration for real position of the sensor on the structure. In the previous chapter we claimed that a higher number of sensing points reduces the measurement errors, we have then here shown how the preference to use distributed sensors by comparing the results with fiber Bragg gratings is confirmed. The comparison with commercial devices, also, revealed how our technique is competitive, concerning the results, but most of all is easier to exploit and it can be used autonomously, unlike some others. The difference between Brillouin and Rayleigh backscatterings is mainly visible on the strain measurements, as Rayleigh scattering obtains more regular results. This is however true as we perform the cross-correlation between subsequent measurements and not between each measurement and the reference, as it would give cross-correlation errors. The method is validated also in the more complex case, where aside from the loading there is a reaction in the orthogonal direction, hence we can state with confidence that the method can be used in more complex cases, with structures of whichever shape, as it is possible not only to calculate convergence but also the shape of the structure.
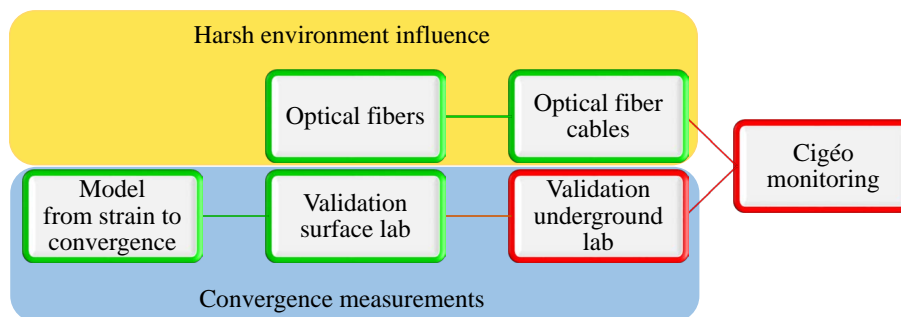
FIGURE 4.36: Schematic of the Ph.D. methodology: thanks to this test in controlled conditions, we have proven the capacity of our convergence measurement method to be robust and with a proper resolution for the application.

Chapter 5

Convergence measurement validation in Andra's underground laboratory

Contents

5.1 Introduction
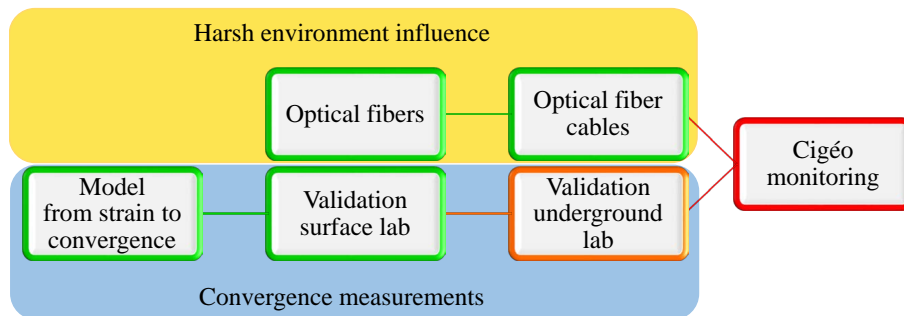
FIGURE 5.1: Schematic of the Ph.D. methodology: at this point, the convergence measurement method is here evaluated for validation in uncontrolled and real case conditions.

In the CMHM center, built in the same Callovo-Oxfordian clay layer and depth (100 m thick layer 500 m underground) as where Cigéo will be constructed, mock-ups of HLW and ILW-LL repository cells are built to carry out studies and tests that are helpful in order to setup the monitoring approaches for Cigéo. In Andra's underground laboratory, many galleries are built to follow various parameters with as many kinds of sensors. In the center, depicted in Fig. 5.2, some galleries are also instrumented with distributed optical fiber sensors for convergence monitoring, among other sensors.

The validation of the method is in these cases more complex: the uncertainty in the load distribution comes often together with the uncertainty linked to the location of the measurement points on the structure. An improved method, that would consider these two aspects as parameters, would be then useful to automatise the positioning of the strain measurement trace and the loading around the structure. Furthermore, measurements acquired in a uncontrolled environment, where the load is not imposed in a controlled way, can be more affected by fluctuations of strain and also temperature. The HLW repository cell, of dimensions close to the mock-up tested in
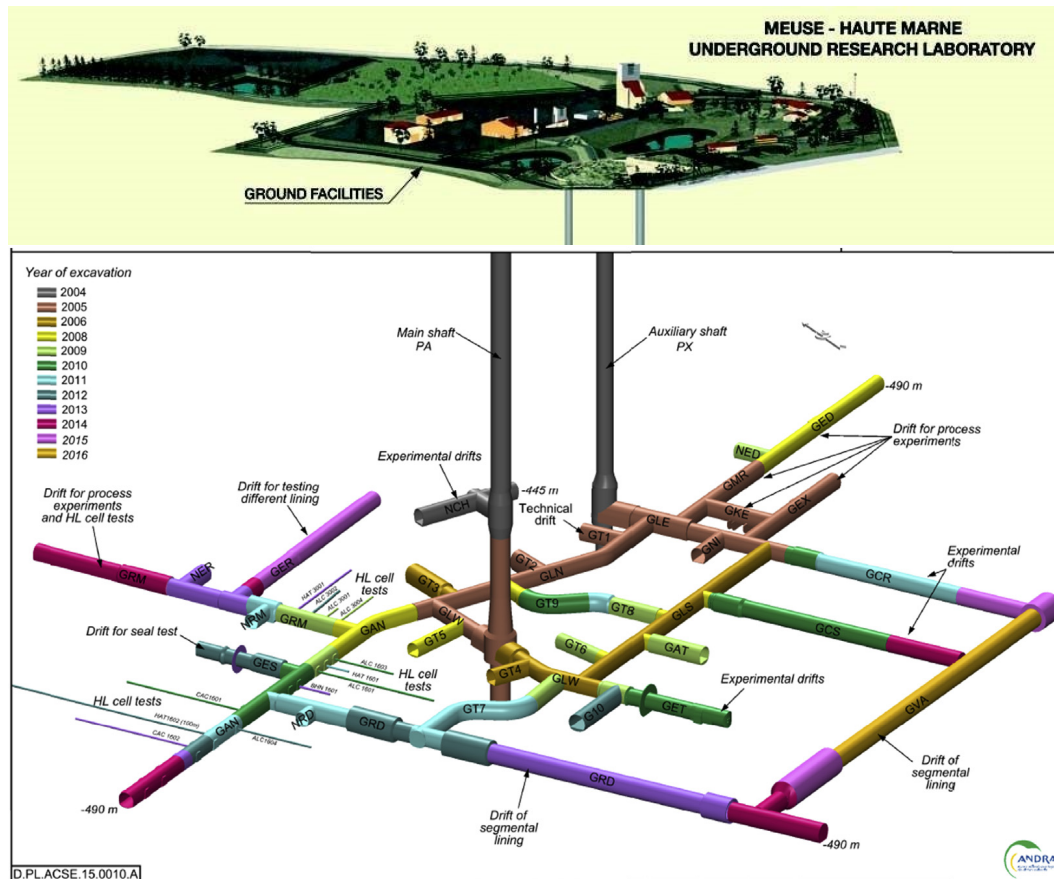
FIGURE 5.2: CMHM Andra's underground laboratory, with detail of the different
galleries.

Ch. 4, is for example loaded not simply by the rock, but by the filling grout, cement or bentonite, between the rock and the cell's casing (Fig. 5.3). The ILW-LL repository cell mock-up liner, instead, is made of concrete and subjected to creep and shrinkage which affect strain measurements (Fig. 5.4).

(A)
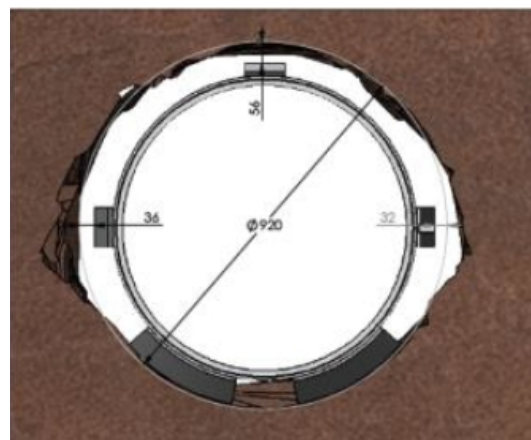
(B)

FIGURE 5.3: View of a HLW repository cell mock-up in the CMHM laboratory: the
steel liner is set up after the full excavation and the void between the casing and the
rock is filled with cement/bentonite grout.
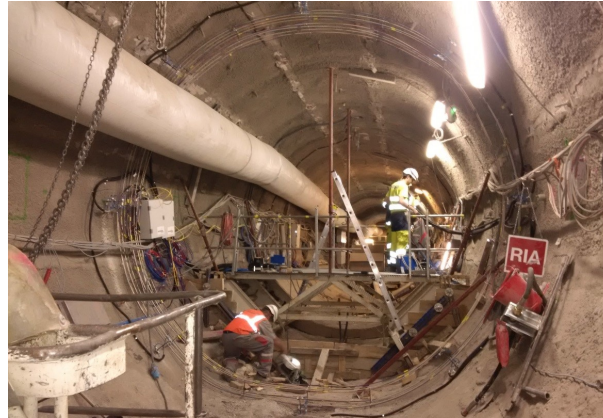
FIGURE 5.4: Construction of an ILW-LL repository cell, big as a railway tunnel and with concrete liner.

In both cases, the seasonal and daily thermal cycles cause the thermal expansion of the used materials, which reflects on the measurements acquired by optical fiber sensing cables. As a matter of fact, the cables are glued at the external surface of the steel liner of the HLW repository cells or embedded into the concrete liner of ILW-LL repository cells mock-ups.

This adds more complexity to the application of the method and the calculation of convergence, as it is not easy to discriminate the effect of all these elements. During this thesis, we have already started to evaluate underground measurements for an application to the convergence measurements method.

5.2 ILW-LL mock-up: GER gallery

In the underground laboratory many galleries are instrumented for different analysis and measurements. One gallery was built as mock-up of the ILW-LL repository cell, with many sections instrumented with different sensors. The gallery we consider is the GER (acronym for "Galerie d'Essais de Revêtements", which means "Gallery for lining tests", Fig. 5.2), where in fact the different linings, shotcrete and poured concrete, are evaluated and the mechanical behaviour is measured. This gallery is built along the minor principal horizontal stress σ_h, where the ratio of the vertical closure to the horizontal one is about $\rho_a = 4$. The gallery, after the excavation of the rock, is first lined by a layer of shotcrete. In a second time, the optical fiber cables are installed before the pouring of concrete, by the company Solexperts AG. The selected cables, put in the intrados and in the extrados part of the liner, at least 5 cm deep in the concrete, are fixed to some glass fiber supports to be sure the cable stays along the same circumference and at the same depth inside the liner (Fig. 5.5A). Each 45°, from the center of the vault, some vibrating wires of the SG2 type are installed alongside the optical fiber cables to work as strain reference. These are strain gauge sensors, whose thermal expansion properties are similar to those of concrete, the host material. As a consequence, this sensing method seems immune to direct temperature influence, whose example is shown in Fig. 5.5B. For comparison, it will be important to select those vibrating wires which are at the same depth of optical fiber cables inside concrete.

After the installation of the cables, the pouring of the concrete is done in two steps: first the tunnel invert, then the vault to complete the liner section. This is visible for example in Fig. 5.6A, where the cables comes out from the tunnel invert. More than one section is instrumented, in order to have redundancy in case a cable breaks or move. In Fig. 5.6B an example of an unsuccessful cables installation is shown: during the curing of the tunnel invert concrete, the cables were moved away from the supports limiting their utility. This shows one of the main difficulties when measurements must be carried out in a construction site.

(A)   (B)
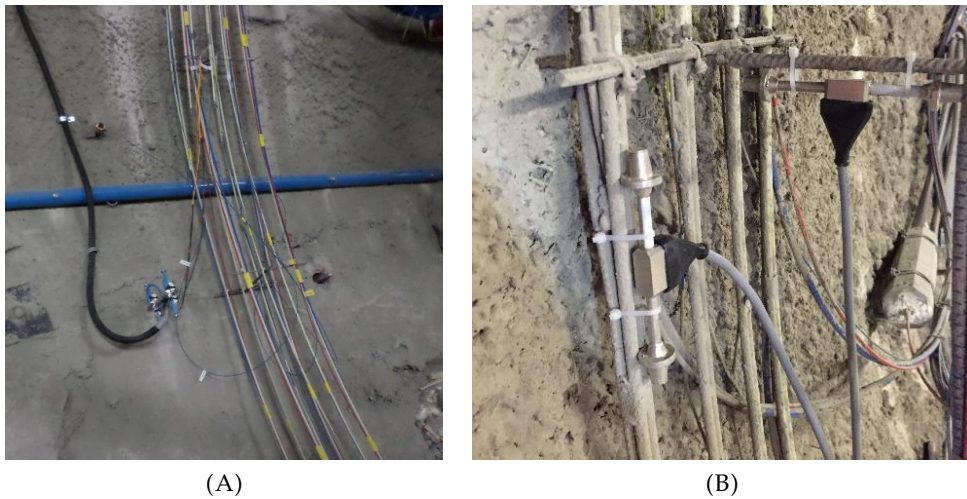
FIGURE 5.5: GER gallery in construction instrumented with optical fiber sensing cables and vibrating wires.

(A)   (B)
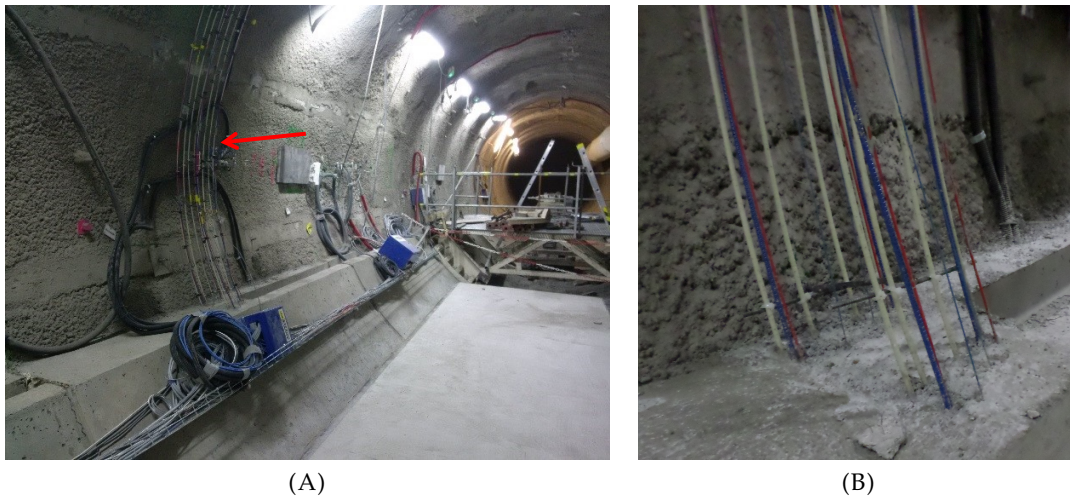
FIGURE 5.6: GER concrete pouring: the invert is firstly poured, fixing the position of the cables (A). Example of a difficult cables' installation in the CMHM laboratory (B).

Measurements on the strain sensing cables, a V3 from the company Solifos AG (Fig. 2.15B) and the AFL cable (Fig. 2.14), are acquired thanks to a BOTDA sensing system via the DiTeSt interrogating unit from the company Omnisens SA. Measurements are automatically acquired with a spatial resolution of 1 m and a sampling interval of 50 cm every hour, in order to follow the behaviour of all points in the circumference over time. A cable of 40 m is installed, which covers the length of the whole section (for a section long ∼20 m and of 5 m of diameter) and the amount of cable necessary to reach the general box where another cable is connected to the acquisition instrument. This leads to about 800 m of total distance range, which is way more than the needed measured distance. In Fig. 5.7A an example of a raw measurement is shown. The zone of interest is only the part in the middle, highlighted in Fig. 5.7B. Within these 40 m, it is necessary to identify the start and end points of the gallery's section, to analyse the strain around the structure.

This is important not only to select which are the strain values to consider, but also to have a correspondence between measurements and structure's coordinates to calculate convergence. To allow the recovery of the localisation of measurement traces, two specific points of the cable inside
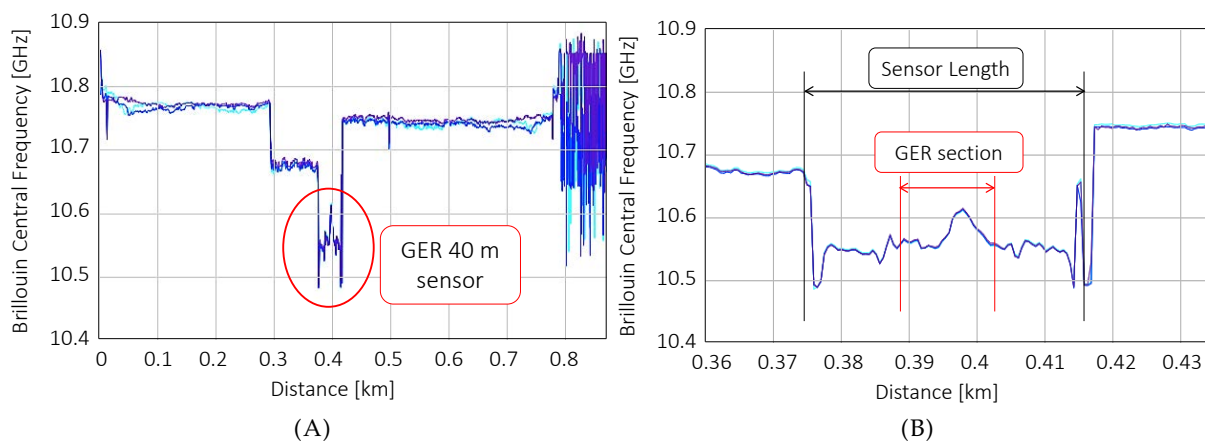
FIGURE 5.7: Examples of Brillouin central frequencies along the optical line which reaches a section in the GER gallery. In (B) the focus on the 40 m of sensor which are used to measure the GER section.

the section have been heated before the concrete pouring by the technicians in the construction site, causing a recognisable frequency shift along the trace. However, with a spatial resolution of 1 m, it is not possible to precisely define the exact start and end points in the section with this method. Without the possibility to access the cables and dealing only with strain measurements acquired by others, we can only perform an estimation on the measurement location, which is however not enough to obtain accurate convergence results. It is indeed complicated to have certain knowledge on the spatial position of the possessed measurements when these are acquired in a real environment. The installation must, in this sense, be carefully programmed to avoid this issue defining, for example, more of these "spatial recovery" points. The fact that the mock-up construction and instrumentation are not always performed and followed by the same people who will post-process the data, as it was the case here, can also take to lacks of information if reports are not properly done. Furthermore, some faults of the acquisition system led to even more trouble in the determination of the GER section location. The required change of the instrument took to a shift of a couple of meters of the strain trace for a certain period of time, further complicating the data analysis.

The spatial localisation of strain traces is thus the most important and, at the same time, the most difficult operation to be done in order to properly exploit measurements. Once we were able to have an idea of where the section is located within our measurements, it is possible to explore what can be obtained with such information. After the instrumentation of the considered gallery in mid-2016, we have started to analyse measurements that go from early 2017 to early 2019, in order to check the behaviour of the structure and eventually apply the method for convergence measurement. We have ignored one year of measurements to avoid the most of the concrete creep and shrinkage.

Considering for example the V3 type cable, whose datasheet is in Annex A, at the intrados of one of the instrumented sections, we can plot the obtained orthoradial strain traces along the circumference at different dates as a function of the position (Fig. 5.8A) or as a function of time (Fig. 5.8B). From these graphs it is possible to see two things: from Fig. 5.8A, where each trace represents a different date, no evident shape is visible, which could mean that the rock is not yet loading the structure. This is even clearer looking at Fig. 5.8B, where each trace represents a point in the circumference. They have the same distribution along the two years, which is mainly due to the alternation of hot and cold seasons. Temperature inside the galleries can in fact change daily, with a variation between 3.6 °C and -2.7 °C, while the seasonal change can take the temperature from 30 °C to 12 °C as a maximum variation, depending on the area of the section. Considering
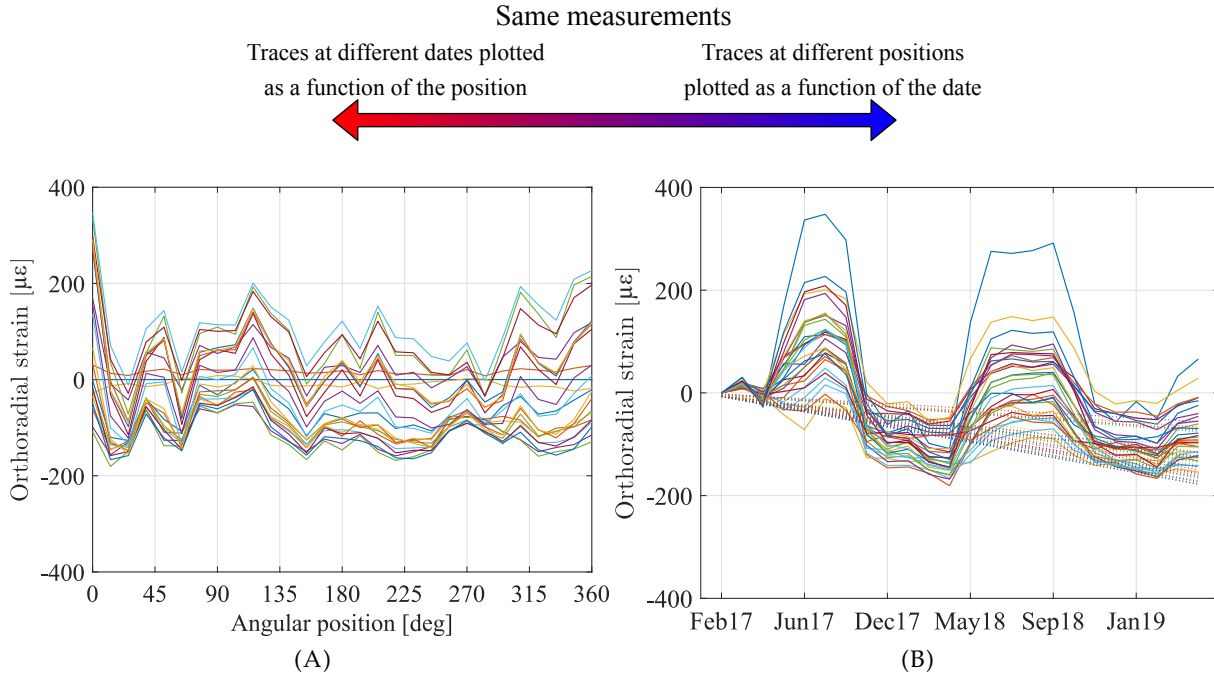
FIGURE 5.8: Orthoradial strain traces for the ILW-LL repository cell mock-up at the intrados along the circumference at different dates as a function of the position (A) or of time, where the tendency of the traces is shown (B).

for example a mean variation of 10 °C between the hotter and the colder temperature between seasons, using $C_T = 2$ MHz/°C as temperature sensitivity and $C_\varepsilon = 0.05$ MHz/με, we obtain an overall strain of 400 με, which is in the same order of magnitude of the measured values. Nevertheless, there are also variations linked to the ventilation system (different at weekends, or during excavations) and also inside the concrete where there is the combination of the thermal expansion of materials. The slight general slope towards negative strain along time, highlighted in pointed lines, could then be due to the shrinkage in concrete, which is the main source of strain in the early period of the construction. The same is visible comparing these results with those of some of the vibrating wires installed in the same section and at the same depth inside the concrete. Considering the orthoradial strain at each of the four quadrants acquired from these two types of sensor, we can first compare the trend of optical fiber strain sensing cables and the vibrating wires strain, in Fig. 5.9A. From experimental tests, it has been studied that two years of shrinkage take to around -120 με inside the concrete, which is perfectly in line with vibrating wire results. Although optical fiber-based values are not strictly the same, the results of the two sensors are comparable being in the same order of magnitude. If we subtract the original strain, instead, we obtain the result plotted in Fig. 5.9B. As the vibrating wires strain response is only influenced by temperature induced strain in the concrete, it is sure that this behaviour is linked to temperature seasonal variations. In order to obtain proper strain measurements it would be then necessary to i) discard shrinkage effects in the concrete and ii) neglect temperature influence. For the first point, it is necessary to wait for the concrete to settle and, most of all, for the rock to begin to induce a preponderant strain. Although at the beginning of this Ph.D. we have started some research to take into account concrete shrinkage and measure it with optical fiber cables (Annex C), its complex nature pushed us in another direction, to focus more on the sensor itself.

Regarding the temperature influence on strain measurements, it has been seen that a simple compensation of temperature done by multiplying temperature values (acquired with other sensors) to the temperature sensitivity coefficient of the sensor was not enough. In fact, the thermal
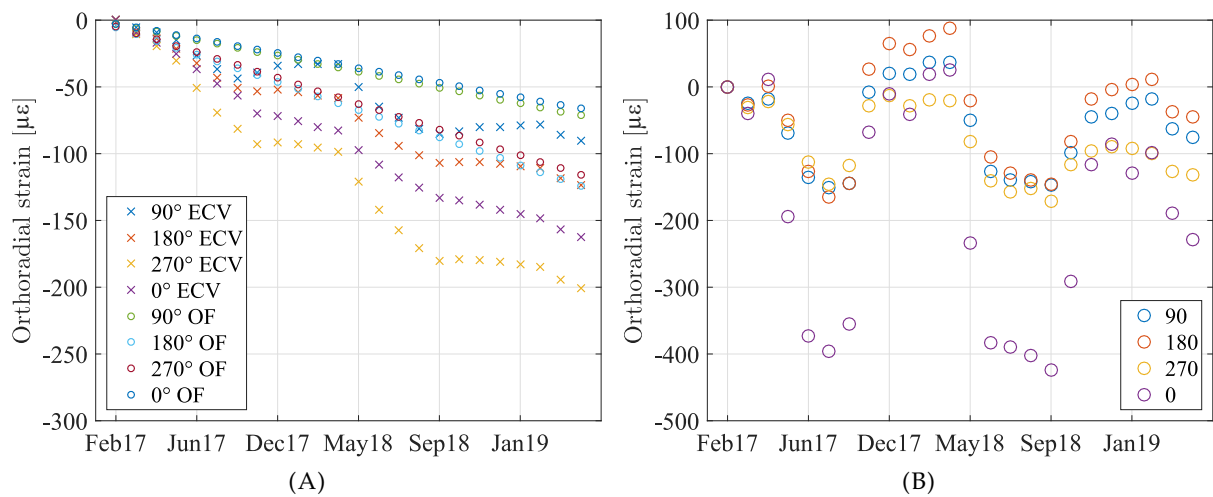
FIGURE 5.9: Comparison between the orthoradial strain of vibrating wires (ECV)
and optical fiber strain sensing cables (OF) in a ILW-LL repository cell section (A)
and their difference (B).

expansion of the structure's materials and, also, of the sensor's materials, complicate the discrimination between temperature and rock loading impact on measurements.

For all these reasons, it appeared premature to search for convergence results relying on these measurements without a proper prior data treatment. It would be necessary, in the future, to concentrate on these aspects here ignored, due to lack of resources, to obtain something meaningful.

5.3 HLW mock-up

In another gallery, the GAN (standing for "Galerie d'Accès Nord", i.e. "north access gallery", in Fig. 5.2), some mock-up cells are built to simulate the HLW repository cells behaviour under the rock pressure (Fig. 5.10).

FIGURE 5.10: HLW repository cells mock-ups in the CMHM underground laboratory.

They are built orthogonally to the gallery, going along the major principal horizontal stress σ_H, for which the ratio of the vertical closure to the horizontal one is about $\rho_a = 0.5$ [Guayacán-Carrillo et al., 2016]. These mock-ups are instrumented with different sensors, among which a portion of 2 m is instrumented with an optical fiber cable for convergence monitoring and some displacement sensors for reference measurements. As visible in Fig. 5.11, the mock-up is instrumented before being taken underground and then installed in place by the company Solexperts. The optical fiber strain sensing cable is from Neubrex and it was specifically developed for the

(A)   (B)
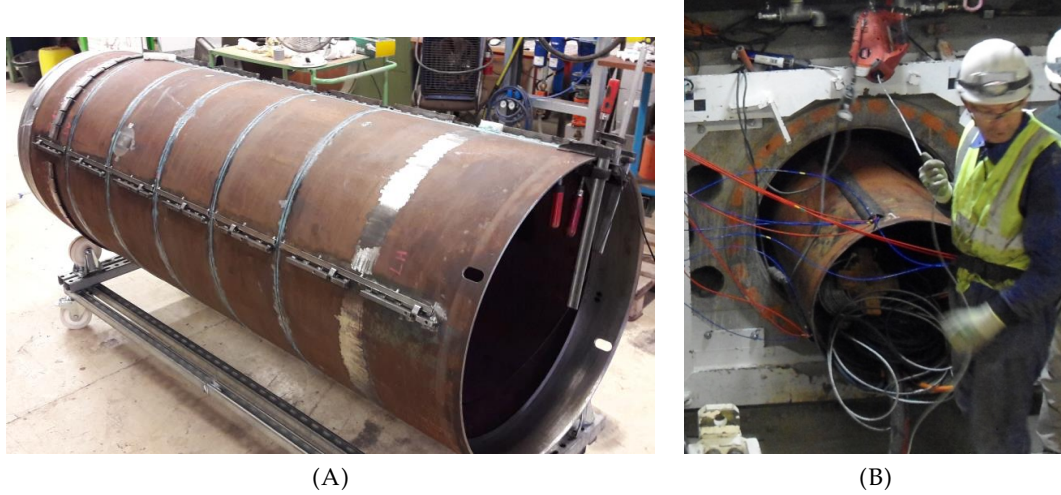
FIGURE 5.11: Instrumented HLW repository cell mock-up for strain measurement acquisition, during instrumentation and in-place.

application starting from the Embossed FN-SILL-3 strain and temperature sensing cable (details in Annex A). This strain and temperature sensing cable, the Embossed FN-SILL-4, is a flat cable with one single-mode fiber and a multi-mode fiber, in order to be able to discriminate the effects of strain and temperature. The cable is glued in an helical shape around the structure, performing five complete rounds around 1.4 m on the external surface of the 2 m portion of the mock-up. Measurements are acquired with the Neubrescope NBX-7020 from the company Neubrex Co. Ltd, with the PPP-BOTDA and TW-COTDR techniques and a spatial resolution of 10 cm, with a frequency that goes from every 40 minutes in the early stages to every 6 hours when the behaviour of the loading is more regular. The automatic measurements acquisition parameters (in Tab. B.8) and rate were decided by a colleague in Andra in collaboration with Neubrex. Brillouin frequency shifts are obtained by simply subtraction of the Brillouin central frequencies, while we have considered a measurement each 20 days to perform cross-correlation on Rayleigh raw measurements to obtain Rayleigh frequency shifts. The total optical line, from the instrument to the mock-up and back, is 719 m long, while the considered section is about 12 m long. An example of frequency shift obtained in the first 20 days of stable loading on the structure is represented in Fig. 5.12, for Brillouin (Fig. 5.12A) and Rayleigh (Fig. 5.12B) scatterings.

Considering the highlighted part of the traces, the 12 m for convergence monitoring, we use the strain sensitivity coefficients given by Neubrex, $C_\varepsilon^B = 0.047$ MHz/µε for Brillouin and $C_\varepsilon^R = -0.1485$ GHz/µε for Rayleigh scatterings, to obtain strain measurements from the acquired frequency shifts. For simplicity, we ignore the impact of temperature, as seasonal thermal cycles are less important on the metallic liner. From the 20th of December 2018, one month after the mock-up installation, to the 30th of July 2019 we obtain the strain in Fig. 5.13. Strain traces are coherent with the conclusions on Brillouin vs Rayleigh reported in Section 4.4.2. Rayleigh-based strain traces are less noisy than Brillouin, thanks to the cross-correlation technique. A cross-correlation each 20 days was enough to obtain proper measurements as the strain grows slow over time. It
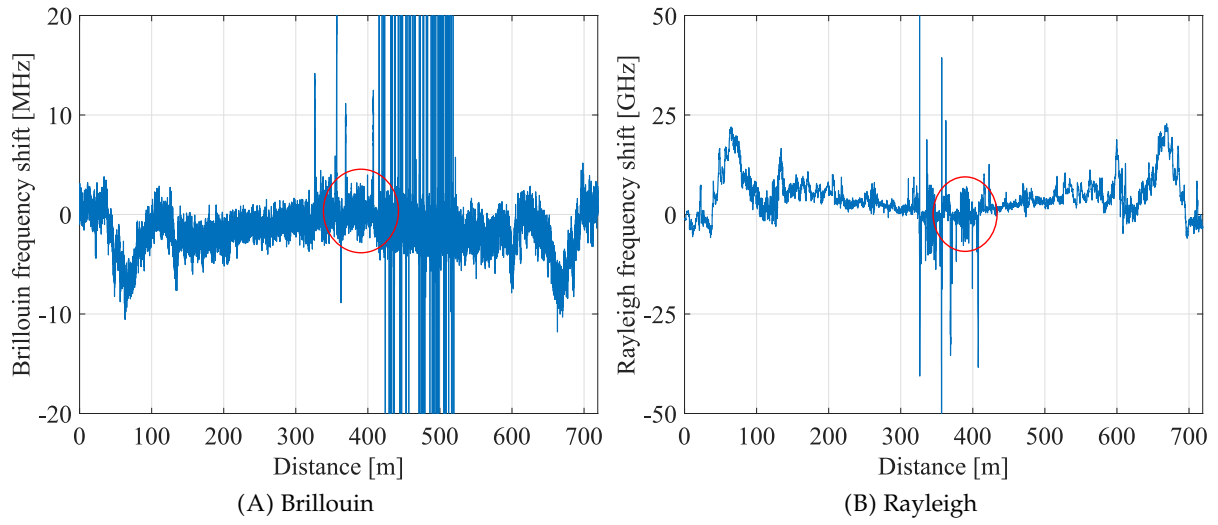
FIGURE 5.12: Example of frequency shift obtained from the optical fiber strain sensing cable for convergence monitoring anchored around an underground mock-up of the HLW repository cell in Bure. A red circle is around the portion of cable considered for the convergence analysis.

is however important to consider this factor, as in case of higher strain it would be necessary to consider a smaller period of time, which would lead to a great amount of data to process. Brillouin data is, for this reason, more immediate to use to understand the behaviour of a structure.
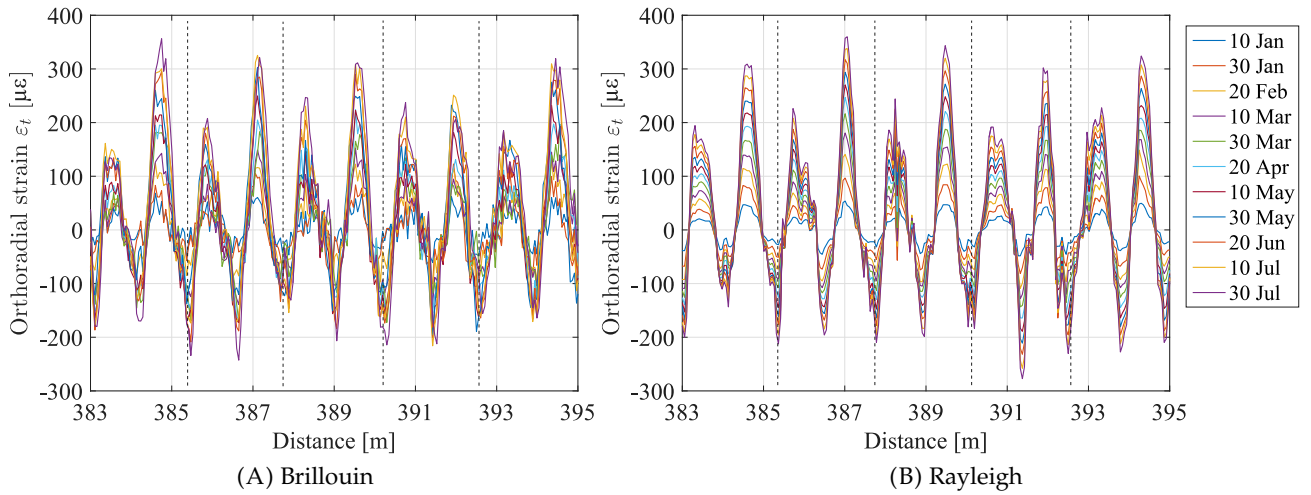
FIGURE 5.13: Orthoradial strain values over the five rounds of optical fiber strain sensing cable on a mock-up of HLW repository cell.

The resulting strain can be divided into five parts, each of them representing the same load behaviour linked to the five spires. Each of them reports a double sine wave, similarly to Fig. 4.6 and 4.7. There is compression in the vertical direction and elongation in the horizontal, giving a reduction of the vertical diameter. In order to obtain the best and most representative results, we select the most regular portions of spires to be given as input to our convergence measurement method.

The load scheme used for this simulation is represented in Fig. 5.14, where $\sigma_x = \alpha \cos(\theta)$ and $\sigma_y = \beta \sin(\theta)$, α and β being the amplitudes of the distributed pressure to be found and θ the angle

around the structure.
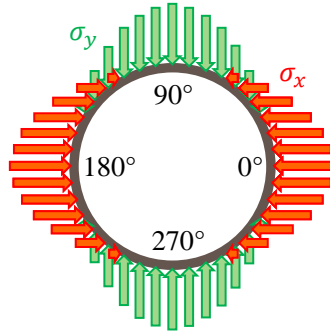
FIGURE 5.14: Scheme of the loading imposed for the HLW repository cell mock-up.

The simulated strain calculated with the finite element method is interpolated on the experimental measurement in order to perform the error minimisation. In fact, we want to find convergence all around the section, thus simulating a load with unitary amplitude which gives us the result in Fig. 5.15A. However, the spires in Figs. 5.13 are in a different shape around the structure and start from the top of it (90° in Fig. 5.14), thus we consider the simulated strain along the spire as in Fig. 5.15B, interpolating the section values over the experimental spire coordinates.
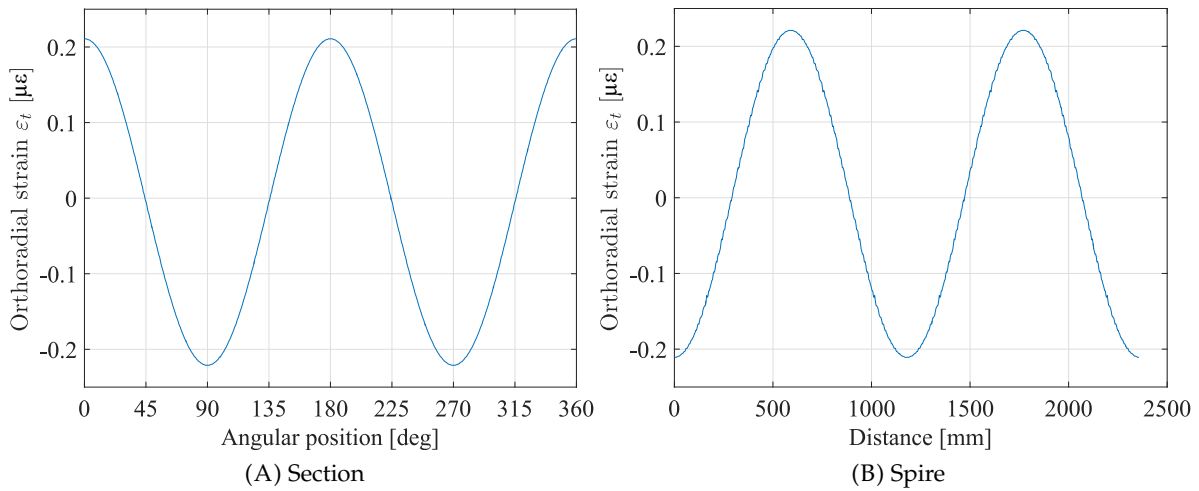
(A) Section

(B) Spire

FIGURE 5.15: Strain obtained by simulating a unitary amplitude loading over a section (A) and strain interpolated over the length of one of the spires (B).

Minimising the error between the simulated and experimental strain over the same portion of spire, an example of the obtained results is represented in Fig. 5.16. The amplitude of σ_x, α, is zero and therefore there is only σ_y, with β growing along time.

Doing the same for the same portions of different spires, each optimal and theoretical applied force is obtained and the convergence values are calculated. Averaging the results to obtain one value for each date, we obtain convergence all around the structure's section as, for example, depicted in Figs. 5.17A and 5.17B, where convergence is calculated every 20 days. The comparison with standard displacement sensors measurement shows how the convergence method using optical fiber strain measurements is able to obtain good results. This is truer for the Rayleigh scattering-based sensing technique, where strain is less noisy thanks to the used cross-correlation approach.

Focusing only in the vertical and horizontal direction, we follow convergence over time for both Rayleigh and Brillouin-based sensing techniques, obtaining the results in Figs. 5.17C and
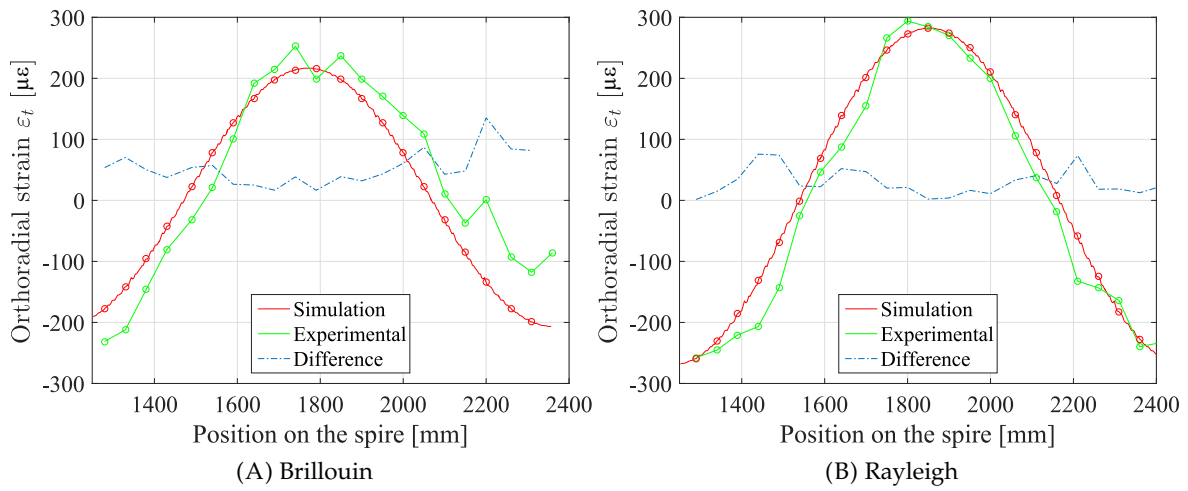
FIGURE 5.16: Comparison between the optimised and experimental orthoradial strains after 7 months loading of a HLW repository cell mock-up.
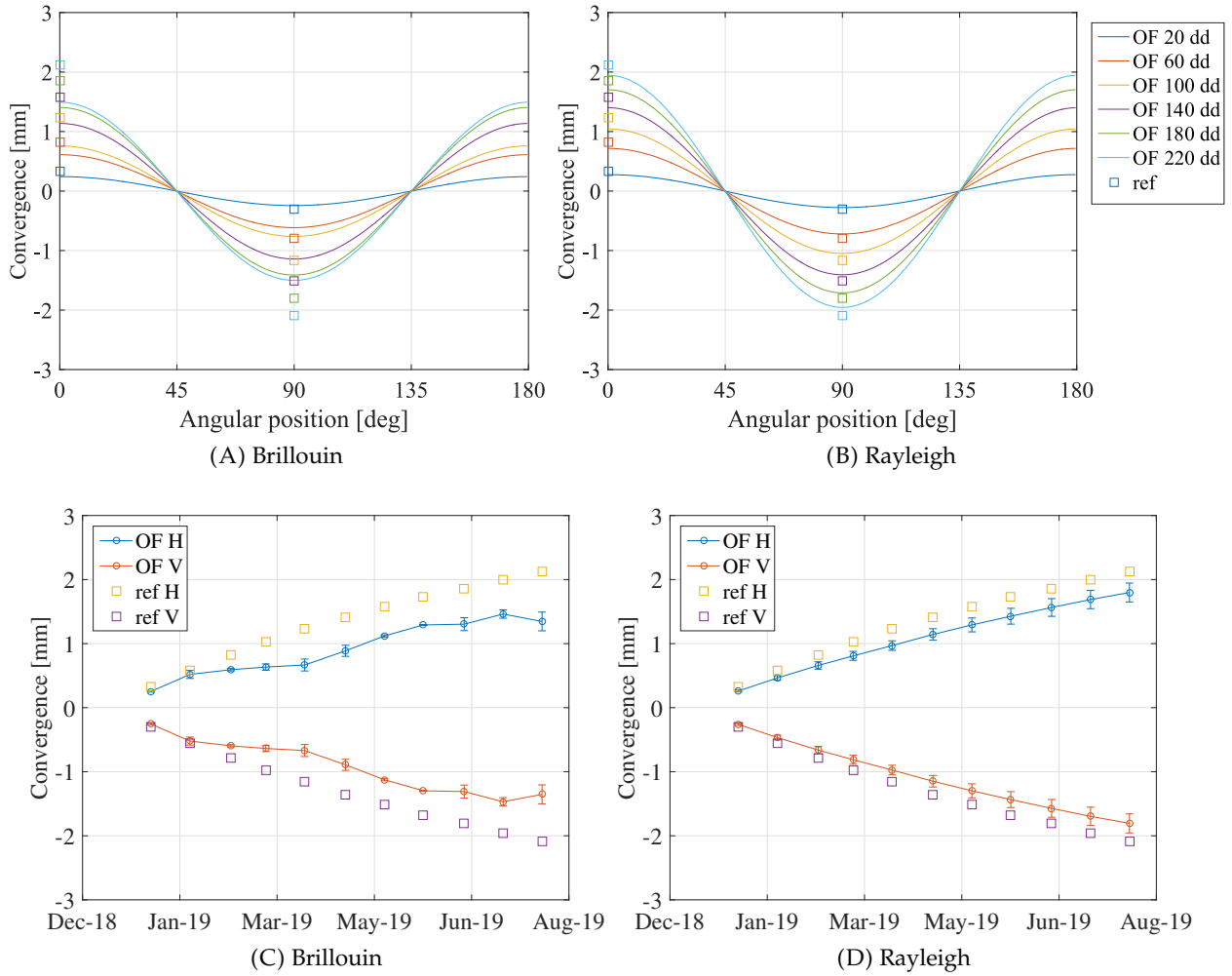
FIGURE 5.17: Reference and optical fiber strain sensing cable convergence results all around the section (A and B) and in the vertical (V) and horizontal (H) direction (C and D) of the HLW repository cell mock-up in Andra's underground laboratory.

5.17C. The error between the reference values and the ones obtained via optical fiber sensing is about 15% for Rayleigh scattering, while 25% in average for Brillouin scattering. The error bars represent the dispersion of the results.

At this point, we have demonstrated that our convergence measurement method can be applied also in-situ, having a little more attention into considering the non-controlled environment and the possible noisy measurements.

5.4   Conclusion

In this chapter we have dealt with the final step for the validation of the method for convergence measurement on repository cells. Considering strain measurements from optical fiber strain sensing cables, already acquired in a ILW-LL and a HLW repository cells mock-ups of Andra's underground laboratory, we have tried to use them as input to our convergence measurement method.
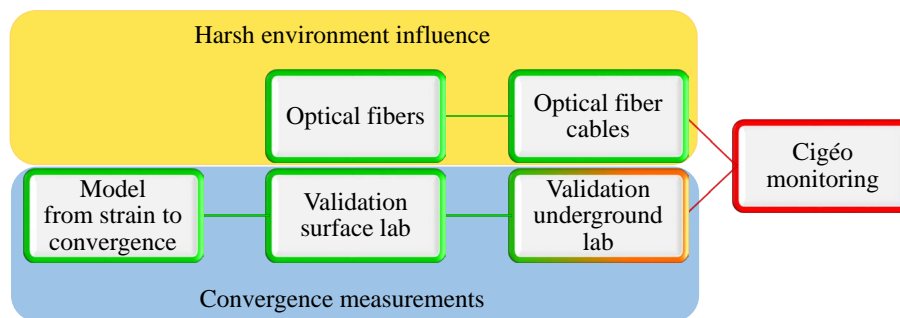
FIGURE 5.18: Schematic of the Ph.D. methodology: the convergence measurement method is here validated for HLW repository cells mock-ups, while for ILW-LL cells a deeper analysis must be performed.

For the ILW-LL repository cell mock-up, made of a concrete liner of 6 m in diameter and instrumented with a V3 strain sensing cable from Solifos, the main issue is related to the nature of the materials and the uncertainties on the loading distribution. The concrete shrinkage appears to contribute to the majority of the strain to which the structure is subjected, making it difficult to identify the impact of loading looking at strain values. The temperature seasonal variation, moreover, influences a lot the strain results. Not only temperature itself impacts on measurements, but it induces thermal expansion on the structure's and sensor's materials, making the discrimination of strain and temperature influences more difficult. For this reason, we did not apply our convergence measurement method to these measurements in their actual state, acquired with a BOTDA interrogation device from the company Omnisens. A more careful measurements post-processing is needed to achieve proper results.

Regarding the chosen HLW repository cell mock-up, a steel tunnel of 762 mm of external diameter and 25 mm thick, the materials are easier to deal with, at least considering the first years after the structures' construction. Raw measurements, acquired with the same Neubrescope used in the whole thesis and using both Brillouin (PPP-BOTDA technique) and Rayleigh (TW-COTDR technique) scatterings, reveal a clear behaviour. The double sine wave confirms the expected loading, which leads to the reduction of the size of the cell in the vertical direction. The strain, that grows over time due to loading, can be then used for convergence calculation, obtaining 2 mm of convergence and a good comparison with reference sensors especially with Rayleigh scattering-based results. Despite the actual need of selecting manually the measurement to be analysed, this is a very good result to state that the developed convergence measurement method can be used in-situ once it is generalised.

Conclusion

This thesis assesses the use of distributed optical fiber sensors for convergence measurement in the harsh environment of Cigéo, the future French underground repository for high-level (HL) and intermediate-level long-lived (IL-LL) radioactive waste. Two main goals were considered: i) the evaluation of the impact of harsh environment on distributed optical fiber sensors, and ii) how we can exploit their strain measurements to obtain convergence values, i.e. following the reduction of the structure's section size. This was evaluated under the use of both Brillouin and Rayleigh scatterings, using two main techniques: the Pulse Pre Pump Brillouin Optical Time Domain Analysis (PPP-BOTDA) and the Tunable Wavelength Coherent Time Domain Reflectometry (TW-COTDR).

Regarding the first topic, we have considered two new research paths in the evaluation of harsh-environment influence on distributed optical fiber sensors: one focused on optical fibers in primary coating, one on a complete strain sensing cable.

Distributed optical fiber strain sensing based on Brillouin and Rayleigh scatterings is known to be compatible with harsh environment, such as in presence of radiation, if a proper optical fiber dopant is selected. Fluorine doping, for example, improves the fibers' radiation resistance, with reduced measurement uncertainty and higher total distance range than standard Ge-doped fibers. In the vast majority of the past researches, however, the impact of different agents present in an environment as Cigéo, for example the temperature and the γ-radiation, is evaluated separately whereas ageing processes on-site might not be independent one from another. The hypothesis of independence between environmental factors had then to be verified. With the help of the IRMA ^{60}Co facilty of IRSN (Saclay, France), we have organised an ageing test where both temperature and γ-rays influences have been imposed, at the same time, on optical fibers in their primary coating. During the test, Brillouin and Rayleigh scatterings traces were acquired online (during the irradiation process) to avoid the error brought by the recovery effects on the fiber that occur once irradiation is over.

We have here evaluated the coupled influence of temperature up to 120 °C and radiation up to 1 MGy on two types of optical fiber: one standard, germanium doped, the other fluorine-doped, both with a polyimide coating to withstand high temperature. The considered temperature and radiation values are representative for the target one hundred years of monitoring of an high-level waste repository cell. Apart from confirming the choice of the fluorine-doped fiber for radiation hard sensors, we have observed that temperatures around 100 °C reduce the impact of radiation on the fiber attenuation, allowing a longer maximum distance range. The reachable sensing range doubles or even triples at higher temperatures with respect to samples at room temperature. The radiation induced frequency shift is however not impacted by temperature, and the values remain small. For F-doped fibers, the error after 1 MGy is in the order of 20 $\mu\varepsilon$ for Rayleigh scattering (-3 GHz) and 40 $\mu\varepsilon$ for Brillouin scattering (2 MHz). These values agree with previous tests performed with the same scatterings but different techniques, for example Rayleigh OFDR, confirming the dependence of the results on the physical scattering process regardless of the interrogation technique and instrument. This experimental test allowed for the first time to properly assess how Cigéo foreseen conditions will affect the lifespan of optical fiber sensors, finding them suitable for the application. Knowing the radiation induced frequency shift on Brillouin and Rayleigh scatterings, we have combined this information to more deeply identify and, especially, quantify the physical process that generates this phenomenon, linked to light propagation. Radiation impacts

on the refractive index of the optical fibers, which concerns both scatterings, while Brillouin scattering suffers also from the acoustic velocity variation. Despite this variation is very little, around 1 m/s after 1 MGy, the effect is still present.

At this point, optical fibers must be inserted into specific cables in order to be used in civil engineering structures as Cigéo will be. Thanks to the MODERN2020 European project, a strain sensing cable specific for the application was developed and produced. The considered cable, a strain sensing cable of the V9 type from the company Solifos AG, includes the designed F-doped fiber for radiation hardening and a high-temperature acrylate coating instead of a polyimide coating to respond to fabrication requirements. The fiber was inserted in the cable, made of an external polyamide layer and an inner metal tube to increase the mechanical resistance, and also in the metal tube itself only (called FIMT). These two cables were irradiated as well in the same irradiation campaign at the IRMA ^{60}Co facility, reaching a total dose of γ-radiation up to 500 kGy. Once irradiated, these cables were analysed and characterised post-mortem under Brillouin and Rayleigh scatterings in the Solifos laboratory, where I have spent two months of my secondments within ITN-FINESSE. They were compared not only with the same types of cables before being irradiated, but also with standard V9 type samples provided by the company. Many tests have been carried out, mainly mechanical tests to assess the cable behaviour when in use. These tests were meant to determine the impact of the protective layers on the cable behaviour and, most of all, the impact of radiation. To the best of my knowledge, this is the first ageing test realized on a real sensing systems, on a commercial cable paired with a commercial opto-electronic unit. According to our results, radiation appears to impact mainly the polyamide external sheath of the V9 type cable, reducing its ductility and taking to early cracks and breaks. The difference between irradiated and not irradiated samples regarding measurement errors, in this case represented by the computation of the strain sensitivity coefficients, is lower than 5%, hence negligible for our application. A greater influence is to attribute to the protection layers, which change the sensitivity of the optical fiber sensor, going from the bare fiber to the complete cable, of about 10%. The same is found for the temperature sensitivity of the considered optical fiber strain sensing cable: coefficients values are very close to each other between irradiated and not irradiated samples, while the major difference is due to the external sheath and the influence of their different dilatation coefficient. Despite in this thesis we have not considered the influence of temperature on Brillouin and Rayleigh frequency shift, dealing always with controlled environments, this information is fundamental to analyse on-site measurements. From the same measurements used to assess the strain sensitivity of the samples we can evaluate their elasto-plastic behaviour. In fact, the presence of polyamide and steel lead the sensor to show a plastic behaviour after 2000 $\mu\varepsilon$, which is the elasto-plastic limit for steel. After reaching the 10,000 $\mu\varepsilon$ of imposed strain, the cabled samples are subjected to residual strain, from 1300 to 2000 $\mu\varepsilon$, even if the sample is relaxed and not elongated, which is not negligible for some applications. This behaviour is practically unchanged in accelerated ageing conditions, staying the same whether the sample absorbed a radiation dose or not.

These results, first on optical fibers in primary coating and then on optical fiber strain sensing cables, show that radiation appears to have a low impact on distributed optical fiber sensors, when using both Brillouin and Rayleigh scatterings. Overall, this proves their suitability for long-term monitoring in harsh-environment.

Once the sensing system is validated, we can move on to the description of how to use this kind of sensor to measure convergence. In all types of horizontal tunnels, therefore also in Cigéo radioactive waste repository cells, convergence is one of the main problems as the reduction of the section's size over time interferes with their operability. Thanks to optical fiber sensing cables it is possible to measure many structural parameters, however convergence cannot be measured directly in this case. Considering an optical fiber strain sensing cable which is installed around the structure's section in one or more rounds (in section or helix), it is possible to use the acquired orthoradial strain along the sensor to calculate convergence values. Starting from a basic

finite-element model, we have added an inverse-analysis approach that minimizes the error between the experimental strain of the structure and the one calculated with the numerical model. Starting from the mesh of the structure and knowing the direction of the load, this minimization determines the magnitude of the load applied to the physical structure, which is necessary to find the loaded structure's new coordinates and convergence values, knowing the original conditions. This method is able to achieve convergence all around the structure without dead zones and it can be used also for other structural shapes, differently from other methods that works better with few measurement points and mainly with curved bars as MEMCOT [Barbosa et al., 2009].

Once developed, we have evaluated the performances of the method. We have assessed the importance to build a mesh that represents at its best the behaviour of the structure, without overloading the calculations, and how the structure's diameter and thickness homogeneity plays an important role in the accuracy of results. We have also evaluated the impact of uniform noise and the number of measurement points, highlighting that, while the error remains under 3%, a higher number of measurement points decreases the error and its standard deviations. This means that it is preferable to use distributed sensors rather than local ones in order to obtain better results.

Afterwards, we validate the developed inverse-analysis finite-element method for convergence measurements on an experimental test. A readapted mock-up of the HLW repository cell, a steel ring of about 80 cm in diameter and 10 mm of thickness, has been instrumented and loaded to reach a maximum of 10 mm of convergence, the representative value for the targeted first one hundred years of monitoring. The structure was instrumented with two portions of the same type of optical fiber strain sensing cable, the previously characterised V9 type from Solifos, in this case with a standard Ge-doped fiber inside. These two portions were anchored to the mock-up in two different ways, glueing one part all along its length and punctually soldering the other part every 4 cm. Both Brillouin and Rayleigh scatterings-based interrogation techniques were considered as well. Other sensors have been also considered: displacement and force sensors as reference sensors, some fiber Bragg gratings and two commercial shape sensing systems. In this test we have considered two configurations of loading, representative, with more or less accuracy, of the application case.

For the simplest loading case, where the structure is loaded along one direction simulating a vertical loading of the rock, the developed convergence measurement system is able to obtain results with a resolution of 1 mm as required by the application, whatever the anchoring method or the backscattering choice. Regarding the measurement accuracy, Brillouin scattering takes to a convergence error with respect to the reference displacement sensor of around 10%, while Rayleigh scattering results have an error compared to the target value of <5%. This result derives from a good cross-correlation performed between Rayleigh raw measurements, needed to obtain frequency shifts and, consequently, strain values. In fact, to obtain good Rayleigh results, we had to perform cross-correlation between subsequent measures to minimize the strain difference. For the same reason the difference between Brillouin and Rayleigh scatterings-based techniques is mainly visible on strain measurements results, as Rayleigh scattering obtains less noisy results but with error peaks due to cross-correlation. In general, the main difference between results is not given by the technique itself but by the calibration of the sensor and the consideration for the real position of the sensor on the structure. Concerning the calibration, a variation of the strain sensitivity coefficient around 10% for Brillouin and around 3% for Rayleigh scatterings leads to a convergence error close to zero. Then, the correspondence between distributed strain measurements and coordinates of the structure is always tricky, needing a careful attention in the installation of sensors (for example heating punctually the cable to have position references). The distributed nature of measurements however helps reducing the error linked to malpositioning. It is hence more problematic to go wrong, of the same amount, in the positioning of local sensors, such as FBGs for example. We have installed eight punctually soldered FBGs and four glued FBGs in the proximity of the V9 type strain sensing cables, in order to compare our approach with results obtained using a punctual optical fiber sensor, which is also the most commonly used optical

fiber-based sensor in the market. Applying the acquired FBGs strain measurements to the convergence measurement method, we can confirm the fact that a higher number of sensing points reduces the measurement errors. The error in the loading direction between the displacement sensor and the FBGs was of about 30% for the glued sensors and 40% for soldered ones, which is too much for the application. A proper reason for this behaviour, however, has yet to be verified. Lastly, we have compared our convergence results from distributed optical fiber strain sensing with two commercial devices for shape sensing, from Sensuron and Morphosense companies, to check whether our sensing system can compete with products already present in the market. This revealed not only that our technique is competitive from the convergence values point of view, but most of all it is easier to exploit than Sensuron, it can be used autonomously and without the presence of the sensing system technicians as Morphosense, which is moreover a bit intrusive and not confirmed to be radiation proof.

The method was validated also in the more complex case, where aside from the vertical loading there are two reaction forces in the orthogonal direction, one at each side of the diameter. Despite a reduced accuracy in the results with respect to the imposed values of convergence, distributed strain sensing-based convergence values were close to the reference displacement sensors. We can therefore state with confidence that the method can be used in more complex cases, with structures of whichever shape, as it is possible not only to calculate convergence but also the shape of the structure.

Finally, a more representative validation of the method is being performed by applying it to strain measurements obtained in Andra's underground laboratory, the Centre Meuse/Haute-Marne in Bure (FR). In the center, the mock-ups of the HLW and ILW-LL repository cells are instrumented with many sensors, among which some optical fiber cables that are interrogated regularly over time. The cables are glued at the external surface of the steel liner of the HLW repository cells or embedded into the concrete liner of ILW-LL repository cells mock-ups. The validation of the method is however even more complex here: the mock-ups are loaded by the rock above, whose load distribution and direction can only be inferred by knowledge on its mechanical behaviour. The uncertainty in the load distribution comes often together with the uncertainty linked to the location of the measurement points on the structure. A first, brief analysis revealed these issues related to the non-controlled environment of the underground laboratory, despite the absence of radioactive waste, as well as the influence of concrete shrinkage on strain measurements for ILW-LL mock-ups. These conditions took to an initial failure in the analysis of strain measurements of an ILW-LL mock-up, which appeared more influenced by concrete shrinkage and seasonal thermal cycles than by the physical loading of the rock. For strain measurements took on a HLW mock-up, however, results are clearer and a convergence value of 2 mm is obtained 7 months after the installation, using both Brillouin and Rayleigh scatterings (via PPP-BOTDA and TW-COTDR techniques with the Neubrescope). The strain measurements remind the two-points loading case, reporting a double sine wave behaviour. The results show that while more work must be done to achieve proper convergence values in a non-controlled environment, especially for concrete structures, our convergence measurement method can be also used in-situ and validated in the future with very good results as done in a controlled environment.

Perspectives

Now that we have successfully validated the whole convergence measurement chain via distributed optical fiber sensors, i.e. starting from the optical fiber, going through the sensing mechanism and cable, ending with the development, performance analysis and laboratory validation of the measurement method, we can look forward the next steps to further improve and extend our results.
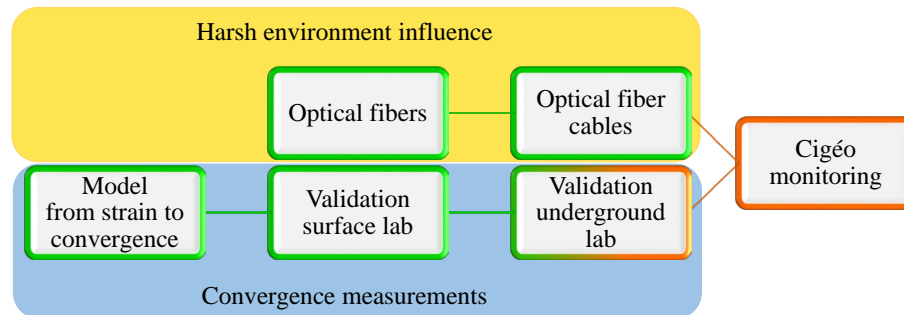
FIGURE 6.1: This thesis deals with the validation of a convergence measurement method for Cigéo monitoring. After the validation of the sensors and the convergence method itself, it is possible to consider their use in our final application.

First of all, in order to enlarge and further confirm our results considering the Cigéo environment, i) it would be useful to reduce the sensors' irradiation dose rate, bringing it a little bit closer to the one of the application (1 Gy/h). In our tests the dose rate reached 3.3 kGy, which may be too much for the sensors, burning rapidly the surface and leading to delusive results. It is important however to remember that it is not possible to use the same dose rate of the application due to obvious temporal limits. Another way to be closer to the application is to ii) test the sensors to neutron radiation, which is emitted by radioactive waste packages along with γ-radiation. Moreover, in order to confirm the feasibility of using these optical fiber strain sensing cables during the 100 years monitoring, iii) it is necessary to extend the study irradiating the cables up to 1 MGy. A step further is also to iv) consider the coupled influence of the application existing conditions: hydrogen, humidity and water content, as well as the influence on the concrete liner which impacts, in turn, on measurements.

In parallel, it would be useful to v) analyse different kinds of cables, like for example the flat ones, which would be particularly suitable to be instrumented on surfaces when they cannot be embedded inside the material (as for metallic liners). Having more time and resources, also, it would be possible to design and develop a new cable, for example inserting the custom F-doped carbon coated fiber inside a flat cable, perfectly suited for the application.

Finally, it would be necessary to vi) enlarge the reproducibility of the results, testing many samples of the same cable in all these conditions.

Regarding the convergence measurement method, it could be improved by generalising its functioning. For example, this could be done by adding other degrees of freedom in the search for minimisation. The method here presented considers as known the position of the measurement points of the cable (i.e. the correspondence between the position of the cable and the coordinates of the structure) and the location and direction of the load. In the future, the implementation of the method with these parameters set as unknown, using a more powerful computing environment, could extend its advantages and its range of applications.

Finally, it is possible to improve the analysis of strain measurements acquired in Andra's underground laboratory. As mentioned before, the validation of the method is more complex, having to deal with uncertainties in the load distribution and in the location of the measurement points on the structure. An improved method, that would consider these two aspects as parameters,

would be then useful to automatise the positioning of the strain measurement trace and the loading around the structure. Furthermore, measurements acquired in a uncontrolled environment, where the load is not artificially imposed, can be more affected by other strain sources, as the concrete is subjected to creep and shrinkage which affect strain measurements. Moreover, all along the thesis we have ignored the contribution of temperature variations, as tests were always carried out in controlled environments where temperature remained stable. In a real environment it is necessary to take into account also the Brillouin and Rayleigh frequency shifts induced by temperature. The fluctuations due to the heating coming from radioactive waste and the seasonal thermal cycle cause not only such induced frequency shifts but also the thermal expansion of the used materials, which sums up to the strain to which the structure is subjected. For this reason we have characterised the V9 type cable, irradiated or not, also determining the temperature sensitivity coefficient. This adds more complexity to the application of the method and the calculation of convergence, as it is not easy to discriminate the effect of all these elements.

In the end, these considerations are further ways to improve this already successful work. This amount of results took me to publish three peer reviewed papers along the three years of Ph.D., and participate to many international conferences and workshops. Five of these conference papers were published in proceedings, with three oral presentations and two poster presentations. This thesis proved the feasibility of using distributed optical fiber sensors to measure convergence in a harsh environment similar to that of Cigéo, the future French underground repository for radioactive waste. Results showed how, choosing the proper fiber and protection cable, it is possible to achieve suitable results for the application, succeeding in the goal of this research.

Appendix A

Distributed optical fiber sensing cables and interrogators datasheets

Function	Property											
General Function	Separation of strain and temperature measured in single fiber, PPP-BOTDA / BOTDR / TW-COTDR / COTDR											
Function	PPP-BOTDA (BOTDR)						TW-COTDR					
Laser wavelength	1550±2 nm						1530 nm ~ 1560 nm					
Distance range	50 m, 100 m, 250 m, 500 m, 1 km, 2.5 km, 5 km, 10 km, 25 km											
Measurement frequency range	9~13 GHz						192300 ~196000 GHz					
Range of strain measurements	-30,000 to +40,000 µε (-3% to +4%)						-15,000 to +20,000 µε (-1.5 % to +2 %)					
Measurement frequency scan step	1, 2, 5, 10, 20, 50 MHz						100, 200, 250, 500 MHz					
Readout resolution	5 cm (default), 1cm (minimum)											
Sampling points	600,000 (default), 3,000,000 (maximum)											
Average count settings	$2^5 \sim 2^{23}$ times (including Hardware Average Count $2^5 \sim 2^{16}$)											
Pulse width, ns	0.2	0.5	1	2	10	20	0.2	0.5	1	2	10	20
Spatial resolution, cm	2	5	10	20	100	200	2	5	10	20	100	200
Dynamic range, dB *1	0.5	1	1.5	3 (1)	6 (5)	8 (8)	0.5	1	3	6	10	11
Max. measurement Distance, km *2	0.5	1	2	5 (1)	18 (15)	25 (25)	0.5	1	10	20	25	25
Optical budget, dB *1*8	1	2	5	7 (3)	10 (8)	12 (10)	1	2	5	7	13	15
Measurement accuracy *3*4	15 µε/0.75 °C		7.5 µε/0.35 °C		5 µε / 0.25 °C		0.5 µε / 0.05 °C					
Repeatability *3*4*5	10 µε / 0.5°C		2.4 µε / 0.1 °C		2 µε / 0.1°C		0.2 µε / 0.01 °C					
Measurement Accuracy of BOTDR *3*4	-			75 µε/ 3.5°C	50µε / 2.5°C	30 µε/ 1.5°C	-					
Repeatability of BOTDR *3*4*5	-			20 µε / 1 °C			-					
Measurement time *6*7	5 seconds (minimum)						60 seconds (minimum)					
Measurement accuracy for hybrid mode *9	10 µε / 0.5 °C											
Repeatability for hybrid mode *9	5 µε / 0.25 °C											
Input-output fiber	Single mode optical fiber											
Fiber connector	FC-APC / SC-APC (factory option)											
Suitable fiber	Single mode optical fiber											
Power supply	AC 100~240V 50/60 Hz 250 VA											
Laser class	Class 1 (IEC60825-1 : 2001)											
Dimensions / Weight	approx. 456(W) × 485(D) ×286(H) mm / 30 kg											
Operating temperature	10 ~ 40 °C, Humidity below 85 % (no dew condensation)											
Storage temperature	0 ~ 50 °C											
Place of production	Japan											

*1 Based on 2^15 average cycles
*2 Based on average fiber loss of 0.3dB/km using SM fiber(UV type)
*3 Based on the measurement of strain free SM fiber(UV type)
*4 Based on the measurement of strain-free SM fiber(UV type) and in constant temperature environment
*5 The maximum deviation range of measurement value for 5 consecutive measurements for 100 consecutive points

PERFORMANCE

Parameter		Specification			Units
Wavelength Range (nominal)					
OBR 4600		1525 - 1610			nm
OBR 4613		1270 - 1340			nm
Maximum Device Length					
Standard mode		30 or 70			m
Extended range mode		2000			m
Sampling Resolution					
30 m mode		10			µm
70 m mode		20			µm
Extended range mode (2000 m)		1			mm
Dead zone		Equals 2-pt sampling resolution			
Wavelength					
Resolution (max)		0.02			pm
Accuracy[1]		±1.5			pm
Integrated Return Loss Characteristics					
Dynamic range	30 and 70 m modes	80			dB
	Extended range mode	60			dB
Total range		0 to -125			dB
Sensitivity		-130			dB
Resolution[2]		±0.05			dB
Accuracy[2]		±0.10			dB
Integrated Insertion Loss Characteristics					
Dynamic range[3]		18			dB
Resolution[2]		±0.05			dB
Accuracy[2]		±0.10			dB
Group Delay					
Accuracy		1.0			ps
Distributed Sensing[4,5]					
Spatial resolution		±1.0			cm
Temperature resolution		±0.1			°C
Strain resolution		±1.0			µε

Scan time	Scan range	Standard	Fast[6]	Spot Scan[6]	
Scan time for 30 m mode	5 nm	2.7	1.3	0.4	s
	65 nm/88 nm[7]	14.2	6.3	2.5	s
Scan time for 70 m mode	5 nm	3.2	1.8	0.5	s
	32 nm/43 nm[7]	9.7	5.8	2.1	s
Scan time for Extended Range	0.8 nm	16	-	-	s
	3.2 nm	-	-	6.5	s
Physical					
Class 1 Laser		<10			mW
Operating power		100			W
Weight (controller not included)		25 (11.4)			lb (kg)
Case size (W x D x H)		14.4 x 13.6 x 6.5 (366 x 345 x 165)			in (mm)

NOTES

Specifications are for single-mode performance. For multimode operation, specifications are nominal.

1. Accuracy maintained by an internal NIST-traceable HCN gas cell.

2. With integration width of 0.5 m.

3. IL dynamic range is the one-way loss that can be suffered before the scatter level of standard SMF is lower than the noise floor (~ -118 dB/mm).

4. Distributed sensing uses Rayleigh spectral shift method and is relative to reference scan. Maximum sensing length is typically 70 m.

5. Sampling resolutions listed are ideal to get the temperature and strain resolutions listed; they are not minimums or maximums.

6. Times are with laser tuning speed set at 100 nm/s.

7. Maximum wavelength scan for O band is 65 nm or 32 nm; maximum wavelength scan for C and L band is 88 nm or 43 nm.

LUNA

BRUsens DSS 3.2mm V9 grip

3_50_2_005

LLK-BSST V9 3.2 mm

Fiber optic strain sensing cable, mini, flexible, armored with central metal tube, structured PA outer sheath, one optical fiber, strain range up to 1% (10000 µstrain).

Description

- Compact design, good flexibility, small bending radius
- Metal tube, central, extra small, with one strain locked optical fiber, hermetically sealed
- Outer sheath, robust, abrasion resistant, halogen free, structured for better strain transfer
- High chemical resistance
- Good rodent protection
- Laterally watertight
- High strain sensitivity
- Good tensile strength and crush resistance

Application

- Strain
- Soil movement
- Pipeline monitoring
- Stuctural monitoring
- Precision measurement and alarm systems
- Brillouin, FBG
- Outdoors, harsh environment, subsea
- Direct burial in soil, concrete

Remarks

- Standard fiber color code: 1 red, 2 green, 3 yellow, 4 blue, 5 white, 6 violet, 7 orange, 8 black
- For improved UV resistance, black cable sheath available upon request
- Deployment training upon request
- Standard cable marking with meter marks, special labeling of outer sheath upon request
- Other cable designs and temperature ranges upon request
- Accessories such as mounting brackets, loops, fan-outs, splice enclosures, connectors, patch-panels, repair- and field-termination-kits etc. are available
- Accessories such as anchors, mounting brackets, loops, fan-outs, splice enclosures, connectors, patch-panels, repair kits etc. are available
- Final test reports OTDR, BOTDA measurement available upon request

Technical data

Type	Max. no. of fibres	Cable ø	Weight	Installation Max. tensile strength	Typical Load at 1 % elongation
	units	mm	kg/km	N	N
1F	1	3.2	10.5	260	470

Type	with tensile load Min. bending radius mm	without tensile load Min. bending radius mm	Max. crush resistance N/cm
1F	64 (20xD)	48 (15xD)	250

Optical fiber data (cabled) at 20°C

Fiber Type	Attenuation	Temperature sensitivity df_B/dT Typical Brillouin parameters BOTDR or BOTDA at 1550 nm	Strain sensitivity $df_B/d\varepsilon$ Typical Brillouin parameters BOTDR or BOTDA at 1550 nm	Centr. Brillouin Freq. Typical Brillouin parameters BOTDR or BOTDA at 1550 nm
	dB/km 1550 nm	MHz/°C	MHz/%	GHz
SMF	≤0.5	2.0	450	10.8

BRUsens DSS 7.2mm V3 grip

3_50_2_002

LLK-BSST V3 7.2 mm

Fiber optic strain sensing cable, extra robust, with central metal tube, metallic armoring wires and structured PA outer sheath, one optical fiber, strain range up to 1% (10000 µstrain).

Description

- Compact design, good flexibility, small bending radius
- Metal tube, central, extra small, with one strain locked optical fiber, hermetically sealed
- Outer sheath, robust, abrasion resistant, halogen free, structured for better strain transfer
- High strain sensitivity
- Excellent rodent protection
- High chemical resistance
- Laterally watertight
- High tensile strength and crush resistance

Application

- Strain
- Soil movement
- Pipeline monitoring
- Stuctural monitoring
- Brillouin, FBG
- Outdoors, harsh environment, subsea
- Direct burial in soil, concrete

Remarks

- Standard fiber color code: 1 red, 2 green, 3 yellow, 4 blue, 5 white, 6 violet, 7 orange, 8 black
- For improved UV resistance, black cable sheath available upon request
- Deployment training upon request
- Standard cable marking with meter marks, special labeling of outer sheath upon request
- Other cable designs and temperature ranges upon request
- Accessories such as mounting brackets, loops, fan-outs, splice enclosures, connectors, patch-panels, repair- and field-termination-kits etc. are available
- Accessories such as anchors, mounting brackets, loops, fan-outs, splice enclosures, connectors, patch-panels, repair kits etc. are available
- Final test reports OTDR, BOTDA measurement available upon request

Technical data

Type	Max. no. of fibres units	Cable ø mm	Weight kg/km	Installation Max. tensile strength N	Typical Load at 1 % elongation N
1F	1	7.2	75	600	1600

Type	with tensile load Min. bending radius mm	without tensile load Min. bending radius mm	Max. crush resistance N/cm
1F	144 (20xD)	108 (15xD)	500

Optical fiber data (cabled) at 20°C

Fiber Type	Attenuation dB/km 1550 nm	Temperature sensitivity df_B/dT Typical Brillouin parameters BOTDR or BOTDA at 1550 nm MHz/°C	Strain sensitivity $df_B/d\varepsilon$ Typical Brillouin parameters BOTDR or BOTDA at 1550 nm MHz/%	Centr. Brillouin Freq. Typical Brillouin parameters BOTDR or BOTDA at 1550 nm GHz
SMF	≤0.5	2.0	450	10.8

FutureNeuro™ FN-SILL-3
Embossed Sensing Cable

SPECIFICATIONS

Fiber Type	10 / 125 μm Single-mode Fiber
Fiber Count	2
Attenuation	< 0.5 dB/km
Strain Sensing Range* (Δε)	5000 με
Temperature Sensing Range	-20 to +80 °C
Bending Radius	> 40 mm
Strength Member	φ0.3mm, SUS304 x2
Tensile Strength	25 kg-f
Dimension (W x H)	4.3 x 1.7 mm
Max. Delivery Length	2000 m
Weight	12 g /m
Operation Temperature	-20 to +80 °C
Storage Temperature	-40 to +85 °C

* Will depending on the real applying situation of the cable. Please contact us for more information.
** All specifications above are subject to change without notice.

CONFIGURATIONS

FN-SILL-4

○ :φ0.3ᵐᵐ SUS304

● :φ0.25ᵐᵐ Singlemode fiber (FUJIKURA: FutereGuide SR-15)

● :φ0.25ᵐᵐ Multimode fiber (Corning::ClearCurve OM3)
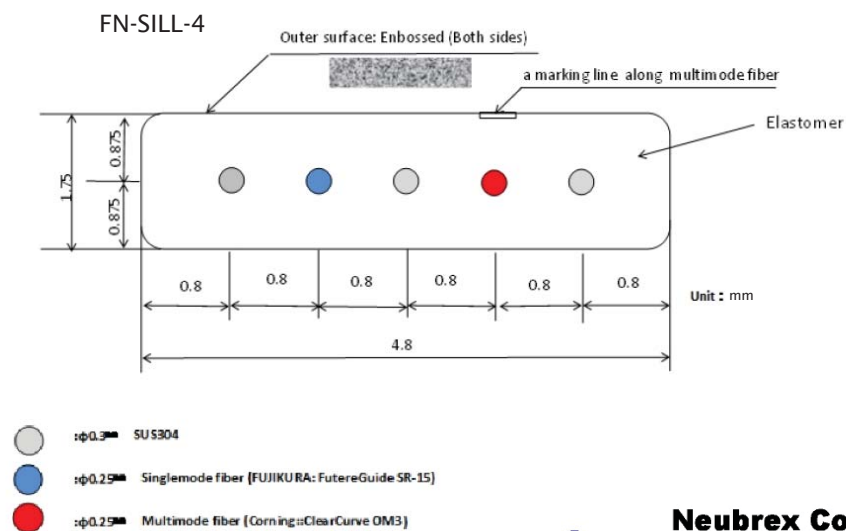
Neubrex Co., Ltd.

Sakaemachi-dori 1-1-24, Chuo-ku, Kobe
Hyogo 650-0023, Japan
Tel: +81-78-335-3510
www.neubrex.com

Appendix B

Acquisition parameters

B.1 Coupled radiation and temperature influence on bare optical fiber sensors

TABLE B.1: Coupled temperature and radiation effects, Neubrescope parameters.

	Brillouin		Rayleigh	
	High Temperature	Room Temperature	High Temperature	Room Temperature
Spatial Resolution	100 cm	100 cm	100 cm	100 cm
Sampling Interval	20 cm	20 cm	20 cm	20 cm
Averaging Count	2^{17}	2^{17}	2^{17}	2^{16}
Probe Output Power	+1 dBm	+1 dBm	-	-
Pump Output Power	+30 dBm	+30 dBm	+27 dBm	+26 dBm
Frequency Range	[10.70-11.40] GHz	[10.60-11.30] GHz	[194-194.25] THz	[194-194.25] THz
Frequency Span	2 MHz	2 MHz	250 MHZ	250 MHZ

- **OBR settings**: gage length 5 cm, scan between 1555.99 and 1577.36 nm with a sweep rate of 10 nm/s and gain of 24 dB.

B.2 Post-mortem radiation and temperature influence on strain sensing cables

TABLE B.2: Traction, Neubrescope parameters.

	Brillouin	Rayleigh
Spatial Resolution	20 cm	20 cm
Sampling Interval	10 cm	10 cm
Averaging Count	2^{14}	2^{14}
Probe Output Power	0 dBm	-
Pump Output Power	+26 dBm	+26 dBm
Frequency Range (*[min max] overall)	[10.45-12.45]* GHz	[194-194.3] THz
Frequency Span	1 MHz	250 MHz

TABLE B.3: Crush, Neubrescope parameters.

	Brillouin	Rayleigh
Spatial Resolution	2 cm	2 cm
Sampling Interval	1 cm	1 cm
Averaging Count ($_F$ = custom samples)	2^{14}	2^{14}-$2^{15}{}_F$
Probe Output Power	0 dBm	-
Pump Output Power	+26 dBm	+26 dBm
Frequency Range (*[min max] overall)	[10.30-11.95]* GHz	[194-194.3] THz
Frequency Span	1 MHz	300 MHz

TABLE B.4: Impact, Neubrescope parameters.

	Brillouin	Rayleigh
Spatial Resolution	2 cm	2 cm
Sampling Interval	1 cm	1 cm
Averaging Count	2^{14}	2^{15}
Probe Output Power	0 dBm	-
Pump Output Power	+26 dBm	+26 dBm
Frequency Range (*[min max] overall)	[10.30-11.95]* GHz	[194-194.3] THz
Frequency Span	1 MHz	300 MHz

TABLE B.5: Bending, Neubrescope parameters.

	Brillouin	**Rayleigh**
Spatial Resolution	20 cm	20 cm
Sampling Interval	10 cm	10 cm
Averaging Count	2^{14}	2^{15}
Probe Output Power	0 dBm	-
Pump Output Power	+26 dBm	+26 dBm
Frequency Range (*[min max] overall)	[10.30-11.95]* GHz	[194-194.3] THz
Frequency Span	1 MHz	300 MHz

TABLE B.6: Thermal sensitivity, Neubrescope parameters.

	Brillouin	**Rayleigh**
Spatial Resolution	20 cm	20 cm
Sampling Interval	10 cm	10 cm
Averaging Count	2^{15}	2^{16}
Probe Output Power	0 dBm	-
Pump Output Power	+26 dBm	+26 dBm
Frequency Range (*[min max] overall)	[10.30-11.95]* GHz	[194-194.35] THz
Frequency Span	1 MHz	250 MHz

B.3 Convergence measurement method application in the surface laboratory

TABLE B.7: Strain measurements surface laboratory, Neubrescope parameters.

	Brillouin	**Rayleigh**
Spatial Resolution	2 cm	2 cm
Sampling Interval	1 cm	1 cm
Averaging Count	2^{15}	2^{13}
Probe Output Power	+1 dBm	-
Pump Output Power	+30 dBm	+26 dBm
Frequency Range	[10.45-10.88] GHz	[194-194.25] THz
Frequency Span	1 MHz	500 MHz

B.4 Convergence measurement method application in the underground laboratory

TABLE B.8: Strain measurements underground laboratory, Neubrescope parameters, HLW mock-up.

	Brillouin	Rayleigh
Spatial Resolution	10 cm	10 cm
Sampling Interval	5 cm	5 cm
Averaging Count	2^{15}	2^{13}
Probe Output Power	0 dBm	-
Pump Output Power	+25 dBm	+25 dBm
Frequency Range	[10.25-11.05] GHz	[194-194.40] THz
Frequency Span	2 MHz	200 MHz

Appendix C

Optical fiber strain sensing cables in shotcrete

In the framework of my Ph.D., the convergence monitoring of the repository cells is foreseen for both the metallic lined HLW cell and the concrete lined ILW-LL cell. Regarding ILW-LL cells, optical fiber strain sensing cables will be inserted into the poured concrete liner. We had however the possibility to analyse whether the optical fiber sensing cables are suitable to be inserted in the shotcrete layer that lies between the rock and the poured concrete. The main bottleneck to be solved was to select a sensing cable robust enough to endure the shotcrete spraying pressure and high levels of strain during concrete shrinkage.

For this reason, we have planned a test where different optical fiber strain sensing cables were installed inside some wood boxes, at different depths. We have first of all used three types of sensing cables, to determine which one would better withstand shotcrete spray and be properly embedded in concrete without air bubbles around. These cables were the V9 type from Solifos AG and the AFL type, both of them already used within Andra, and the Fujikura type, used by FINESSE partners and known for its resistance to high deformation. These cables were presented in Figs. 2.14 and 2.15. The installed cables are visible in Fig. C.1A, where they are already fixed in one of the 45x45 cm^2 wood boxes.

Cables embedding

In order to guarantee the feasibility of the sensing in such conditions, we have first of all to check the quality of the sensing cable embedding, while strain measurements are done after the shotcrete spray in order to verify the sensitivity of the cables to the phenomena occurring inside the boxes (Fig. C.1B).

One of the boxes has thus been cut in order to see the distribution of shotcrete around the section of cables. Fig. C.2 shows how, regardless of the type of strain sensing cable, the shotcrete is homogeneous around their section. This guarantees the goodness of measures.

At the same time, the shotcrete spray caused the breaking of the cable in some cases, due to the high pressure of the shotcrete casting that impacted on the cables which are stretched. Breaks occurred in the less resistant type of cables, i.e. for one of the AFL type, while a V9 type cable broke at the position of entry into the box, maybe due to a not properly done splice. In fact, being the first time I have ever dealt with this kind of cables, it was initially difficult to properly splice the cable and the pigtail without suffering the stiffness of the metallic part. In fact, in order to splice the V9 type cable, it is necessary to remove firstly the rigid polyamide plastic layer, then removing the metallic tube without breaking the fiber, and then splicing it. If the splice is not performed and protected correctly, however, the interface between the metallic tube and the naked fiber can become at high risk of twist and, consequently, break. Performing splicings on this kind of cable many other times I have perfected the technique, which is now very easy for me. Overall, considering three instrumented boxes (6 cables of the same type in total), half of the AFL type cables and 2/3 of the V9 type cables survived without breaking. The only cable that had no

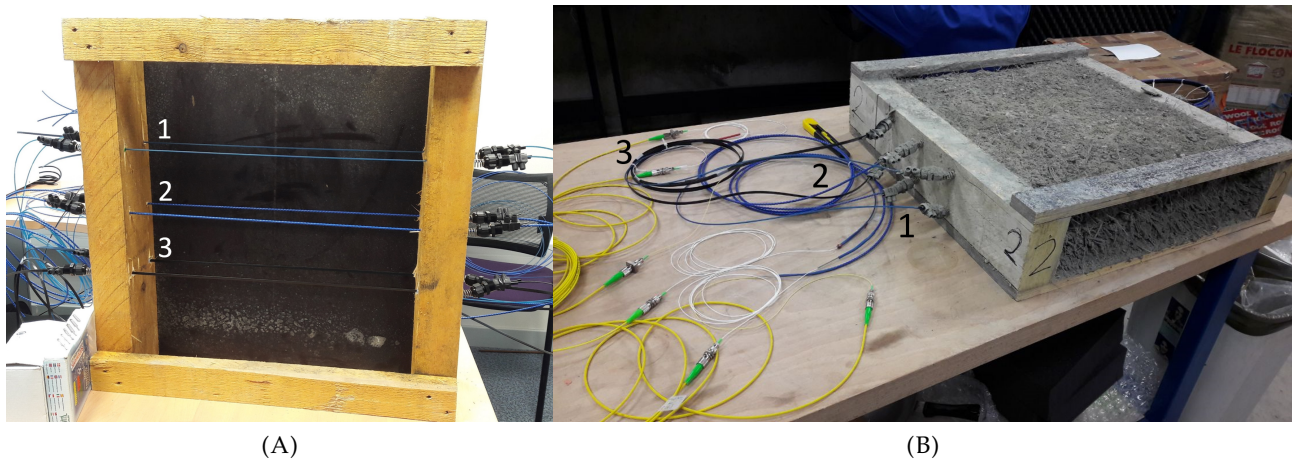(A)   (B)

FIGURE C.1: One of the wood boxes instrumented with three types of strain sensing
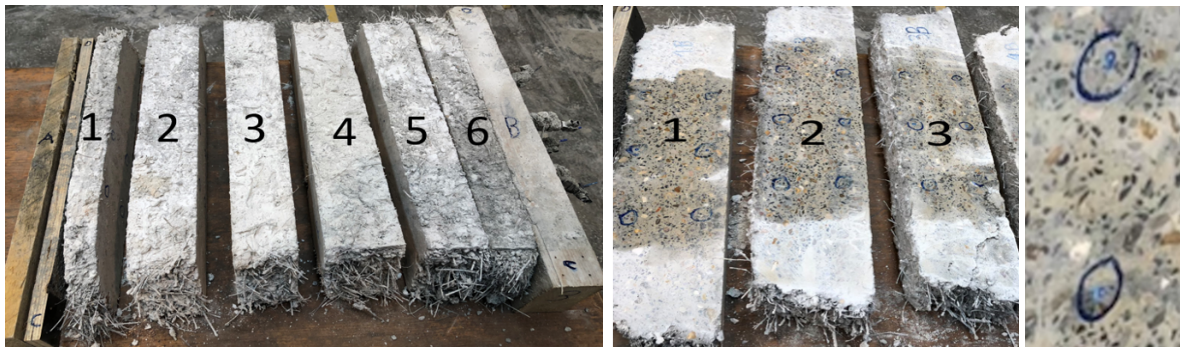cables, before and after the injection of shotcrete. 1) AFL, 2) V9, 3) Fujikura.

FIGURE C.2: Some sections of a shotcrete box, which was cut to see the adhesion
of shotcrete around the cables (encircled in the images). No air bubbles are found
around the cables, the embedding was thus optimal.

breaking during the shotcrete spraying and handling was the Fujikura type, which seemed giving
proper raw measurements for the shrinkage analysis.

Shrinkage analysis

Being the first experimental experience, some mistakes have been made during the planning: only
one extremity of the cable samples has been connected to a pigtail, thus only one-end techniques
such BOTDR or TW-COTDR, using the Neubrescope interrogation device, could be used. As
BOTDR did not give good measurements, the only exploitable values were given by TW-COTDR.
Results are plotted in Fig. C.3.

Doing just few measurements, once each some months, is not enough to be able to see a good
shrinkage behaviour of the shotcrete. Moreover, the temperature difference was not taken into
account as the box was moved of laboratory between measurements. For all these reasons we
have abandoned this topic to concentrate on the influence of harsh environment on the sensor, but
it was still useful to start dealing with different types of optical fiber sensing cable.

Other tests

Other boxes and the corresponding cables were still tested at the University of Lille (FR) by Marcel
Landolt (from Andra) and a Ph.D. student, Yasir Bhewa. The working cables were able to measure

strain along time, imposed by a three-points flexion over the cabled portions of the box (Fig. C.4).
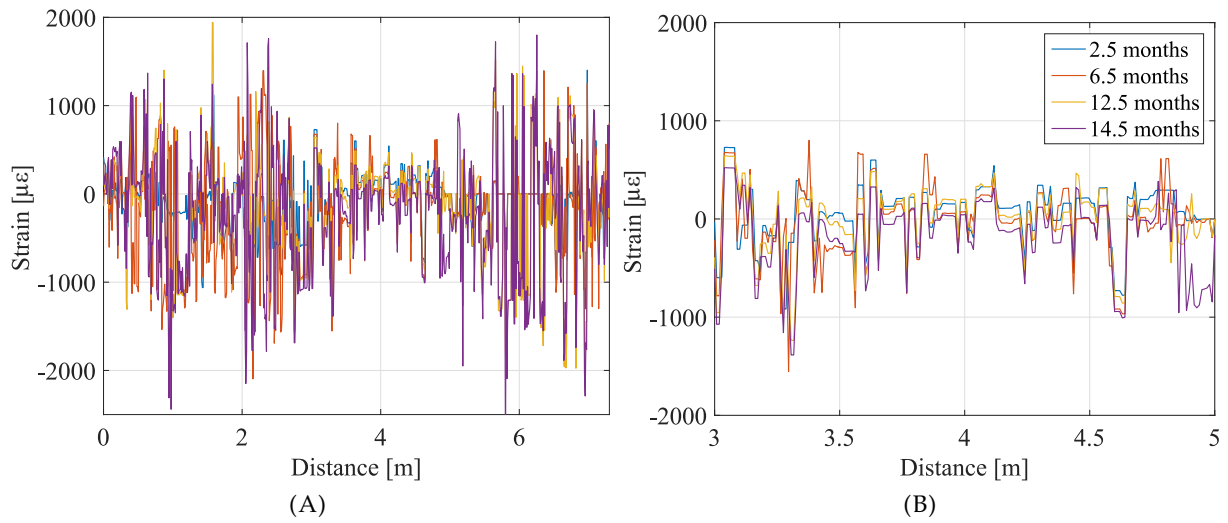

FIGURE C.3: Strain measurement along time of one of the Fujikura type cable: whole line (A) and detail on the part of the cable inside the concrete (B).
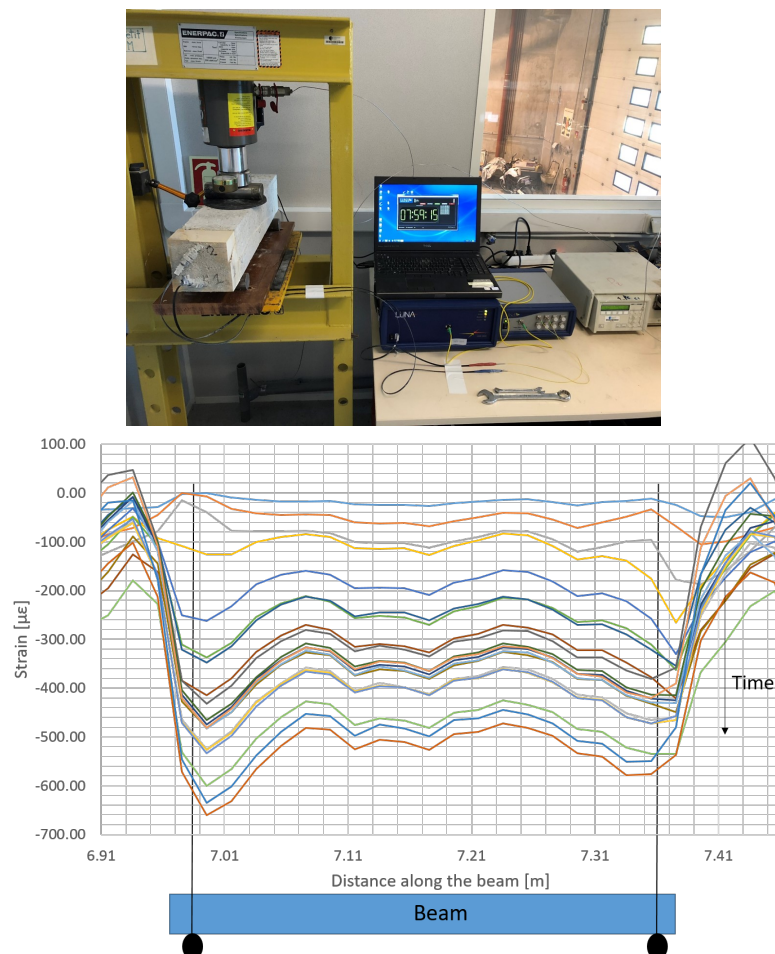

FIGURE C.4: Three-points flexion test.

Bibliography

Alasia, Dario et al. (2006). "The effects of gamma-radiation on the properties of Brillouin scattering in standard Ge-doped optical fibres". In: *Measurement Science and Technology* 17.5, p. 1091. URL: http://stacks.iop.org/0957-0233/17/i=5/a=S25.

Alba, M et al. (2010). "Development and testing of a method for tunnel monitoring via vision metrology". In: *Int Arch Photogramm Remote Sens Spat Inf Sci* 38.5, pp. 17–22.

Alessi, A. et al. (2017). "Irradiation Temperature Influence on the In Situ Measured Radiation Induced Attenuation of Ge-Doped Fibers". In: *IEEE Transactions on Nuclear Science* 64.8, pp. 2312–2317. ISSN: 0018-9499. DOI: 10.1109/TNS.2016.2627598.

Andra. *Cigéo*. URL: https://international.andra.fr/solutions-long-lived-waste/cigeo (visited on 04/13/2020).

— (2016). *Safety Options Report - Operating Part*. Tech. rep. eprint: https://international.andra.fr/sites/international/files/2019-03/Safety%20Options%20Report%20-%20Operations_2.pdf.

— (2018). *National Inventory of Radioactive Materials and Waste*. Tech. rep. eprint: https://international.andra.fr/sites/international/files/2019-03/Andra-Synthese-2018_EN_relu_HD.pdf.

Ariznavarreta-Fernández, Fernando et al. (2016). "Measurement system with angular encoders for continuous monitoring of tunnel convergence". In: *Tunnelling and Underground Space Technology* 56, pp. 176–185.

Armand, G et al. (2013). "Short-and long-term behaviors of drifts in the Callovo-Oxfordian claystone at the Meuse/Haute-Marne Underground Research Laboratory". In: *Journal of Rock Mechanics and Geotechnical Engineering* 5.3, pp. 221–230.

Bao, Xiaoyi and Liang Chen (2011). "Recent Progress in Brillouin Scattering Based Fiber Sensors". In: *Sensors* 11.4, pp. 4152–4187. ISSN: 1424-8220. DOI: 10.3390/s110404152. URL: http://www.mdpi.com/1424-8220/11/4/4152.

— (2012). "Recent Progress in Distributed Fiber Optic Sensors". In: *Sensors* 12.7, pp. 8601–8639. ISSN: 1424-8220. DOI: 10.3390/s120708601. URL: http://www.mdpi.com/1424-8220/12/7/8601.

Barbosa, Cristina B et al. (2009). "Fiber Bragg grating system for continuous large-scale monitoring of convergence in Rossio Tunnel". In: *20th International Conference on Optical Fibre Sensors*. Vol. 7503. International Society for Optics and Photonics, 75035S.

Barrias, António, Joan R. Casas, and Sergi Villalba (2016). "A review of distributed optical fiber sensors for civil engineering applications". In: *Sensors* 16.5, p. 748.

— (2017). "Application study of embedded Rayleigh based Distributed Optical Fiber Sensors in concrete beams". In: *Procedia engineering* 199, pp. 2014–2019.

— (2019). "Fatigue performance of distributed optical fiber sensors in reinforced concrete elements". In: *Construction and Building Materials* 218, pp. 214 –223. ISSN: 0950-0618. DOI: https://doi.org/10.1016/j.conbuildmat.2019.05.072. URL: http://www.sciencedirect.com/science/article/pii/S0950061819312310.

Bassil, Antoine (Nov. 2019). "Distributed Fiber Optics Sensing for Crack Monitoring of Concrete Structures". Ph.D. manuscript. University of Nantes, France.

Billon, Astrid et al. (July 2014). "Quantitative Strain Measurement with Distributed Fiber Optic Systems: Qualification of a Sensing Cable Bonded to the Surface of a Concrete Structure". In:

EWSHM - 7th European Workshop on Structural Health Monitoring. Ed. by Vincent Le Cam, Laurent Mevel, and Franck Schoefs. IFFSTTAR, Inria, Université de Nantes. Nantes, France. URL: https://hal.inria.fr/hal-01022049.

Bisby, Luke A and MB Briglio (2004). "ISIS Canada Educational Module No. 5: An Introduction to Structural Health Monitoring". In: *Prepared by ISIS Canada* 3.

Biswas, D. R. (1993). *Optical fiber coatings*. Ed. by Dilip K. Paul. International Society for Optics and Photonics. DOI: 10.1117/12.181374. URL: https://doi.org/10.1117/12.181374.

Bumbieler, F. et al. (2015). "Mechanical and SCC Behavior of an API5L Steel Casing Within the Context of Deep Geological Repositories for Radioactive Waste". In: *ASME 2015 Pressure Vessels and Piping Conference* 56963, V003T03A015. DOI: 10.1115/PVP2015-45234. URL: http://dx.doi.org/10.1115/PVP2015-45234.

Cangialosi, C. et al. (2015). "Steady state γ-ray radiation effects on Brillouin fiber sensors". In: *24th International Conference on Optical Fibre Sensors*. Ed. by Hypolito J. Kalinowski, José Luís Fabris, and Wojtek J. Bock. SPIE. DOI: 10.1117/12.2194990. URL: https://doi.org/10.1117/12.2194990.

Di Murro, Vanessa et al. (2016). "Distributed fibre optic long-term monitoring of concrete-lined tunnel section TT10 at CERN". In: *International Conference of Smart Infrastructure and Construction, ICE Publishing, Cambridge*.

Dragic, P. D. (2009). "Simplified model for effect of Ge doping on silica fibre acoustic properties". In: *Electronics Letters* 45.5, pp. 256–257. ISSN: 0013-5194. DOI: 10.1049/el:20093739.

Dunnicliff, John (1993). *Geotechnical instrumentation for monitoring field performance*. John Wiley & Sons.

Farrar, Charles R and Keith Worden (2007). "An introduction to structural health monitoring". In: *Philosophical Transactions of the Royal Society A: Mathematical, Physical and Engineering Sciences* 365.1851, pp. 303–315.

Faustov, A (2014). "Advanced fibre optics temperature and radiation sensing in harsh environments". PhD thesis. Ph. D. dissertation, Univ. de Mons, Mons, Belgium.

Girard, S. et al. (2013a). "Combined High Dose and Temperature Radiation Effects on Multimode Silica-Based Optical Fibers". In: *IEEE Transactions on Nuclear Science* 60.6, pp. 4305–4313. ISSN: 0018-9499. DOI: 10.1109/TNS.2013.2281832.

Girard, S. et al. (2013b). "Radiation Effects on Silica-Based Optical Fibers: Recent Advances and Future Challenges". In: *IEEE Transactions on Nuclear Science* 60.3, pp. 2015–2036. ISSN: 0018-9499. DOI: 10.1109/TNS.2012.2235464.

Glisic, Branko and Daniele Inaudi (2008). *Fibre optic methods for structural health monitoring*. John Wiley & Sons.

Grattan, KTV and T Sun (2000). "Fiber optic sensor technology: an overview". In: *Sensors and Actuators A: Physical* 82.1-3, pp. 40–61.

Guayacán-Carrillo, Lina-María et al. (2016). "Analysis of Long-Term Anisotropic Convergence in Drifts Excavated in Callovo-Oxfordian". In: *Rock Mechanics and Rock Engineering* 49, pp. 97–114. DOI: 10.1007/s00603-015-0737-7.

Guyard, Romain (2015). "Capteur à fibre optique pour la mesure de déformation au sein des matériaux". PhD thesis. Nantes.

Hauswirth, Dominik (2015). "A study of the novel approaches to soil displacement monitoring using distributed fiber optic strain sensing". PhD thesis. ETH Zurich.

HBM (2016). *SysTunnel: Optical monitoring system for strain and convergence measurement*. Tech. rep.

Henault, Jean-Marie (Nov. 2013). "Methodological approach for performance and durability assessment of distributed fiber optic sensors: application to a specific fiber optic cable embedded in concrete". Theses. Université Paris-Est. URL: https://tel.archives-ouvertes.fr/tel-00962388.

Her, Shiuh-Chuan and Chih-Ying Huang (2011). "Effect of Coating on the Strain Transfer of Optical Fiber Sensors". In: *Sensors* 11.7, pp. 6926–6941. ISSN: 1424-8220. DOI: 10.3390/s110706926. URL: https://www.mdpi.com/1424-8220/11/7/6926.

Huang, Hongwei and Dongming Zhang (2018). "Non-intrusive Inspection and Real-Time Monitoring for Tunnel Structural Resilience". In: *Resilience Engineering for Urban Tunnels*, pp. 29–42.

Inc., Luna (2018). *Optical backscatter reflectometry (OBR) - overview and applications*. eprint: http://lunainc.com/wp-content/uploads/2018/09/OBR-White-Paper-2018.09.12.pdf.

ITN FINESSE (2016). URL: http://itn-finesse.eu/ (visited on 04/13/2020).

Jen, Cheng-Kuei et al. (1993). "Acoustic Characterization of Silica Glasses". In: *Journal of the American Ceramic Society* 76.3, pp. 712–716. DOI: 10.1111/j.1151-2916.1993.tb03664.x. eprint: https://onlinelibrary.wiley.com/doi/pdf/10.1111/j.1151-2916.1993.tb03664.x. URL: https://onlinelibrary.wiley.com/doi/abs/10.1111/j.1151-2916.1993.tb03664.x.

Joe, Hang-Eun et al. (2018). "A review on optical fiber sensors for environmental monitoring". In: *International Journal of Precision Engineering and Manufacturing-Green Technology* 5.1, pp. 173–191.

Kashyap, R. (1999). *Fiber Bragg gratings*. Optics and Photonics, Academic Press.

Kishida, Kinzo, Yoshiaki Yamauchi, and Artur Guzik (2014). "Study of optical fibers strain-temperature sensitivities using hybrid Brillouin-Rayleigh System". In: *Photonic sensors* 4.1, pp. 1–11.

Kobyakov, Andrey et al. (2005). "Design concept for optical fibers with enhanced SBS threshold". In: *Opt. Express* 13.14, pp. 5338–5346. DOI: 10.1364/OPEX.13.005338. URL: http://www.opticsexpress.org/abstract.cfm?URI=oe-13-14-5338.

Koyamada, Y. et al. (2004). "Simulating and designing Brillouin gain spectrum in single-mode fibers". In: *Journal of Lightwave Technology* 22.2, pp. 631–639. ISSN: 0733-8724. DOI: 10.1109/JLT.2003.822007.

Laurent, Rémy et al. (May 2016). "Compaction in optical fibres and fibre Bragg gratings under nuclear reactor high neutron and gamma fluence". In: *IEEE Transactions on Nuclear Science* 63.4, pp. 2317 –2322. DOI: 10.1109/TNS.2016.2570948. URL: https://hal.archives-ouvertes.fr/hal-01528162.

Lemaire, P. J. et al. (1988). "Hydrogen permeation in optical fibres with hermetic carbon coatings". In: *Electronics Letters* 24.21, pp. 1323–1324. ISSN: 0013-5194. DOI: 10.1049/el:19880899.

Leung, Christopher KY et al. (2015). "Optical fiber sensors for civil engineering applications". In: *Materials and Structures* 48.4, pp. 871–906.

Li, Dongsheng, Liang Ren, and Hongnan Li (2012). "Mechanical Property and Strain Transferring Mechanism in Optical Fiber Sensors". In: *Fiber Optic Sensors*. Ed. by Moh. Yasin, Sulaiman W. Harun, and Hamzah Arof. Rijeka: IntechOpen. Chap. 18. DOI: 10.5772/27731. URL: https://doi.org/10.5772/27731.

Li, Hong-Nan, Dong-Sheng Li, and Gang-Bing Song (2004). "Recent applications of fiber optic sensors to health monitoring in civil engineering". In: *Engineering structures* 26.11, pp. 1647–1657.

Li, Jie et al. (2018). "Optical fibers for distributed sensing in harsh environments". In: *Fiber Optic Sensors and Applications XV*. Ed. by Alexis Mendez, Christopher S. Baldwin, and Henry H. Du. Vol. 10654. International Society for Optics and Photonics. SPIE, pp. 137 –156. DOI: 10.1117/12.2305433. URL: https://doi.org/10.1117/12.2305433.

Li, Qingbin, Guang Li, and Guanglun Wang (2003). "Elasto-plastic bond mechanics of embedded fiber optic sensors in concrete under uniaxial tension with strain localization". In: *Smart Materials and Structures* 12.6, pp. 851–858. DOI: 10.1088/0964-1726/12/6/001. URL: https://iopscience.iop.org/article/10.1088/0964-1726/12/6/001.

Li, Yuan-hui, Jian-po Liu, et al. (2015). "A new convergence monitoring system for tunnel or drift based on draw-wire displacement sensors". In: *Tunnelling and Underground Space Technology* 49, pp. 92–97.

Li, Zili, Kenichi Soga, and Cedric Kechavarzi (2018). "Distributed fibre optic sensing of a deep excavation adjacent to pre-existing tunnels". In: *Géotechnique Letters* 8.3, pp. 171–177.

López-Higuera, José Miguel et al. (2011). "Fiber optic sensors in structural health monitoring". In: *Journal of lightwave technology* 29.4, pp. 587–608.

Lynch, Brian K et al. (2017). "Mobile LiDAR-based convergence detection in underground tunnel environments". In:

Mamdem, Y. S. (2012). "Capteurs à fibres optiques répartis par effet Brillouin: séparation de la dépendance à température et à la déformation". PhD thesis. Télécom ParisTech.

Mesquita, Esequiel et al. (2016). "Global overview on advances in structural health monitoring platforms". In: *Journal of Civil Structural Health Monitoring* 6.3, pp. 461–475.

Minardo, A., R. Bernini, and L. Zeni (2013). "Bend-Induced Brillouin Frequency Shift Variation in a Single-Mode Fiber". In: *IEEE Photonics Technology Letters* 25.23, pp. 2362–2364. ISSN: 1941-0174. DOI: 10.1109/LPT.2013.2285283.

Modern2020 (2019). *Milestone n°39: Design and performances of a sensing system to provide distributed radiation, hydrogen strain and temperature measurements in geological repository environments*. Tech. rep.

Mohamad, Hisham et al. (2011). "Monitoring twin tunnel interaction using distributed optical fiber strain measurements". In: *Journal of geotechnical and geoenvironmental engineering* 138.8, pp. 957–967.

Monsberger, Christoph et al. (2017). "Performance assessment of geotechnical structural elements using distributed fiber optic sensing". In: *Sensors and Smart Structures Technologies for Civil, Mechanical, and Aerospace Systems 2017*. Ed. by Jerome P. Lynch. Vol. 10168. International Society for Optics and Photonics. SPIE, pp. 254 –265. DOI: 10.1117/12.2256711. URL: https://doi.org/10.1117/12.2256711.

Morana, A. et al. (2018). "Steady-State Radiation-Induced Effects on the Performances of BOTDA and BOTDR Optical Fiber Sensors". In: *IEEE Transactions on Nuclear Science* 65.1, pp. 111–118. ISSN: 0018-9499. DOI: 10.1109/TNS.2017.2772333.

Motil, Avi, Arik Bergman, and Moshe Tur (2016). "State of the art of Brillouin fiber-optic distributed sensing". In: *Optics & Laser Technology* 78, pp. 81–103.

Nikles, Marc, Luc Thevenaz, and Philippe A Robert (1997). "Brillouin gain spectrum characterization in single-mode optical fibers". In: *Journal of Lightwave Technology* 15.10, pp. 1842–1851.

Omnisens. *DiTeSt Dual Reading Unit*. URL: https://smartec.ch/en/product/ditest-reading-unit-2/ (visited on 04/13/2020).

Palmieri, Luca and Luca Schenato (2013). "Distributed optical fiber sensing based on Rayleigh scattering". In: *The Open Optics Journal* 7.1.

Phéron, Xavier et al. (2012). "High γ-ray dose radiation effects on the performances of Brillouin scattering based optical fiber sensors". In: *Opt. Express* 20.24, pp. 26978–26985. DOI: 10.1364/OE.20.026978. URL: http://www.opticsexpress.org/abstract.cfm?URI=oe-20-24-26978.

Piccolo, A. et al. (2018a). "Combined Radiation and Temperature Effects on Brillouin Scattering based Sensing with Ge-Doped Optical Fibers". In: *26th International Conference on Optical Fiber Sensors*. Optical Society of America, WF44. DOI: 10.1364/OFS.2018.WF44. URL: http://www.osapublishing.org/abstract.cfm?URI=OFS-2018-WF44.

Piccolo, A. et al. (2019a). "Coupled temperature and γ-radiation effect on silica-based optical fiber strain sensors based on Rayleigh and Brillouin scatterings". In: *Opt. Express* 27.15, pp. 21608–21621. DOI: 10.1364/OE.27.021608. URL: http://www.opticsexpress.org/abstract.cfm?URI=oe-27-15-21608.

Piccolo, A. et al. (2019b). "Distributed optical fiber strain and temperature sensing system performances: Brillouin vs Rayleigh". In: *Seventh European Workshop on Optical Fibre Sensors*. Ed. by Kyriacos Kalli, Sinead O. O'Keeffe, and Gilberto Brambilla. Vol. 11199. International Society for Optics and Photonics. SPIE, pp. 307 –310. DOI: 10.1117/12.2539843. URL: https://doi.org/10.1117/12.2539843.

Piccolo, Arianna (2016). "Discrimination of strain and temperature in Brillouin Optical Time Domain Analyzers via Artificial Neural Networks". Master's Thesis. Università degli Studi di Padova. eprint: http://tesi.cab.unipd.it/53200/1/piccolo_arianna_tesi.pdf.

Piccolo, Arianna et al. (2018b). "Tunnel convergence analysis by distributed optical fiber strain sensing with means of finite element – inverse analysis method". In: *9th European Workshop on Structural Health Monitoring (EWSHM 2018)*. NDT. URL: https://www.ndt.net/search/docs.php3?id=23335.

Piccolo, Arianna et al. (2018c). "Tunnel monitoring: Performances of several innovative shape sensing systems". In: *International Conference on Technological Innovations in Nuclear Civil Engineering*, WF44. eprint: https://www.researchgate.net/profile/Arianna_Piccolo/publication/328199078_Tunnel_monitoring_Performances_of_several_innovative_shape_sensing_systems/links/5c74f90ca6fdcc47159c0eb5/Tunnel-monitoring-Performances-of-several-innovative-shape-sensing-systems.pdf.

Piccolo, Arianna et al. (2019c). "Durability and Mechanical Properties of Optical Fiber Strain Sensing Cable for Structural Health Monitoring in Harsh Environment". In: *12th International Workshop on Structural Health Monitoring*.

Piccolo, Arianna et al. (2019d). "Non-invasive tunnel convergence measurement based on distributed optical fiber strain sensing". In: *Smart Materials and Structures* 28.4, p. 045008. DOI: 10.1088/1361-665x/ab04cc. URL: https://doi.org/10.1088%2F1361-665x%2Fab04cc.

Piccolo, Arianna et al. (2020). "Mechanical Properties of Optical Fiber Strain Sensing Cables under γ-Ray Irradiation and Large Strain Influence". In: *Sensors* 20.3, p. 696. ISSN: 1424-8220. DOI: 10.3390/s20030696. URL: http://dx.doi.org/10.3390/s20030696.

Planes, Isabelle et al. (2017). "Steady γ-Ray Effects on the Performance of PPP-BOTDA and TW-COTDR Fiber Sensing". In: *Sensors* 17, p. 396. ISSN: 1424-8220. DOI: 10.3390/s17020396. URL: http://www.mdpi.com/1424-8220/17/2/396.

Porubská, Mária (2016). "Radiation Effects in Polyamides". In: *Radiation Effects in Materials*. Ed. by Waldemar A. Monteiro. Rijeka: IntechOpen. Chap. 10. DOI: 10.5772/62464. URL: https://doi.org/10.5772/62464.

Rizzolo, S. et al. (2015a). "Radiation effects on optical frequency domain reflectometry fiber-based sensor". In: *Opt. Lett.* 40.20, pp. 4571–4574. DOI: 10.1364/OL.40.004571. URL: http://ol.osa.org/abstract.cfm?URI=ol-40-20-4571.

Rizzolo, S. et al. (2015b). "Radiation Hardened Optical Frequency Domain Reflectometry Distributed Temperature Fiber-Based Sensors". In: *IEEE Transactions on Nuclear Science* 62.6, pp. 2988–2994. ISSN: 0018-9499. DOI: 10.1109/TNS.2015.2482942.

Schmid, Steven R. and Anthony F. Toussaint (2007). "Chapter 4 - Optical Fiber Coatings". In: *Specialty Optical Fibers Handbook*. Ed. by Alexis Méndez and T.F. Morse. Burlington: Academic Press, pp. 95 –122. ISBN: 978-0-12-369406-5. DOI: https://doi.org/10.1016/B978-012369406-5/50006-0. URL: http://www.sciencedirect.com/science/article/pii/B9780123694065500060.

Senior, John M and M Yousif Jamro (2009). *Optical fiber communications: principles and practice*. Pearson Education.

Smith, W. F. and J. Hashemi (2010). *Foundation of Material Science and Engineering. Fifth Edition*. McGraw-Hill.

Stolov, A. A., D. A. Simoff, and J. Li (2008). "Thermal Stability of Specialty Optical Fibers". In: *Journal of Lightwave Technology* 26.20, pp. 3443–3451. DOI: 10.1109/JLT.2008.925698.

Tartara, Luca et al. (2009). "Full modal analysis of the Brillouin gain spectrum of an optical fiber". In: *Optics Communications* 282.12, pp. 2431 –2436. ISSN: 0030-4018. DOI: https://doi.org/10.1016/j.optcom.2009.03.012. URL: http://www.sciencedirect.com/science/article/pii/S0030401809002296.

Yeniay, Aydin, Jean-Marc Delavaux, and Jean Toulouse (2002). "Spontaneous and stimulated Brillouin scattering gain spectra in optical fibers". In: *Journal of lightwave technology* 20.8, p. 1425.

Yüksel, Kıvılcım (2018). "Rayleigh-based optical reflectometry techniques for distributed sensing applications". In:

Zhang, Li et al. (2018). "Rayleigh-based distributed optical fiber sensing using least mean square similarity". In: *Optical Fiber Sensors*. Optical Society of America, ThE29.

Zienkiewicz, Olek C, Robert L Taylor, and Jian Z Zhu (2005). *The finite element method: its basis and fundamentals*. Elsevier.

Zou, Weiwen, Xin Long, and Jianping Chen (2015). "Brillouin Scattering in Optical Fibers and Its Application to Distributed Sensors". In: *Intech: Advances in Optical Fiber Technology: Fundamental Optical Phenomena and Applications*, pp. 1–53.

Résumé : Dans le cadre du projet Cigéo, stockage géologique des déchets radioactifs à vie longue, la surveillance des infrastructures contribuera à confirmer la récupérabilité des déchets, prévue sur des durées pluridécennales. Les structures sont apparentés à des tunnels horizontaux, sous 500 m de couverture. Leur convergence (réduction progressive de leur section) doit être mesurée par des systèmes peu intrusifs, sensibles, compatibles avec un environnement sévère. Une méthode inverse, utilisant un modèle par éléments finis, a été développée pour déterminer la convergence à partir de mesures réparties de déformations acquises par rétrodiffusion Rayleigh et Brillouin dans des cables à fibre optique. Elle a été validée sur un démonstrateur d'alvéole, au laboratoire en surface et en souterrain. Sur une échelle de 10 mm représentative de l'application, la convergence est déterminée à 1 mm près par les fibres optiques, proche des capteurs de référence.

La sensibilité à la mise en oeuvre, au chargement, au bruit de mesure, a été étudiée. La tenue des fibres optiques à l'impact couplé des radiations et de la température a été étudiée pour des fibres optique en revêtement primaire: une dose totale de 1 MGy dégrade moins la mesure de déformation à 100 °C qu'à température ambiante. La fibre optique la plus résistance a été placée dans un câble de mesure de déformations, soumis à des radiations gamma et des sollicitations thermiques. Les coefficients de sensibilité thermique et mécanique des rétrodiffusions Brillouin et Rayleigh restent stables après 500 kGy, ainsi que ses caractéristiques mécaniques du câble. L'étude a aussi permis de quantifier les processus de plasticité, jusqu'à 10000 µε.

Abstract: In the framework of Cigéo, the future underground repository for long-lived radioactive waste, the monitoring of the structures must be guaranteed for almost a century to ensure its reversibilit. The horizontal repository cells will be loaded by 500 m of rock which will reduce their section over time. This reduction, called convergence, must be monitored by sensors with resistance to harsh environment, low intrusiveness, proper sensitivity. We propose the use of distributed optical fiber strain sensing cables, whose strain measurements are used to calculate convergence via an inverse-analysis finite-element method, using Brillouin and Rayleigh backscatterings. The method is described, assessing the influence of structural parameters and measurements noise on its sensitivity. We validate it in a laboratory test, in controlled conditions and underground, reproducing convergences up to the representative value of 10 mm on a mock-up of the high-level waste repository cell. We compare two fixation methods and loading schemes, using other sensors as reference. Results show how distributed optical fiber sensors can achieve the required 1 mm of resolution, close to standard methods.

The fibers have been firstly analysed under the coupled effect of temperature and radiation up to a total γ-rays dose of 1 MGy. Temperatures around 100°C preserve the fiber functioning better than being at room temperature. A specific cable for strain sensing, with a radiation resistant fiber inside, is then developed and tested, reporting that temperature and strain sensitivities and the mechanical behaviour remain stable up to 500 kGy. We evaluate also the role of the protective layers of the tested cable and its plastic behaviour up to 10000 µε.